1-1-2017

Exploring The Physics Of Proteins At Molecular Level By Neutron And X-Ray Scattering

Utsab Raj Shrestha
Wayne State University,

EXPLORING THE PHYSICS OF PROTEINS AT MOLECULAR LEVEL BY NEUTRON AND X-RAY SCATTERING

by

UTSAB R. SHRESTHA

DISSERTATION

Submitted to the Graduate School

of Wayne State University,

Detroit, Michigan

in partial fulfillment of the requirements

for the degree of

DOCTOR OF PHILOSOPHY

2017

MAJOR: Physics

Approved By:

_____

Advisor

_____

_____

_____

_____

DEDICATION

I dedicate this work to my loving parents and wife, Prema for their constant support, encouragement and belief on me. Specially, this dissertation is dedicated to my daughter, Utsaha.

DECLARATION

I, **Utsab R. Shrestha**, declare that this dissertation titled, **Exploring the Physics of Proteins at Molecular Level by Neutron and X-ray Scattering** and the work reported in it are from my own original research.

I confirm that:

- This work was done wholly or mainly while in candidature for a research degree at Wayne State University.
- Where any part of this dissertation has previously been submitted for a degree or any other qualification at this University or any other institution, this has been clearly stated.
- Where I have consulted the published work of others, this is always clearly cited.
- Where I have quoted from the work of others, the source or reference is always provided or cited. With the exception of such quotations, this dissertation is completely my own work.
- I have acknowledged all main sources of help.
- Where the dissertation is based on work done by myself jointly with others, I have made clear exactly what was done by others and what I have contributed myself.

Signed: _____ Date: _____

ACKNOWLEDGEMENTS

I would like to start with my sincere thanks to the department chairs Prof. David Cinabro (current) and Prof. Ratna Naik (former). My sincere gratitude to Prof. Jogindra Wadehra for his continuous guidance and support from the very first day. His advice for registering the courses and making the plan of work for the degree were really helpful.

I was very fortunate to take two courses, Thermal Physics and Advanced Soft Matter Physics with Prof. Paul Keyes before he got retired. I learned a lot from his classes. I also learned a lot from Statistical Mechanics course taught by Prof. Zhi-Feng Huang. Their lessons were very helpful that provided me the solid conceptual framework for conducting the research in biophysics. I also thank all other professors with whom I took other courses.

I earned a good experience by teaching the undergraduate laboratories and quiz classes while I was a GTA. I would like to thank our lab instructor Dr. Scott Payson and faculty members for their guidance and support for preparing the labs and quiz classes. I am also thankful to all my colleagues from the department with whom I took the courses. Specially, I thank Abir for having discussions in the course works that we took together. Apart from teaching the courses, I received a huge support for all the administrative works from all the staff members of physics department. They were more than generous to provide all the necessary office help.

I joined Dr. Xiang-Qiang Chu's group in winter 2012. I am very honored to have one of the very young, talented, and enthusiastic professors as my research advisor, who always encouraged and motivated me to think independently. Throughout my fruitful years under her supervision, I have received a great opportunity to learn and explore some of the major challenges in biophysics. Her guidance has led me to implement the knowledge of physics in the interdisciplinary fields such as biophysics and nanomaterials. She was always available there to provide the necessary help whenever I needed. She always encouraged and provided the opportunities to participate in local or national conferences. Therefore, I participated at least a couple of conferences and presented our work each year, which boosted my confidence

and provided the opportunity to explore the ongoing research activities. I sincerely thank her for all the support and I do not have any word to express my gratitude to her.

I had a wonderful time (academically and personally) with the ex-postdoctorate fellow, Dr. Debsindhu Bhowmik during his time of two and half years in our group. He was a very helpful person with a good knowledge of neutron scattering and molecular dynamic simulation. We had very productive experiments and discussions together. We became good friends and I feel lucky to have a friend like him.

My sincere thanks to all the dissertation committee members, Prof. Zhi-Feng Huang, Prof. Takeshi Sakamoto, Prof. Christopher Kelly, and Prof. Wen Li. Specially, I thank Prof. Wen Li for accepting to become the external committee member at the last moment. I appreciate their valuable time for reading, evaluating and suggesting the work on this dissertation.

I would also like to acknowledge the graduate school for providing the graduate teaching and research assistantships for pursuing the degree. This program has helped me for the successful completion of the degree. I am also very grateful to the Rumble fellowship from the university that I received in the 2015-2016 academic year, which gave me a huge opportunity to focus and spend more time on the research activities.

All of our experiments are performed at the neutron and X-ray scattering sources at different national laboratories. These experiments and the science what we do would not have been possible without the support from those labs and the staffs working there. Therefore, I am very much thankful to the instrument scientists and staffs, Dr. Eugene Mamontov, Dr. Shuo Qian, Dr. William Heller, Dr. Hugh O'Neill, Dr. Andrey Podlesnyak, Dr. Sai Venkatesh Pingali, Dr. Linin He, Dr. Qiu Zhang, and Dr. Naresh Osti from Oak Ridge National Laboratory; Dr. Madhusudan Tyagi, Dr. John Copley, Dr. Wei Zhou, and Dr. Juscelino Leão from NIST Center for Neutron Research; Dr. Ahmet Alatas and Dr. Bogdan Leu from Argonne National Laboratory; and Dr. Vito Graziano from Brookhaven National Laboratory for their help. I greatly appreciate their suggestions and discussions for planning

the experiments at the beamlines.

Apart from my academic career, I feel very privileged to have friends Raj Shrestha, Sandip Aryal, and Shankar Karki who have always been there in my good and bad times. I am also thankful to my other family members, relatives and friends for their kind words of motivation. I specially thank my younger brother, Utsuk and sister-in-law, Trishna for their support to the family.

Finally, I would like to remember my parents, who are always my source of inspiration. I think all I have achieved in my life is from their guidance to choose the right path to succeed. Before I finish, I am very thankful to my wife, who has supported in every step of my life and always been there for me through my ups and downs. I truly appreciate for understanding me despite the whatever time I spent with her.

"Everything that living things do can be understood in terms of the jigglings and wigglings of atoms."

- Richard P. Feynman

PREFACE

This dissertation comprises a four and half years of research work carried out to pursue a Ph.D. degree at the department of Physics and Astronomy, Wayne State University. The main goal of research is to understand the biological activities of proteins by investigating the structure and dynamics at molecular level. All the experiments were performed at national neutron and X-ray facilities of the United States. The works presented here mainly demonstrate the use of various state-of-the-art neutron and X-ray spectrometers to unravel the protein enzymatic activities. The experimental methods, data analysis and the interpretation of the results extensively use the broad knowledge of physics for understanding the mechanisms of living systems. Therefore, this work comes under one of the elevating topic in interdisciplinary science, 'biophysics'.

In the recent years, neutron and X-ray scattering are widely increasing techniques in biomolecular research. Such techniques can be used to study the biomolecular structure and dynamics at sufficiently high-resolution. Several neutron and X-ray scattering techniques have provided a new insight into the existing biomolecular problems. In this dissertation, some of the major biophysical questions are addressed with comprehensive solutions. Chapter 1 gives a very brief introduction to the biomolecular structure and dynamics pivotal for their functions. Chapter 2 provides the basic description of the neutron and X-ray scattering theory, techniques, and applications in the study of structure and dynamics of biomolecules. The next four chapters 3, 4, 5 and 6 cover the current biophysical challenges. These challenges (projects) are investigated using neutron or X-ray scattering methods, which provides a new insight for understanding the underlying biological mechanism. Finally, a brief summary of the dissertation is discussed in chapter 7.

Utsab R. Shrestha
Detroit, United States

TABLE OF CONTENTS

LIST OF TABLES

LIST OF FIGURES

LIST OF ABBREVIATIONS

1D	One-dimensional
2D	Two-dimensional
3D	Three-dimensional
tRNA	transfer ribonucleic acid
COX	Cyclooxygenase
PGH_2	Prostaglandin H_2
ACE	Angiotensin converting enzymes
MBP	Maltose-binding protein
MppA	Murein peptide permease A
IPPase	Inorganic pyrophosphatase
PPi	Pyrophosphate
Pi	Orthophosphate
Tt	Thermococcus thioreducens
HEWL	Hen-egg white lysozyme
GPCR	G-protein-coupled receptor
7TM	Seven alpha-helical transmembrane
DDM	n-dococyl-β-D-maltoside
CHAPS	3-[(3-cholamidopropyl)dimethylammonio]-1-propanesulfonate
DDAO	Dodecyldimethylamine oxide
RDM	Rhodopsin disk membrane
GFP	Green fluorescent protein
HSA	Human serum albumin
BSA	Bovine serum albumin
PBP	Periplasmic ligand-binding protein
IPTG	Isopropyl-D-thiogalactopyranoside
AFP	Anti-freeze protein

AFGP	Anti-freeze glycoprotein
ND	Nanodiamond
GF	Graphene foam
PDC	Protein-detergent complex
CMC	Critical micellar concentration
SDS	Sodium dodecyl sulfate
PAGE	Polyacrylamide gel electrophoresis
NMR	Nuclear magnetic resonance
SDSL	Site-directed spin labeling
BNS	Brillouin neutron spectroscopy
AFM	Atomic-force microscopy
CVD	Chemical vapor deposition
ATP	Adenosine triphosphate
SAS	Small-angle scattering
SANS	Small-angle neutron scattering
SAXS	Small-angle X-ray scattering
WAXS	Wide-angle X-ray scattering
TOF	Time-of-flight
QENS	Quasi-elastic neutron scattering
INS	Inelastic neutron scattering
IXS	Inelastic X-ray scattering
EINS	Elastic incoherent neutron scattering
FWS	Fixed window scan
MD	Molecular dynamics
SLD	Scattering length density
HWHM	Half-width at half maximum
FWHM	Full-width at half maximum

EISF	Elastic incoherent structure factor
ISF	Intermediate scattering function
iFT	inverse fourier transform
MSD	Mean-square displacement
MCT	Mode coupling theory
TH	Thermal hysteresis
NV	Nitrogen-vacancy
EL	Energy landscape
DHO	Damped-harmonic oscillator
DS	Dark-state
LAS	Light-activated state
LED	Light emitting diode
EC	Enzyme commission
PDB	Protein data bank
SD	Standard deviation
UV	Ultraviolet
CS	Conformational substate
PAN	Peak analysis software
DAVE	Data analysis and visualization environment
BASIS	near-backscattering spectrometer
HFIR	High-flux isotope reactor
SNS	Spallation neutron source
DCS	Disk chopper spectrometer
HFBS	High flux backscattering spectrometer
NIST	National institute of standards and technology
NCNR	NIST center of neutron research
BNL	Brookhaven national laboratory

NSLS National synchrotron light source

ORNL Oak Ridge national laboratory

APS Advanced photon source

LIST OF SYMBOLS

T_D	Dynamic transition temperature
λ	Wavelength
$\vec{k}$	Momentum-vector
$\vec{v}$	Velocity
$\vec{Q}$, $\vec{q}$	Wave-vector transfer or scattering vector
ω	Energy tranfer
b	Scattering length
σ	Scattering cross-section
ρ	Scattering length density
$S(Q)$, $S(q)$	Static structure factor
$I(q)$	Scattering intensity
$I(0)$	Forward scattering intensity
$P(r)$	Particle form factor
R_g	Radius of gyration
D_{max}	Maximum dimension of a particle
$S(Q,\omega)$	Dymnamic structure factor
$I(Q,t)$	Intermediate scattering function
$< x^2 >$	Mean-square displacement
$\Gamma(Q)$	Half-width at half maximum
a	Radius of a confined sphere
p_0	Fraction of immobile atoms
τ_β	Characteristic β-relaxation time

LIST OF PHYSICAL CONSTANTS

$k_B = 1.38\times10^{-23}$ J/K	Boltzmann's constant
h = 6.626×10^{-34} J s	Planck's constant
c = 2.99×10^{8} m/s	Speed of light
R = 8.314 J/mol K	Ideal gas constant

CHAPTER 1 INTRODUCTION

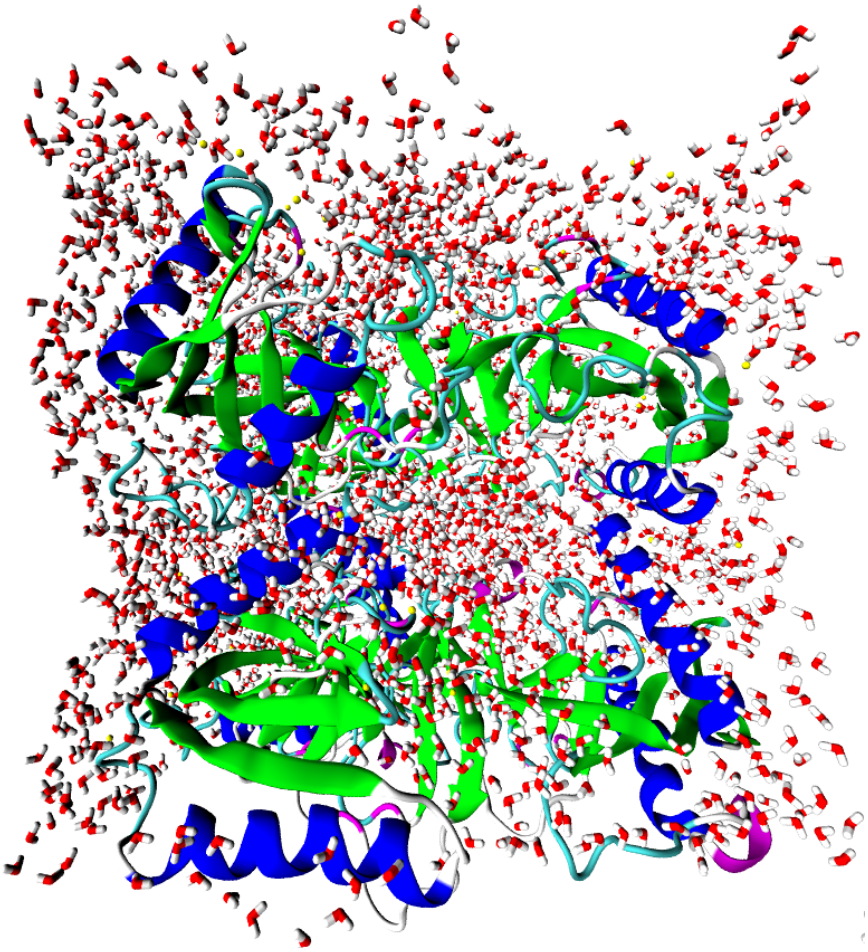

"Life ... is a relationship between molecules."
- Linus Pauling

1.1 Biomolecules

Biological molecules are the basis of all the living organisms that help in growth and survival. They are mainly made up of complex organic compounds with carbon, hydrogen and oxygen as fundamental constituents along with other elements like nitrogen, sulphur, phosphorous etc to form macromolecules. These macromolecules are present in the cells and tissues that enable an organism to function biological activities. The four main classes of

biological macromolecules are carbohydrates, lipids, nucleic acids and proteins [1]. Carbohydrates such as starch and glycogen act as energy storage molecules. Plants store their food in the form of starch during the photosynthesis, whereas many animals store energy as glycogen. Cellulose is carbohydrate that is present in the cell wall of bacteria and plants to provide rigidity to the organisms. Some carbohydrates are associated to several proteins and lipids in the form of glycoproteins and glycolipids respectively for specific functions. Lipids are non-polar organic molecules, which are insoluble in water responsible for long-term energy storage. Ribonucleic acid (RNA) such as messenger RNA, transfer RNA and ribosomal RNA carry out the synthesis of necessary proteins. On the other hand, deoxyribonucleic acids (DNAs) are capable of storing the genetic information in the cells. Similarly, proteins are another important biomolecules that play vital roles in catalytic activities, cellular signaling, regulations of biological processes and defense against bacteria and viruses. One of the major roles is the transportation of oxygen through blood to different tissues by haemoglobin, a protein attached to heme group. Therefore, the biological macromolecules are responsible for all life processes.

Enzymes are the proteins that catalyze the biochemical reactions by the processes such as bond formation and break-down. They are responsible for the synthesis of biological macromolecules, break-down of nutrients and transforming chemical energy into metabolic activities. Many enzymes require the additional chemical groups, such as Mg^{2+}, Zn^{2+}, Mn^{2+}, Fe^{2+} or complex organic molecules, known as coenzymes to perform the catalytic activities. Specific functional groups are transiently carried by the coenzymes during the cellular processes. In general, enzymes are provided the name by adding *-ase* in the suffix. They are categorized into six different classes according to the types of the reaction they catalyze:

Isomerases - rearrange atoms within a molecule, *Hydrolases* - transfer functional groups to water, *Oxidoreductases* - transfer hydride ions, *Transferases* - transfer group reactions, *Lyases* - add groups to double bonds and *Ligases* - form C═C, C═S, C═O and C≡N bonds by condensation reactions coupled to ATP cleavage. All these catalytic reactions at cellular levels are affected by the activity of proteins and their positions within the cells. The collective mechanism of all the processes carried out by the enzymes and coenzymes at the level of cells and tissues affect the physiological properties and hence overall function of the organisms [1].

Due to the predominant role of proteins in the life processes, loss in their activity can cause many severe diseases in humans such as Alzheimer, Parkinson, cancer and many other metabolic deficiencies. Thus, about 80% of the therapeutic drug targets are proteins. Most of the pharmaceutical drugs bind with the active sites of enzymes, which deactivate them and hence help in reducing or curing the particular diseases. For example, a drug like ibuprofen helps in reducing pain, inflammation or fever by restraining *Cyclooxygenase* (COX) enzymes, which convert arachidonic acid to prostaglandin H_2 (PGH_2). Similarly, the anti-hypertensive classes of drugs are used to treat the high blood pressure. These drugs inhibit the activity of angiotensin converting enzymes (ACE). Furthermore, enzymes have growing application in industry due to their catalytic behavior on the substrates to yield high-efficiency under the ambient conditions. These applications include starch processing, dairy, baking, brewing, detergent, animal feed, bio-sensors and many other [1].

1.2 Complex structures of protein

Proteins are the complex hierarchically organized structures with overcrowding molecules. The fundamental structure of protein starts with the long chain or sequence of amino acids,

known as primary structure [2, 3]. The different segments or groups of such amino acids form ordinary shapes like helices, sheets or loops. These are called secondary structures. Further, the secondary structure provides three-dimensional configuration by folding into specific shape, termed as tertiary structure. In general, most of the proteins perform the biological activities based on their tertiary structure and hence it is considered as the native structure [4, 5]. Nevertheless, many proteins exist in nature with more than one tertiary structure folded together to form a biologically active complex, known as quaternary structure. The schematic of protein structures are shown in Fig. 1.1 *A* [6], *B* [7], *C* [8], and *D* [9]. These structures play a vital role in biochemical functions such as catalysis, molecular signaling, providing structural components, molecular switches and binding with substrates.

The primary structure of protein consists of 20 different amino acids held together by peptide bonds. The amino acids comprise the central carbon atom or α-carbon (C_α), surrounded by four different substituents. These substituents are hydrogen atom, carboxyl group (COOH), amino group (NH_2) and side-chain (R). All the amino acids have common α-carbon along with hydrogen atom, carboxyl and amino groups, which is called a backbone. But, they differ from each other due to their side-chain group. Thus, amino acids are often considered as residues when included within protein chain due to the uniqueness of the side-chain group. The 20 natural amino acids are: Glycine (Gly), Alanine (Ala), Valine (Val), Leucine (Leu), Isoleucine (Ile), Proline (Pro), Phenylalanine (Phe), Serine (Ser), Threonine (Thr), Cysteine (Cys), Asparagine (Asn), Glutamine (Gln), Glutamate (Glu), Aspartate (Asp), Histidine (His), Arginine (Arg), Lysine (Lys), Methionine (Met), Tyrosine (Tyr) and Tryptophan (Trp). Due to their tendency to interact with each other and water, they have important role in biochemical property of proteins. The amino acids, Ala, Val, Leu, Ile, Pro,

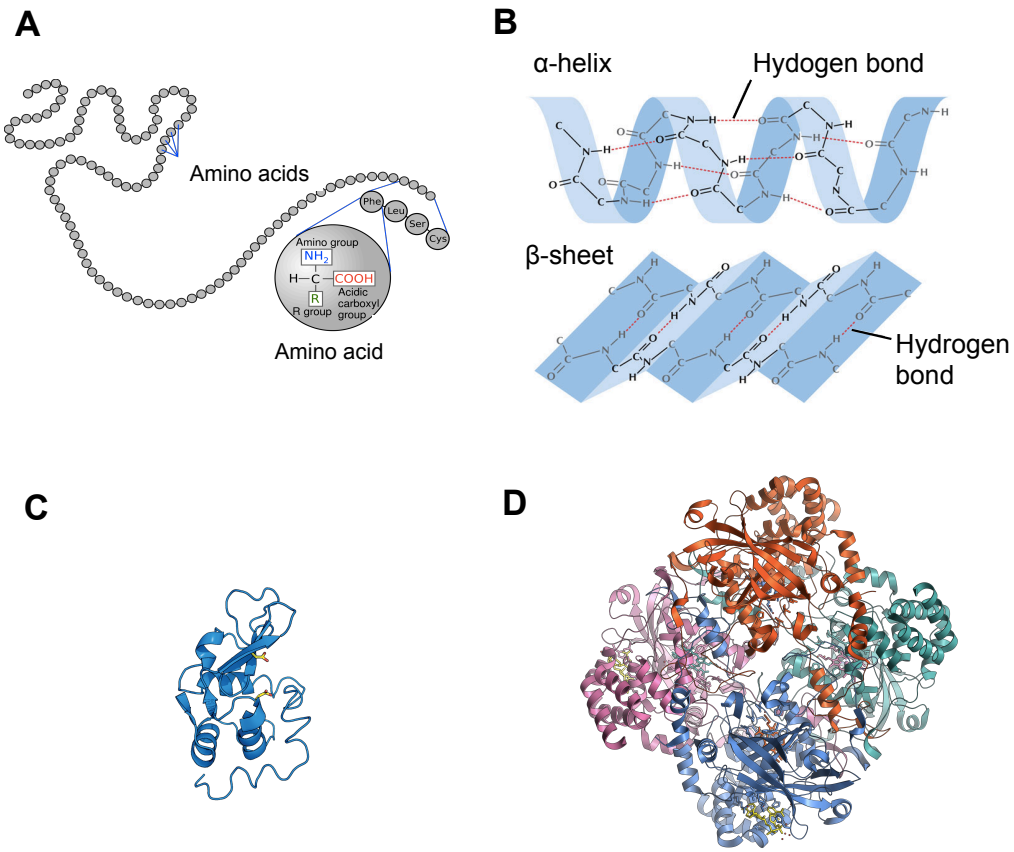

Figure 1.1: Schematic of protein structures. (A) Primary structure, (B) Secondary structures - Alpha helix and beta-sheet, (C) Monomer of lysozyme (tertiary structure), and (D) Quatenary structure of catalase. All the figures are taken from google.

Phe and Ser are hydrophobic in nature that only interact with *van der Waals* force giving rise to hydrophobic effect. On the other hand, amino acids, Thr, Cys, Asn, Gln, Glu and Arg are hydrophilic, which make hydrogen bonds with each other, peptide backbone, organic molecules and water. The remaining amino acids, Lys, Met, Tyr and Trp are amphipathic (both hydrophobic and hydrophilic) that help them to form interfaces.

The residues in polypeptide chain fold into helical or spiral structure, which is the first type of secondary structure discovered by Linus Pauling in 1951 and it is termed as α-helix.

It consists of hydrogen bonds inside forming the repeating pattern and the oxygen atom on the carbonyl group. Each helix turn contains 3 or 4 residues with distance between adjacent C_α as 1.5 Å, giving rise to very compact structure. On the other hand, a very less compact structure with 5 to 10 residues and distance of about 3.5 Å between the adjacent C_α is formed. This is the second type of secondary structure, known as β-strand and the number of β-strands forms a β-sheet that are linked together by the regular hydrogen bond between N—H and C—O in the backbone of amino acids. α-helices and β-sheets are very common structures within proteins to provide the compactness to fit into the overcrowded cytoplasm of the cell. Such nature of secondary structures helps to fold into specific configuration, which is the basis for the global three-dimensional structure, known as tertiary structure. The tertiary structure executes the complex biological functions. Futhermore, the tertiary structure can be globular or fibrous. The globular proteins are soluble in water with almost spherical shape that are responsible for most of the enzymatic activities, whereas fibrous proteins are water-insoluble with elongated structure that provide mechanical strength to the organisms. Quaternary structure of protein consists of several tertiary structures folded together by non-covalent bonds to gain the compactness and stable configuration. Based upon the number of polypeptide chains, such structure is termed as monomer (only 1 chain), dimer (2 chains), trimer (3 chains) and so on. Protein is considered as oligomer, if it exceeds more than one chain, in general, with even number of chains.

The folded structure of protein is stabilized by the following bonds: covalent bond, disulfide bond, salt bridge, hydrogen bond, electrostatic interaction and *van der Waals* interaction. All these forces bring amino acids together for interaction with each other and thus help to fold. Most of the interactions between different residues are non-covalent that

allow stabilization of folded structure. These interactions are very weak compared to the covalent bond, thus leading the protein as dynamic entity. The electrostatic interactions mainly occur on the surface of the protein due to interaction between the polar residues and ions of the solvent. Non-polar interactions take place inside the protein cores providing compactness that optimize *van der Waals* interactions.

1.3 Protein motion: A heterogeneous dynamic picture

It has been well understood that the proteins are the heterogeneous dynamic entities rather than the static pictures. They continuously fluctuate about their average structure showing the wide variety of internal motions from femtoseconds to seconds [10]. Such diverse motions are responsible for many biological activities within the organisms. A large number of functional groups in protein is connected by the strong covalent bonds with the polypeptide chain providing the structural rigidness. However, the side-chain groups are intrinsically capable of rotating and jumping from one position to the other due to the available thermal energy [10]. Such local motions have very small atomic displacements that occur in a very short time-scale of the order of few femtoseconds to a nanosecond. On the other hand, the large amplitude motions in slow time-scale (hundreds of nanoseconds to a few seconds) are due to the rigid body motions such as loop movement, hinge motion, collective domain motion, and movement during the protein folding mechanism. All these motions in proteins play a major role in several biochemical processes crucial for biological activities such as - formation and breakdown of covalent bonds; making of hydrogen bonds; transfer of protons, electrons, hydride ions between chemical groups; electron tunneling; structural reorganization of solvent; enzyme catalysis; ligand binding and allostery; protein folding and denaturation [1]. The wide variety of motions in proteins occurring at different time-scale

are listed in Table 1.1 below [1].

Protein dynamics are crucial for the biophysical and biochemical processes. However,

Table 1.1: Types of motions in proteins at different time-scale.

Time-scale (second)	**Type of protein motions**
$10^{-14} - 10^{-13}$	Bond vibration
$10^{-12} - 10^{-11}$	Elastic vibration of globular region
$10^{-12} - 10^{-9}$	Methyl group rotation
$10^{-11} - 10^{-10}$	Roatation of surface side-chains
$10^{-11} - 10^{-7}$	Hinge bending of domain interfaces
$10^{-9} - 10^{-6}$	Loop movement
$10^{-8} - 10^{-7}$	α-helix formation
$10^{-6} - 10^{-3}$	Large domain motions
$10^{-6} - 10^{4}$	Protein folding

the direct correlation of a wide range of protein dynamics to its function still remains a matter of broad discussion. There are several indirect experimental evidence that supports the heterogeneous motion to the protein activity, which is also theoretically validated by the molecular dynamic simulations. The fast motions from femtosecond to picosecond promotes the hydrogen-transfer reactions essential for enzyme-mediated catalysis. Such chemistry of enzyme has been observed from the study of kinetic isotope effects and computational methods [11–13]. The experimental and theoretically simulated observations of the atomic fluctuations in the hinge regions of adenylate kinase occurring in the time-scale of picosecond to nanosecond expedite the large amplitude, slow lid motions [14]. This helps in producing catalytically competent state suggesting the linkage between the fast motions and the catalytic activities. The folding mechanism of protein to its functional conformation occurs from the nanoseconds to microseconds [15]. NMR study of the three-helix bundle protein

Engrailed homeodomain suggests the sudden collapse of protein structure to the intermediate structure with a large number of α-helices during the folding process. Such structures are the major component of the denatured state under the conditions that favors the folding with unstructured side chains. This study has allowed to characterize all of the necessary structures along the folding and unfolding pathways in proteins [15]. Recent single-molecule kinetic analysis on maltose-binding protein (MBP) provided the direct evidence of ligand binding and dissociation by studying the intrinsic opening rate of the protein. Such hinge motion occurs from microsecond to second that is essential for signal transducin, enzyme catalysis, and cellular regulation [16, 17].

1.4 Energy landscape and conformational substates

Proteins are the dynamic soft matter rather than a static objects for physicists. Thus, the understanding the real-time activity of protein requires the inclusion of the fourth dimension as 'time' in addition to the physiologically freeze-trapped three-dimensional crystal structures [14, 18]. This introduces the idea of the multidimensional free energy landscape, which defines the relative probabilities of several protein conformations at equilibrium or non-equilibrium state [14, 18]. The thermal energy of the order of k_BT per atom, where k_B is the Boltzmann constant and T is the absolute temperature, triggers the biomolecules to sample different conformations around the average structure. Such slightly different conformations are called conformational substates (CSs) [19]. CSs are due to the wide range of spatial and temporal scales of protein internal motions. They are usually separated by the energy barrier in the multidimensional free energy landscape that is rugged forming hills and valleys of varying heights and depths [20]. Each valley represents the CS, which may have the same overall structure and biological activity, but significantly different structural details and the rate of

the activity [19]. The available thermal energy is very crucial for the specific CS. Protein structure switches the CS instantaneously exploring the free energy landscape. At very low temperature, the protein conformation remains confined in a particular CS. But, at the physiological temperature, protein samples CSs for the minimum potential energy. Such sampling motions of the protein conformation can be described similar to the equilibrium fluctuations and relaxation processes in glasses and spin glasses [21].

The idea of protein free energy landscape along with CSs has been well-accepted and has

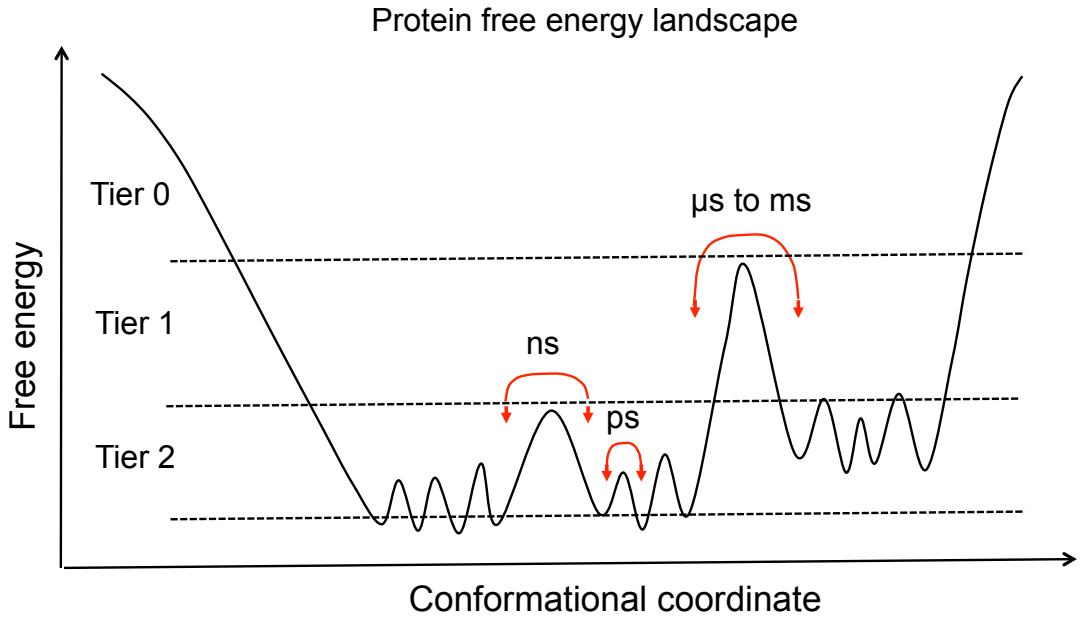

Figure 1.2: Time-scale of protein motion in protein free energy landscape.

become very intuitive for exploring the protein dynamics at different time-scale. Accordingly, the slow and fast dynamics of proteins can be represented in the free energy landscape divided into three distinct tiers as shown in Fig 1.2 [18]: tier-0 defines the larger amplitude and slower dynamic processes in the time-scale of microseconds to milliseconds, whereas

tier-1 and tier-2 represent the small amplitude fast dynamic processes from picoseconds to nanoseconds [18]. Tier-0 dynamics (slow process) includes the slow transition between protein conformations separated by the energy barrier much larger than k_BT. Such events occur rarely due to the less probability of the conformation that allows the transitions [14, 18]. The conformational transitions in tier-0 are essential for the various biological processes such as protein-protein interaction, enzyme catalysis, ligand binding and signal transduction. On the other hand, tier-1 and tier-2 dynamics include the rapid fluctuations within the valleys of tier-0. Such fluctuations are the transitions between CSs usually separated by the energy barriers less than k_BT. These dynamics are the statistically distributed CSs due to the fluctuations of small groups of atoms on the nanosecond time-scale such as loop motions and the local atomic fluctuations on the picosecond time-scale such as side-chain rotations [14, 18]. The biochemical processes such as hydride transfer, electron transport, and electron tunneling that are crucial for the enzyme catalysis, fall within these tiers. These slow and fast conformational dynamics allow proteins to inherit the local and global flexibility necessary for enzyme activity.

1.5 Glassy behavior of proteins

Many studies suggest the short-time small amplitude fluctuations of residues in proteins are liquid-like, whereas the large amplitude motions for the stabilization of folded structures are analog to the solids [10]. In fact, they are the densely packed complex molecules that can be considered as aperiodic crystals. Thus, from the physics point of view, proteins are many-body systems that fold into the three-dimensional structures. Although some of their properties are similar to the liquids and solids, they possess characteristic structure and dynamic phenomena analog to the glasses and spin glasses. The most common feature of

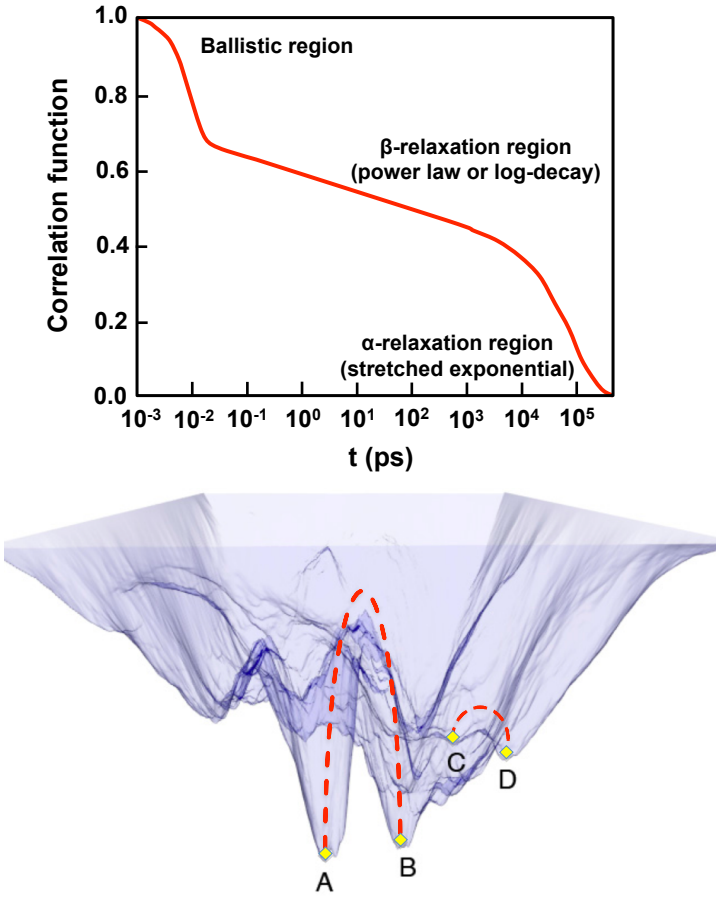

Figure 1.3: Schematic of the correlation function of different relaxation processes in proteins (top) and the transition between conformational substates of such processes in the multidimensional free energy landscape (bottom).

proteins and glasses is the noncrystallinity, which are amino acid residues in proteins and glassy liquids in glasses [22]. Therefore, they both consist of nonperiodic spatial arrangement of atoms or molecules. Such structure is randomly oriented in glasses, whereas selected by the evolution for the biological function in proteins [23]. The atoms in glasses and spin glasses are held together by the strong forces in all three directions. Similary, the large number of functional groups are connected to the backbone or polypeptide chain by the strong covalent bonds and the cross-links are made by the weak forces such as hydrogen bonds,

disulfide bonds, *van der Waals* interaction and salt bridges in proteins. Furthermore, several experimental results have elucidated the glass-like behavior of proteins. Such behaviors are the existence of both short- and intermediate-range orders forming the random elastic networks; the dynamic transition at temperature T_D ∼200 K - 240 K due to the rapid onset of anharmonic motions; the transition from liquid-like to solid-like behavior upon folding into the native structure; the denaturation of protein yields strong-to-fragile liquid transition; the existence of a boson peak, one of the typical characteristics of the glass formers; the slow α-relaxation process due to the large domain motions and the fast β-relaxation process due to the local structures and the side chains [22]. Basically, proteins possess a non-exponential relaxation of the density correlation function over a wide range of time-scale similar to the glasses. Such processes can be simplified into three different regions: (i) very fast Gaussian-like ballistic region of the order of few femtoseconds, (ii) β-relaxation region in the time-scale of few picoseconds to a couple of nanoseconds that can be represented either by the power-law or logarithmic decay, and (iii) finally followed by the α- relaxation region in the time range of hundreds of nanoseconds to few milliseconds governed by the stretched exponential decay or Kohlrausch-Williams-Watts law [22]. The α- and β-relaxation processes can be represented in the multidimensional free energy landscape by the transitions A$\longleftrightarrow$B and C$\leftrightarrow$D respectively as shown in Fig. 1.3. For the α-relaxation process, $E_a \gg k_BT$, whereas for β-relaxation process, $E_a \lesssim k_BT$.

1.6 Protein hydration

Hydration water in biomolecules is an essential component of the biological activities. It dramatically influences the enzyme reaction rates, folding and unfolding of the native structure, ligand-binding and many other biological functions of globular proteins as observed

experimentally from structural, dynamical and thermodynamical investigations [24, 25]. For the full hydration of a globular protein with at least a monolayer of water requires hydration level (h) of $\sim$0.38 (i.e., 0.38 gram of water per gram of protein) [24, 25]. Protein behaves more like solid at such hydration and the hydration water is more viscous compared to the bulk water [24, 25]. Moreover, the water in the hydrated protein can be considered at two specific regions bound to the protein ignoring any presence of bulk water on the outermost surface: (i) the strongly bound internal water molecules in the cavities and deep clefts of the protein, and (ii) surface bound water molecules that are structurally and dynamically different from the bulk one [26]. The former water molecules are responsible for providing flexibility with sufficient amount of thermal energy, but may unfold or denature the protein molecules under extreme conditions such as high temperature or pressure. On the other hand, the latter water molecules largely influence the rapid onset of anharmonic motions of protein at physiological temperature. Such dynamic behavior of protein and hydration water has been observed at temperature 200 K - 240 K, known as dynamic transition temperature, T_D in several inelastic and quasielastic neutron scattering experiments [27–32].

The coupled motions of the protein-water system have been still under investigation to comprehend the role and influence of hydration water to protein motions and functions. The long-debated issue is that, whether the protein dynamic heterogeneity slaves to such hydration shell or it is just coupled to some extent [33–36]. One of the evidence of such controversial topic is the dynamic transition observed at T_D in the hydrated protein analog to that of the bulk water [27, 28, 35, 37–42]. H. Frauenfelder and colleagues proposed the folding mechanism of protein, which slaves to the solvent dynamics occurring in the time-scale of microseconds to hours [34]. In addition, P. W. Fenimore et al. revealed both solvent-slaved

and non-slaved dynamic processes in protein [33]. On the other hand, S. Khodadadi et al. showed the experimental evidence of solvent independent dynamics and strongly suggested to reconsider the concept of slaved dynamics of protein to hydration shell [36]. Thus, the universal picture of pathways for the dynamic processes in hydrated protein has yet to be discovered.

1.7 Role of temperature on protein flexibility

The native conformation of protein that we consider is the most stable state or the state with the minimum energy under the physiological conditions. However, the protein can sample the CSs with slightly different energy through the available thermal energy in the absence of other force [1]. Thus, the distribution of CSs in protein is statistical in nature and depends on the surrounding temperature. The protein has the thermal energy of the value equal to RT, where R is the gas constant and T is the absolute temperature. This thermal energy at room temperature can be converted into the kinetic energy for the bond vibration and atomic fluctuations. Thermal fluctuations act as the lubricant in protein that enables the conformational changes on a physiological time-scale [42]. At absolute zero temperature, the atoms are tightly bound within a single conformation. When the temperature is increased, the protein starts to vibrate harmonically about its equilibrium position in one CS. Further, if the temperature is raised to provide the sufficient thermal energy, then the motion of protein changes from harmonic to anharmonic due to jump between CSs [42]. Thus, the protein becomes soft and flexible and, hence biologically active. Such dynamic transition in proteins including other biomolecules is observed at T_D $\sim$200 K - 240 K. Therefore, the temperature plays a major role for the conformational flexibility of proteins for enzymatic activities by increasing their conformational fluctuations. Nonetheless, the protein structure

gets distorted and denatured at extreme temperature.

CHAPTER 2 METHODS: NEUTRON AND X-RAY SCATTERING

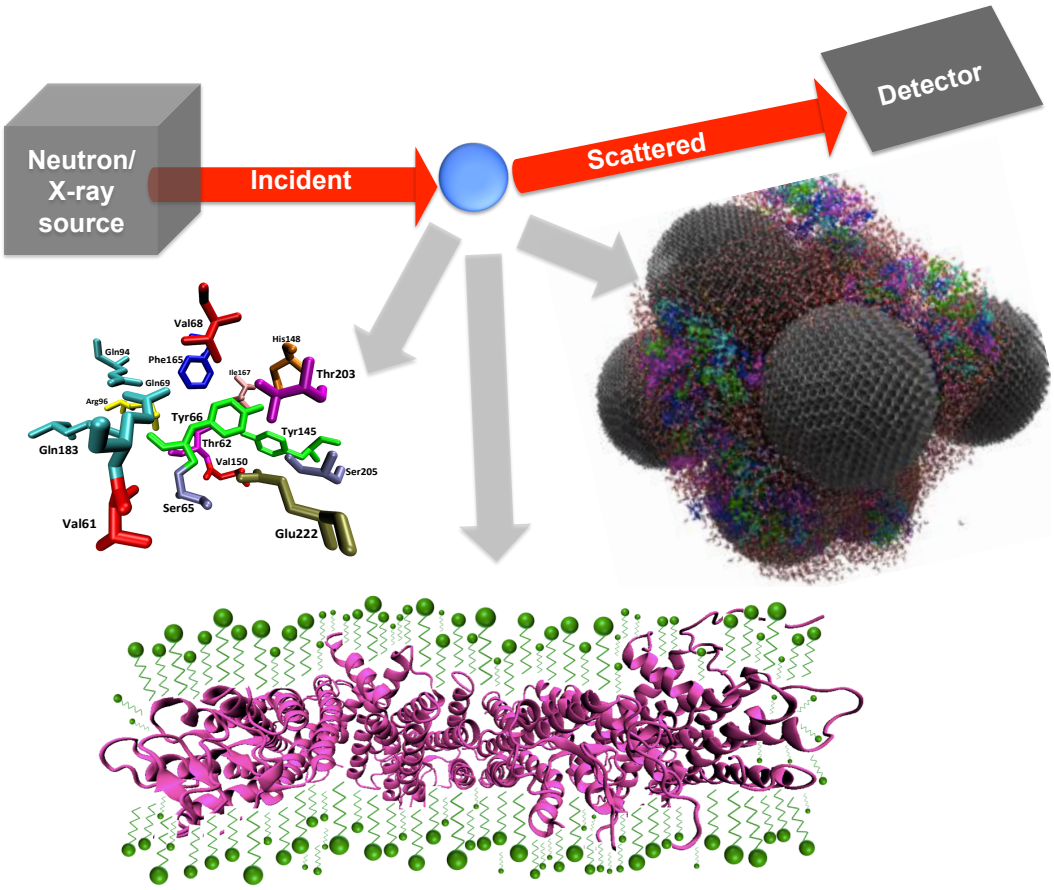

"Neutrons tell us where atoms are and how they move."
- Clifford Shull

2.1 Background

The structural and dynamical features of solids and liquids at atomic resolution can be studied by the fundamental nature of X-rays and neutrons. The wavelengths of both X-rays and neutrons are comparable to the atomic spacing in solids and liquids, thus, they can probe the structural features within the length scale from ~1 to 1000 Å. On the other hand, they have kinetic energies comparable to the dynamic phenomena in matters, which makes them possible to explore the dynamic processes of characteristic time scale from 10^{-15} to

10^{-6} seconds [43–47].

The low energy X-rays and neutrons interact weakly with matters and can penetrate deeply. Thus, both are non-destructive to the samples under the beam. However, the interactions of X-rays and neutrons with matters are significantly different from each other. X-rays interact with the electron cloud surrounding the atomic nuclei. Thus, the heavier atoms with a large number of electrons scatter more compared to the lighter atoms with a fewer number of electrons. This means the probability of interaction of X-rays with matters increases monotonically as a function of electron numbers [45, 48]. On the other hand, neutrons are chargeless particles with almost zero electric dipole moment so that they can penetrate more than X-rays and the charged particles like electrons. Neutrons interact through the nuclear forces with atoms, which are short-range of the order of fermi (1 fermi = 10^{-15} m). The interaction between neutrons and atomic nuclei depends upon the nuclear state and nuclear spin (since neutron has non-zero magnetic moment) [43, 44, 49, 50]. Furthermore, neutrons are isotope sensitive and thus, for instance, deuterium (^{2}H) scatters about 3 times more than hydrogen (^{1}H), which is indistinguishable for X-rays [43, 44].

X-ray and neutron scattering are widely used techniques in all forms of natural sciences such as physics, chemistry, biology, medicine, engineering, geology and many other [47, 48, 51, 52]. The most successful technique is diffraction that have revealed the crystal structures at atomic resolution of many solids including complex structure of biomolecules like proteins, DNA, RNA etc. In last couple of decades, the small-angle scattering has been successfully implemented to resolve the macromolecular structures in solution [47, 48]. Specifically, solution scattering has become the most successful technique to study the structure of biomolecules over X-ray/neutron crystallography and NMR spectroscopy. Since the

crystallography and NMR techniques require the good crystals and the low molecular mass samples respectively, a significant number of biomoleucles cannot be synthesized in such manner. In such cases, small-angle solution scattering has become an important complementary tool for these initiatives. For instance, the membrane proteins such as rhodopsin and aquaporin-0 are difficult to crystallize, but they can be solubilized and stabilized using detergent (amphiphilic molecules) in solution [53–56]. Thus, the solution scattering of protein-detergent complex can be useful tool to predict the structure of membrane proteins mimicking the native environment as with lipids. In addition, neutron and X-ray spectroscopies have been widely used to investigate the quantum phase transitions and critical points; phonons and electronic excitations in solids; boson peaks in glasses; diffusive motions in glasses and glass forming liquids; phase diagrams of surfactants; magnetic order and spin fluctuations in highly correlated systems; glass transition and reptation in polymers; transport phenomena in solids and glasses; lipid-membrane and protein-protein interactions. Furthermore, neutron scattering has a great advantage over most of the available techniques for studying the dynamics of biomoleucles. This is because more than one-half of the atoms in biological macromolecules are hydrogen, which has the largest incoherent neutron scattering cross-section [50, 52].

2.2 Scattering theory

The energy of X-ray and neutron are given by Eq. 2.1 and Eq. 2.2 respectively as expressed below,

$$E_X = \frac{hc}{\lambda} = hc|\vec{k}| \tag{2.1}$$

and

$$E_N = \frac{1}{2} m_N v^2 = \frac{\hbar^2 k^2}{2m_N} \tag{2.2}$$

where $|\vec{k}| = \frac{2\pi}{\lambda}$, $\vec{k}$ is the momentum or wave vector, λ is the wavelength, $\hbar = \frac{h}{2\pi}$, h is the planck's constant, c is the speed of electromagnetic wave, v is the velocity of neutron and m_N is the mass of neutron. In a scattering experiment, the scattered X-ray or neutron undergoes a change in momentum and energy after interacting with the sample as depicted in Fig. 2.1. The change in momentum is described by a momentum transfer vector or the scattering vector ($\vec{Q}$) given by,

$$\vec{Q} = \vec{k}_s - \vec{k}_i \tag{2.3}$$

where $\vec{k}_i$ and $\vec{k}_s$ are the incident and scattered wave vectors respectively. The change in momentum is $\hbar Q$. Also, the change in energy due to the change in magnitude of the wave vector ($\vec{k}$) for X-ray and neutron are given by Eq. 2.4 and Eq. 2.5 respectively:

$$\Delta E_X = E_s - E_i = \hbar\omega = \hbar c(|\vec{k}_s| - |\vec{k}_i|) \tag{2.4}$$

and

$$\Delta E_N = E_s - E_i = \hbar\omega = \frac{\hbar^2}{2m_N}(k_s^2 - k_i^2), \tag{2.5}$$

where ω is the frequency of energy transfer, E_i and E_s are the energies of incident and scattered X-ray/neutron respectively.

According to the wave theory, X-ray and neutron scattering experiments involve the interference phenomena between the wavelets scattered by the different scattering centers in the sample. These scattering centers are electrons for X-rays and nuclei for neutrons. The

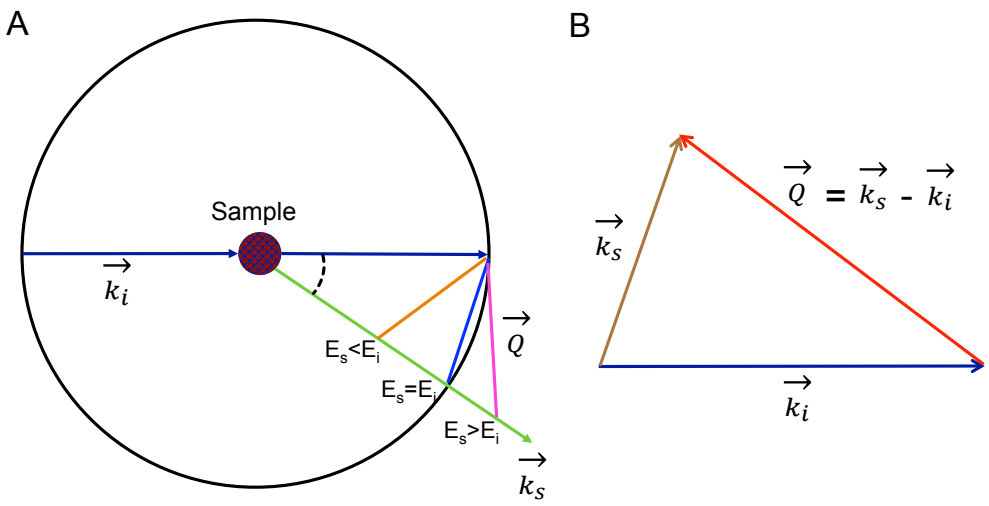

Figure 2.1: Schematic diagram of scattering event. (A) A plane wave of X-ray/neutron with momentum vector, k_i is scattered from the sample, which is scattered with momentum vector, k_s. (B) Representation of scattering vector ($\vec{Q}$), which is the difference between the incident momentum vector ($\vec{k_i}$) and the scattered momentum vector ($\vec{k_s}$).

incident beam of X-rays or neutrons is considered as the monochromatic wave that can be represented by a plane wave as,

$$\psi_i = e^{ikz} \tag{2.6}$$

where z is the distance between the scattering center and the detector. For a scattering event considering a fixed scattering center, the scattered wave is a speherical wave given by,

$$\psi_s = -\frac{b}{r}\, e^{ikr} \tag{2.7}$$

The quantity b is known as the scattering length of the scattering center, which is defined as the measure of the scattering ability of the scattering center after interaction with the incident X-ray or neutron. The negative sign in Eq. 2.7 is arbitary, which is used so that the positive

value of b indicates a repulsive interaction. The scattering length b is a complex number; the real part represents the scattering event, whereas the imaginary part corresponds to the absorption by the sample. Therefore, when the incident beam of X-rays/neutrons interacts with the sample, X-rays/neutrons are absorbed or scattered or both. The absorption is due to trapping by electron cloud (for X-rays) and by nucleus (for neutrons). On the other hand, scattering phenomenon is due to the very low energy of incident X-rays/neutrons that is not enough to create the internal excitations of the electronic shell (for X-rays) and the nucleus (for neutrons) [57]. However, the motions of the scattering centers such as thermal fluctuations and diffusion phenomena can be detected, which correspond to the energy much smaller than the incident X-rays/neutrons. If we consider the absorbing and scattering cross-sections of the target as σ_a and σ_s respectively, then the number of absorbing and scattering events after interaction of target with the incident beam of X-rays/neutrons are given by Eq. 2.8 and Eq. 2.9 respectively as expressed below,

$$N_a = \phi_i \sigma_a \tag{2.8}$$

and

$$N_s = \phi_i \sigma_s \tag{2.9}$$

where ϕ_i is the flux of incident beam, which has a unit in number of scattering events per second per barn (1 barn = 10^{-24} cm^2). The fundamental quantity determined in any scattering experiment is the differential scattering cross-section ($d\sigma_s/d\Omega$), which is defined as the probability of scattering event that will occur in the elemental solid angle $d\Omega$ in the

direction $\vec{\Omega}/|\vec{\Omega}|$ as shown in Fig. 2.2 and is given by,

$$\frac{d\sigma_s}{d\Omega} = \frac{N_s}{\phi_i d\Omega} \tag{2.10}$$

Then, assuming the scattering event is axially symmetric that depends only on the zenith

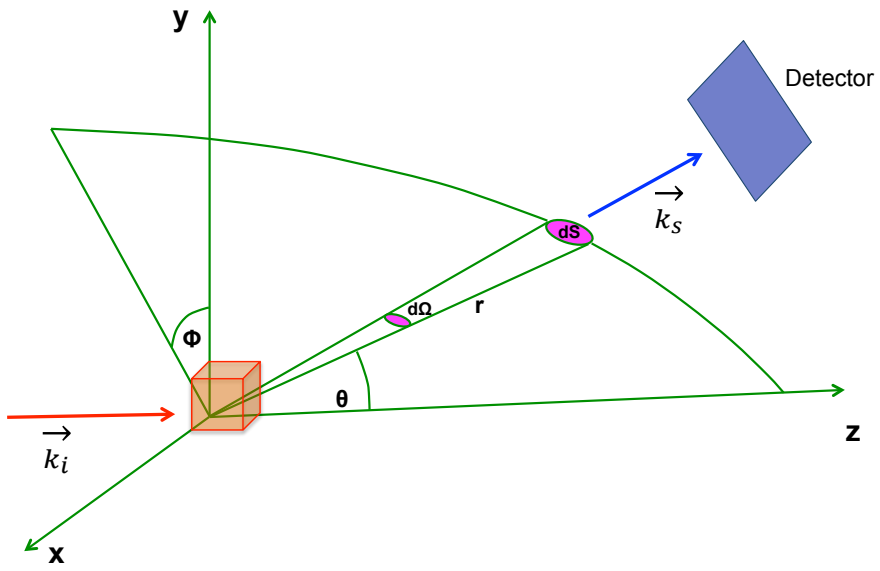

Figure 2.2: Schematic of scattering event.

angle (θ), but not on the azimuthal angle (ϕ), the total scattering cross-section ($\sigma_{s,tot}$) is given by,

$$\sigma_{s,tot} = \int_0^{\pi} 2\pi \, sin\theta \, d\theta \, \frac{d\sigma_s}{d\Omega} = \sigma(say) \tag{2.11}$$

Further, the differential scattering cross-section, $d\sigma/d\Omega$ from a single fixed scattering center due to incident beam of X-rays/neutrons moving with a velocity v (for X-ray, $v = c$) and flux ϕ_i can be calculated as below:

Considering the elastic scattering, the number of scattered X-rays/neutrons passing through an elemental area dS per second is,

$$v\ dS|\Psi_s|^2 = v\ dS\frac{b^2}{r^2} = vb^2 d\Omega \tag{2.12}$$

The incident flux can be written as,

$$\Phi = v|\Psi_i|^2 = v \tag{2.13}$$

Then, using Eq. 2.10,

$$\frac{d\sigma}{d\Omega} = \frac{vb^2\ d\Omega}{\Phi\ d\Omega} = b^2 \tag{2.14}$$

Again, using Eq. 2.11 and Eq. 2.14, and integrating all over the space,

$$\sigma = 4\pi b^2 \tag{2.15}$$

Depending upon the nature of the scattering centers, there can be a distribution of scattering cross-section. For X-rays, the scattering cross-section of elements are always coherent. On the other hand, neutrons are isotope sensitive due to the nuclear spin and thus there can be coherent and incoherent scattering cross-section for different elements. Therefore, the total scattering cross-section can be expressed as,

$$\sigma = \sigma_{coh} + \sigma_{inc} \tag{2.16}$$

where σ_{coh} and σ_{inc} are the coherent and incoherent scattering cross-sections respectively.

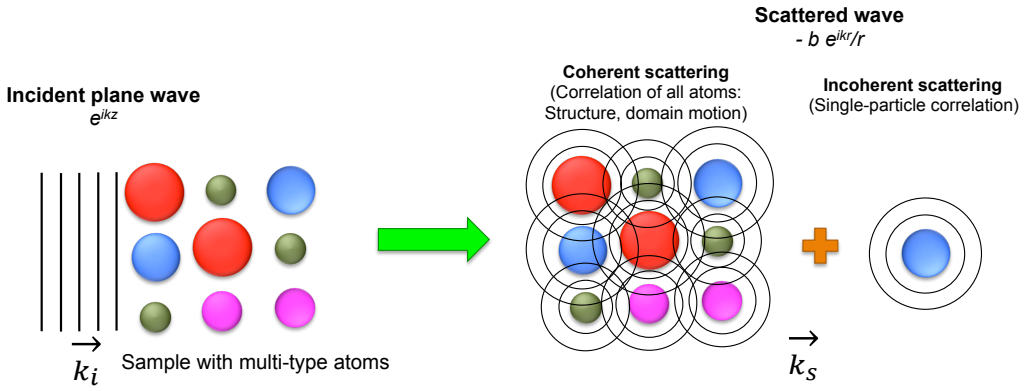

Figure 2.3: Schematic diagram of coherent and incoherent scattering from the system of muti-type atoms. Coherent scattering represents the correlation of all the atoms over time, whereas incoherent scattering corresponds to the correlation of same atom over time. Thus, coherent signal is useful for the structural studies as well as collective motions. On the other hand, incoherent signal provides the dynamical information of the sample. Neutron scattering contains both coherent and incoherent scattering information, whereas X-ray scattering does not have incoherent signal from the sample.

Furthermore, σ_{coh} and σ_{inc} can be written as,

$$\sigma_{coh} = 4\pi < b >^2 \tag{2.17}$$

$$\sigma_{inc} = 4\pi(< b^2 > - < b >^2) \tag{2.18}$$

such that

$$\sigma = 4\pi < b^2 > \tag{2.19}$$

The coherent scattering cross-section produce the interference and thus gives the structural information of the sample as well as collective motion in the sample. On the other hand, incoherent scattering cross-section provides the correlation of same atom over time or the single-particle dyanmics. Thus, neutron scattering contains both coherent and incoherent

scattering signals, whereas X-ray scattering contains only the coherent signal from the sample. The X-ray and neutron coherent and incoherent scattering cross-section of some of the major elements in biomolecueles are listed in Fig. 2.4.

Considering the scattering from N number of scattering centers having scattering length

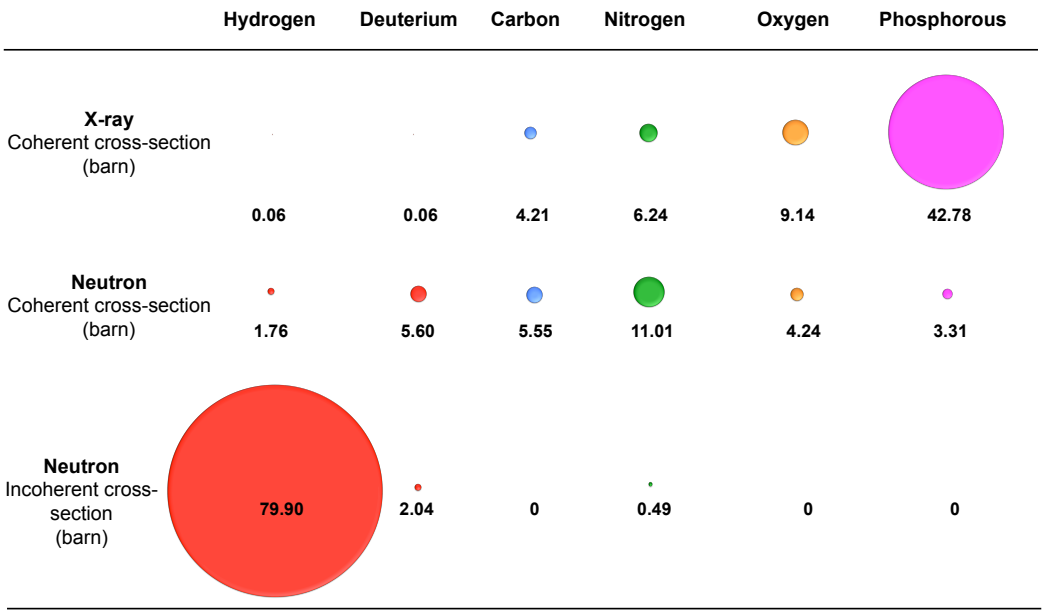

Figure 2.4: X-ray and neutron coherent and incoherent scattering cross-section of some of the major elements in biomolecules.

b within the sample, the differential scattering cross-section, $d\sigma/d\Omega$ can be expressed in terms of scattering vector Q as shown in Eq. 2.20 below, which provides the structural information of the measured sample.

$$\frac{d\sigma}{d\Omega}(Q) = \frac{1}{N}\left|\sum_{i}^{N} b_i e^{i\vec{Q}\cdot\vec{r}}\right|^2 \tag{2.20}$$

For the study of dynamic process in the sample, another fundamental scattering quantity is measured in the experiment. It is called a double differential scattering cross-section $d^2\sigma/d\Omega dE$. It is proportional to the probability of an incident beam with energyy E_i and

scattered with energy E_s making an elemental solid angle $d\Omega$ in the direction $\vec{\Omega}/|\vec{\Omega}|$ with the change in energy $\Delta E = \hbar\omega = E_s - E_i$. In the experiment, for the study of structure, the differential scattering cross-section can also be calculated by integrating the double differential scattering cross-section over all the possible energies within the instrumental resolution.

Considering the initial phase of the wave, the wavefunction for the incident and scattered waves after interacting with the target of scattering cross-section b can be written as,

$$\psi_i = e^{i(k_i z - \omega t)} \tag{2.21}$$

and

$$\psi_s = -\frac{b}{r}\, e^{(i\vec{k}_s \cdot \vec{r} - \omega t)} \tag{2.22}$$

Assuming the short-range nuclear potential for neutrons, the Fermi pseudo-potential ($V(\vec{r})$) for the nucleus at $\vec{r}_i$ can be written as,

$$V(\vec{r}) = \frac{2\pi\hbar^2}{m} \sum_i b_i \delta(\vec{r} - \vec{r}_i) \tag{2.23}$$

Then, the total double differential scattering cross-section can be expressed as,

$$\left(\frac{\partial^2\sigma}{\partial\Omega\,\partial\omega}\right)_{tot} = \frac{1}{2\pi}\,\frac{k_s}{k_i} \sum_i \sum_j \int_{-\infty}^{+\infty} \frac{1}{N} < b_i b_j\, e^{i\vec{Q}\cdot\vec{r}_i(t)} \cdot e^{-i\vec{Q}\cdot\vec{r}_j(0)} > \; e^{-i\omega t}\, dt \tag{2.24}$$

Since neutron scattering considers the coherent and incoherent scattering cross-section of the elements, Eq. 2.24 can be expressed as the sum of coherent and incoherent contributions as shown in Eq. 2.25 below. However, for X-ray scattering, only the coherent contribution

is considered. Therefore,

$$\left(\frac{\partial^2\sigma}{\partial\Omega\,\partial\omega}\right)_{tot} = \left(\frac{\partial^2\sigma}{\partial\Omega\,\partial\omega}\right)_{coh} + \left(\frac{\partial^2\sigma}{\partial\Omega\,\partial\omega}\right)_{inc} \tag{2.25}$$

In the above equation, the coherent term represents the correlation of an atom with all other atoms as shown in Fig. 2.3, which is due to the interference phenomemon. On the other hand, the incoherent term corresponds to the correlation of same atom at $t = 0$ and after some time t. Thus, using neutron, the density-density correlation function can be measured by increasing the coherent signal from the sample, whereas the single-particle correlation function can be measured by increasing the incoherent signal. For an instance, the incoherent cross-section of hydrogen atom for neutron is about 80 barn, which is the largest value compared to other elements in the periodic table and nearly 40 times larger than its isotope, deuterium. Therefore, hydrogen-riched sample is good for the study of dynamics, but it needs to be deuterated, if one would like to study the correlation of one atom with respect to the other atoms and specially for the structural study of the sample. On the other hand, X-ray scattering only measures the coherent signal from the sample. Thus, the structure and the collective motions of the samples can be investigated using X-ray scattering.

For the dynamical study of the sample using X-ray/neutrons scattering, the dynamic structure factor is calculated from the measured double differential scattering cross-section, which can be coherent, incoherent or both for the neutron scattering, whereas only coherent for the X-ray scattering as discussed earlier. If we consider n different types of atoms such as hydrogen, deuterium, carbon, oxygen etc such that the number of atoms of types α and

β be N_α and N_β respectively. Also, let b_α and b_β be the scattering lengths of atoms of type α and β respectively. Then, the coherent and incoherent double differential cross-section in terms of dynamic structure factor are expressed as:

$$\left(\frac{\partial^2\sigma}{\partial\Omega\,\partial\omega}\right)_{coh} = \frac{1}{N}\frac{k_s}{k_i}\sum_{\alpha=1}^{n}\sum_{\beta=1}^{n} b_\alpha^{coh} b_\beta^{coh}\sqrt{N_\alpha N_\beta}\, S_{coh}(Q,\omega) \tag{2.26}$$

and

$$\left(\frac{\partial^2\sigma}{\partial\Omega\,\partial\omega}\right)_{inc} = \frac{1}{N}\frac{k_s}{k_i}\sum_{\alpha=1}^{n} b_\alpha^{inc}\, S_{inc}(Q,\omega) \tag{2.27}$$

where

$$S_{coh}(Q,\omega) = \frac{1}{2\pi}\frac{1}{\sqrt{N_\alpha N_\beta}}\int_{-\infty}^{+\infty}\sum_{i_\alpha=1}^{N_\alpha}\sum_{j_\beta=1}^{N_\beta} < e^{i\vec{Q}\cdot\vec{r}_{i_\alpha}(t)}\cdot e^{-i\vec{Q}\cdot\vec{r}_{j_\beta}(0)} > \;\; e^{-i\omega t}\,dt \tag{2.28}$$

and

$$S_{inc}(Q,\omega) = \frac{1}{2\pi}\frac{1}{N_\alpha}\int_{-\infty}^{+\infty}\sum_{i_\alpha=1}^{N_\alpha} < e^{i\vec{Q}\cdot\vec{r}_{i_\alpha}(t)}\cdot e^{-i\vec{Q}\cdot\vec{r}_{i_\alpha}(0)} > \;\; e^{-i\omega t}\,dt \tag{2.29}$$

The dynamic structure factor is the Fourier transform of the intermediate scattering function as expressed below:

$$S_{coh}(Q,\omega) = \frac{1}{2\pi}\int_{-\infty}^{+\infty} I_{coh}(Q,t)\, e^{-i\omega t}\,dt \tag{2.30}$$

and

$$S_{inc}(Q,\omega) = \frac{1}{2\pi}\int_{-\infty}^{+\infty} I_{inc}(Q,t)\, e^{-i\omega t}\,dt \tag{2.31}$$

Therefore,

$$I_{coh}(Q,t) = \frac{1}{\sqrt{N_\alpha N_\beta}}\sum_{i_\alpha=1}^{N_\alpha}\sum_{j_\beta=1}^{N_\beta} < e^{i\vec{Q}\cdot\vec{r}_{i_\alpha}(t)}\cdot e^{-i\vec{Q}\cdot\vec{r}_{j_\beta}(0)} > \tag{2.32}$$

and

$$I_{inc}(Q,t) = \frac{1}{N_\alpha} \sum_{i_\alpha=1}^{N_\alpha} < e^{i\vec{Q}\cdot\vec{r}_{i_\alpha}(t)} \cdot e^{-i\vec{Q}\cdot\vec{r}_{i_\alpha}(0)} > \tag{2.33}$$

The intermediate scattering function is known as the single-particle correlation function for incoherent scattering, whereas density-density correlation function for the coherent scattering. It is usually an essential quantity to describe the dynamic processes in sample, which is considered as the primary quantity of theoretical interest related to the scattering experiments.

2.3 Scattering techniques

2.3.1 Small-angle scattering

As discussed earlier, X-rays and neutrons interact with individual atoms and produce the secondary wavelets. The secondary wavelets are due to the coherent scattering for X-ray and both coherent and incoherent scattering for neutrons, which can interfere constructively or destructively. Small-angle scattering (SAS) is the difrraction pattern due to coherent scattering from the individual atom or molecule in the crystal or solution [58]. In general, it is measured at very small scattering angle (scattering vector), which is in contrast to the crystal diffraction at very high scattering angle. Therefore, SAS is often described as the low-resolution technique compared to crystal diffraction, which cannot provide the atomic resolution information but appropriate for the structural study of the particles of size varying from 1 to 100 nanometers (nm). Moreover, it is capable of providing the precise information regarding the overall shape of the particle. The low-resolution of SAS is due to the rotational averaging of the data from the particle in solution. In the past few years, this technique is widely used for investigating the overall structure and conformational changes

in biological molecules such as globular proteins, membrane proteins, RNAs, and DNAs in aqueous solution [59, 60].

SAS technique relies on the quality of the sample. In order to extract the precise size parameters from the particle in solution, the solution should be monodispersed. Therefore, the characterization of sample using the techniques such as dynamic light scattering, UV-vis absorption, and SDS PAGE and gel filtration are highly encouraged before performing the SAS experiment [58]. In general, protein solution with concentration in the range of 1-5 mg/ml is used for small-angle X-ray scattering (SAXS), whereas 2-10 mg/ml is used for small-angle neutron scattering (SANS).

The schematic of SAS experimental setup is shown in Fig. 2.5. The highly collimated

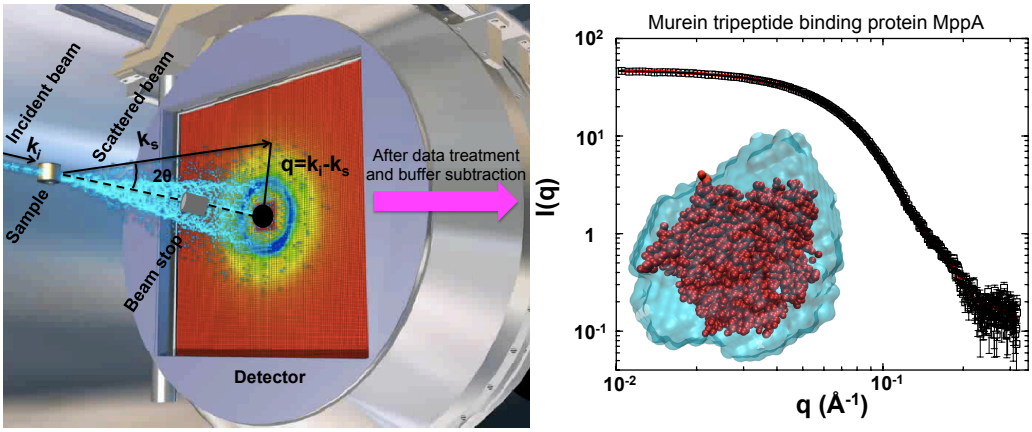

Figure 2.5: Schematic of small-angle scattering experiment. (Left) A plane wave of X-ray/neutron with momentum vector (k_i) is scattered from the sample, which is scattered with momentum vector (k_s) and 2D data is recorded at the detector . (Right) SAXS intensity profile of murein tripeptide binding protein MppA. Inset: 3D reconstruction of structural envelope of MppA (cyan color) calculated from *ab-initio* modeling of SAXS intensity profile, which is overlayed on the protein data bank (PDB) structure 3O9P (red color) obtained from X-ray diffraction of crystal MppA.

beam of X-ray or neutron is illuminated on the sample and the scattered radiation is recorded on the detector at specific sample to detector distance to achieve the desirable q-range. The

direct beam is usually absorbed by the beam stop and its size and positioning is very crucial for achieving the smallest q measurement [58, 59].

Based on the number of photons or neutrons count at the detector, the scattering pattern is defined by the intensity (I) as a function of scattering vector q, where q is defined as,

$$q = \frac{4\pi sin\theta}{\lambda} \tag{2.34}$$

where 2θ is the angle between the incident and the scattered X-ray or neutron and λ is the wavelength of the incident radiation. Scattered radiation is collected by two-dimensional (2D) position-sensitive detector with high pixel resolution. The 2D data are corrected for detector pixel sensitivity, as well as the dark current, from ambient background radiation and the detector's electronic noise. The reduced 2D data are finally averaged azimuthally (rotationally) to yield the 1D scattering profile, in terms of $I(q)$ vs. q. Mathematically, $I(q)$ can be expressed as,

$$I(q) = \left\langle \int |(\rho(\vec{r}) - \rho_s) e^{i\vec{q}.\vec{r}} d\vec{r}|^2 \right\rangle \tag{2.35}$$

where $(\rho(\vec{r}) - \rho_s)$ is the difference in scattering length densities (SLDs) between the volume element at position $\vec{r}$ and the solvent, termed as contrast. SLD for neutron scattering is defined as the ratio of scattering length per molecule and the molar volume as expressed in Eq. 2.36,

$$\rho = \frac{\sum_{i=1}^{n} b_i}{V_m} \tag{2.36}$$

where b_i is the scattering length of i^{th} atom and V_m is the total molecular volume. For X-ray scattering, b_i can be replaced by $Z_i r_e$, where Z_i is the atomic number of i^{th} atom and $r_e = 2.81 \times 10^{-13}$ cm is the classical radius of electron. $I(q)$ contains the information about the particle size, shape and interparticle interaction, where the latter one is only for the highly concentrated solution sample. Furthermore, *ab-initio* modeling of 1D scattering profile can be done to reconstruct the 3D structure. SAS intensity profile of murein tripeptide binding protein MppA is shown in Fig. 2.5 (right). Using *ab-initio* reconstruction of 1D SAXS intensity [59–61], 3D structure of MppA is generated, as shown in right inset of Fig. 2.5.

2.3.2 Inelastic and quasi-elastic neutron scattering

The dynamic behaviour at atomic or molecular level in soft and condensed matter can be investigated using low-energy neutron due to its remarkable property of comparable kinetic energy and wavelength to that of molecular energy levels [44]. Based on the interaction of neutrons with various atoms in the sample, there can be coherent and incoherent scattering as discussed earlier. Moreover, based on the energy gain or loss, neutron spectrum can be resolved into three types of signal. If the incident neutrons do not transfer energy after interacting with the sample (case I: $\hbar\omega = 0$), then it is called elastic scattering. Due to finite resolution of designed instrument in the laboratory, no instrument can detect the perfectly elastic scattering. In such case, the elastic scattering is limited by the instrumental resolution. Elastic signal is represented by the central peak at frequency, $\omega = 0$, which corresponds to the immobile or static atoms or molecules within the instrumental resolution. In general, the elastic spectrum in represented by a delta function. Inelastic scattering is due to gain or loss of energy by the scattered neutrons after interacting with the sample. If the energy transfer is very small (case II: $\hbar\omega \sim 0$), it is called quasi-elastic scattering, which mainly

represents the rotational or translational diffusive motion in the sample. It can be observed at frequency, $\omega \sim 0$, which is broadened by the instrumental resolution. Quasi-elastic broadening is described by the Lorentzian function of finite width. It represents to the energy transfers with the atoms or molecules of the sample, typically of the order of ± 1 micro-electron volts (μeV) to ± 2 mille-electron volts (meV) [44]. Such motions occur in the time scale of few nanoseconds (ns) to picoseconds (ps). Lastly, if the scattered neutrons exchange significantly larger energy of the order of tens of meV (case III: $\hbar\omega \neq 0$), it is considered as inelastic scattering. Inelastic neutron or X-ray scattering describes the transitions between different vibrational modes in the sample that occur in the time scale of femtoseconds (fs) to sub-ps [44]. The schematic of elastic, quasi-elastic and inelastic picture is shown in Fig. 2.6.

The inelastic and quasi-elastic scattering events can be measured by different spectrom-

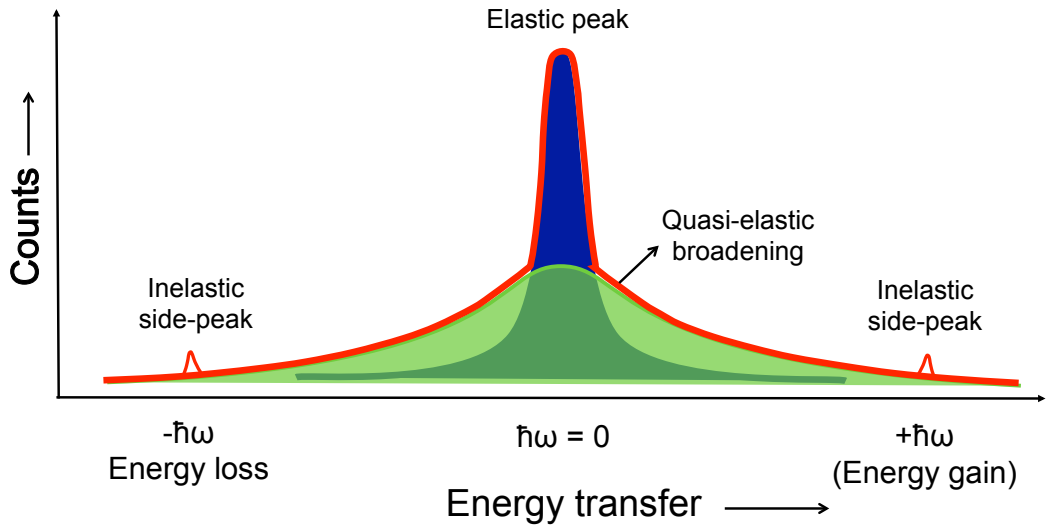

Figure 2.6: Schematic of elastic, quasi-elastic and inelastic scattering spectra.

eters with specific energy resolution. Based on the desired energy resolution, different types

of spectrometers are designed. Although the instrumentation of X-ray scattering experiments/techniques are quite different from neutrons, the basic concept of scattering theory is same. Therefore, I will describe very briefly about the different neutron scattering spectrometers that I have used for the dissertation, which is also conceptually/theoretically same for X-ray scattering techniques.

Time-of-flight spectrometer

The time-of-flight (TOF) spectrometer is very useful instrument to study the dynamics

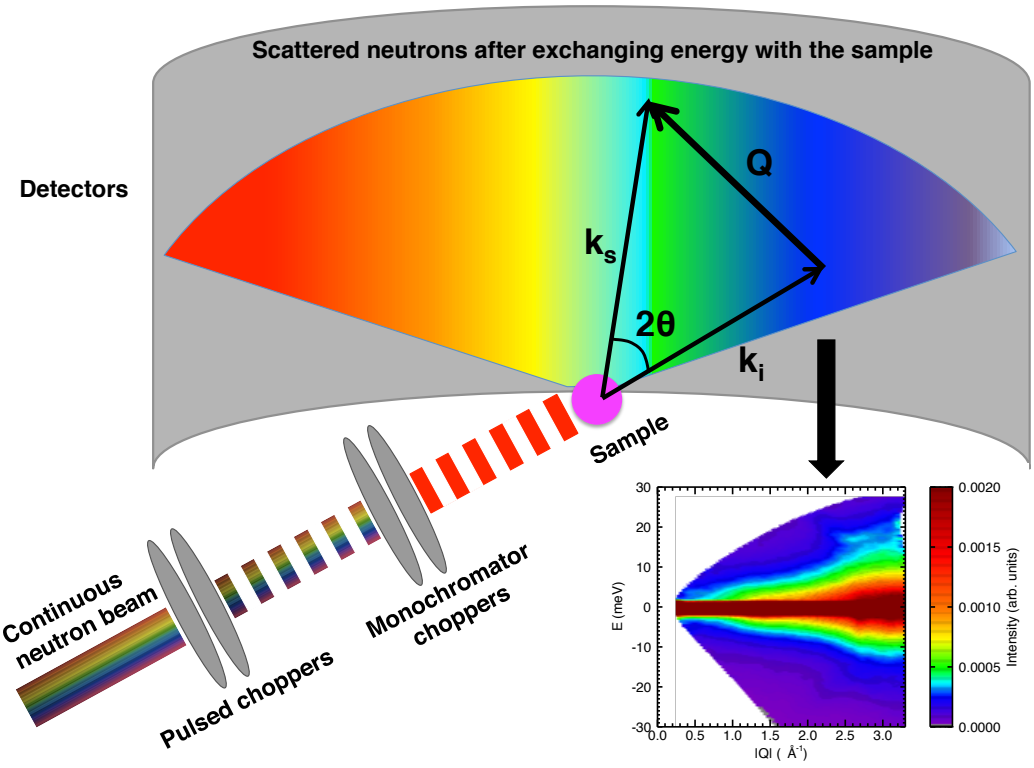

Figure 2.7: Schematic of time-of-flight (TOF) spectrometer with cold neutron source. 2D color plot shown here is the raw data from protein sample at 270 K measured using direct TOF spectrometer.

at atomic or molecular level that basically measures the quasi-elastic and inelastic signals [62]. This instrument determines the final neutron energies through a direct measurement of

their velocities [44]. Specifically, TOF measures the momentum and energy transfers of the scattered neutrons after interacting with the sample as expressed in Eq. 2.3 and Eq. 2.5, respectively. The schematic diagram of TOF instrument is shown in Fig. 2.7. The white beam of neutrons produced from the reactor or the spallation source is monochromatized by a set of choppers, which rotate with a certain frequency to allow neutrons of only specific velocity. Thus, the choppers that are in general neutron absorbing material select the neutrons of particular wavelength given by the Eq. 2.37,

$$\lambda = \frac{h}{mv} = \frac{h}{m\frac{L_{chopp}}{\tau_{chopp}}} \tag{2.37}$$

where h is planck's constant, v is the velocity of neutron, L_{chopp} is the length of the choppers and τ_{chopp} is the flight time between the choppers. The monochromatic pulsed-beam of neutrons hits the sample and scatters away, which are measured as neutron counts at the detector at an angle of 2θ. The energy transfer by neutrons is determined from the flight time between the sample position and the detector due to elastic, quasi-elastic or inelastic scattering, which is expressed as in Eq. 2.38

$$\Delta E = \hbar\omega = \frac{1}{2}mv^2 = \frac{1}{2}L_{TOF}^2\left(\frac{1}{t_0} - \frac{1}{t_1}\right)^2 \tag{2.38}$$

where L_{TOF} is the distance between the sample and the detector, t_0 and t_1 are the elastic and quasi-elastic or inelastic flight times, respectively. Therefore, the neutron counts is measured at the 2D detector as a function of Q and ω. Using Eq. 2.5, Q can be expressed as a function

of both 2θ and ω as:

$$\frac{Q}{k_i} = \sqrt{2 - \frac{\hbar\omega}{E_i} - 2cos(2\theta)\Big(2 - \frac{\hbar\omega}{E_i}\Big)^{\frac{1}{2}}} \tag{2.39}$$

Since the energy loss or gain of the neutrons cannot exceed the incident energy (E_i), ω is always less than or equal to $\frac{E_i}{\hbar}$. Thus, at $\omega = 0$, there is a perfect elastic peak and for $\omega \neq 0$, different modes can be detected in the scattering signal due to translational/rotational diffusion or harmonic vibrations of different modes.

Backscattering spectrometer

The backscattering spectrometer is the high-resolution instrument designed to measure the

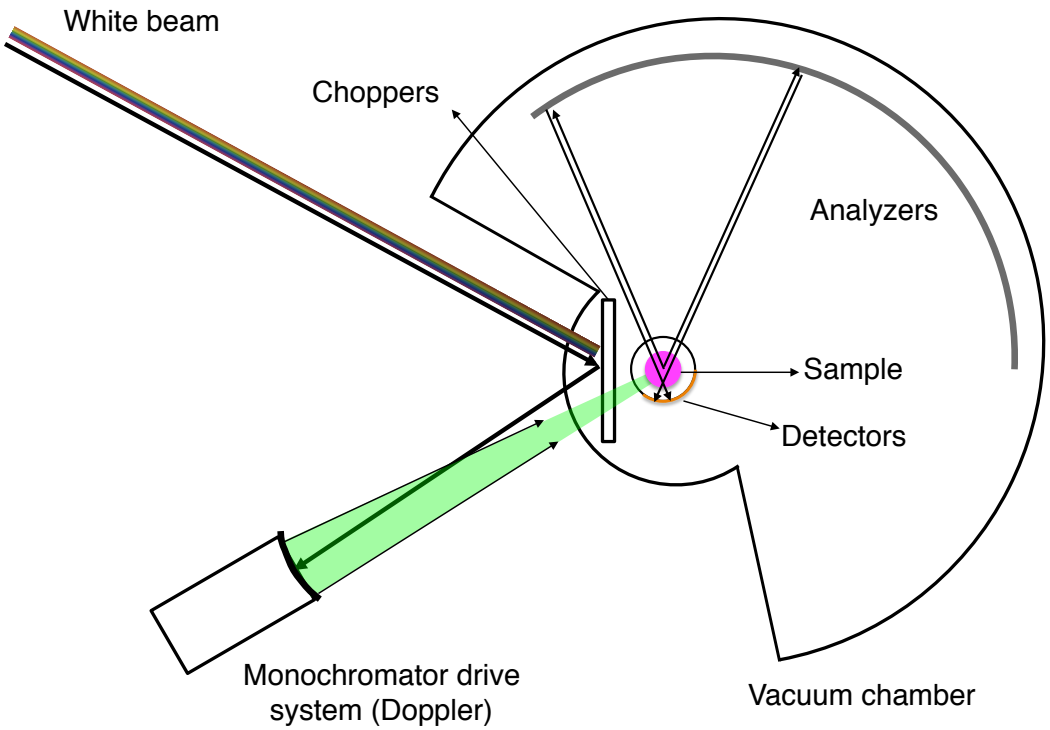

Figure 2.8: Schematic of backscattering spectrometer.

QENS spectra to probe the rotational motions of molecules and slow diffusion dynamics (typically tens of ps to a few ns) [63, 64]. It scans the spectra of varying energies incident on

the sample, which is analyzed at the fixed energy after scattered from the sample and hence are recorded at the detectors. It consists of the monochromator or the analyzer crystals to gain the high-resolution without going to very long wavelengths, which prevents the limiting of the Q-range as in case of TOF spectrometer. The velocity of an incident monochromatic beam is distributed either by generating the pulse of neutrons using the choppers or by using the Doppler at certain frequency (crystal analyzer is driven back and forth along the direction of the incident beam causing the shift in the neutron energy) to vary the wavelengths and therefore varying the energies incident to the sample. This setup measures the neutron counts as a function of Q and ω. Fig. 2.8 shows the schematic of backscattering spectrometer.

In backscattering instrument, a perfectly collimated beam cannot be achieved, which undergoes a spread of incident neutron angles by $\Delta\theta$. Recalling the Bragg's law and taking the differential, we get,

$$\frac{\Delta\lambda}{\lambda} = \frac{\Delta\theta}{tan\theta} + \frac{\Delta d}{d} \tag{2.40}$$

For $\theta \to 90^o$, wavelength spread is minimum. Therefore, in order to achieve the high energy resolution, the neutron beam is incident on the single-crystal monochromator such that Bragg's reflection occurs at Bragg angle, $\theta = 90^o$.

Furthermore, since this instrument is capable of modulating the incident beam, it is also possible to measure the perfectly elastic scattering data within the instrumental resolution [64]. The elastic scattering measurements from the sample is carried out as a function of temperature. If the point of inflection in the elastic scattering data is observed at particular temperature, then such temperature provides an idea of onset of dynamics from harmonic to anharmonic behavior, above which QENS measurements can be made. Moreover, elastic

scan measurements are very important for calculating the precise values of mean-square displacement of atoms in the sample using Debye-Waller factor. The accesible time-scale of motion at atomic or molecular length-scale that can be probed by the QENS and some other techniques are shown in Fig. 2.9.

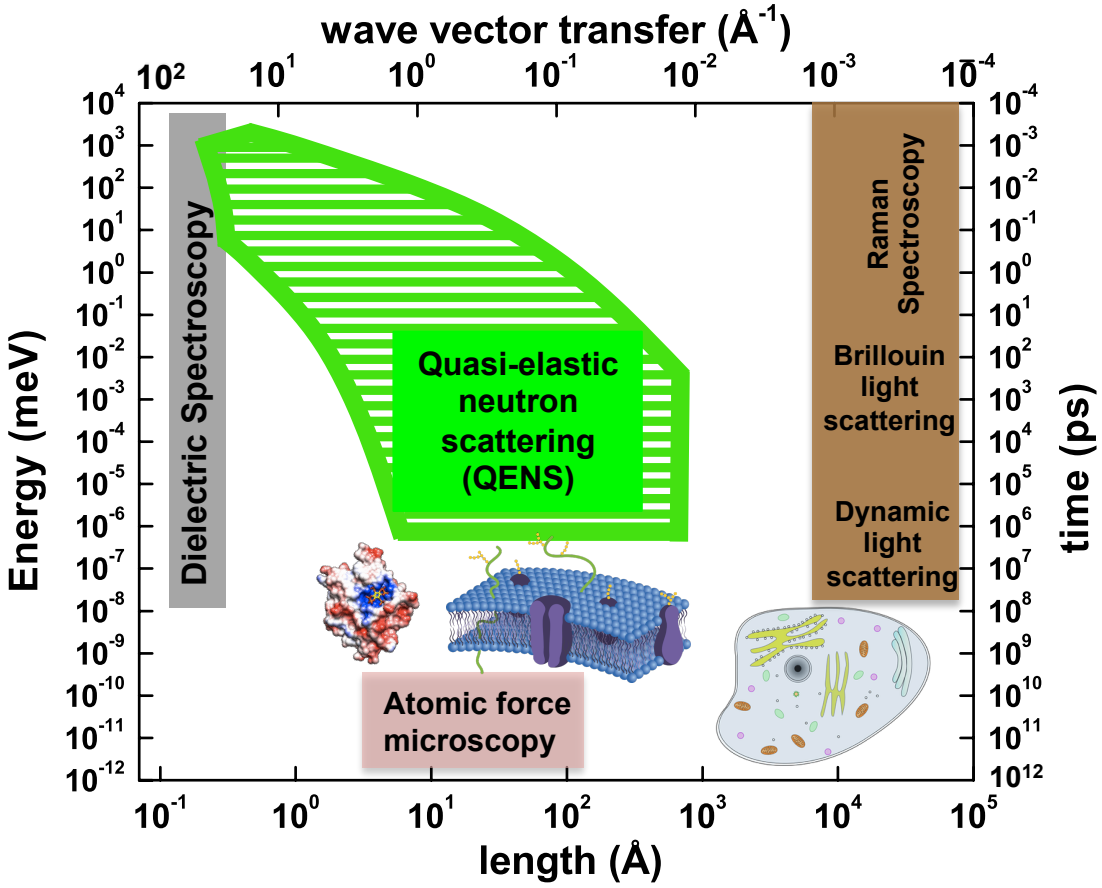

Figure 2.9: Schematic diagram of accessible time-scale of motion at atomic/molecular length-scale in biomolecules by QENS spectrometers and other widely used instruments.

CHAPTER 3 DYNAMICS OF A DEEP-SEA PROTEIN

3.1 Introduction

The biological functions of proteins, such as enzyme catalysis, are often understood from their crystallographic structures [65]. On the other hand, it is crucial to take into account dynamic behavior to fully comprehend these functions [14, 18, 66]. In vivo, proteins are in constant motion among different conformations [14, 18, 19, 67]. The thermal energy, which is of the order of k_BT per atom, where k_B is the Boltzmann constant and T is the absolute temperature, triggers biomolecules to sample different conformations around the average structure. These conformations are also known as conformational substates (CSs) [19]. Fluctuations among these CSs play an important role in protein function [14, 18, 19]. These lead to the concept of a multidimensional potential energy landscape (EL) that specifies a complete description of CSs in proteins [21, 68–70]. The existence of an EL was proposed by H. Frauenfelder and others in the 1970s and has been validated both by computations and by experiments [21, 68–73].

Proteins show various dynamic phenomena over a wide range of timescales, from picoseconds to milliseconds [18]. A fast dynamic process, on a timescale of a picosecond to 10 ns, also known as β-relaxation, occurs due to small amplitude fluctuations in atoms/molecules, such as loop motions and side-chain rotations [74]. The energy barrier or activation energy (E_A) between different CSs for this process is smaller than k_BT [22]. On the other hand, slow motions, on the timescale of microseconds to milliseconds mainly occur due to the large-amplitude collective motions such as protein-protein interactions and enzyme catalysis [75]. This process, for which the energy barrier separating CSs is much larger than k_BT [22, 74], is called α-relaxation. The fast and slow dynamics of proteins are connected to each

other and provide the necessary balance between stability and flexibility required for their enzymatic activity [18]. In our study, the quasi-elastic neutron scattering (QENS) technique was used to investigate the fast dynamics in the picosecond-to-nanosecond time range on the length scale from angstroms to nanometers within the protein secondary structure. Because more than one-half of the atoms in biological macromolecules are hydrogen (H), which has the largest incoherent neutron scattering cross-section [50], incoherent QENS experiments on biological macromolecules predominantly measure the motions of individual H-atoms.

Over the past two decades, considerable research effort on protein dynamics has emphasized the effects of temperature and pressure, and has reported significant effects on the motions [76–80]. In general, below the physiological temperature limit, the volume of protein molecules increases with increase in temperature due to expansion in the subatomic-sized spaces within the molecules and the hydration layer surrounding the protein [81]. Temperature provides conformational flexibility to proteins for enzymatic activities by increasing their conformational fluctuations [82]. Nevertheless, sufficiently high temperature may also distort protein structure and cause unfolding or denaturation [83–85]. Another thermodynamic parameter, pressure, also plays an important role in protein structure and dynamics [86–91]. It changes the protein volume [91] and affects protein intermolecular and intramolecular structures explicitly [86, 90]. Evidently, the cavities in folded or native proteins are reduced at high pressure. This perturbs the CSs, giving rise to protein unfolding or denaturation [91–93]. Therefore, high temperature and pressure together may prevent enzymatic processes in many biomolecules.

Despite the above, some of the microorganisms found in deep-sea thermal vents are able to resist the effects of high temperature and pressure [94–96]. Without any light energy

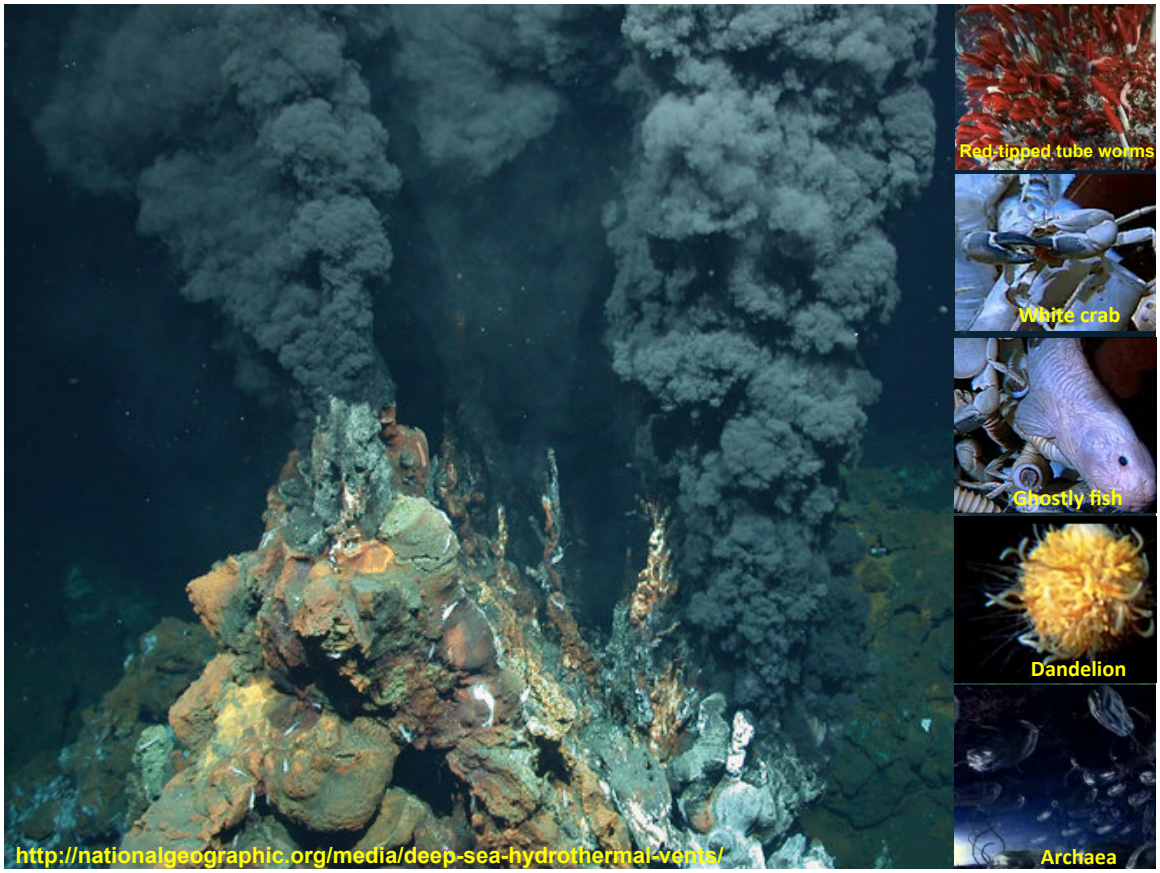

Figure 3.1: Hydrothermal vent of Galapagos Rift along the mid-ocean in eastern Pacific and the organisms that can survive near it.

from the sun, these organisms survive, depending on mineral-enriched hydrothermal fluids, and can perform their metabolic activities, synthesize proteins, and maintain their native conformations. Thus, they engender great interest among researchers in understanding the possible factors or mechanisms that are unique to these living systems, permitting them to survive under such critical circumstances.

One of the deep-sea microorganisms, *Thermococcus thioreducens*, is a hyperthermophilic sulfur-reducing euryarchaeote found in hydrothermal vents of the Mid-Atlantic Ridge under abnormal thermodynamic conditions of high pressure and temperature [97, 98]. It lives its life under hydrostatic pressures of about 100 MPa, having an optimal growth temperature

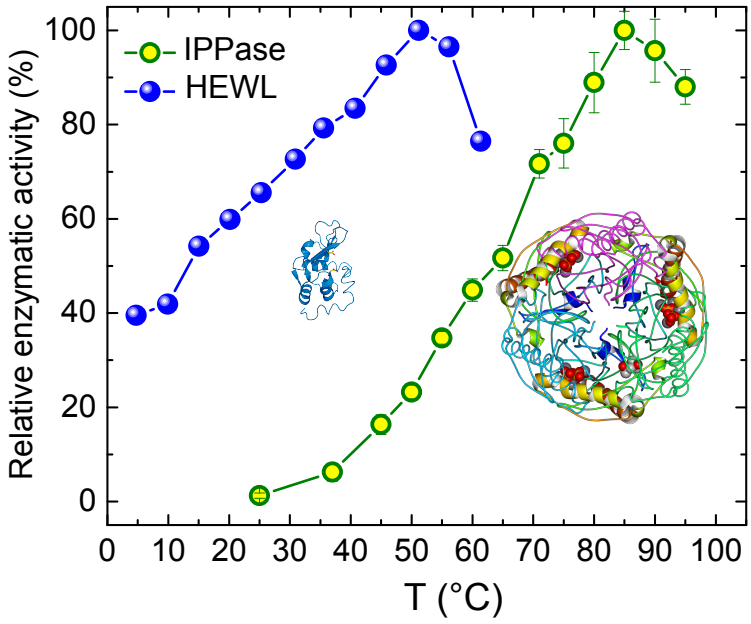

Figure 3.2: Enzymatic activities for Tt-IPPase and HEWL as functions of temperature. The optimal temperatures for activity are 323 K (50 ^{0}C) and 358 K (85 ^{0}C) for HEWL and IPPase, respectively.

range of 356–358 K (83–85 ^{o}C) [98]. Inorganic pyrophosphatase (IPPase) (enzyme entry EC 3.6.1.1) is an enzyme from this organism, which is of great interest due to its high thermal and biochemical stability [97]. It catalyzes the hydrolysis of inorganic pyrophosphate (PPi) to form orthophosphate (Pi), which helps in several biochemical processes such as nucleic acid polymerization, lipid metabolism, and the production of proteins [98]. The static structure of IPPase has recently been overexpressed and characterized by neutron protein crystallography [97]. Its quaternary structure is a homohexamer with an oligomeric molecular mass of ∼120 kDa (each subunit is about 20 kDa) [97]. Like its mesophile, it has a complicated network of noncovalent interactions that mainly correspond to the interaction of hydrogen bonds [97]. However, in contrast to these mesophilic equivalents, this enzyme has the ability to perform

catalytic activity at extreme pressures and temperatures. It can resist denaturation even at high temperatures above 348 K (75 ^{o}C), and its optimal temperature for enzymatic activity is 358 K (85 ^{o}C) [27, 97]. From the structure point of view, to form the stabilizing interactions for its quaternary oligomeric structure, IPPase reduces its translational and rotational entropy for the monomers. These interactions include polar/apolar, hydrophobic, ion pairs, and hydrogen bonds between monomers and non-solvent-exposed cavities [27]. Therefore, the oligomeric IPPase has a highly symmetric and closed hexameric structure, which makes it stable and biologically active at extreme temperatures and pressures. For comparison, we use a small monomeric protein, hen egg white lysozyme (HEWL) as a model protein. It is a well-studied protein and has been used as a model protein for QENS experiments for decades [40, 74]. It consists of 129 amino acid residues that destroy the polysaccharide architecture of bacterial cell walls [99]. It catalyzes the hydrolysis of 1,4-β linkages between alternating units of N-acetylmuramic acid and N-acetylglucosamine. At a pH of 2.0, rapid denaturation in HEWL begins above 320 K (47 ^{o}C) and at higher temperatures it loses its enzymatic activity [100]. The comparison of enzymatic activities of IPPase and HEWL is shown in Fig. 3.2 [27, 101]. In the previous investigation carried out by Chu and colleagues [27] at ambient pressure with QENS, IPPase was shown to have distinguishably slower dynamics than that of HEWL in the β-relaxation time range of 10 ps to 0.5 ns, which is intimately related to the local flexibility of the oligomeric structure of IPPase. Such dynamic behavior was observed at all of the measured temperatures from 220 K (-53 ^{o}C) to 353 K (80 ^{o}C). It is of great interest to investigate whether the same dynamical behavior holds at high pressure, which reflects the natural living condition of IPPase found in the seabed.

In this study, the relaxation dynamics of both IPPase and HEWL were studied by QENS

in two different time ranges on two instruments at the National Institute of Standards and Technology (NIST) Center for Neutron Research (NCNR), in the temperature range from 298 K (25 ^{o}C, room temperature) to 363 K (90 ^{o}C) at a pressure of 100 MPa, the native environment for IPPase. Due to the limited dynamic range available on the individual instruments, two QENS spectrometers were used to probe the dynamics in a wide time range from subpicoseconds to nanoseconds. Thus, the dynamics in the time range from 2 to 25 ps was measured using the disk chopper time-of-flight spectrometer (DCS) [62] and from 100 ps to 2 ns was determined using the high-flux backscattering spectrometer (HFBS) [64]. The experimental results were quantitatively analyzed using two analytical models in both the energy and the time domains. The relaxation dynamics of IPPase and HEWL were directly compared in the time domain. Both proteins demonstrate a non-exponential logarithmic-like decay in their relaxation dynamics. Our results demonstrate that, even though IPPase is a complex oligomeric protein, it continues to preserve its conformation, residual motions, and hence enzymatic activity under high temperature and pressure, which is naturally favorable to these microorganisms. However, our model protein, HEWL, lacks the above in its distinguishable dynamic behavior due to imposed high temperature and pressure. We explain these results based on the highly symmetric and closed oligomeric structure of IPPase, which helps to maintain its native conformation and flexibility under high pressure and temperature conditions. We further derive from our experimental observations a scenario of distorted energy landscape of proteins under pressure and a schematic denaturation phase diagram that can be used as a general picture to describe protein dynamics under extreme conditions.

3.2 Materials and methods

3.2.1 Sample preparation

Both IPPase and HEWL samples were purchased from iXpressGenes. The recombinant construct of IPPase was derived from *Thermococcus thioreducens*, an obligate sulfur-reducing hyperthermophilic archaeon [97, 102]. Escherichia coli Rosetta 2 (EMD Biosciences) was used as the main recombinant expression host. Labile hydrogen atoms were exchanged for deuterium by taking the concentrated, purified protein (∼30 mg/mL) and mixing with 9 vol of pure D_2O (99.8% D; Cambridge Isotope Laboratories) in the presence of 10 mM NaCl. The resulting resuspension was concentrated using a 50 K cutoff Spin-X UF concentrator (Corning) until the original protein concentration was achieved. This process was repeated twice and the product was lyophilized with a Labconco FreeZone lyophilizer and stored at -80 ^{o}C. Before the neutron scattering measurements, the protein sample was lyophilized overnight and dried. IPPase powder was hydrated isopiestically at 25 ^{o}C by exposing it to D_2O vapor in a closed chamber while monitoring the hydration level by weight measurement using an analytical scale. The final hydration level was determined to be 0.37 g of D_2O per g of IPPase ($h = 0.37$) to ensure at least a monolayer of heavy water covering the protein surface [25]. Similarly, the commercially purchased purified sample of hen egg white lysozyme (HEWL) (EC 3.2.1.17) was used without additional purification. Before the QENS experiments, it was also lyophilized overnight to remove residual water, followed by D_2O hydration [27, 74, 82]. The final hydration level was determined to be the same as that prepared for IPPase ($h = 0.37$).

3.2.2 Quasi-elastic neutron scattering measurements

QENS experiments were performed using time-of-flight disk chopper spectrometer (DCS) [62] and high flux backscattering spectrometer (HFBS) [64] at NIST Center for Neutron Research (NCNR). The DCS was operated at 6 Å, at which wavelength its energy resolution was 64 μeV (full width at half maximum), and a dynamic range suitable for our QENS data analysis of $\pm$1.0 meV. The other spectrometer HFBS was used with an energy resolution of 0.8 μeV (FWHM, for the Q-averaged resolution value) and a dynamic range of $\pm$17 μeV. The QENS measurements were performed at 100 MPa (1 kbar), at six temperatures ranging from 298 K (25 ^{o}C, room temperature) to 363 K (90 ^{o}C), in a wave vector transfer range from Q = 0.4 Å^{-1} to 1.8 Å^{-1}. The resolution function at HFBS was measured at 4 K, and that at DCS was from the measurement of a vanadium standard sample, where most of the signal is completely elastic. The elastic scattering data were obtained by performing fixed window scans at HFBS from 298 K down to 19 K, with a ramp rate of 1 K/min. In this mode, the Doppler drive (and therefore the monochromator) is stopped and only neutrons with the same final and initial energies are counted. High pressure was achieved using a commercially available two-stage helium intensifier. The samples were loaded into an aluminum alloy vessel with an inner sample space of 1.5 cm^3. The pressure vessel was connected to the intensifier through a high-pressure capillary. Pressure was adjusted only at temperatures well above the melting curve of helium.

3.3 Data analysis

3.3.1 Energy domain data analysis

In a neutron scattering experiment, the double differential scattering cross-section $\delta^2\sigma/\delta\Omega\delta\omega$ in a solid angle $\delta\Omega$ with energy exchange of $\delta\omega$ is measured. The measured QENS spectra

$S_m(Q,\omega)$, also known as the self-dynamic incoherent structure factor, is represented as the following expression [27, 29, 82]:

$$S_m(Q,\omega) = [S_H(Q,\omega) + B(Q,\omega)] \otimes R(Q,\omega) \tag{3.1}$$

where $R(Q,\omega)$ is the resolution function of the instrument and $B(Q,\omega)$ is a linear background, which can be written in the form of $B(Q,\omega) = C_1(Q) + C_2(Q)\omega$, $S_H(Q,\omega)$, is a combination of elastic and quasi-elastic components that can be represented by a delta function $\delta(\omega)$ and the sum of a set of Lorentzian functions $L_i(Q,\omega)$, respectively. For only one type of diffusion process (translational or rotational) within instrumental resolution, a single Lorentzian is sufficient to fit the data at the measured temperatures and Q values [27, 82]. Thus, the model scattering function $S_H(Q,\omega)$ can be written as follows:

$$S_H(Q,\omega) = [A_0(Q)\delta(\omega) + [1 - A_0(Q)]L(Q,\omega)] \tag{3.2}$$

where $A_0(Q)$ represents the fraction of elastic scattering and the Lorentzian function is given by,

$$L(Q,\omega) = \frac{1}{\pi}\frac{\Gamma(Q)}{\Gamma^2(Q) + \omega^2} \tag{3.3}$$

In the above Eq. 3.3, $\Gamma(Q)$ is the half width at half maximum (HWHM) of the Lorentzian function.

Using the elastic and quasi-elastic components of the experimental data, an analytical quantity called the elastic incoherent structure factor (EISF) can be derived. It is defined as the fraction of elastic intensity in the QENS spectra [50]. Modeling of the EISF provides the

geometry of diffusive motions in the protein [103]. For the data fitted with single Lorentzian function, EISF can be fitted with the expression for single diffusive motion of atoms within a sphere. According to this model, each atom diffuses freely within an impermeable sphere [50, 103, 104]. The complete expression for the model can be written as follows:

$$EISF = p_0 + (1 - p_0)\left(\frac{3j_1(Qa)}{Qa}\right)^2 \tag{3.4}$$

where $j_1(Qa)$, p_0, and a denote the spherical Bessel function of the first kind of order 1, the elastic fraction, and the radius of the diffusion sphere, respectively. For the purely translational diffusive motions, the EISF is zero, whereas it takes non-zero values in other cases.

The data fitting was done using the peak analysis software PAN in the package DAVE developed at the NCNR [105].

3.3.2 Time domain data analysis

The measured QENS spectra $S_m(Q, \omega)$ is expressed by the convolution of the self-dynamic incoherent structure factor of the H-atoms in the sample, $S_H(Q, \omega)$, with the energy resolution function $R(Q, \omega)$ of the instrument, as shown by Eq. 3.1. By taking the inverse Fourier transform (iFT) of $S_m(Q, \omega)$ and dividing by the iFT of the instrumental resolution function $R(Q, \omega)$, the intermediate scattering function (ISF) $I(Q, t)$ of H-atoms in the time domain can be calculated as follows:

$$I(Q, t) = \frac{iFT[S_m(Q, \omega)]}{iFT[R(Q, \omega)]} \tag{3.5}$$

In this process, a constant background is subtracted before the iFT [74]. The ISF is also known as the single-particle correlation function of H-atoms in the sample, which is the

key function to connect theoretical prediction to the neutron scattering experimental data. The time range of picoseconds to nanoseconds of relaxation process (β-relaxation) observed from QENS instrument is non-exponential and is much shorter than α-relaxation time range. Thus, it can be fitted with an asymptotic expression derived from the mode coupling theory (MCT) [22]:

$$I(Q,t) = f(Q,T) - H_1(Q,T)ln\left(\frac{t}{t_\beta(T)}\right) + H_2(Q,T)ln^2\left(\frac{t}{t_\beta(T)}\right) \tag{3.6}$$

where $\tau_\beta(T)$ is the characteristic β-relaxation time and $f(Q,T) = exp[-A(T)Q^2]$ is a temperature-dependent prefactor proportional to the Debye-Waller factor for small Q values. $H_1(Q,T)$ and $H_2(Q,T)$ are the Q and T dependent first and second order logarithmic decay parameters, respectively. $H_1(Q,T)$ can be written as follows:

$$H_1(Q,T) = h_1(Q)B_1(T) \tag{3.7}$$

where $h_1(Q)$ is a power law of Q for small Q values with a power b between 1 and 2. Therefore, $H_1(Q,T)$ can be fitted as follows:

$$H_1(Q,T) = B_1(T)Q^b \tag{3.8}$$

3.3.3 Mean-square displacement

The mean-square displacement (MSD), $< x^2 >$, of H-atoms were calculated from elastic incoherent neutron scattering (EINS) measurements [39, 40, 42, 77, 106]. The EINS experiment was be carried out with a fixed resolution window with FWHM of 0.8 μeV at HFBS

[64]. The fixed window scan (FWS) data were collected by cooling the sample from 298 to 19 K that covers the dynamic transition temperature (T_D) in proteins. MSD is calculated from the linear fit of the logarithm of the Debye-Waller factor vs. Q^2. The Debye-Waller factor can be expressed as follows:

$$I_{el}(Q,T) = I_0(Q,T_0)exp(-Q^2 < x^2 >) \tag{3.9}$$

$$ln\left(\frac{I_{el}(Q,T)}{I_0(Q,T_0)}\right) = -Q^2 < x^2 > \tag{3.10}$$

where $I_{el}(Q,T)$ and $I_0(Q,T_0)$ are the elastic signals measured from the sample. $I_0(Q,T_0)$ is usually determined from the lowest temperature measurements, which is 19 K in our case. This model assumes that motions responsible for the decrease in elastic intensity with respect to purely elastic intensity that can be represented by a Gaussian (simple harmonic) model as shown in Eq. 3.9 with $< x^2 >$ (MSD) of the moieties moving faster than instrument resolution of about 2 ns. We have used the Q range of 0.35 Å^{-1} – 1.50 Å^{-1} available at HFBS to evaluate the MSDs at different temperatures from 19 K to 298 K.

3.4 Results and discussion

3.4.1 Diffusive motions of protein molecules analyzed in energy domain

Fig. 3.3 shows the normalized measured self-dynamic incoherent structure factor $S_m(Q,\omega)$, derived from QENS experiments at DCS (A–D) and HFBS (E–H). Each sample of IPPase and HEWL was hydrated using D_2O to a hydration level $h = 0.37$. Since D_2O has a small neutron incoherent scattering cross-section compared with that of the H-atoms within the protein molecules, the QENS signals can be considered to derive from protein contributions only [32, 82]. Clearly, the central peaks are broadened from the resolution function, charac-

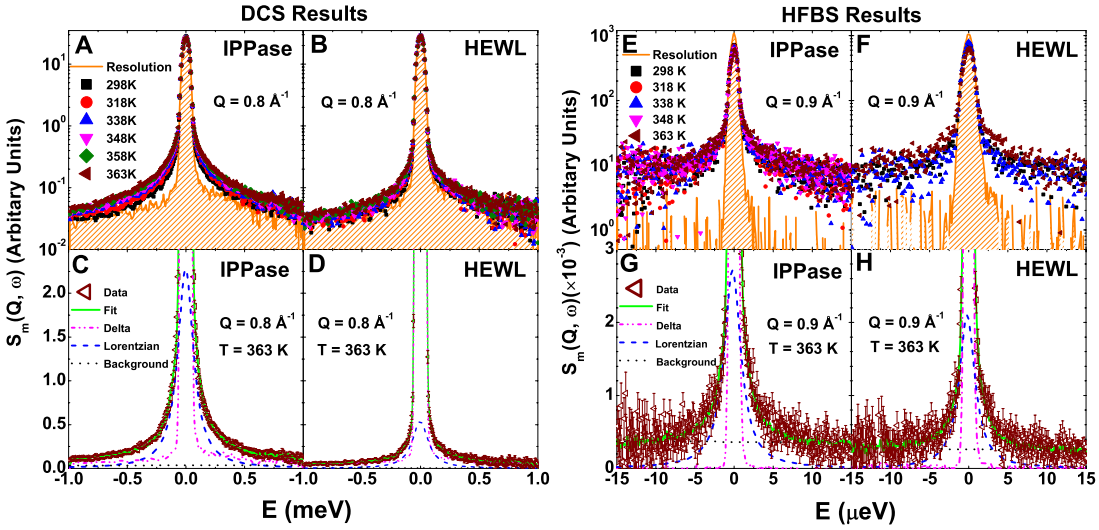

Figure 3.3: Normalized QENS spectra from protein samples and data fitting. Spectra measured at DCS from (A) IPPase and (B) HEWL, respectively, at $Q = 0.8$ Å^{-1} for temperatures from 298 to 363 K along with resolution. DCS data fitted in energy domain for (C) IPPase and (D) HEWL, respectively, at $Q = 0.8$ Å^{-1} and $T = 363$ K. Spectra measured at HFBS from (E) IPPase and (F) HEWL, respectively, at $Q = 0.9$ Å^{-1} for temperatures from 298 to 363 K along with resolution. HFBS data fitted in energy domain for (G) IPPase and (H) HEWL, respectively, at $Q = 0.9$ Å^{-1} and $T = 363$ K. The background is fitted linearly, and elastic and quasi-elastic components are fitted with delta and Lorentzian functions, respectively. In this figure, and in subsequent figures, error bars represent ±1 SD.

terizing the quasi-elastic scattering from the samples. The quasi-elastic component resembles the diffusive motion or the relaxation process of H-atoms within the protein molecules in a confined volume and associated with a protein's conformational flexibility [103, 107]. We observe that, for each sample, the higher the temperature, the broader the quasi-elastic width, implying faster dynamics of the protein molecules. It is clear that the normalized QENS data show faster motions in IPPase than in HEWL at comparable temperatures and length scales. This suggests that IPPase has more conformational flexibility than that of HEWL under 100 MPa of pressure. The QENS data in the energy domain were fitted according to Eq. 3.1. In Fig. 3.3, the lower four panels show the fitted data along with a

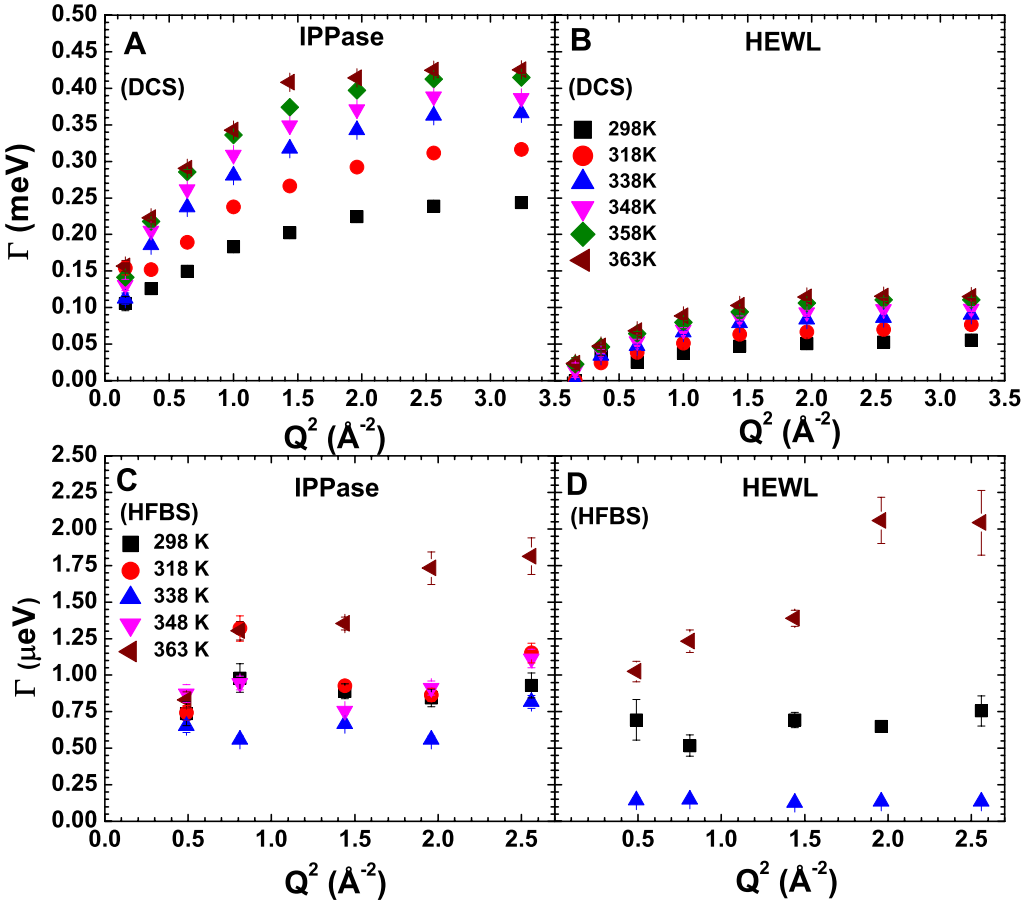

Figure 3.4: Analysis of QENS data in the energy domain at all measured temperatures. Lorentzian half width at half maximum (HWHM) of IPPase and HEWL from DCS (A and B) and HFBS (C and D), respectively.

linear background at the wave vector transfer $Q = 0.8$ Å^{-1} for the DCS data and at $Q = 0.9$ Å^{-1} for the HFBS data, at $T = 363$ K. The elastic component is represented by a delta function, and the quasi-elastic component is represented by a Lorentzian function, and both are broadened by the instrumental resolution function. The elastic component in the QENS spectra represents the immobile H-atoms; whereas the quasi-elastic component originates from mobile H-atoms in the protein. Half widths at half maximum (HWHMs), designated as ($\Gamma(Q)$) of Lorentzians derived from the QENS data for IPPase and HEWL, are calculated

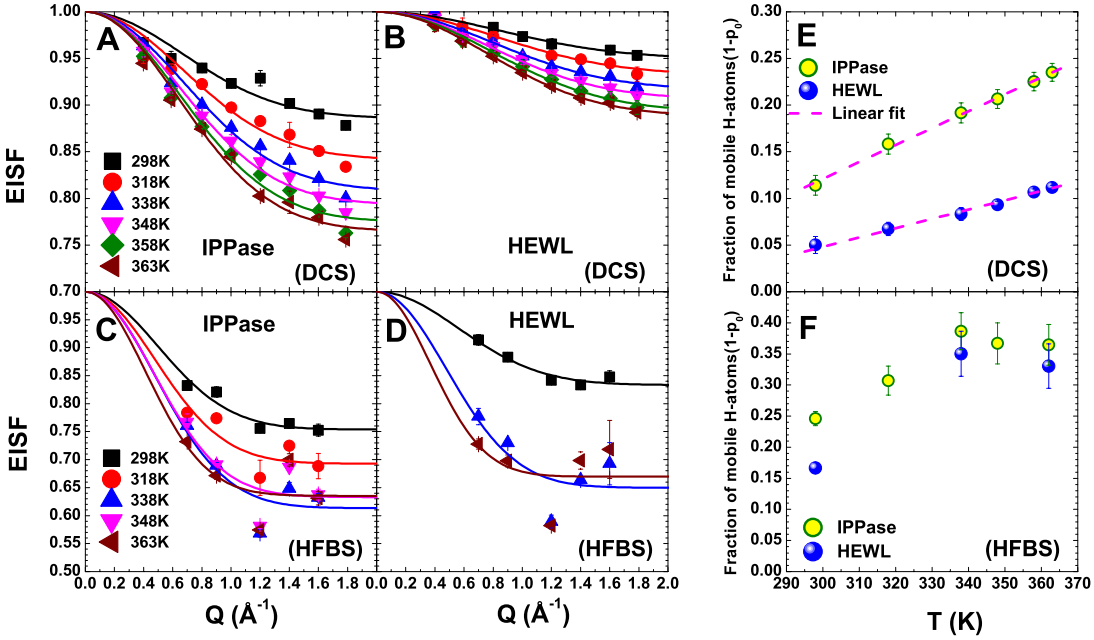

Figure 3.5: Analysis of QENS data in the energy domain at all measured temperatures. Elastic incoherent structure factor (EISF) for (A) IPPase and (B) HEWL, calculated from the data measured at DCS. Elastic incoherent structure factor (EISF) for (C) IPPase and (D) HEWL, calculated from the data measured at HFBS. Fraction of mobile H-atoms in a confined diffusion sphere $(1 - p_0)$ as a function of temperature for IPPase (yellow circles) and HEWL (blue spheres), calculated from the data obtained at (E) DCS and (F) HFBS.

from fitting of the measured QENS spectra with Eq. 3.1 and shown in Fig. 3.4. HWHMs plotted as a function of Q^2 at all of the measured temperatures for IPPase and HEWL, increase with Q^2 and become flat at higher Q values. The Q^2 dependence of the HWHMs suggests diffusive motions of mainly H-atoms in a confined volume of space [103, 107]. The HWHMs increase with temperature in both protein samples, suggesting an increase in diffusive motion. In addition, the HWHM values are larger for IPPase compared with HEWL, suggesting a faster diffusive process and hence more conformational flexibility in IPPase than in HEWL. The calculated values of the HWHMs are of the order of milli-electronvolts (for DCS) to microelectronvolts (for HFBS), representing diffusive processes in the timescale of

picoseconds to nanoseconds.

In Fig. 3.5 *A*–*D*, we show the EISFs derived from the QENS measurements as a function

Table 3.1: Radius of confined diffusion sphere a (Å) in IPPase and HEWL calculated at different temperatures using Eq. 3.4.

	DCS		**HFBS**	
T (K)	IPPase (Å)	HEWL (Å)	IPPase (Å)	HEWL (Å)
298	2.37±0.30	1.89±0.34	3.18±0.28	2.80±0.24
318	2.36±0.22	1.93±0.22	3.31±0.51	NA
338	2.35±0.18	1.99±0.17	3.27±0.50	3.30±0.69
348	2.43±0.17	2.05±0.10	3.38±0.63	NA
358	2.44±0.15	2.02±0.07	NA	NA
363	2.48±0.15	2.10±0.05	3.80±0.87	4.25±1.46

of Q at different temperatures for both IPPase and HEWL. The decrease in the EISF with increase in temperature for both proteins suggests that the fraction of immobile H-atoms decreases with increase in temperature. EISF curves are fitted well with the expression for single diffusive motion of atoms within a sphere given by Eq. 3.4. The fractions of mobile H-atoms, $1-p_0$ for the two proteins are plotted in Fig. 3.5 E and F, as functions of temperature, calculated from DCS and HFBS data, respectively. It is clear that the population of mobile H-atoms, $1-p_0$, is much higher for IPPase than for HEWL at all the temperatures, indicating that more mobile H-atoms in IPPase are observable within our measurement's dynamic window. This result is consistent for the data obtained at both instruments. Moreover, the increase in $1-p_0$ with increase of temperature indicates that more H-atoms are in motion as the temperature rises. The radius of the confined diffusion sphere a is listed in Table 3.1. The value of a increases with increase in temperature and is larger for IPPase

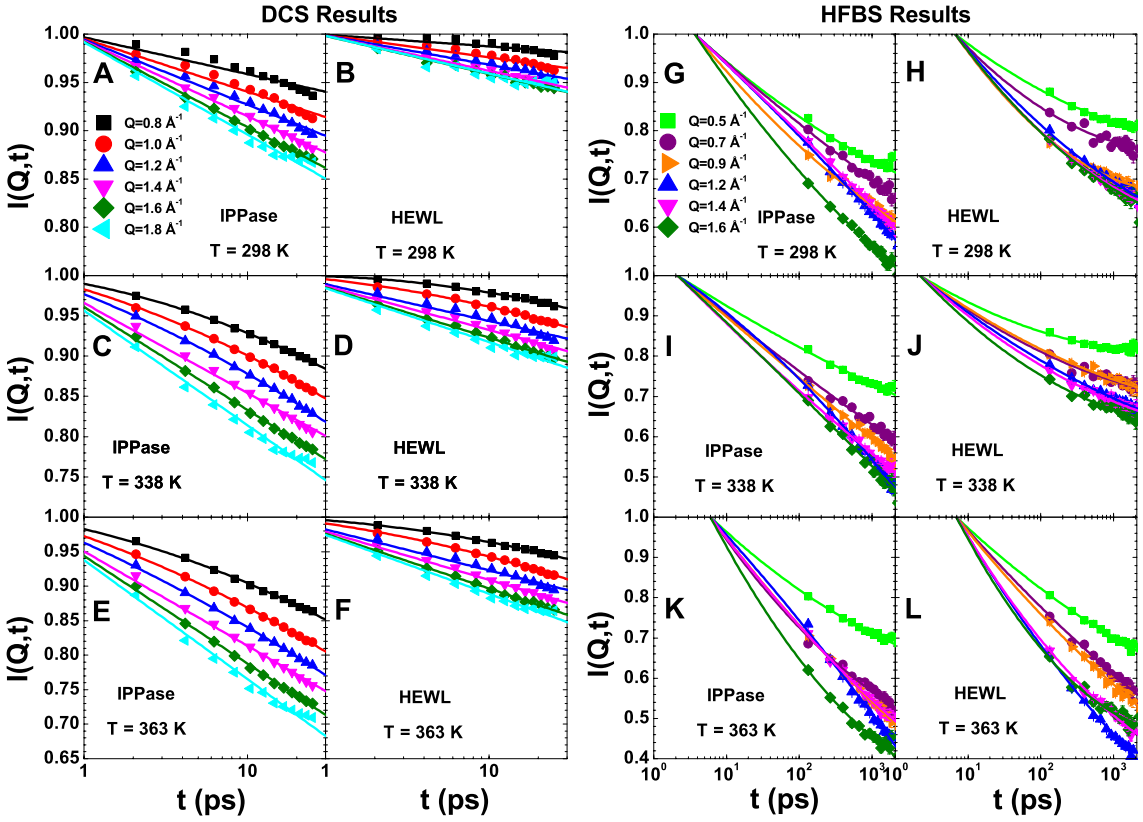

Figure 3.6: Intermediate scattering function (ISF) calculated from DCS and HFBS spectra. (A–F) ISFs of H-atoms in hydrated IPPase (A, C, and E) and HEWL (B, D, and F), respectively, calculated from DCS data. (G–L) ISFs of H-atoms in hydrated IPPase (G, I, and K) and HEWL (H, J, and L), respectively, calculated from HFBS data. Here, we show results at three temperatures: $T = 298$ K, 338 K, and 363 K. ISFs are calculated at a series of Q values from 0.5 Å^{-1} to 1.8 Å^{-1}. Solid lines represent the curves fitted by Eq. 3.6

than that of HEWL. This indicates that IPPase has a larger diffusing volume of space and hence has more conformational flexibility compared with HEWL. These calculated values of radii are consistent with the values observed in other biomolecules [103].

3.4.2 Relaxation dynamics of proteins analog to supercooled liquids or glasses

The intermediate scattering function (ISF) $I(Q,t)$ in the time domain is calculated by taking the inverse Fourier transform of the measured self dynamic incoherent structure factor $S_m(Q,\omega)$ divided by the inverse Fourier transform of the resolution function $R(Q,\omega)$, as

described in detail in SI Materials and Methods. The ISF is also known as the single particle correlation function, and is normally used as an essential tool to describe the relaxation dynamics in protein molecules [22, 50, 74, 108]. Previous studies show that proteins share similar dynamic features as glass forming liquids [109–112] that can be described by mode coupling theory (MCT) [22, 113]. The MCT has successfully predicted a non-exponential logarithmic-like decay in the β-relaxation region (picoseconds to nanoseconds) of protein dynamics, and has proved effective in explaining protein dynamical behavior both in experiments and in molecular dynamics (MD) simulations [22, 27, 29, 74, 82]. Therefore, the non-exponential relaxation dynamics in the ISF is analyzed and fitted using an asymptotic expression derived from the MCT, which is given by Eq. 3.6. In Fig. 3.6, the ISFs for IPPase and HEWL are plotted and analyzed at three temperatures $T = 298$, 338, and 363 K at Q values from 0.5 Å^{-1} to 1.8 Å^{-1}. The left and right panels demonstrate the ISFs calculated from QENS data measured at DCS and HFBS, respectively, in the β-relaxation region. One observes an apparent logarithmic-like relaxation process for both proteins in the measured time range. This non-exponential dynamic behavior has been observed in proteins and other biopolymers in many previous studies [22, 27, 29, 74, 82]. The ISFs are fitted according to Eq. 3.6, and fitted curves are shown in Fig. 3.6 with solid lines. We obtain four fitting parameters, $A(T)$, τ_β, $H_1(Q,T)$, and $H_2(Q,T)$ by global fitting at all six Q values, where $A(T)$ comes from the Debye-Waller factor. In Fig. 3.7 A and B, $H_1(Q,T)$ as a function of Q at all temperatures for IPPase and HEWL are respectively plotted. $H_1(Q,T)$ represents qualitatively the slope of the decay, or the power of decay, and is further fitted by a power law of Q given by Eq. 3.7. $B_1(T)$ is a temperature-dependent parameter, shown in the inset of Fig. 3.7B for both proteins. Evidently $B_1(T)$ is larger for IPPase than for HEWL at

all temperatures and increases linearly with increase in temperature, implying larger flexibility in IPPase than in HEWL in the measured energy/time window. The characteristic β-relaxation time τ_β is plotted vs. 10^3/T (the so-called Arrhenius plot) in Fig. 3.7*C*. The relaxation times can be fitted using the Arrhenius expression, $\tau_\beta = \tau_0 exp(E_A/k_BT)$, where E_A is the activation energy that enables conformational transition across energy barriers between CSs. This result is consistent with our previous observations of the relaxation time in other proteins including IPPase and HEWL, at temperatures higher than 300 K and at ambient pressure [27, 29, 82]. The calculated values of activation energy E_A from the Arrhenius law are 30 ± 4 meV and 43 ± 4 meV for IPPase and HEWL, respectively, slightly higher than the thermal energy k_BT at room temperature, which is ∼25 meV. These values correspond to the low-frequency modes of excitations in proteins that are perceptible in the β-relaxation process [74, 114]. The larger value of E_A for HEWL suggests more rigidity due to unfolding/denaturation compared with IPPase at the pressure of 100 MPa. The astonishing observation is that the β-relaxation time τ_β is smaller for IPPase than for HEWL at all of the measured temperatures, contrary to what it was observed at ambient pressure [27].

3.4.3 Mean-square displacement of hydrogen atoms reveals protein flexibility

Fig. 3.7*D* shows the mean-square displacement (MSD), $< x^2 >$, of H-atoms in the protein samples, calculated from the elastic incoherent neutron scattering data measured at HFBS. From the MSD vs. temperature plot, changes in the slopes of both curves indicate that both proteins undergo a dynamic transition at a temperature T_D around 220–240 K, as observed in many other experiments [27, 82, 106, 115, 116]. The dynamic transition temperature T_D can be considered as the lowest temperature that enables proteins to have the necessary flexibility for different CSs. Our observed T_D value at high pressure is consistent with

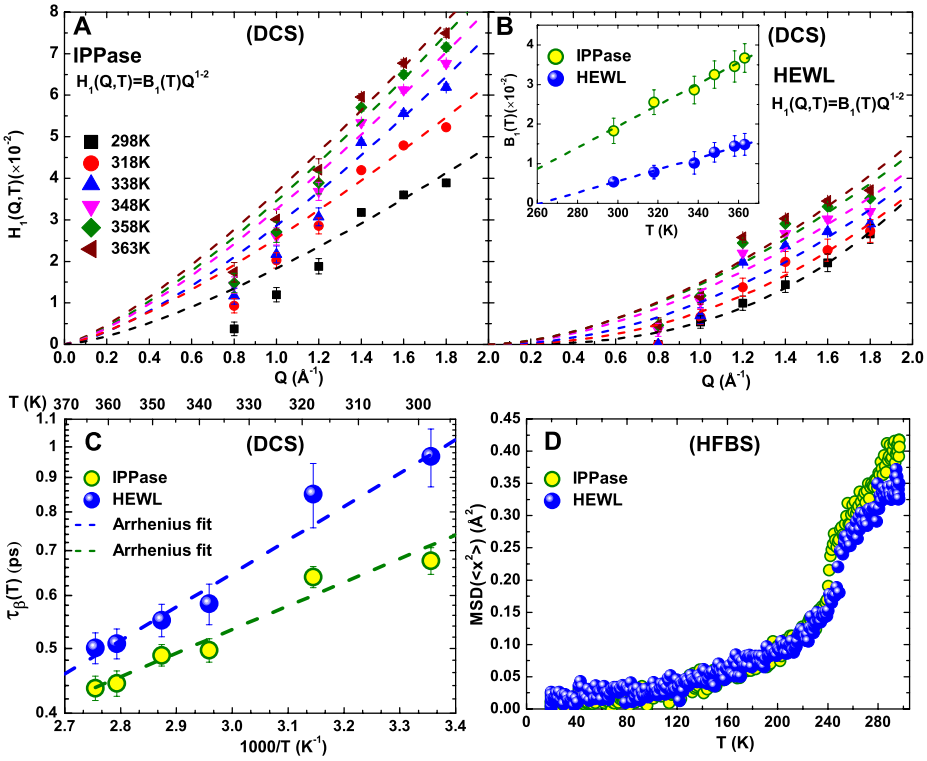

Figure 3.7: Fitting parameters obtained from the MCT analysis of the ISF from DCS data and mean-square displacement (MSD) of IPPase and HEWL from HFBS data. First-order logarithmic decay parameter $H_1(Q,T)$ as a function of Q for (A) IPPase and (B) HEWL, respectively. (Inset) $B_1(T)$ as a function of temperature for IPPase and HEWL. (C) β-relaxation time constant, τ_β plotted as a function of temperature. Dashed lines represent Arrhenius fit of the relaxation time τ_β for IPPase and HEWL. (D) MSD ($< x^2 >$) of H-atoms in protein samples, IPPase and HEWL, measured by elastic incoherent neutron scattering at HFBS. The dynamic transition temperature T_D for IPPase and HEWL are observed around 220-240 K.

previous observations at ambient pressure [27]. Therefore, the dynamic transition appears to be pressure independent, which is consistent with previous MD simulation results [117]. However, a significant difference between the MSDs of IPPase and HEWL is observed above T_D at 100 MPa, which is completely different from the nearly identical MSDs of IPPase and HEWL observed at ambient pressure [27]. This contrast in MSDs is due to a pressure induced effect on the CSs of the proteins, which causes a change in the flexibility of the two proteins above T_D. This observation is consistent with a recently published MD simulation

calculation [118]. Here, we observe a smaller slope of the MSD in HEWL above T_D, which is proportional to the structural resilience of the protein [42, 51], implying that HEWL has increased stability (greater rigidity) and decreased activity, i.e., it loses its conformational flexibility due to pressure-induced unfolding. At the same time, IPPase tends to maintain its conformational flexibility under the same high pressure.

3.4.4 Effects of pressure and the scenario of distorted energy landscapes

Our results indicate that pressure affects the dynamics of proteins and therefore brings about a reversal in the dynamical behavior of two protein samples at high pressure from ambient pressure [27]. Previous MD simulations have addressed the effect of pressure on protein ELs and have suggested that an invariant description of protein ELs should be subsumed by a fluctuating picture [117]. Fig. 5 shows schematic pictures of the denaturation phase diagram and ELs for both proteins, based upon our experimental results with respect to pressure and temperature [79, 88]. In Fig. 3.8 (Left), IPPase has a larger region of folded state in the phase diagram compared with HEWL (shaded region with cyan lines). The magenta dashed line shows the outline of our current measurements at 100 MPa. This phase diagram clearly demonstrates that, along the magenta dashed line, HEWL is unfolded/denatured at 100 MPa at all of the measured temperatures, whereas IPPase remains in its native state until a relatively high temperature of 363 K (90 ^{o}C). On the other hand, in our previous measurements at ambient pressure [27], both proteins were at their native states below 320 K. This explains why the dynamical behaviors of the two proteins are completely reversed at high pressures of 100 MPa compared with ambient pressure.

The right two panels of Fig. 3.8 represent the schematic ELs of atomic fluctuations in IPPase and HEWL at ambient pressure and at a pressure of 100 MPa. Previous studies

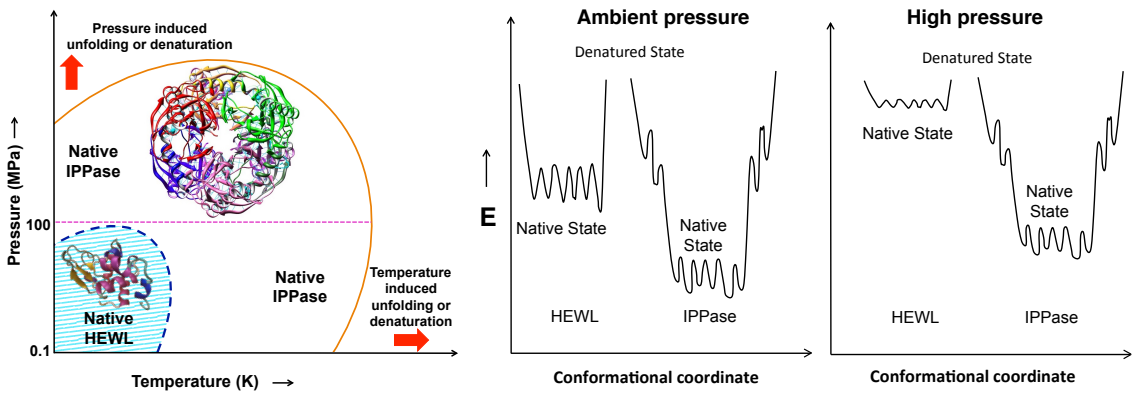

Figure 3.8: Schematic picture of phase diagram and energy landscape in IPPase and HEWL under high pressure and temperature. (Left) Denaturation phase diagram of IPPase and HEWL (shaded region) as functions of temperature and pressure. The axes in the diagram are not drawn to scale. (Right) Schematic plot of cros-sections through a highly simplified energy landscape of atomic fluctuations for different conformational substates (CSs) in IPPase and HEWL under ambient and 100 MPa (1 kbar) of pressure.

reported that pressure causes a decrease in the length of hydrogen bonds that are formed by backbone amide groups to carbonyl groups or surrounding water molecules, which shrinks the cavities in the native/folded state [119]. Such a reduction in the volume of cavities [91, 119, 120], induced by pressure, will further cause changes in protein conformations [121]. Therefore, a change in volume of the cavities will agitate different CSs within the protein ensemble and hence distort the ELs. At high pressure, the ELs of a mesophilic protein such as HEWL are largely affected, resulting in a decrease of energy barriers between the native and denatured states. This makes it easy to cross the energy barrier to reach the unfolded denatured state irreversibly, even at room temperature. On the other hand, the ELs of IPPase are also distorted by high pressure of 100 MPa, but the energy barriers between the native and denatured states are still high enough to sustain its conformational flexibility in its native state.

In general, high pressure dissociates the subunits of oligomers and destabilizes the pro-

tein, but the interesting aspect here is to understand why IPPase, an oligomeric protein, reflects physiological dynamic behavior under high pressure. This can be explained by assuming that cavities inside the protein are not disturbed due to its highly symmetric and closed oligomeric structure, which helps to maintain its native conformation and flexibility under high pressure as well as temperature. Previous work has also studied the enzymatic functions of several hyperthermophiles from the deep-sea and found that they demonstrate higher rates of enzymatic activity at high pressure and temperature than that of simple monomeric proteins under the same conditions [96]. This exotic property of specific proteins such as IPPase enables some microorganisms to defy the effects of high pressure and temperature to sustain their lives under the deep seabed [122].

3.4.5 Conclusion

In summary, our study reveals the effects of pressure on a large hyperthermophilic oligomeric protein IPPase and shows how it steadily maintains its conformational and dynamic properties in its native environment at high temperature and pressure. Also, our results indicate that, under a pressure of 100 MPa, IPPase displays much faster relaxation dynamics than a mesophilic model protein, HEWL, at all of the measured temperatures, opposite to what it was observed previously under ambient pressure [27]. In addition, our experimental results indicate that pressure drives the volume reduction of intramolecular spacing [121] that causes mesophilic HEWL to lose its conformational flexibility as suggested by MSD results, and consequently, its catalytic activity. However, the hyperthermophilic protein IPPase is able to preserve its conformational flexibility and maintain its enzymatic activity at high pressure and temperature, supposedly due to its highly symmetric and closed oligomeric structure. Furthermore, we investigated the relaxation dynamics

of proteins in the β-relaxation region in the time domain, vital to their biological activities. Both proteins follow a nonexponential logarithmic-like decay in the ISF as suggested by MCT for glass-forming liquids. The relaxation dynamics due to diffusion of H-atoms in the time range of picoseconds to nanoseconds, decays more rapidly in IPPase than in HEWL at respective temperature under high pressure, opposite to what we observed under ambient pressure [27]. This dynamic reversal can be explained by a general schematic denaturation phase diagram together with ELs for the two proteins. Such a scenario can be further used as a general picture to understand the functional activities of thermophilic proteins under pressure. Our observation also strongly supports the hypothesis that the protein ELs are distorted by high pressure [86, 117], which are significantly different for hyperthermophilic (IPPase) and mesophilic (HEWL) proteins.

CHAPTER 4 MECHANISM OF ACTIVATION OF RHODOPSIN

4.1 Background

G-protein-coupled receptor (GPCR) constitutes a large family of membrane proteins that mediates extracellular (physical and chemical) signals such as light, odor, taste, hormones, and neurotransmitters into the distinct intracellular signaling pathways [123–125]. GPCR shares a common seven alpha-helical transmembrane (7TM) structure, which changes its conformation upon activation across the biological membranes [123, 126]. The conformational change on the intracellular surface of the receptor binds and activates several hundreds of heterotrimeric guanylate nucleotide-binding protein, known as G protein, which in turn triggers the events that ultimately modulate and amplify the cellular response [127]. Fig. 4.1 shows the schematic of mechanism of G-protein-coupled receptor, rhodopsin binding G protein (transducin) upon photoactivation [128]. The cell membranes of almost all the animals such as mammals, insects and flatworms contain GPCRs [123]. The GPCR superfamily encompasses approximately 950 genes in the human genome, including nearly 500 sensory GPCRs [125, 127]. Thus, more than 50% of the therapeutic drug targets are GPCRs, which work by regulating the behavior of specific 7TM receptor protein [123, 125, 127, 129]. Understanding the mechanism of GPCR activation is still a major challenge in biophysical research. In this chapter, I will show how GPCR activation mechanism is studied using neutron scattering techniques. First section 4.2 and the next section 4.3 comprise the studies of changes in GPCR rhodopsin conformation and intrinsic dynamic behavior upon photoactivation, respectively.

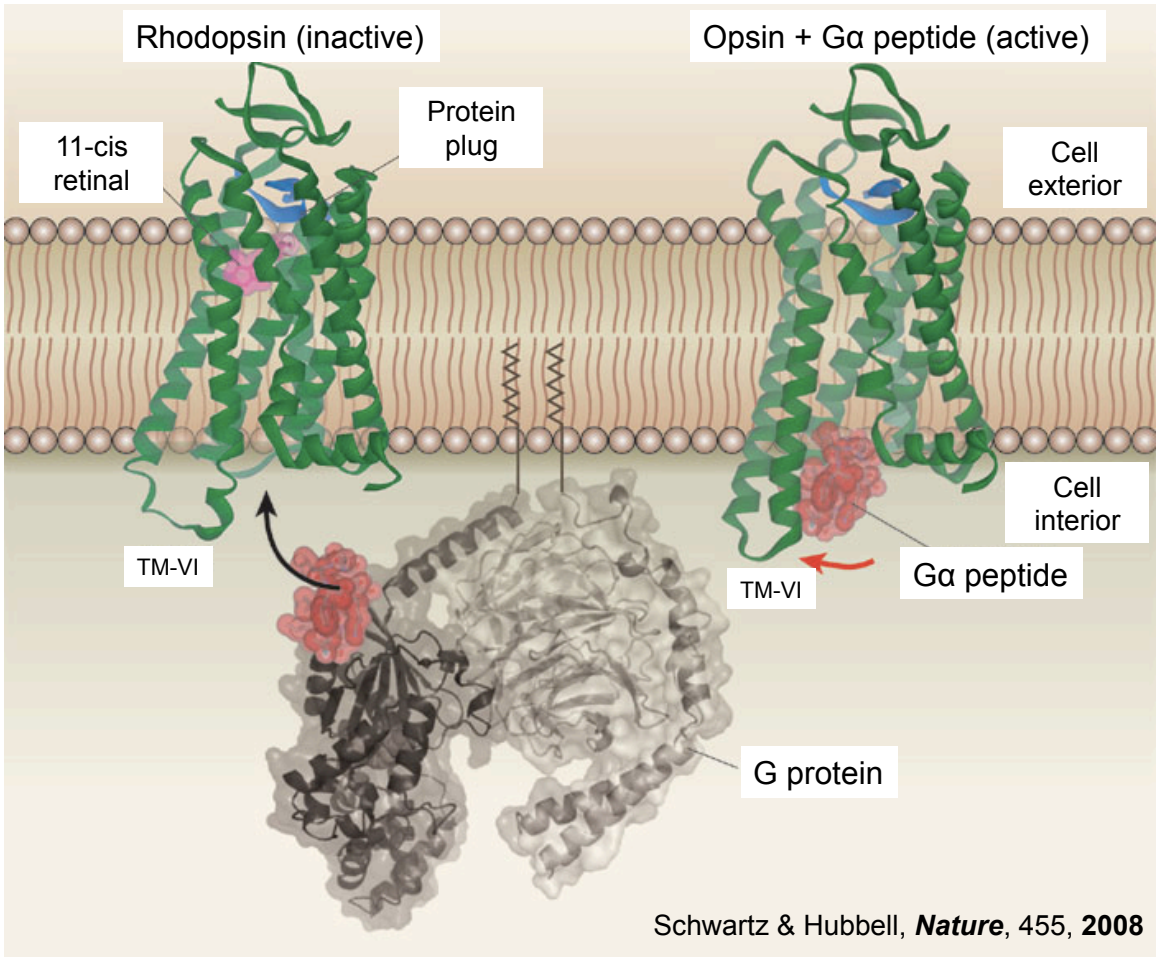

Figure 4.1: Schematic diagram of mechanism of G-protein-coupled receptor, rhodopsin binding heterotrimeric guanylate nucleotide-binding G protein (transducin) upon photoactivation.

4.2 Photoactivation mechanism of rhodopsin in detergent solution

4.2.1 Introduction

Rhodopsin is the family A GPCR, responsible for vision under dim light conditions in all the vertebrates [123, 130]. In vertebrate retinal, rod and cone photoreceptors contain rhodopsin and opsin, respectively. Their chromophore, 11-*cis* retinal, is covalently bound via a protonated Schiff base to the polypeptide chains of each opsin, embedded within the transmembrane domain [127]. The chromophore 11-*cis* retinal locks the rhodopsin in the

inactive dark state, and acts as an inverse-agonist by preventing interaction with its cognate G protein, transducin [130, 131]. Upon light absorption, the chromophore undergoes isomerization of 11-*cis* retinal to all-*trans* retinal, inducing a significant change in the opsin conformation from its inactive to active state as shown in Fig. 4.2 [123, 130, 131]. Such activation causes the expansion due to outward tilting of the cytoplasmic end of helix 6 (H6), creating a cleft for binding the G protein [127, 132]. At the same time, the cytoplasmic end of helix 5 (H5) elongates providing more interface for G protein interaction [127]. The active state is also known as Metarhodopsin II, which binds the intracellular G protein [123, 126, 133, 134]. This initiates the visual signaling, which culminates in an electrical impulse to the visual cortex of the brain [123]. X-ray crystallography studies conducted on the prototypical visual GPCR rhodopsin have revealed valuable information about the conformational changes that occur during activation [127, 133, 135–138]. However, such freeze-trapped structure (at very low temperature) may not represent the native conformation of rhodopsin [130]. Moreover, they lack the clear depiction regarding how the rhodopsin conformational change occurs in the native membrane. In this work, we used small-angle scattering to study the change in conformation of rhodopsin upon photoactivation in detergent solution, where detergent mimics the membrane-like environment.

It has been one of the fundamental questions how the GPCR rhodopsin organizes and operates itself in the native membrane for the signal transduction [130, 139, 140]. Infrared-laser atomic-force microscopy and transmission electron microscopy experiments have confirmed the series of densely packed dimers of rhodopsin in the native disc membrane [139, 140]. Not only in the native disc membrane, but the dimerization of rhodopsin was also observed in the detergent micelles of n-dodecyl-β-D-maltoside (DDM) [141]. In addition, the higher order

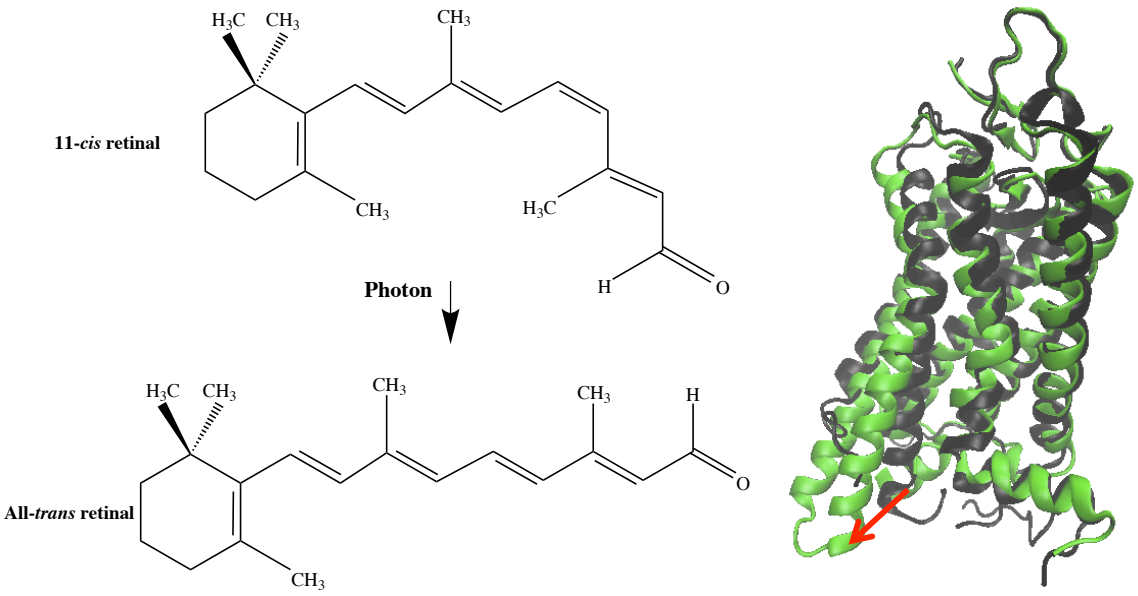

Figure 4.2: Mechanism of conformational change in rhodopsin upon activation. (Left) Isomerization of 11-*cis* retinal to all-*trans* retinal upon photoactivation. (Right) Conformational change in rhodopsin, where green is Metarhodopsin II structure (PDB 3PQR) due to light activation and black is dark state rhodopsin (PDB 1F88).

oligomers were formed in detergent micelles of n-tetradecyl-D-maltoside and n-hexadecyl-D-maltoside [142]. The photoactivation of monomer or dimer of rhodopsin are found to be capable of further activating the G protein, transducin. However, the transducin activation is rapid when rhodopsin is in the form of organized dimers or higher order oligomers [142]. Therefore, the quaternary structure of rhodopsin is a crucial aspect for signaling G protein, transducin [139, 141–143].

Small-angle scattering (SAS) is an appropriate technique to study the macromolecular structures in solution [59, 144, 145]. SAS is not the high-resolution method like diffraction [146], however it is a very useful technique that complements the higher resolution methods [59, 61, 147, 148]. Small-angle X-ray scattering (SAXS) and small-angle neutron scattering (SANS) can probe the macromolecular structures in solution at the resolution of a nanometer

(nm) [149, 150]. They are widely used for the study of biomolecules, which are very hard to crystallize such as membrane proteins [53, 151–153]. SAXS is very robust in data collection due to its bright intensity, whereas SANS requires longer data collection time with good statistics because of its low intensity. In contrast to SAXS, SANS is very useful in studying the multi-component structures in solution [151, 154, 155]. Since hydrogen and its isotope deuterium have very different coherent scattering cross-sections for neutron, each component in solution can be studied separately by varying H_2O/D_2O proportion, a method called contrast match [156–159]. On the other hand, SAXS considers the uniform electron density from the protein-detergent complex (PDC), therefore it is difficult to differentiate the scattering signal from free detergent micelles, detergent molecules, corona formed by detergent around protein and the protein molecules in the complex macromolecular solution [53, 150, 152]. Thus, SAXS is not a suitable technique for the study of protein structure in PDC. On the other hand, membrane protein structure can be studied in PDC by SANS contrast match method, where the signal from the detergent molecules and free detergent micelles can be ruled out by varying H_2O/D_2O proportion in solution [56, 145, 151, 154]. Therefore, here we used SAXS to study the structure of detergent micelles and PDCs, whereas the protein structure in PDCs was studied using contrast match SANS technique.

Previous SANS and SAXS studies of rhodopsin could not provide the information regarding the conformational change in rhodopsin activation [55, 56]. Using contrast match SANS technique, we reveal the conformational change in detergent-solubilized rhodopsin mimicking the native membrane-like environment under physiological conditions. We used two different types of detergent in solution, zwitterionic 3-[(3-cholamidopropyl) dimethylammonio]-1-propanesulfonate (CHAPS) and non-ionic DDM having critical micellar concentration

(CMC) 8 mM and 0.17 mM respectively to solubilize and stabilize rhodopsin [160] and further investigate the conformational change in rhodopsin upon photoactivation. Both detergents are considered to be suitable for the structural studies of membrane proteins [161]. We observed the activation leads to the expansion of rhodopsin conformation, which is consistent with the previous studies of rhodopsin activation [127, 130, 139–141]. Moreover, the activation of rhodopsin takes place in higher order oligomeric form, where we observed the densely packed ensemble of two dimers, forming tetramers. The activation of rhodopsin in higher order oligomeric form suggests that the conformational expansion of rhodopsin entropically favors the more open configuration for binding G protein [130, 140–142]. These results indicate that the quaternary structure of rhodopsin is crucial for the rapid signaling of the G protein, transducin. This experiment impacts the further insights to the GPCR activation mechanism, crucial for understanding signal transduction across the biological membranes.

4.2.2 Materials and methods

Sample preparation

The detergent-solubilized rhodopsin samples using detergents CHAPS and DDM were prepared according to the protocol in reference [162] for small-angle scattering experiments. Furthermore, each protein-detergent samples were prepared with certain H_2O/D_2O proportion such that solvent scattering length density (SLD) was matched with that of detergent for SANS experiment. Also, the corresponding buffers with same H_2O/D_2O proportion without protein and detergent were prepared for background subtraction. The dark state (DS) rhodopsin was prepared in completely dark room using red dim light (λ_{max} <680 nm) at biochemistry lab of High Flux Isotope Reactor (HFIR), which was then put into the banjo

cell surrounded by the green LEDs (for activation) wired to the switch that can be turned on/off remotely. The use of red dim light cannot activate rhodopsin and has been often used for rhodopsin extraction and purification [163]. On the other hand, the photobleaching of rhodopsin with green LED light of 515 nm wavelength activates to form metarhodopsin-II [164]. The whole sample cell along with green LEDs was wrapped with aluminum foil to prevent any ray of light reaching the sample and loaded into the sample chamber for SANS measurements (note: aluminum is transparent to neutrons). The light activated state (LAS) of rhodopsin was achieved by photobleaching the sample with green actinic light source surrounding the sample.

Small-angle scattering measurements

SAXS experiment was performed at beamline X9, National Synchrotron Light Source-I (NSLS-I), Brookhaven National Laboratory (BNL) [165]. The SAXS measurements were done to characterize the structure of detergent micelles and PDCs. The data from two detector configurations were combined to cover the q-range of 0.008 - 1.75 $Å^{-1}$, with overlapping data between 0.005 $Å^{-1}$ and 0.210 $Å^{-1}$ at 14.1 keV incident energy, sufficient for biological solution. On the other hand, the SANS data of PDCs were measured, where the detergent SLD was contrast matched with that of solvent varying H_2O/D_2O ratio such that the data after subtracting the corresponding buffer provided the signal from protein only. SANS experiment was performed at Bio-SANS instrument, High Flux Isotope Reactor (HFIR), Oak Ridge National Laboratory (ORNL) [166]. The data were measured at 15 ^oC using 1 mm path length quartz cells from the protein concentration of $\sim$6 mg/mL, where detergent to protein ratio were 150:1 for CHAPS-rhodopsin complex and 200:1 for DDM-rhodopsin complex in solution. Scattered neutrons were collected with a 1 m by 1 m two-dimensional

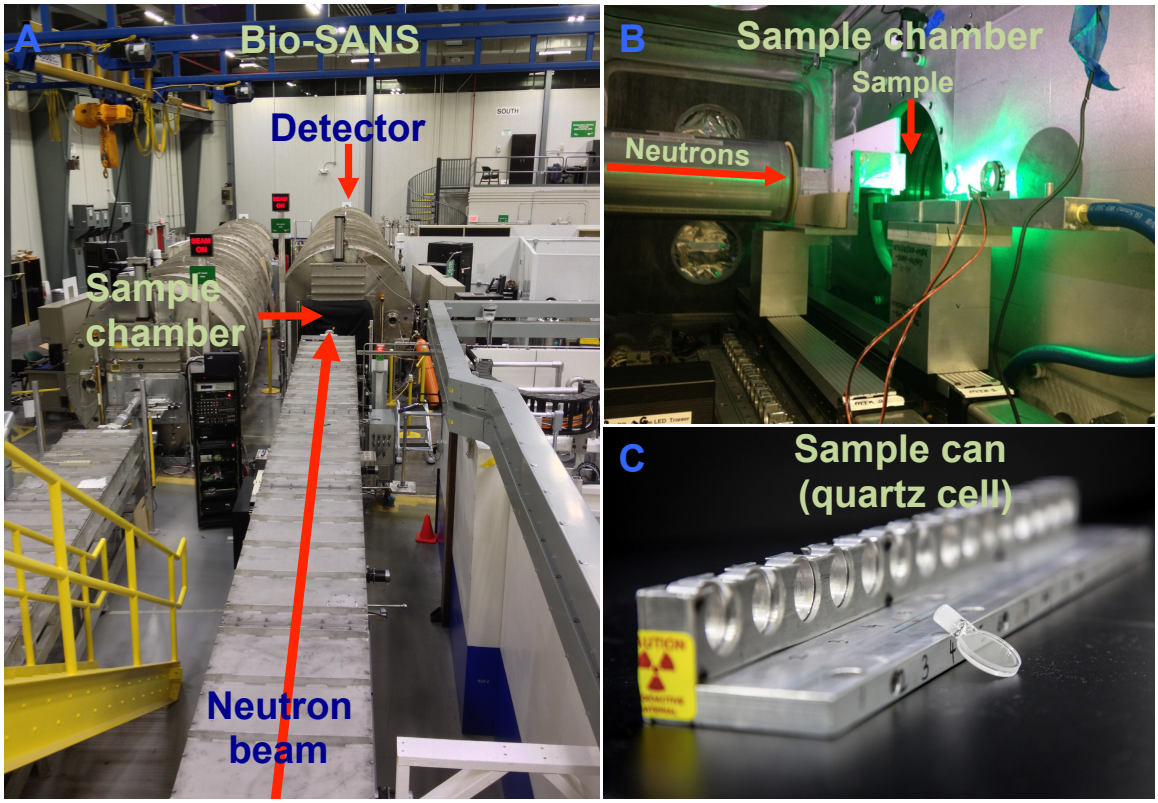

Figure 4.3: Bio-SANS instrument at High Flux Isotope Reactor (HFIR), Oak Ridge National Laboratory (ORNL).

(2D) position-sensitive detector with 192 by 192 pixel resolution. The data in the q-range of 0.008 $Å^{-1}$ - 0.152 $Å^{-1}$ and 0.024 $Å^{-1}$ - 0.737 $Å^{-1}$ were measured from the sample to detector distance of 6 m and 30 cm respectively, with overlapping data between 0.024 $Å^{-1}$ and 0.152 $Å^{-1}$. The measured 2D small-angle scattering data were corrected for detector pixel sensitivity, as well as the dark current, from ambient background radiation and the detector's electronic noise. The reduced 2D data were azimuthally averaged to yield the 1D scattering intensity $I(q)$ vs. q, where q is the scattering vector defined by Eq. 4.1,

$$q = \frac{4\pi sin\theta}{\lambda} \tag{4.1}$$

where 2θ is the scattering angle and λ is the X-ray/neutron wavelength.

Small-angle scattering theory

For a monodisperse solution of nearly spherical particles, the measured scattering intensity can be written as a function of momentum transfer q given by [160],

$$I(q) = cP(q)S(q,c) \tag{4.2}$$

where c is the particle concentration, $P(q)$ is the form factor (also known as particle structure factor), and $S(q,c)$ is the solution structure factor. $P(q)$ corresponds to the orientationally averaged scattering profile of a single particle and can be computed from a structural model. $S(q,c)$ accounts for the particle interactions in solution and modifies the measured scattering profile at finite concentrations. The solution structure factor $S(q,c)$ modifies $I(q)$ most strongly at small momentum transfer q. $S(q,c)$ can in principle be computed, at least approximately, from solution theory. For weakly interacting particles at low enough concentrations, $S(q,c)$ is equal to unity and the scattering intensity is given by the particle form factor alone. In such case, the scattering intensity data can be fitted using the one or two component shape models for the particle form factor, $P(q)$. Furthermore, in the limit that interparticle correlations are negligible, the scattering intensity for very low momentum transfer q is given by the Guinier approximation as expressed below [59, 160],

$$I(q) \approx I(0)e^{-R_g^2 q^2/3} \tag{4.3}$$

where $I(0)$ is the forward scattering intensity, which is the shape-independent function of

the total scattering power of the sample and R_g is the radius of gyration. The linear fit of $lnI(q)$ vs. q^2, also known as Guiner plot provides R_g and $I(0)$ from the slope and y-intercept, respectively. The Guiner approximation is only valid for small $q_{max}R_g$, such that $q_{max}R_g \leq 1.3$ (in theory). In addition, the pair distance distribution function, $P(r)$ can be calculated using the indirect Fourier transform of measured $I(q)$. The scattering profile of dilute monodisperse solution may be written in terms of the pair distance distribution function, $P(r)$ with D_{max} as the maximum intramolecular distance, given by Eq. 4.4,

$$I(q) = \int_0^{D_{max}} P(r)\frac{sin(qr)}{qr}dr \tag{4.4}$$

$P(r)$ provides the approximate shape and size of the monodisperse particle in solution. Moreover, the theoretical SANS intensity profiles were calculated using the package CRYSON in ATSAS program [167] using the known protein data bank (PDB) structures 1F88 and 3PQR for DS and LAS of rhodopsin, respectively. Furthermore, the fitting of SAXS intensity profiles of detergent micelles with theoretical model were done using a program SasView to calculate the geometric shape and size. The ellipsoidal model (one component) as expressed in Eq. 4.5 is used to fit the SAXS intensity profile of CHAPS micelle.

$$I(q) = \frac{c}{V}\left[\frac{\left(3\Delta\rho\ V\ \ sin(qr) - qr\ \ cos(qr)\right)}{(qr)^3}\right]^2 + Background \tag{4.5}$$

where

$$r(R_a, R_b, \alpha) = (2R_b\ \ sin2\alpha + 2R_a\ \ cos2\alpha)^{\frac{1}{2}}$$

where c is scale factor, the angle between the axis of the ellipsoid and scattering vector is represented by α, $\Delta\rho$ is the scattering length density difference between particle and the solvent, whereas the ellipsoid volume is V, and R_a and R_b are the radii along and perpendicular to the rotation axis, respectively. Moreover, the SAXS intensity profiles of DDM micelle and PDCs are fitted with core-shell ellipsoidal model given by,

$$I(q) = \frac{c}{V_s}\Bigg[3V_c(\rho_c - \rho_s)\frac{\Big(sin(qr_c) - qR_c\ cos(qr_c\Big)}{(qr_c)^3} + 3V_s(\rho_s - \rho_{solv})\frac{\Big(sin(qr_s) - qr_s\ cos(qr_s\Big)}{(qr_s)^3}\Bigg]^2 + Background \tag{4.6}$$

where

$$r_c(R_a^c, R_b^c, \alpha) = (2R_b^c\ sin2\alpha + 2R_a^c\ cos2\alpha)^{\frac{1}{2}}$$

and

$$r_s(R_a^s, R_b^s, \alpha) = (2R_b^s\ sin2\alpha + 2R_a^s\ cos2\alpha)^{\frac{1}{2}}$$

Here, V_s is the volume of the outer shell, and V_c is the volume of the core. R_a^c and R_b^c are the core radii along and perpendicular to the rotation axis, respectively. R_a^s and R_b^s are the shell radii along and perpendicular to the rotation axis, respectively. ρ_s is the shell SLD, ρ_c is the core SLD, and ρ_{solv} is the solvent SLD. The quality of fitting is determined by converging towards the least value of reduced chi-square (χ^2), where $\chi^2 = (1/N)\Sigma\Big(I_{exp}(q)$ - $I_{model}(q)\Big)^2/(\sigma^2)$, where N is the number of free parameters and σ is the uncertainty (or standard deviation) of the data.

4.2.3 Results and discussions

Conformational stability of detergent-solubilized rhodopsin in solution

At first, SAXS measurements were performed to study the shape and size of detergent

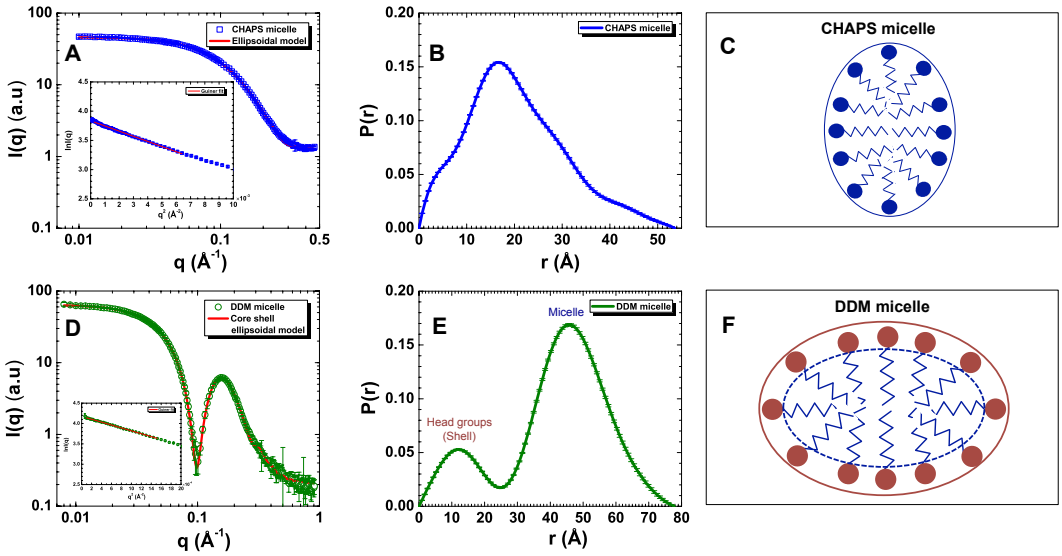

Figure 4.4: SAXS intensity profiles, pair distance distribution function and the schematic of structure of detergent micelles. The pair distance distribution function, $P(r)$ is calculated from the inverse Fourier transfer of $I(q)$.

(CHAPS and DDM) micelles in the absence of protein (rhodopsin) having hydrophobic tail and hydrophilic head groups [160]. The SAXS intensity profiles of CHAPS and DDM micelles are shown in Fig. 4.4 *A* and *D* respectively, where the second maximum in DDM micelle data indicates the characteristic head group due to huge contrast in SLD between the head and tail groups. However, no such maximum is observed in CHAPS micelle intensity since there is no contrast in SLD between head and tail groups. Using Guinier approximation, as shown in insets of Fig. 4.4 *A* and *D*, R_g values of CHAPS and DDM micelles were determined to be 16.2 $\pm$ 0.1 Å with $q_{max}R_g = 1.29$ and 32.7 $\pm$ 0.3 Å with $q_{max}R_g = 1.28$,

respectively. Moreover, assuming the monodisperse particles in solution, the corresponding pair distance distribution function, $P(r)$ of CHAPS and DDM micelles were calculated, which are shown in Fig. 4.4 B and E respectively. Clearly, there exist only one maximum peak in calculated $P(r)$ at 18 Å from CHAPS data, which corresponds to the approximate size of nearly spherical CHAPS micelle indicating only one component system. Thus, the scattering intensity was fitted with one-component ellipsoidal model (Eq. 4.5) as shown in Fig. 4.4A to determine the exact shape and size of the CHAPS micelle and the corresponding schematic diagram is shown in Fig. 4.4C. CHAPS micelle is found to have prolate ellipsoidal structure. On the other hand, in DDM, the two distinct maxima are observed in the calculated $P(r)$ at 12 Å and 47 Å corresponding to the two components system, where the former and latter size indicate the spacing of outermost head group (shell) from the core of the micelle and approximate dimension of DDM micelle, respectively. Therefore, the SAXS intensity of DDM micelle was fitted with two-component core-shell ellipsoidal model (Eq. 4.6) as shown in Fig. 4.4D with corresponding schematic diagram in Fig. 4.4F. The free micelle of DDM has oblate ellipsoidal structure. The calculated R_g and fitted model parameters from CHAPS and DDM micelles are consistent with previously published SAXS and SANS results [160, 168], and are listed in Table 4.1.

The real challenge for the study of membrane proteins like rhodopsin is that they are insoluble in aqueous buffers due to their hydrophobic regions [53, 55, 56, 151, 160]. They require amphiphilic molecules like detergents having hydrophilic head groups and hydrophobic tail groups, which maintain the native protein conformation avoiding the aggregation [53, 160, 169]. Therefore, detergent micelles play a major role in biochemical and biophysical studies of membrane proteins. Many detergents are widely used for the extraction and

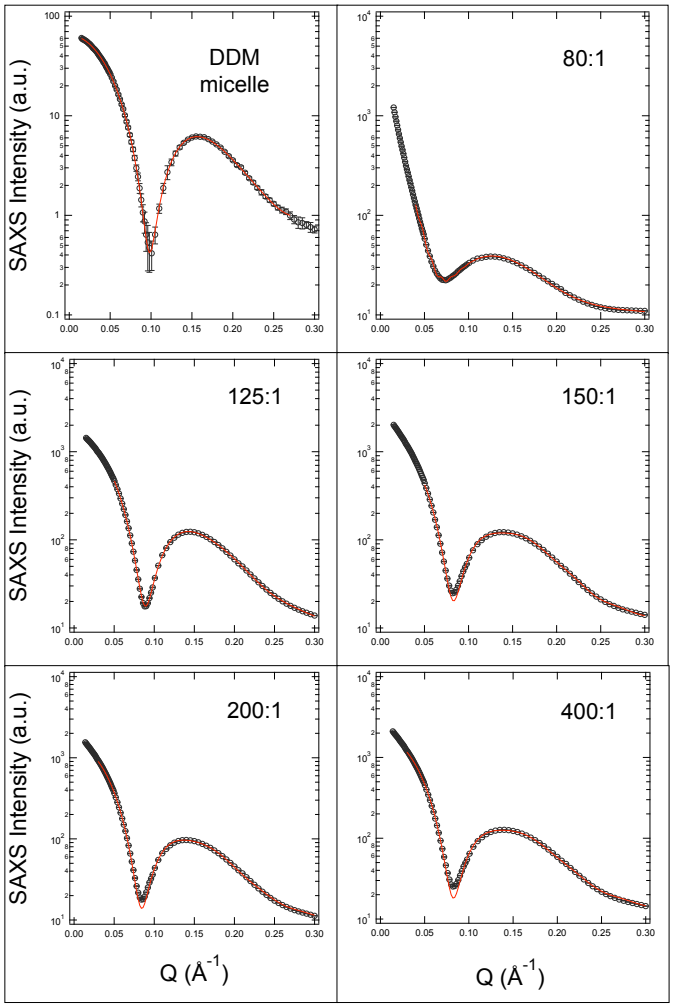

Figure 4.5: SAXS intensity profiles of rhodopsin-DDM complex at various detergent to protein ratio. The solid red curves are the fitting of SAXS profiles by core-shell ellipsoidal model (Eq. 4.6).

purification of membrane proteins, and further used for the structural and functional characterization [170]. Specifically, detergent acts as artificial lipid bilayers because of their self-assembling properties, which helps to solubilize and stabilize membrane proteins in solution. In addition, such detergent molecules are bound to the membrane protein forming different possible binding structures such as micellar binding, monolayer binding, or prolate ring that help to preserve the native conformation of membrane proteins. In other words,

the detergent molecules form a corona around the hydrophobic transmembrane region of the protein with polar head groups facing the aqueous solution [53]. In the past years, various detergent solutions were extensively used in structural biology of membrane proteins that are hard to crystallize in laboratory. Earlier structural study of rhodopsin free from lipid in the presence of polyoxyethelene alcohol detergents indicate that hydrated rhodopsin have an elongated shape with the hydrophobic part at the center that prevents any hydration layer or segment to go through the protein [56]. This region is dense and attractive to the detergents. The detergent orientation is asymmetric compared to the protein. In other study with non-ionic dodecyldimethylamine oxide (DDAO) detergent [55], a cylindrical shape was assumed for rhodopsin, which is homogeneously hydrated and placed itself perpendicular to the membrane stretching the lipid-bilayer evenly, while Ramakrishnan et al. proposed the model of inverted lipids micelle (in hexane) covering the protein whose hydrophobic region acts as the cross-linker [171].

The effect of buffer and its subtraction in the solution scattering experiment is always crucial. In addition, for the study of PDC in solution, subtracting the signal of free detergent micelle becomes more strenuous job. Thus, the study of solution scattering from PDC requires addition SAXS data of detergent containing buffer solution, which we discussed above. We found the difference between the reduced data using detergent containing buffer solution and detergent free buffer solution, as background, is negligible. To estimate the negligible free detergent micelle effect different ways were used. As we have pointed out, the effect of empty detergent micelle can play a critical role in deducing the PDC scattering intensity. Estimating the amount of empty micelle is important because of its possible over or under estimation. We examined the idea of Lipfert et al. in our work [156, 160]. Effectively, the

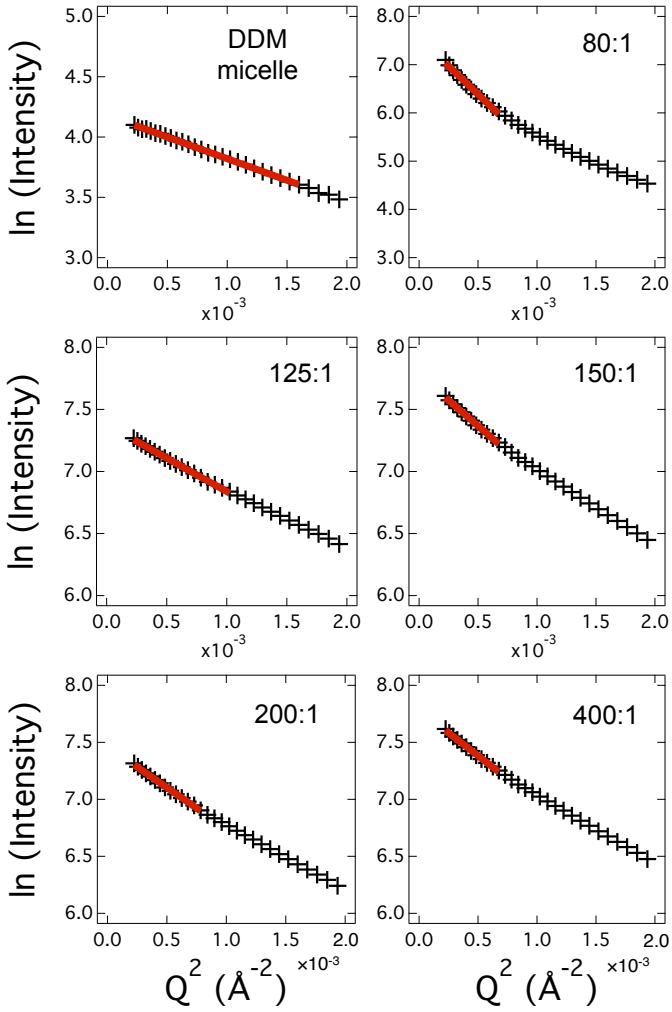

Figure 4.6: Guinier analysis of rhodopsin-DDM complex at various detergent to protein ratio. The solid red lines are the Guinier fits.

goal is to get an upper and lower bound of the PDC signal. The upper bound is estimated by the ratio of empty micelle and the difference in PDC from buffer intensity, weighted by their respective concentrations. Its smaller value indicates small micelle concentration in the complex and weaker signal due to free detergent micelle compared to the PDC. On the other hand, calculating the same way but using the intensity difference between the PDC and the micelle draws the lower bound. In case, where free micelle scattering is low compared to PDC, the two limits are very close. We have examined that in our work detergent free

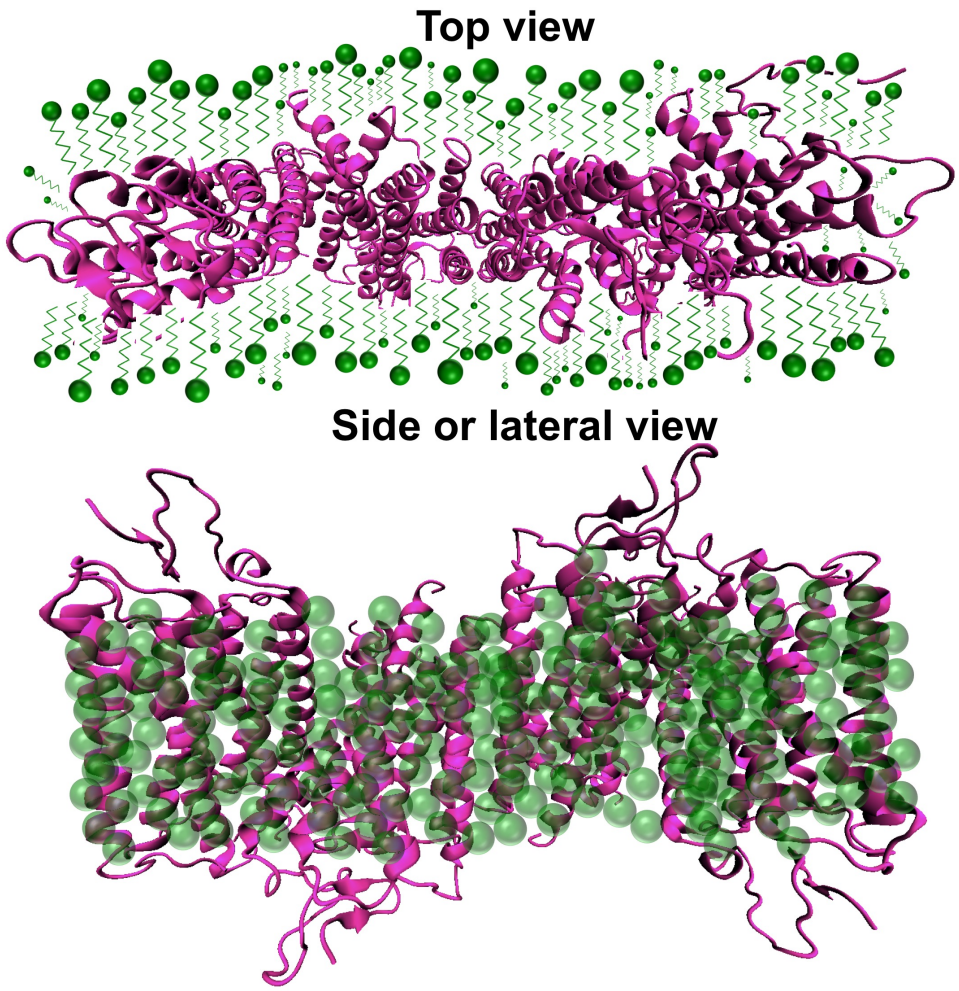

Figure 4.7: Schematic of rhodopsin-DDM complex based on core-shell ellipsoid model fit parameters, where core is rhodopsin (pink color) and the shell is DDM micelle (green color).

buffer solution and detergent signal both are very low in intensity compared to the scattering intensity from the PDC. Also, from the comparison of the troughs between bulk detergents and PDC signals, a bigger shell dimension in the complex is noted with much higher intensity indicating little free micelle effect. And only as we increase the detergent ratio in the complex, the fitting gets slightly deviated in the trough region indicating a possible smearing effect and polydispersity due to possible formation of few free detergent micelles in solution. The comparison of SAXS intensities calculated by subtracting the signal of only buffer, and

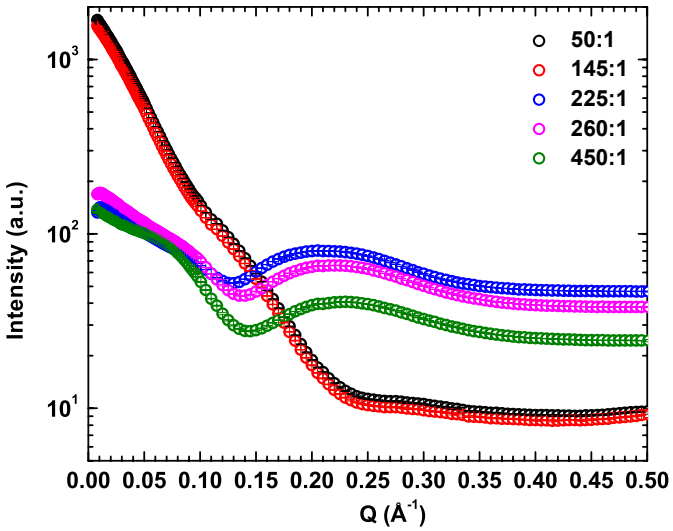

Figure 4.8: SAXS intensity profiles of rhodopsin-CHAPS complex at various detergent to protein ratio.

buffer plus detergent from PDC for rhodopsin-DDM complex are shown in Fig. in appendix A. Such plots clearly demonstrate that the intensity of buffer and buffer plus detergent is much low compared to that of PDC.

In Figs. 4.5 and 4.8, the SAXS intensity profiles are shown for rhodopsin-DDM and rhodopsin-CHAPS complexes at various detergent to protein ratio and the respective Guinier analysis are shown in Figs. 4.6 and 4.9. Clearly, the SAXS data of rhodopsin-DDM complexes at high detergent to protein ratio show that the detergent molecules prevent rhodopsin from aggregation. But, at lower detergent to protein ratio (80:1), the sharp upturn at low q data indicates the possible aggregation of rhodopsin in solution due to lack of detergent molecules required for forming corona around the protein molecules. This claim is validated by the R_g values calculated from Guinier analysis of rhodopsin-DDM complexes, where the sample of 80:1 has the largest value of R_g, almost double than the rest of the higher DDM to rhodopsin ratio samples (125:1, 150:1, 200:1 and 400:1). Next, we also fit the SAXS data

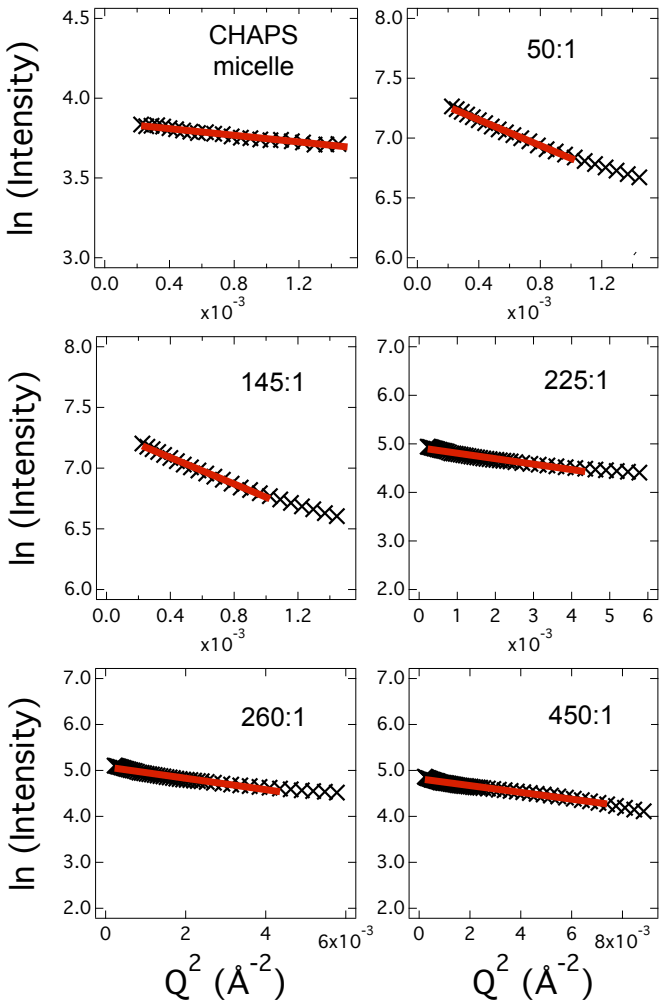

Figure 4.9: Guinier analysis of rhodopsin-CHAPS complex at various detergent to protein ratio. The solid red lines are the Guinier fits.

of rhodopsin-DDM complexes with shape model, core-shell ellipsoid (Eq. 4.6) to estimate to approximate shape and dimensions of PDC. This model fit is shown by the solid red curves in Fig. 4.5. The theoretically estimated values of SLDs for solvent (H_2O), DDM and rhodopsin are 9.43×10^{-6} Å^{-2}, 11.13×10^{-6} Å^{-2} and 10.00×10^{-6} Å^{-2} respectively. At first, the SLD value of solvent was fixed for fitting the data. On the other hand, the SLD values of DDM and rhodopsin were allowed to float since fixing their values could not get the best fit results. In all the cases, the calculated value of SLD of rhodopsin was very close to 10.1×10^{-6}

Table 4.1: Guinier analysis of CHAPS micelle, DDM micelle and PDCs from SAXS data.

Sample	R_g (Å)	R_gQ_{max}	Q_{max}/Q_{min}
CHAPS micelle	16.2±0.1	1.29	2.5
DDM micelle	32.7±0.3	1.28	2.5
CHAPS:rhodopsin			
50:1	40.2±0.4	1.28	2.1
145:1	40.4±0.4	1.29	2.1
225:1	18.4±0.3	1.21	2.1
260:1	19.3±0.3	1.27	4.4
450:1	15.0±0.5	1.29	5.7
DDM:rhodopsin			
80:1	83.9±1.4	1.3	2.7
125:1	40.2±0.3	2.18	1.7
150:1	49.8±0.5	1.28	2.1
200:1	46.6±0.4	1.30	1.9
400:1	49.2±0.5	1.28	1.7

$Å^{-2}$, which gave the minimum χ^2 goodness of fit. Therefore, we fixed the SLD of rhodopsin and solvent both and allowed other parameters to float. The model fit parameters as listed in Table 4.2 confirm that DDM molecules form a belt of corona around rhodopsin, which solubilize and stabilize rhodopsin in aqueous solution as shown in schematic diagram of Fig 4.7. Similarly, SAXS intensities from rhodopsin-CHAPS complex also shows the consitent results to that of rhodopsin-DDM complex. At low CHAPS to rhodopsin ratio (50:1 and 145:1), rhodopsin aggregates, which can be observed from the huge upturn at low q data and the Guinier analysis. But, at higher CHAPS to rhodopsin ratio (225:1, 260:1 and 450:1), detergent molecules form a shell around the protein, as indicated by the second maximum at

Table 4.2: Model fit parameters for detergent micelles and PDCs.

	R_a (Å)	R_b (Å)	Core SLD (Å^{-2})			
CHAPS	39.9±0.2	12.7±0.1	11.5×10^{-6}			
	R_a^c (Å)	R_b^c (Å)	R_a^s (Å)	R_b^s (Å)	Core SLD (Å^{-2})	Shell SLD (Å^{-2})
DDM	34.1±0.6	12.2±0.2	37.3±0.3	27.0±0.2	7.9×10^{-6}	12.5×10^{-6}
DDM	Rhodopsin	Complex				
80:1	315.2±0.5	12.0±0.1	280.0±0.5	31.5±0.1	10.1×10^{-6}	7.9×10^{-6}
125:1	49.1±0.1	11.0±0.1	48.0±0.1	30.0±0.1	10.1×10^{-6}	8.4×10^{-6}
150:1	67.0±0.1	12.0±0.1	61.0±0.1	29.2±0.1	10.1×10^{-6}	7.9×10^{-6}
200:1	52.6±7.5	17.1±3.0	52.6±5.3	27.0±1.7	10.1×10^{-6}	5.3×10^{-6}
400:1	57.5±0.4	18.4±0.3	57.0±0.4	26.0±0.2	10.1×10^{-6}	3.1×10^{-6}

q ~0.22 Å^{-1}. However, the small values of R_g (close to the R_g value of free CHAPS micelle) suggest that there is a significant number of free CHAPS micelles in solution. Due to very strenuous shape of rhodopsin-CHAPS complex, none of the available theoretical shape model could fit the data.

According to the SAXS study of PDCs, we confirmed that DDM and CHAPS solubilize rhodopsin in aqueous solution, where the rhodopsin confirmation is found to be stable above certain detergent to protein ratio. Such detergent concentration is well above CMC. The second maximum in SAXS intensity of PDC clearly suggests detergent micelles form a corona around rhodopsin with hydrophobic tails facing inward to the rhodopsin, whereas polar detergent head groups interact with the water. Such complex prevents rhodopsin from aggregation and thus preserves the native conformation rhodopsin for its activity mimicking

the membrane-like environment. Further, the rhodopsin sample preparation for the study of conformational change upon activation is made based on the results from the SAXS study of PDCs, which is presented in the following section.

Large conformational change in rhodopsin upon activation

Rhodopsin was solubilized and stabilized in solution using detergents CHAPS and DDM

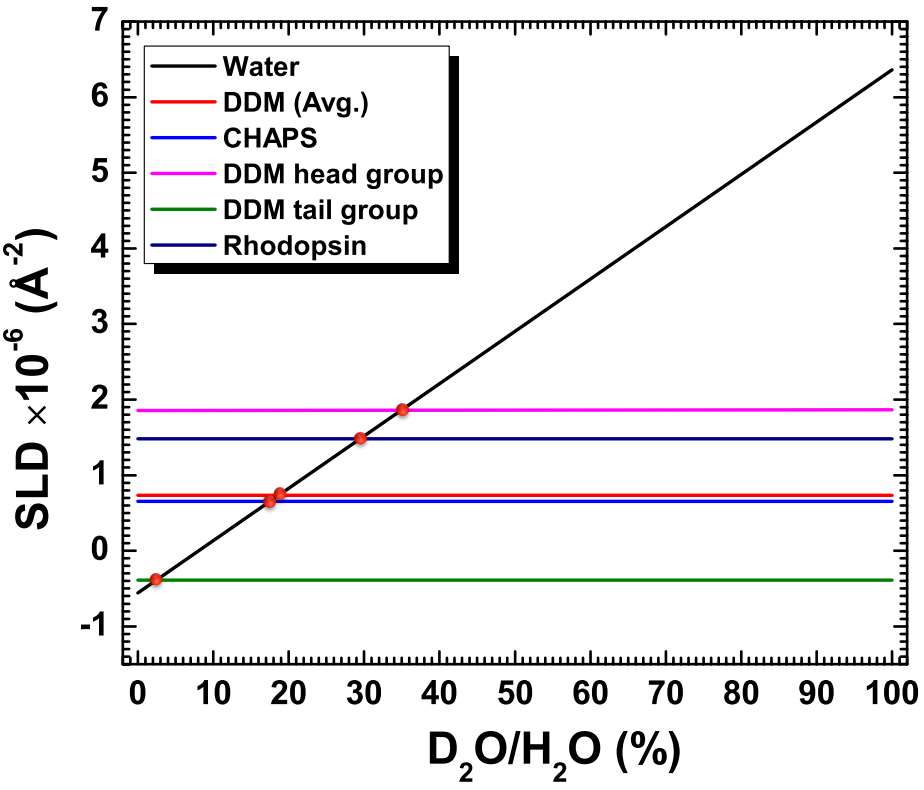

Figure 4.10: Theoretical values of scattering length densities (SLDs) of rhodopsin, DDM and CHAPS. The red dots represent the contrast match point for each of the cases with variation of D_2O/H_2O ratio in solution.

to study its activation after photo-bleached with light source. In order to study the rhodopsin activation, the detergent surrounding rhodopsin was contrast matched varying D_2O/H_2O ratio in solution. The theoretically calculated scattering length densities of rhodopsin, DDM and CHAPS in order to find the contrast matched points are shown in Fig. 4.10. Since

CHAPS head and tail groups scatter almost identically for neutron, SLD of CHAPS micelle was matched with that of solvent using 17% of D_2O in solution such that scattering signal only from rhodopsin was measured after subtracting the subsequent buffer [160]. On the other hand, it is not possible to eliminate the signal from both DDM head and tail groups at the same time varying D_2O/H_2O content in solution due to huge contrast between their SLD values for neutron [160, 168]. Thus, SLD of average DDM micelle was matched with that of solvent using 18% of D_2O [151], whereas 35% of D_2O in solution matched the SLD of DDM head group and rhodopsin both. Therefore, the former measured the signal from DDM head group plus rhodopsin since the DDM tail groups were only contrast matched, whereas the latter measurement only contained the scattering signal from DDM tail group after the subtraction of subsequent buffers. The schematic diagram of contrast variation SANS experiment on PDCs are shown in Fig. 4.11.

SANS data were measured at two states of rhodopsin; the dark state (DS) rhodopsin, where the protein is in its inactive state with its conformation locked by inverse agonist 11-*cis* retinal and the light activated state (LAS), where the rhodopsin conformation is expanded due to isomerization of 11-*cis* retinal to all-*trans* retinal that further activates the G protein transducin. Such expansion takes place due to outward tilting of the cytoplasmic end of helix 6 (H6) by 7.7 Å and the elongation of helix 5 (H5), known as Metarhodopsin II [127]. First, the SANS data were collected from the DS rhodopsin sample. After the measurement of DS of rhodopsin, the same rhodopsin sample was photo-bleached with green actinic light by turning on the switch remotely and the SANS data were collected from LAS. This approach was carried out on both rhodopsin-CHAPS and rhodopsin-DDM samples, where CHAPS micelle, DDM tail group and DDM head group plus rhodopsin were contrast

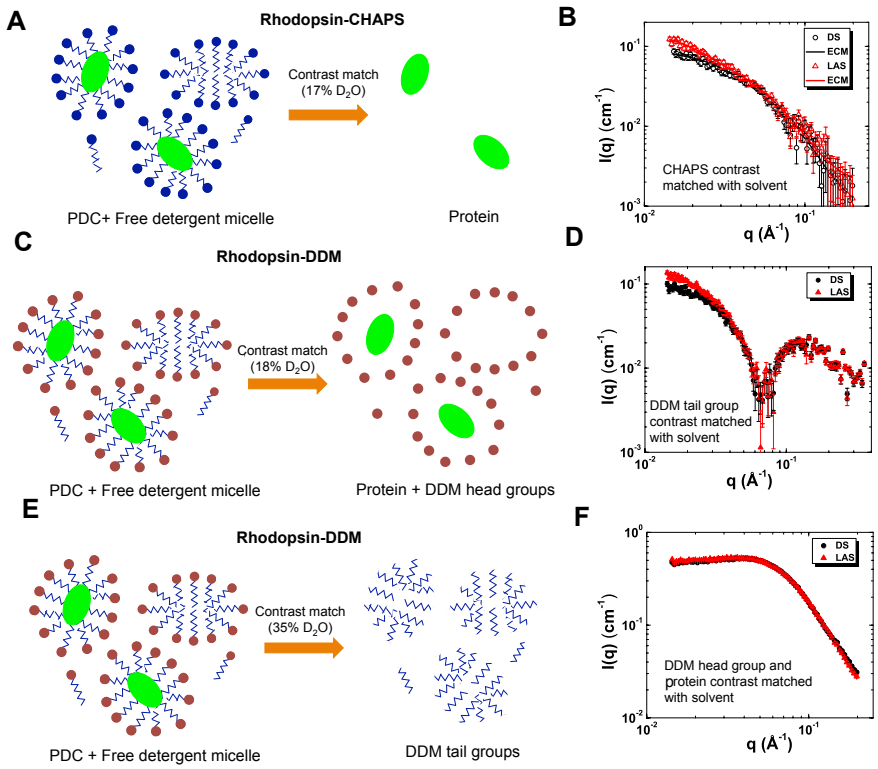

Figure 4.11: Schematic of contrast matched SANS experiment and the corresponding intensity profiles. The data are measured from rhodopsin in dark state (DS) and light-activated state (LAS), where the rhodopsin is stabilized using two detergents CHAPS and DDM. The data from protein-detergent complexes are measured using 17% and 18% D_2O such that scattering length density of detergent is matched with that of solvent. In this way, after the buffer subtraction, measured SANS intensity only contains the signals from protein (rhodopsin).

matched in each case. After the careful reduction of the raw SANS data taking into account of subsequent buffers, dark current, empty can, standard measurement (for absolute unit) and incoherent background, the corresponding SANS profiles from the samples in absolute unit (cm^{-1}) for DS and LAS rhodopsin are shown in Fig. 4.11 B, D and F. SANS data reflects no sign of aggregation of detergent-solubilized rhodopsin in solution. Fig. 4.11B corresponds to the SANS profiles from DS and LAS rhodopsin, where the CHAPS micelle was contrast matched. Clearly, a significant difference in SANS intensity profiles between

DS and LAS of rhodopsin at low q-values can be observed. In Fig. 4.11D, similar difference in the same q-range (as in case of rhodopsin-CHAPS sample) can be observed from rhodopsin-DDM with 18% D_2O sample, where the DDM head group was still present as indicated by the second maximum at q ~0.15 $Å^{-1}$, close to the second maximum of SAXS profile of DDM micelle. However, it is obvious to note that there is no difference between DS and LAS scattering profiles from rhodopsin-DDM with 35% D_2O sample since only the signal from DDM tail group were measured, not from the rhodopsin. These results strongly confirm the difference in rhodopsin conformation upon photoactivation.

The quantitative analysis of SANS intensity profiles was carried out using Guinier ap-

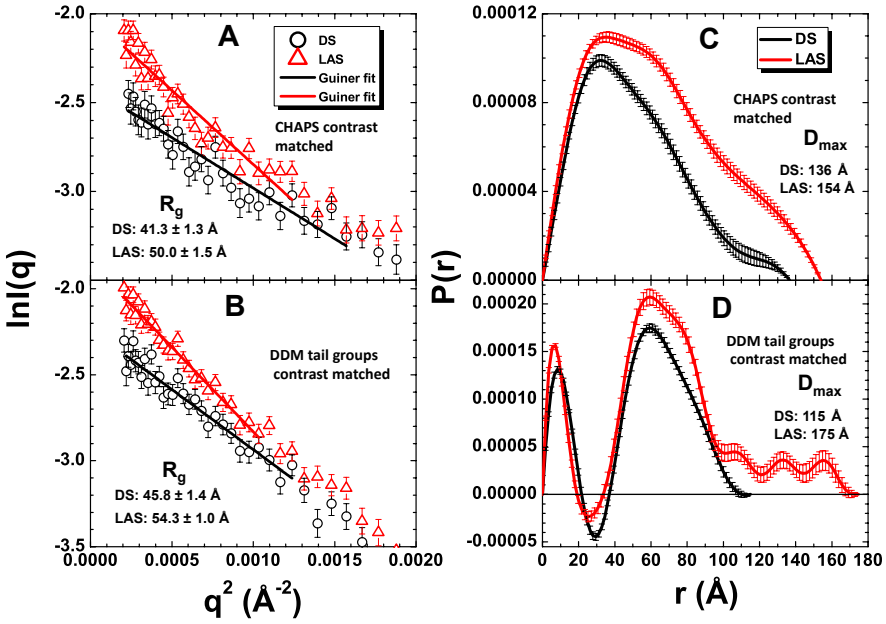

Figure 4.12: Guinier analysis and the pair distance distribution function of dark state (DS) vs. light-activated state (LAS) rhodopsin. The differences between DS vs. LAS of rhodopsin clearly indicates the large conformational change in rhodopsin, crucial for the actiavation of congnate G protein, transducin.

proximation at low q-values, which provides the information regarding average size of the

monodisperse particle in solution. The Guinier fit to the SANS data derived the radius of gyration (R_g) for DS and LAS of rhodopsin in each of the PDC samples, which are shown in Fig. 4.12 *A* and *B* (Guinier plots). R_g values of DS and LAS of rhodopsin in rhodopsin-CHAPS with 17% of D_2O sample were calculated as 41.3 ±1.3 Å and 50.0 ±1.5 Å, respectively. Similarly, R_g values of DS and LAS of rhodopsin in rhodopsin-DDM with 18% of D_2O sample were calculated as 45.8 ±1.4 Å and 54.3 ±1.0 Å, respectively. Clearly, the difference in R_g values between DS and LAS of rhodopsin is found to be ∼9 Å in both the samples, which is a huge change in rhodopsin conformation upon photoactivation. The slight higher R_g value of rhodopsin as calculated from rhodopsin-DDM sample compared to rhodopsin-CHAPS may be due to coupling of SANS data from rhodopsin and DDM head group, where the signal from DDM head group could not be eliminated. Furthermore, the pair distance distribution function, $P(r)$ of DS and LAS of rhodopsin in PDC at contrast match point were calculated as shown in Fig. 4.12 *C* and *D*. R_g values calculated from $P(r)$ fitting and Guinier analysis, agree well to each other as listed in Table 4.3. The calculated $P(r)$ curves are asymmetric indicating non-spherical shape of the monodisperse particle in solution similar to those previously reported for membrane proteins [172]. The calculated $P(r)$ of DS rhodopsin from rhodopsin-CHAPS with 17% of D_2O has a maximum peak nearly at 35 Å and the curve trails to a maximum particle dimension, D_{max} ∼135 Å. Upon photoactivation, very small additional peak is observed nearly at 60 Å with D_{max} ∼155 Å. On the other hand, $P(r)$ of rhodopsin-DDM with 18% of D_2O consists of two distinct peaks, where the first peak nearly at 10 Å (both in DS and LAS) indicates the DDM head group exactly similar to the one observed in DDM micelle and the second maximum peak, which represents the overall size of rhodopsin plus DDM head group, is nearly at 60 Å for DS rhodopsin with D_{max} ∼120 Å.

Similar to the case of rhodopsin-CHAPS contrast matched sample, a very small additional peak next to second maximum nearly at 75 Å with D_{max} ∼175 Å can be observed due to change in protein conformation upon photoactivation. Above analysis of SANS data clearly indicates that the rhodopsin conformation largely expands due to photoactivation, which is consistent with other crystallographic studies [123, 127]. Our results confirm the antagonist 11-*cis* retinal locks the rhodopsin conformation in inactive state and upon activation protein conformation expands in membrane-like detergent environment. These results clearly indicate that the detergent micelles mimic the native environment to rhodopsin preserving the folded conformation, which makes it possible to study the activation mechanism of GPCR rhodopsin in artificial and controlled conditions.

Having observed the conformational change in rhodopsin due to activation of light, it is essential to understand the oligomeric state of rhodopsin in detergent solution both in inactive and active states. Here we found R_g values of rhodopsin in DS and LAS to be 41.3 Å and 50.0 Å in rhodopsin-CHAPS solution respectively. However, the calculated values

Table 4.3: Radius of gyration of DS and LAS of rhodopsin in rhodopsin-CHAPS complex calculated from Guinier and P(r) analysis.

	R_g (Å)	
	Guinier analysis	P(r) analysis
Rhodopsin-CHAPS	(17% of D_2O)	
Dark state	41.3±1.3	40.3±1.0
Light-activated state	50.0±1.5	50.3±0.7
Rhodopsin-DDM	(18% of D_2O)	
Dark state	45.8±1.4	44.3±0.4
Light-activated state	54.3±1.0	55.5±1.6

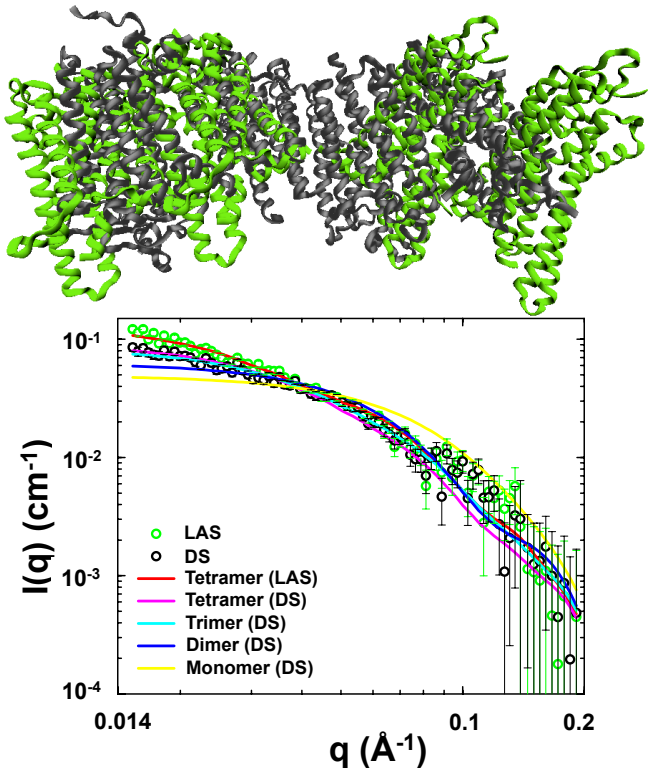

Figure 4.13: Theoretical SANS intensity profile calculation using known protein data bank (PDB) structures. (Top) PDB 1F88 - dark sate rhodopsin (black) and PDB 3PQR - light-activated rhodopsin (green). (Bottom) Theoretical SANS profile of dark state rhodopsin at different oligomeric forms: monomer (yellow curve), dimer (blue curve), trimer (cyan curve), and tetramer (magenta curve). The red curve is generated from the tetramer of light activated structure of rhodopsin. Rhodopsin tetramer structure in dark and light activated states best fit the experimental SANS profile.

of R_g of monomeric rhodopsin in DS (PDB 1F88) and LAS (PDB 3PQR) using CRYSON are 22 Å and 23 Å respectively, which is much smaller than the calculated values from our SANS measurements. These calculations clearly suggest the oligomerization of rhodopsin in detergent solution, which is consistent to the reported observation in native membrane [130, 139, 140, 142]. Further theoretical analysis of rhodopsin in dimer, trimer and tetramer forms using CRYSON suggest that the DS and LAS of rhodopsin is in good agreement with the tetrameric state (two densely packed dimers), which has R_g values of 42 Å and 51

Å respectively, consistent with the experimental R_g values calculated from SANS intensity profiles of DS and LAS rhodopsin in rhodopsin-CHAPS complex (17% D_2O). The tetramer of DS (1F88) and LAS (3PQR) of rhodopsin are shown in Fig. 4.13 top panel. The fitting of experimental SANS curves of rhodopsin-CHAPS (17% D_2O) with the theoretical SANS curves of monomer, dimer, trimer and tetramer generated through CRYSON are shown in Fig. 4.13 bottom panel and the R_g values are listed in the Table 4.4 with corresponding reduced-χ^2 values. We could not calculate the theoretical SANS profiles for rhodopsin in rhodopsin-DDM complex since the experimental SANS profile includes the scattering signal from rhodopsin plus DDM head groups, which is cumbersome to treat with for generating the theoretical SANS profiles.

The oligomerization of rhodopsin in native cell membrane and detergent solution is still

Table 4.4: Theoretical SANS intensity profiles of different oligomeric states of rhodopsin calculated using CRYSON package in ATSAS. PDB 1F88 and PDB 3PQR structures are used for dark state and light-activated state of rhodopsin, respectively.

	R_g (Å)	Reduced-χ^2
Monomer (DS)	21.8	3.1
Dimer (DS)	27.8	1.8
Trimer (DS)	38.9	0.9
Tetramer (DS)	42.1	1.1
Tetramer (LAS)	51.3	1.1

is a huge debated topic. However, several studies have confirmed that there is dimerization or higher order oligomerization of rhodopsin in native membrane and detergent environment [123, 139, 140, 142]. Previous work on the study of DS and LAS of rhodopsin in DDM at low detergent concentration reported the dimeric quaternary structure [142]. The dimerization

of rhodopsin in the native disc membrane was also observed in the recent time-resolved wide-angle X-ray scattering measurements [130]. On the other hand, rhodopsin formed tightly bound dimers (or tetramer) in n-tetradecyl-β-D-maltoside and n-hexadecyl-β-D-maltoside solutions [142]. Such results indicate that the rhodopsin prefers the oligomeric state in native membrane. Since we used the detergents above their CMC with 150:1 and 200:1 detergent to protein ratio for CHAPS-rhodopsin and DDM-rhodopsin complexes respectively, it is expected to form higher order rhodopsin oligomers bound by detergent micelles. Clearly, the quantitative analysis of data suggests the formation of rhodopsin oligomers, both in DS and LAS, which is in good agreement with previously reported results using other techniques [139, 140, 142].

4.2.4 Conclusion

In summary, we report the activation mechanism of GPCR rhodopsin in detergent solution, which mimics the membrane-like environment. The study of PDCs using SAXS confirmed that the detergents CHAPS and DDM with their concentrations well above CMC are good enough to solubilize and stabilized rhodopin in aqueous solution. Moreover, SANS data clearly showed the conformational change in rhodopsin upon photoactivation in PDCs. The quantitative analysis of SANS result provides more intuitive and realistic mechanism of rhodopsin activation in membrane-like environment. We observed the calculated values of R_g in inactive and active states differ by 9 Å, which is much larger than what has been reported from the earlier X-ray crystallography studies. These results clearly suggest the oligomerization (specifically two dimers densely packed to form a tetramer) of rhodopsin bound by the corona of detergent micelles, which is in good agreement to the previously reported results.

4.3 Ligand-induced protein dynamics of rhodopsin

4.3.1 Introduction

Protein dynamics [14, 18, 66] are the key to understanding the biological activities of pharmacologically important proteins such as G-protein-coupled receptors (GPCRs) [124, 129, 173, 174]. The conformational fluctuations of the protein upon extracellular stimulation lead to the activation of GPCRs in a cellular membrane lipid environment. X-ray crystallographic experiments [135] and recent time-resolved wide-angle X-ray scattering (WAXS) studies [130] conducted on the prototypical visual GPCR rhodopsin have revealed valuable information about the conformational changes that occur during activation. However, thus far little information is available regarding how the internal dynamics evolve during GPCR function [175, 176]. In this work, we used quasi-elastic neutron scattering (QENS) technique to study the changes in a GPCR mobility upon activation, using rhodopsin as a prototype.

Rhodopsin is a class A GPCR responsible for vision under dim-light conditions in vertebrates. It is the canonical prototype of the Rhodopsin family of GPCRs [129]. The chromophore 11-*cis* retinal locks the rhodopsin in the inactive dark state [177], and acts as an inverse-agonist by preventing the interaction with its cognate G-protein (transducin). Upon photon absorption, the 11-*cis* retinal isomerizes to all-*trans*, yielding rearrangement of the protein conformation due to two protonation switches [178]. The photoisomerization of retinal occurs within 200 fs, causing rhodopsin to undergo a series of multi-scale transitions [123, 179]. Currently, X-ray crystal structures are available for rhodopsin in the dark state [133, 136], as well as several freeze-trapped photointermediates [135, 137], including the ligand-free apoprotein opsin. In addition to solid-state NMR methods [175, 175, 179],

site-directed spin labeling (SDSL) has been extensively applied to study rhodopsin [132]. Here, we compared the protein dynamics of the dark-state rhodopsin to those of ligand-free opsin, which is structurally similar to active metarhodopsin-II. Both elastic and quasi-elastic neutron scattering [63] were utilized, with the aim of studying the functional protein dynamics that lead to transducin activation [179].

Intrinsic fluctuations of protein structures are due to a large number of conformational substates represented by a hierarchical (rough) energy landscape (EL) [18, 21], as discussed for globular proteins by Frauenfelder et al. [66]. The protein dynamics encompass a broad range of time scales, ranging from local motions (ps-ns) to collective domain motions (ns-μs) [14, 18, 180]. In analogy with glass-forming liquids, the short time dynamics (β-relaxations) include small amplitude local motions (e.g. side chains and methyl group rotations) whereas the long-time dynamics (α-relaxations) are due to collective protein motions of larger amplitude. To date, mainly globular proteins such as myoglobin [66] and lysozyme [74] have been studied with this approach. Experimentally, we prove that the EL concept concept is also valid for membrane proteins such as GPCRs and apply this concept in explaining the ligand-binding mechanisms of GPCR rhodopsin upon photoactivation. Notably, QENS can be used to study the relaxation dynamics of hydrogen atoms due to vibrations, relaxations, and rotations within the protein molecule [181, 182]. Advances in the QENS technique were exploited to probe the effect of the retinal cofactor on the dynamics of rhodopsin in the β-relaxation time range (ps-ns) crucial for its activation. Light-induced isomerization of the 11-*cis* retinal cofactor and the subsequent release of the chromophore unlock the intrinsic protein dynamics in the ligand-free opsin state, followed by interaction with the heterotrimeric G-protein (transducin). Our QENS experiments probed the hydrogen atom

dynamics in the β-relaxation range for the dark-state rhodopsin and ligand-free opsin. We discovered that the local relaxation dynamics in the opsin apoprotein are slower compared to the dark-state rhodopsin, which corresponds to the open conformation of opsin and thus more degree of freedom for the protein movement due to the removal of retinal cofactor [183].

4.3.2 Materials and methods

Sample preparation

Rhodopsin was extracted and purified from bovine rhodopsin disk membranes (RDMs) using a detergent 3-[(3 Cholamidopropyl) dimethylammonio]-1 propanesulfonate) (CHAPS), which is crucial for membrane protein sample preparation [162, 184]. A powdered membrane protein sample containing 73 % (w/w) of photochemically functional bovine rhodopsin and 27 % (w/w) of CHAPS was used for the neutron scattering experiment. A total of about 600 mg of the powdered rhodopsin was used to prepare a dark-state sample, and the photo-bleached ligand-free apoprotein opsin sample. Each of the samples was hydrated with D_2O (h $\sim$0.27), and enclosed in aluminum foil to prevent exposure to light. Finally, each of the samples was inserted in rectangular aluminum sample holder for the neutron scattering experiment.

QENS measurements

The neutron scattering experiments were performed with the near-backscattering spectrometer (BASIS) at the Spallation Neutron Source (SNS) at Oak Ridge National Laboratory (ORNL) [63]. The BASIS measurements had an energy resolution of 3.4 μeV (HWHM for Q-averaged resolution value). The data analysis were conducted in the dynamic range of $\pm$100 μeV in energy domain. The analysis in the time domain used the data collected from -120 to +520 μeV. EINS data were obtained by monitoring the elastic intensity determined

by the integration over a 3.4 μeV interval (HWHM of the elastic peak). The QENS data were collected over the temperature range 220 K - 300 K, and at 10 K to characterize the sample-specific energy resolution of the spectrometer.

4.3.3 Data analysis

The data analysis is similar to the one explained in section 3.3.

4.3.4 Results and discussion

Mean-square displacements of hydrogen atoms of rhodopsin vs. opsin

First, we employed elastic incoherent neutron scattering (EINS) [30, 39] to determine whether the dissociation of the retinal ligand from rhodopsin affects the protein flexibility. The mean-square displacement (MSD), denoted by $< x^2(T) >$, is traditionally used as the index of "softness" or flexibility of globular proteins [42]. The calculated MSDs are plotted as a function of temperature in Fig. 4.14, for both dark-state rhodopsin and the ligand-free apoprotein, opsin. According to the plot, for rhodopsin versus opsin there is no major difference in hydrogen-atom MSDs of the samples within the measured temperature range. Notably, there is a sudden increase in the slope of the MSDs above the so-called dynamic transition temperature [116], $T_D \approx 220$ K, indicating an onset of rapid thermal fluctuations of the substates in both rhodopsin and opsin. This dynamical transition in hydrated proteins reveals the change in motion of the protein groups from harmonic to anharmonic behavior. Above T_D sufficient energy is acquired to move anhrmonically among the various substate potential wells. At this point, we can conclude that above $T_D \approx 220$ K the membrane protein rhodopsin attains the conformational flexibility required to perform its biological function, which is cofactor-independent. In the following sections, we describe how the cofactor-dependent hydrogen dynamics are studied using the QENS technique.

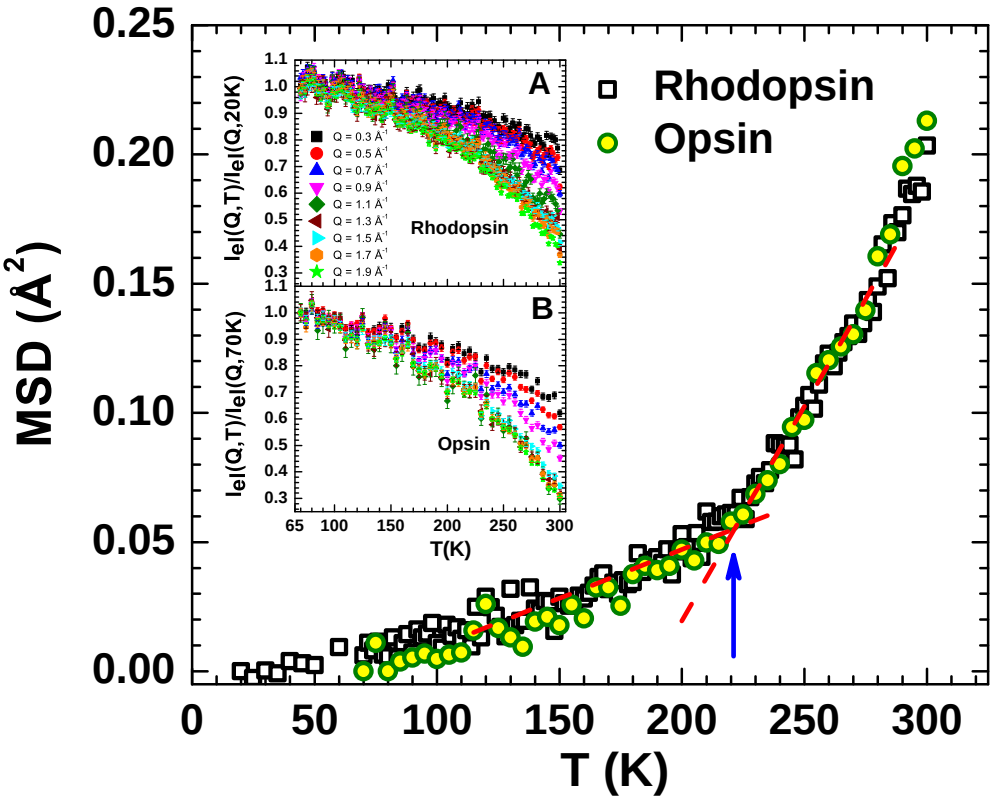

Figure 4.14: Atomic mean-square displacements (MSDs) of hydrogen atom as a function of temperature in the dark-state rhodopsin (open black squares) and the ligand free apoprotein opsin (open green circles) are nearly identical and both show a dynamical transition T_D $\sim$ 220 K. The inset shows the elastic incoherent neutron scattering (EINS) intensities for dark-state rhodopsin and opsin respectively.

Diffusion motions in rhodopsin due to removal of retinal cofactor

Next, we conducted QENS measurements on D_2O-hydrated (h $\sim$0.27) dark-state rhodopsin and ligand-free apoprotein opsin, at temperatures ranging from T = 220 K to 300 K, with Q ranging from 0.3 - 1.9 Å^{-1}. The meausred QENS spectra for both rhodopsin and opsin are illustrated in Fig. 4.15 A and B, respectively, at nine different temperatures and momentum transfer Q = 1.1 Å^{-1}. The measured QENS intensity, i.e. the self-dynamic incoherent scattering factor $S_m(Q,\omega)$, shows increase in quasi-elastic broadening with temperature, in-

dicating faster ps-ns diffusive motions in the hydrogen atoms within protein molecules. In QENS, the elastic component (central peak) originates from the immobile atoms within the experimental energy (or time) window, and the quasi-elastic components (broadenings from the elastic central peak, or the resolution functions) are due to the spatial motion of the mobile atoms.

Using a classical approach of data analysis in energy domain, we are able to decouple

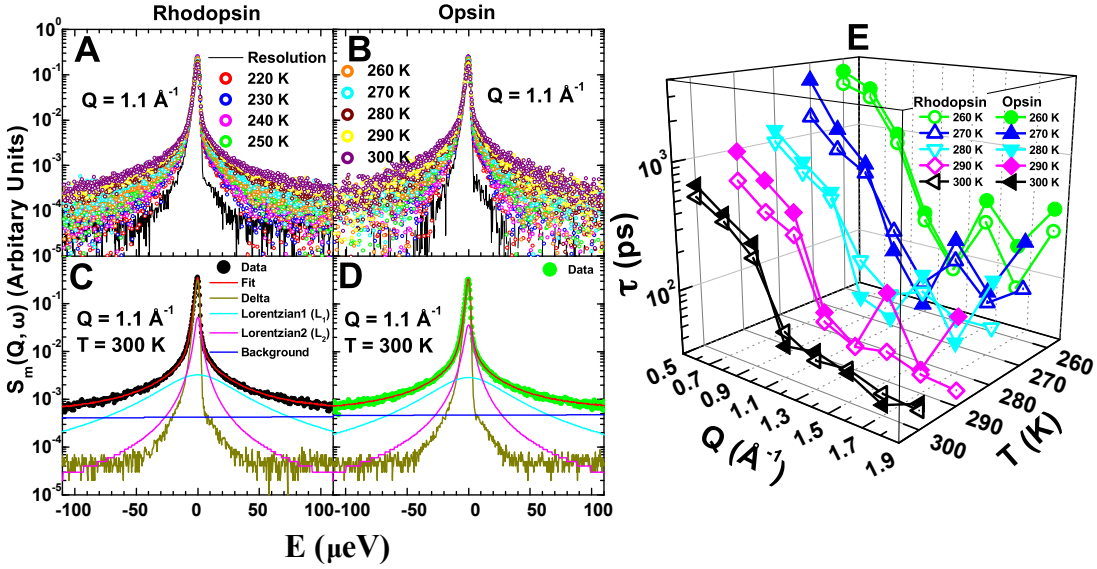

Figure 4.15: Ligand-free opsin apoprotein shows slower hydrogen-atom dynamics compared to the dark-state rhodopsin. Left Panels: QENS spectra for dark-state rhodopsin and ligand-free opsin samples. (A) and (B) Normalized dynamic incoherent scattering function, $S_m(Q,\omega)$ from two samples respectively, at $Q = 1.1$ Å^{-1} from 220 K to 300 K along with resolution. (C) and (D) Analysis of the QENS spectra at $Q = 1.1$ Å^{-1} and $T = 300$ K, showing elastic scattering component (delta function shown as dark yellow line), quasi-elastic scattering components (two Lorentzians indicated by cyan line and magenta line), background (blue line), and the fitted curves (red line). (E) Comparison of the relaxation time (τ) of dark-state rhodopsin and ligand-free opsin as a function of Q for $T = 260$ K to 300 K in 10 K steps.

the motions of the detergent (CHAPS) and protein (33). Fig. 4.15 *C* and *D* demonstrate

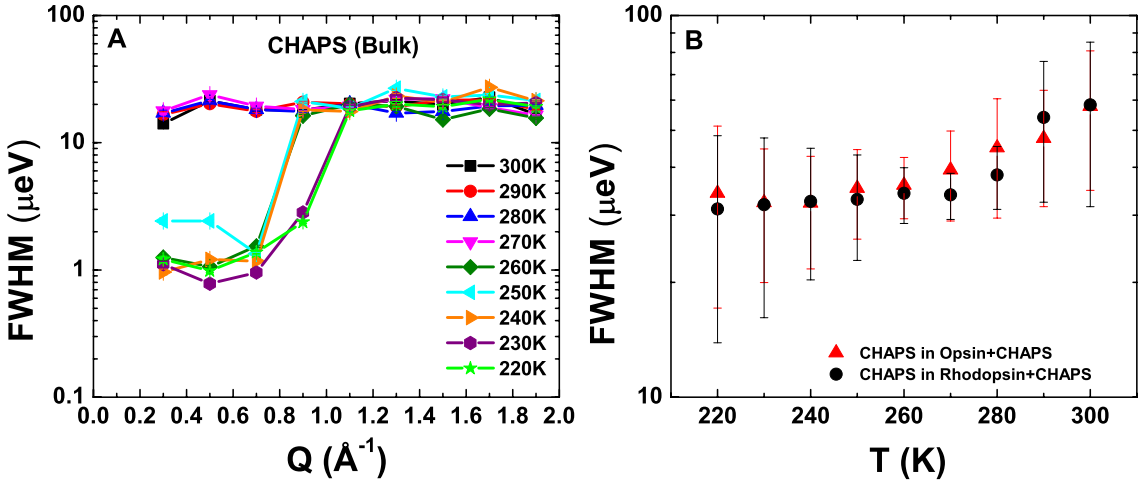

Figure 4.16: Full-width at half-maximum (FWHM) of Lorentzian ($2\Gamma_1$) of CHAPS component in different samples. (A) Dynamics of CHAPS in bulk CHAPS sample as functions of Q at different temperatures ranging from 220 K to 300 K. (B) FWHM of CHAPS compoment in protein-CHAPS complex samples averaged over all Q-values, corresponding to decoupled CHAPS dynamics in these samples at different temperatures. Note that rhodopsin and opsin correspond to the dark-state and the ligand-free apoprotein obtained after light exposure, respectively.

the analysis of the measured $S_m(Q,\omega)$ as a superposition of a Dirac delta function, two Lorentzians (L_1 and L_2), and a linear background convoluted with resolution, within the energy transfer range $\pm$ 110 μeV for rhodopsin and opsin, respectively. The full width at half maximum (FWHM, 2Γ) of the Lorentzians provides information about the motions of hydrogen atoms within the samples. According to the analysis as shown in Fig. 4.15 C and D, the FWHM of L_1 ($2\Gamma_1$) is much broader than the FWHM of L_2 ($2\Gamma_2$)and is Q-independent (details are shown in Fig. 4.16 and Fig. 4.17), with the values very close to the FWHM values extracted from the analysis of the QENS data of the pure CHAPS sample. By contrast, the FWHM of L_2 ($2\Gamma_2$) is much narrower and Q-dependent comparing to that of L_1 ($2\Gamma_1$). Thus, we can confidently attribute the faster CHAPS dynamics to L_1 and the slower protein dynamics to the L_2 component. Using this classical method of decoupling the

motions, we can then readily separate the dynamics of rhodopsin and the detergent CHAPS, which has been successfully applied in the analysis of previous QENS data [181, 185].

The energy domain analysis is summarized in Fig. 4.15E, where we plot the relaxation

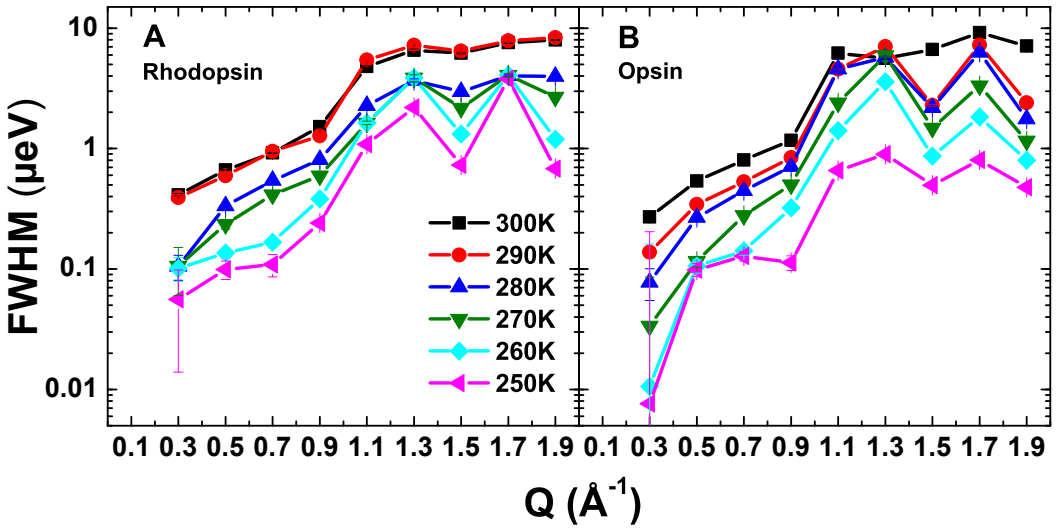

Figure 4.17: Full width at half maximum (FWHM) of Lorentzian ($2\Gamma_2$) of (A) dark-state rhodopsin and (B) opsin as functions of Q at all measured temperatures

time τ for diffusive motion of the hydrogen atoms of rhodopsin and opsin versus Q at temperatures between $T = 260$ K and 300 K. The relaxation time τ was calculated using the relation, $\tau = \hbar/2\Gamma_2$, corresponding to the diffusive motion. Our results show that the diffusive motion of the hydrogen-atoms is slower in opsin (reflected in larger τ values) compared to that of rhodopsin at all measured Qs and temperatures. In the Q range from 0.5 Å^{-1} to 0.9 Å^{-1}, the relaxation time of both states decreases with Q, due to diffusive motion of H-atoms. However, in the Q range from 1.1 Å^{-1} to 1.9 Å^{-1}, the relaxation time reaches its minimum value and is barely Q-dependent, indicating that the motion in the protein is localized in the length scale ∼6 Å. The analysis in energy domain gives us the initial

indication that the diffusive motion of the hydrogen atoms is slower in opsin compared to rhodopsin, prompting us to extend the analysis in the time domain, as we describe below.

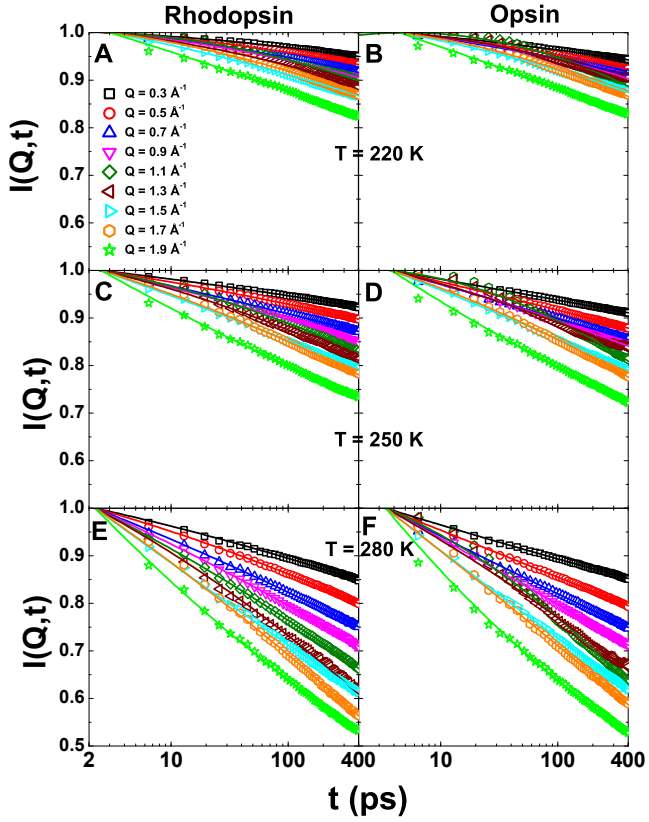

Figure 4.18: Mode-coupling theory (MCT) analysis of QENS data in the time domain. Comparison of intermediate scattering function (ISF) denoted by $I(Q,t)$ for dark-state rhodopsin and opsin at temperatures $T = 260$ K, 280 K, and 300 K for Q-values from 0.3 Å^{-1} to 1.9 Å^{-1} with a step of 0.2 Å^{-1}. The solid lines in the panels are the fitted values to ISF with MCT in β-relaxation region of protein dynamics at the corresponding Q-values and temperatures.

Application of mode-coupling theory to fathom the β-relaxation dynamics

To further investigate the differences in hydrogen-atom motion in dark-state rhodopsin and the ligand-free apoprotein opsin, we evaluated the relaxation dynamics in the real-time domain. The inverse Fourier transform of the measured QENS data in energy domain yields the intermediate scattering function (ISF) as described in 3.3. The contribution of the detergent intensity was subtracted before the Fourier transformation according to our energy

domain analysis [186]. The ISF $I(Q,t)$ of H-atoms in rhodopsin and opsin is plotted at temperatures T = 220, 250 K, 280 K and 300 K in Fig. 4.18 and 4.19 A and B at a series of Q-values.

From theoretical prediction, protein dynamics at different timescales can be approxi-

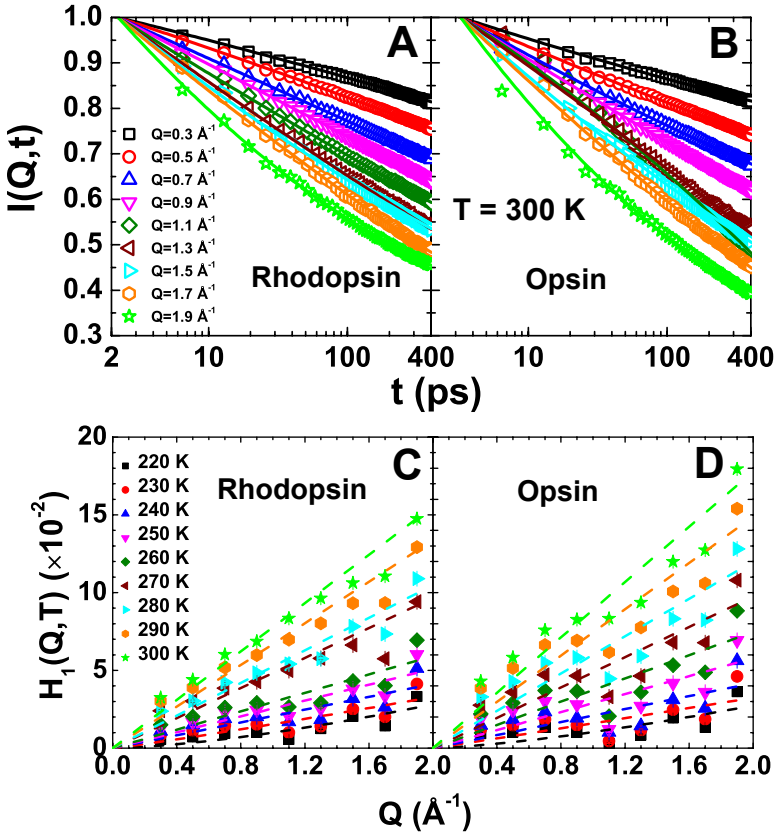

Figure 4.19: Mode-coupling theory (MCT) analysis of QENS data in the time domain. (A) and (B) Intermediate scattering function $I(Q,t)$ of dark-state rhodopsin and opsin at T = 300 K at Q-values from 0.3 Å^{-1} to 1.9 Å^{-1} with 0.2 Å^{-1} step. Solid lines are MCT fits to ISF in β-relaxation region of protein dynamics at various Q-values. (C) and (D) The first order decay parameter $H_1(Q,T)$ as a function of Q for dark-state rhodopsin and opsin respectively.

mately divided into three groups (20, 35): (i) a short-lived Gaussian-like ballistic region due to vibrations; (ii) Fast dynamics in the β-relaxation region (ps-ns) governed by a logarithmic decay; followed by (iii) slow dynamics in the α-relaxation region (μs-ms) governed by a

stretched-exponential decay. The correlation between dynamics and biological activity has been demonstrated on the μs-ms timescale, but fluctuations at the atomic level are much faster than this [21, 69, 70]. Our experimental results correspond to the β-relaxation region within the time window of ps to ns. Upon increasing temperature, the protein local dynamics become faster in both rhodopsin and opsin. Furthermore, there is a striking Q-dependence, showing the relaxation process varies within the different length scales in the sample (from Å upto nm). Notably, rhodopsin and opsin (both membrane proteins) demonstrate the characteristic of broadly distributed decay of ISF in the β-relaxation regime, previously observed only in aqueous soluble globular proteins [28, 74, 82].

Having observed the broadly distributed decay in the ISFs of both rhodopsin and opsin, we applied mode-coupling theory (MCT) to fathom the differences in β-relaxation (10-400 ps) dynamics for opsin versus rhodopsin. The MCT was originally developed to describe the complex dynamics in glass-forming liquids (40-42), but has been successfully used in predicting the decay rates in β-relaxation dynamics of globular proteins and other biopolymers [28, 29, 74, 82]. The ISFs with broadly distributed decay behavior can be fitted with an asymptotic expression derived from the MCT as given by Eq. 3.6.

In Fig. 4.20A, the opsin and the dark-state rhodopsin crystallographic structures [133] are compared. One could expect slower dynamics in opsin, because it is the more open conformation due to absence of retinal. The characteristic β-relaxation time τ_β values from fitting the ISF (Eq. 3.6) are summarized in Fig. 4.20B. Notably, we observed longer β-relaxation times τ_β for temperatures ranging from 220 K to 300 K, which suggests the ligand-free opsin structure is less flexible versus the dark-state rhodopsin. In the temperature range of 220 - 300 K, the τ_β values of both rhodopsin and opsin follow an Arrhenius

behavior: $\tau_\beta = \tau_0 e^{E_a/RT}$, where R is the gas constant and E_a is the average activation energy.

Protein flexibility in visual signaling

Protein flexibility and ligand binding is coupled to each other, and are usually described by different biophysical models [187]. In Fig. 4.20B, we plot a schematic free energy landscape (EL) model representing the rhodopsin activation process. The black curve models the free energy of ligand-binding rhodopsin. The red curve represents the free energy of ligand-free opsin. The free energy differences between different states contains many contributions, including the direct protein-ligand interactions, hydrophobic association and the conformational and vibrational entropy of the rhodopsin and all-*trans* retinal. The hierarchical ELs are reflected by the small fluctuations in the curves. This schematic picture explains the mechanisms of rhodopsin conformational change during the photo-activation.

One of the features of complex systems [22, 113] is highly non-exponential relaxation,

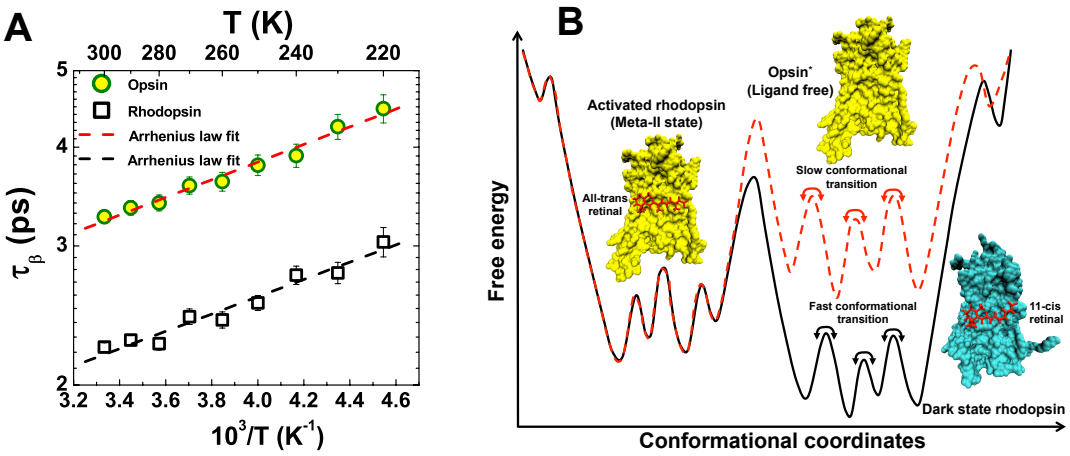

Figure 4.20: A schematic free energy model for the rhodopsin activation process. (A) Arrhenius plot of characteristic β-relaxation time (τ_β) as a function of inverse temperature for dark-state rhodopsin and opsin. (B) Schematic free energy model representing the rhodopsin activation process.

which describes the energy landscape (EL) due to the many conformational substates with similar energies. The different basins of the EL give us a framework for understanding the conformational changes during a reaction, such as GPCR activation of the cognate G-protein. Because the fluctuations are thermally driven, temperature plays a major role [116]. At sufficiently low temperature, the individual protein molecules are trapped in various potential wells, where they undergo harmonic vibrations due to the conformational substates [181]. On the other hand, the higher energy barrier in opsin results in longer relaxation time in the ligand free opsin which is shown in Fig. 4.20B.

According to our experimental results, the dark-state rhodopsin structure is more flexible [130]. Following dissociation of all-*trans* retinal from the Schiff-base linkage, opsin is structurally similar to the active metarhodopsin-II [188]. Using QENS, we found that in the presence of 11-*cis* retinal, the protein has shorter relaxation time which prevents it to sample more conformational substates. Thus, the 11-*cis* retinal confines protein in an energetically less favorable conformation (frustration). Upon photoactivation, the 11-*cis* retinal isomerizes to all-*trans*, yielding greater flexibility of the protein than in ground-state rhodopsin. The increase in protein flexibility is crucial to subsequent binding and catalytic activation of the cognate G-protein (transducin), and is due to lack of stabilizing interactions between the retinal chromophore and the secondary structures involving the receptor binding pocket. The stabilizing forces in opsin are weaker compared to the dark-state rhodopsin, giving an increase in flexibility, consistent with an ensemble-activation mechanism of the visual GPCR rhodopsin [175, 176].

The influences of both temperature and hydration [34, 181, 189, 190] then allow one to further address the EL in terms of a hierarchical organization [66]. As the all-*trans* retinal

binds to the rhodopsin, the water molecules in the solvent shell surrounding the hydrophobic moieties of the ligand and binding site will be released to the bulk solvent and gain entropy, thereby the free energy of the dark-state rhodopsin is lower than opsin [187]. In addition, when binding to small but solvent-accessible hydrophobic cavities of rhodopsin, the disordered water molecules have a density much lower than the bulk water density, which therefore will increase the solvent free energy. Increased hydration upon light activation is fully consistent with recent MD simulations [191].

4.3.5 Conclusion

In summary, the QENS data from the dark-state rhodopsin and the ligand-free apoprotein, opsin, were analyzed in the energy domain by a classical approach to decouple the detergent and protein dynamics, and in the time domain by MCT, as originally formulated to describe the complex dynamics in glass-forming liquids [113]. With this combined approach, we show a larger and detailed picture about the ligand-induced protein dynamics. Significantly, MCT analysis of a membrane protein, rhodopsin, demonstrates the broadly-distributed rates similar to the one previously observed for globular proteins [74]. The light causes isomerization of 11-*cis* retinal, which unlocks the intrinsic dynamics of the dark-state rhodopsin that are pivotal for the activation mechanism. Both energy and time domain analysis of the QENS data show that the dynamics of the ligand-free apoprotein, opsin (yielded after the photoactivation) are significantly slower compared to the dark-state rhodopsin, which is locked by 11-*cis* retinal suggesting the open conformation and thus more degree of freedom for protein movement in opsin crucial for the activation of cognate G-protein (transducin) [177]. These results confirm the retinal cofactor influences the dynamics in the activation mechanism of a canonical prototype for the Rhodopsin (Family A) GPCRs.

Such change in protein dynamics due to the removal of retinal in opsin is necessary for the interaction between the rhodopsin GPCR and its cognate G-protein, yielding the catalytic activation of transducin. Our results are consistent with the regulation of protein structural dynamics by the retinal cofactor of rhodopsin. Furthermore, a schematic free-energy landscape picture explains our findings, which support the protein dynamics changes in the absence of the retinal cofactor due to the open conformation upon removal of the retinal. These findings pave the road to study the crucial dynamic behavior of other biologically important membrane proteins in the GPCR superfamily. An important question remaining for future research is whether active metarhodopsin-II yields results consistent with greater flexibility of the protein structure as compared to the apoprotein opsin due to the presence of all-*trans* retinal.

CHAPTER 5 COLLECTIVE MOTIONS IN PROTEINS

5.1 Role of phonons for enzyme-mediated catalysis in protein

5.1.1 Introduction

Proteins are the complex macromolecules that play a vital role in biological activities [10, 14, 18]. It has been well understood that they are the dynamic systems [192–194] showing the wide variety of internal motions from femtoseconds to milliseconds [18, 194] analogue to the supercooled liquids and glasses [21]. Several studies have shown that the slow binding and conformational changes in protein occurring in the time scale of few microseconds to milliseconds mainly contribute to the enzyme catalytic reactions [195]. However, in the past few years, there has been a substantial initiation to understand the role of fast motions in enzyme catalysis [11]. Specifically, the low-frequency intraprotein collective motions in biomolecules are of considerable interest since they are strongly coupled between the adjacent residues that are subjective to the protein conformations [196, 197]. They are similar to the boson peak in the glass-forming liquids due to collective excitations or density fluctuations as observed in inelastic neutron scattering (INS) experiments [198–201]. Although the proteins lack the long-range structural order compared to the solid crystals, the secondary structures, α-helices and β-sheets exhibit a significant fraction of higher-order structure that is stabilized by the weak bonds like hydrogen bond, van der Waals interaction, and salt brigdes [202]. These structures in protein give rise to the low-frequency phonons that largely influence the stability and the flexibility of protein [196, 197, 203]. Furthermore, these harmonic fluctuations are the precursor for the enzyme catalysis in biomolecules [11, 204–206]. The low-frequency motions, which involve the weak force constants are more substantial than

the high-frequency motions due to the strong forces between the neighbouring molecules in proteins [203, 207]. However, these low-frequency motions are highly damped and short-lived (of the order of tens of femtoseconds) due to the large disordered and the crowded structures in protein [200, 208].

The idea of protein multi-dimensional free energy landscape (EL) has been very successful in explaining the role and importance of protein dynamics in biological activities [21, 68]. According to this theory, a large protein structure samples different conformations around the average structure forming the multi-dimensional free EL through available thermal energy, of the order of k_BT per atom, where k_B is the Boltzmann constant and T is the absolute temperature. Such instantaneous conformations are called conformational substates (CSs) [19]. These CSs fluctuate rapidly in the femtoseconds to picoseconds time scale resembling the vibration of residues, side-chain rotations, or backbone movements. The energy barrier or activation energy (E_a) of such CSs is much smaller than k_BT. These rapid fluctuations in proteins, which make or break the covalent bonds, form hydrogen bonds and transfer hydride ions within the different functional groups are the foundation for the enhancement of decoupled slower domain motion responsible for enzyme catalysis [11]. One of the convincing aspects of the role of rapid structural fluctuations to enzyme catalysis is elucidated in the perspective article by S. D. Schwartz and V. L. Schramm [206]. They have revealed the enzymatic dynamic motion responsible for overcoming the chemical barrier to give the products. The experimental evidences are the hydride and proton transfer of lactate dehydrogenase and the complex reaction of purine nucleoside phosphorylase due to the significant bond loss, intermediate stabilization, group migration and bond formation in a single reaction coordinate [206]. A similar approach can be found in another perspective article by

S. Hay and N. S. Scrutton, where they revealed the notion of coupling between the fast motions and catalytic effect in the intrinsic chemical step [11]. The idea of such process is taken from the studies of quantum mechanical tunneling of hydrogen atom along with the classical approach of crossing the energy barrier in protein EL [11]. Further studies in this area can be found elsewhere [13, 195, 204, 205]. Therefore, the fast motions (femtoseconds - picoseconds) in proteins play a significant role in enzyme catalysis.

Lattice vibrations in solids and collective density fluctuations in amorphous materials, glasses or liquids have been well studied with INS and inelastic x-ray scattering (IXS) techniques [209, 210]. These are the highly resolving techniques for the precise investigation of highly damped collective modes and phonon dispersion in topologically disordered systems [208, 209]. IXS spectrometer has a rather broad and slowly decaying resolution function that is inept to resolve the low-frequency excitations, but very specific in measuring the high-frequency collective vibrational modes [200, 211]. On the other hand, INS experiment is considered as a suitable probe for investigating the low-frequency collective excitations because of the sub-millielectron volt (meV), narrow Gaussian-like resolution function [211]. Thus, here we use the coherent INS technique to study the low-frequency collective motions in perdeuterated green fluorescent protein (GFP). Since more than half of the atoms in biomolecules are hydrogen that has the largest incoherent cross-section for neutrons [50], INS from perdeuterated protein sample predominantly measures the collective (coherent) motions in the biomolecules. This is because the deuteration of protein incredibly minimizes the incoherent signals from the sample [212].

GFP is one of the proteins with different secondary structure compared to that of globular protein [32]. It consists of 238 amino acids with molecular mass of 27 kDa. The monomer

has 11 β-strands that form the β-barrel having the diameter and length of $\sim$30 Å and $\sim$40 Å respectively [213]. The central α-helix is located inside the β-barrel along with the fluorescent center of the molecule and the short helices form caps on each end of the cylinder, representing a new kind of protein fold, called β-can [213, 214]. It has very remarkable regular structure so that even the water molecules on the outside of the barrel form "stripes" around the surface of the cylinder [213]. Moreover, the regularity of the protein itself helps in stability and the resistance to the unfolding of protein [213]. The study of low-frequency intraprotein collective motions of structurally different GFP can be helpful in understanding the correlation among the protein conformations, motions, and enzymatic activities above and below the protein dynamic transition temperature, $T_D \sim$ 220 K - 230 K [32].

The previous study on the fully deuterated GFP by coherent INS experiment concluded that the low-frequency vibrations are mainly contributed by the random or out-of-phase motions of β-strands [200]. It also suggested that the acoustic-like vibrations contribute only to the small fraction of coherent motion, which further decrease upon hydration[200]. Beside those remarks, our results are quite intriguing since we have observed for the first time to our knowledge, the low-frequency acoustic phonon propagation [215–218] in GFP. The existence of such acoustic phonons in proteins is the evidence of thermal energy carrier for crossing the conformational barrier necessary for enzyme catalysis despite inadequate available thermal energy. Furthermore, the apparent temperature and hydration dependence of the localized phonon modes due to the intraprotein collective vibrations in GFP are observed, where the latter one is due to the change in the local structure instigated by the presence of water molecules inside the β-barrels. Therefore, the localized phonons give an evidence of softening of protein with an increase in temperature, essential for biological activities.

5.1.2 Materials and methods

Sample preparation

The fully deuterated samples of green fluorescence protein (GFP) were prepared in bio-deuteration laboratory at Oak Ridge National Laboratory. GFP was extracted and purified according to the method described in the article [219]. The purified protein sample was exchanged in D_2O and lyophilized such that all the exchangable hydrogens were replaced by deuterium. The completely lyophilized and fully deuterated GFP was used as a dry GFP sample. The hydrated sample was prepared by exopsing lyophilized GFP powder to D_2O vapor inside a glove-box in the presence of nitrogen. The final hydration level was made to 0.37 (i.e., 0.37 gram of D_2O per gram of protein). The dry and D_2O hydrated deuterated-GFP samples predominantly gives the coherent signal in the inelastic neutron scattering measurements.

Inelastic neutron scattering experiment

The dynamic coherent structure factor, $S(Q, E = \hbar\omega)$ from dry and hydrated GFP protein samples were measured by inelastic neutron scattering (INS) spectrometer. The INS measurements were performed on a fine-resolution fermi chopper spectrometer, SEQUOIA at the Spallation Neutron Source (SNS), Oak Ridge National Laboratory (ORNL) [220]. The dynamic scan data were collected in the Q-range of 0.2 - 3.6 $Å^{-1}$ with the energy resolution of 0.2 meV. The energy transfer or the dynamic range was within $\pm$30 meV depending upon the Q-values, appropriate for the detection of low-frequency collective excitations in protein samples. The data were fitted using the peak analysis software PAN in the package data analysis and visualization environment (DAVE) developed at NIST Center for Neutron

Research (NCNR) [105].

5.1.3 Results and discussion

Structural change in GFP upon hydration

The static structure factor is calculated from the integration of $S(Q,E)$ over an energy range measured at each Q-value given by the relation, $S(Q) = \int S(Q,E)dE$ in the Q-range of 2.0 - 3.6 Å^{-1} within protein secondary structure to measure the quality and strutural features of the protein samples. Fig. 5.1 shows the static structure factor, $S(Q)$ as a function of wave-vector transfer Q, measured from the elastic intensity of fully deuterated dry and D_2O hydrated GFP with the hydration level of h ∼0.37. Such hydration level forms at least a monolayer of heavy water around the protein [25] that slightly modifies the structure and triggers the dynamic transition [37]. The temperature dependence of the static structure factor in the dry and hydrated samples can be clearly observed above Q ∼1.6 Å^{-1}, where the values of $S(Q)$ decrease with increase in temperature. This indicates the increase in atomic or molecular fluctuations and thus the decrease in rigidity of the sample with the rise in temperature. The smaller peak in $S(Q)$ at Q ∼0.6 Å^{-1} represents the distance between the secondary structures (i.e., central α-helix and β-barrel strand, approximately equal to 10.5 Å) in dry GFP, which shifts to the smaller Q in the hydrated sample due to small expansion of β-barrel in order to accommodate the water molecules [200] (see Fig. 5.2 for the clear view). The prominent peak observed at Q_p ∼1.4 Å^{-1} in dry GFP corresponds to the spacing between the β-barrel strands [200] nearly equal to 4.5 Å. Upon hydration, this peak becomes broader and then shifts towards slightly higher Q value, Q_p ∼1.6 Å^{-1}. The additional broader peak in the dry sample at Q ∼2.9 Å^{-1} may represent the local structure in GFP, a fluorophore and the amino acid residues [213, 214], which flattens out

in the hydrated sample due to disruption in the local structure. These major peaks in both samples confirm the amorphous nature due to density fluctuations trapped by the structural features [221]. The comparison between the static structure factor of dry and hydrated GFP samples are shown in Fig. 5.2. It is interesting to note that the values of $S(Q)$ of the dry samples are less than in hydrated samples from Q values 1.4 Å^{-1} to 3.6 Å^{-1} at all the measured temperatures. This is because the β-barrel accommodates the water molecules that cause the slight change in protein local structure and also stiffens the protein. However, the structure in the long wave-length limit Q <1.4 Å^{-1} is almost temperature and hydration independent. The significant changes in protein secondary and local structures above Q_p due to hydration and temperature further motivate to investigate the low-frequency intraprotein collective vibrational motions in GFP.

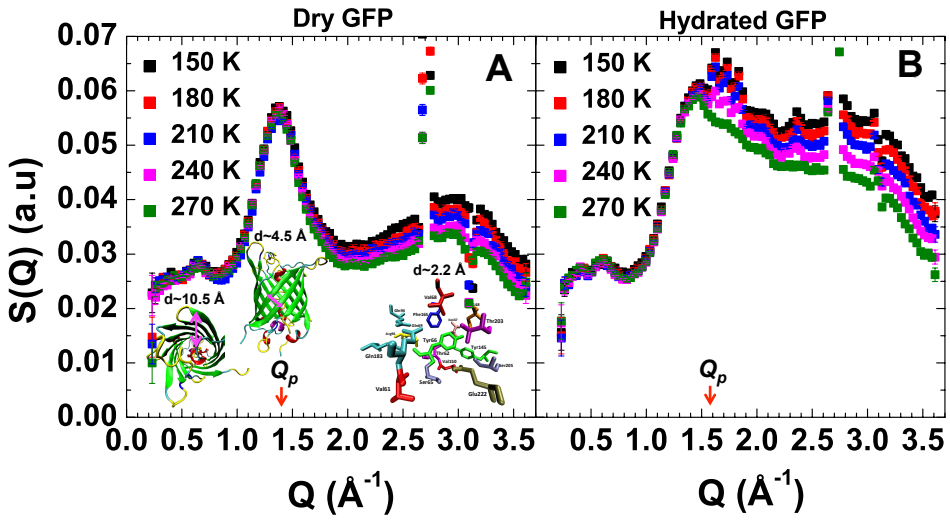

Figure 5.1: Static structure $S(Q)$ factor from dry and hydrated GFP samples. The measured static structure factors of (A) dry GFP and (B) hydrated GFP as a function of wave-vector transfer Q at different temperatures from 150 K to 270 K.

Glass-like low-frequency collective motion

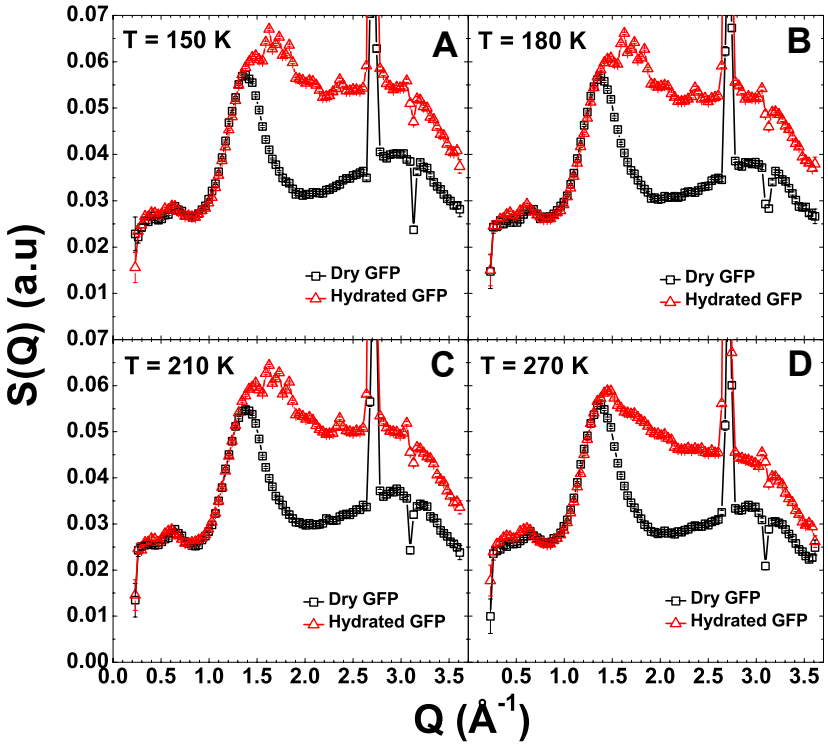

Figure 5.2: Comparison of static structure factor $S(Q)$ of dry and hydrated GFP samples at $T = 150$ K, 180 K, 210 K, 270 K.

The measured INS spectrum $S_m(Q, E = \hbar\omega)$ (also known as the dynamic coherent structure factor) consists of the central elastic peak and the inelastic side peaks, which is broadened by the instrumental resolution function $R(Q, E)$. The fitting function, that is modeled with the sum of the delta function for the central elastic peak and the damped harmonic oscillator (DHO) function for the inelastic side peaks (corrected with the detailed balanced factor $g(E)$), is convoluted with the instrumental resolution function along with the constant background $(A \cdot E + B)$ to fit the INS spectra from the protein samples and is expressed

below as:

$$S_m(Q,E) = \Big[I_0(Q)\delta(E) + g(E)I_1(Q)\frac{\Gamma(Q)}{\pi}\Big\{ \frac{1}{(E-\omega(Q))^2 + (\Gamma(Q))^2} - \frac{1}{(E+\omega(Q))^2 + (\Gamma(Q))^2} \Big\} + (A\cdot E + B) \Big] \otimes R(Q,E) \tag{5.1}$$

where $I_0(Q)$ and $\delta(E)$ are the elastic intensity and delta function respectively in the elastic component, and $I_1(Q)$, $\Omega(Q)$ and $\Gamma(Q)$ are the inelastic intensity, excitation energy, and damping factor respectively of DHO function for collective phonon excitations. Also, the Bose thermal factor $g(E)$ for the temperature-dependent correction in DHO function [222] is given by,

$$g(E) = \frac{1}{(1 - exp(E/k_B T)} \tag{5.2}$$

where k_B is the Boltzmann constant and T is the absolute temperature. The DHO function has been successfully implemented to study the Brillouin-like inelastic side-peaks in liquids [211, 222–224] and amorphous materials [221] including biomolecules [215–217, 225–227].

In Fig. 5.3, the contour plot of measured INS spectra at $T = 150$ K and 270 K from the dry and hydrated GFP samples are shown, while the fitting of $S_m(Q, E = \hbar\omega)$ using Eq. 5.1 at the wave-vector transfer $Q = 0.64$ Å^{-1} are presented in the insets of each of the panels. Clearly, in the insets, the Brillouin side-peaks of DHO are observed (shown by the magenta dashed lines) at the energy position ($\Omega = \hbar\omega$) that indicates the excitation energy of the collective modes. The open squares and triangles represent the dispersion curves (Ω vs. Q) of the low-frequency intraprotein collective vibrations at $T = 150$ K and $T = 270$ K respectively for the dry (Fig. 5.3 A and B) and hydrated (Fig. 5.3 C and D) samples. The

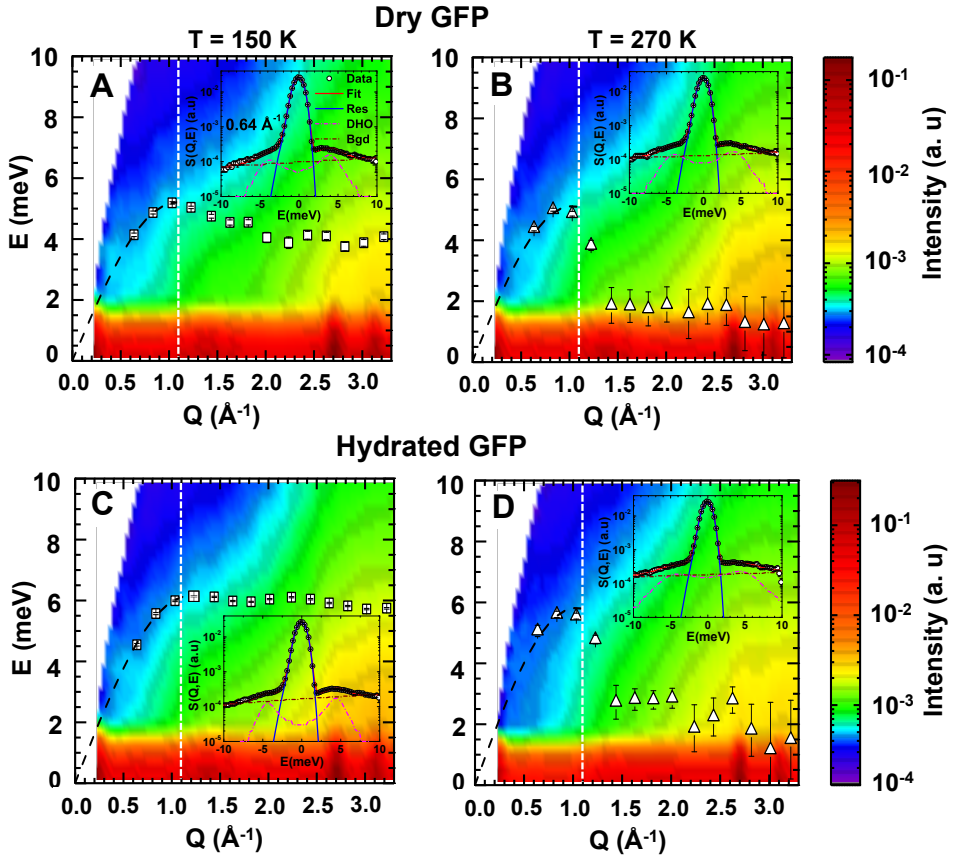

Figure 5.3: Contour plots of INS spectra (raw data) for the lowest (T = 150 K) and the highest (T = 270 K) measured temperatures are shown for the dry and hydrated samples, and the raw data for rest of the temperatures are shown Appendix B. The insets on each of the panels correspond to the fitting of measured spectra with the damped harmonic oscillation (DHO) model as expressed in Eq. 5.1 at wave-vector transfer $Q = 0.64$ Å^{-1}.

acoustic branch in the region $Q \leqslant 1.1$ Å^{-1} (separated by the white dashed lines) of phonon energy dispersion for both dry and hydrated samples are fitted with Eq. 5.3 as represented by the black dashed lines. Clearly, the bending of the energy dispersion curve occurs at the boundary of the acoustic branch (i.e., $Q_m \sim 1.1$ Å^{-1}) suggesting the existence of a pseudo-Brillouin zone [209] with the finite group velocity up to the value of Q_m, after which the plateau starts or $\Omega(Q)$ starts to deviate from the usual Q-dependence. The value of $Q_m \sim 1.1$ Å^{-1} corresponds to the topological disorder length scale in the sample or the half the

distance to the nearest reciprocal lattice point [228]. The plateau or the lack of significant dispersion at higer Q-values above Q_m indicates the end of such wave propagation signifying the localized phonon modes [221, 229].

The energy dispersion curves (Ω vs. Q) at all the measured temperatures are shown in

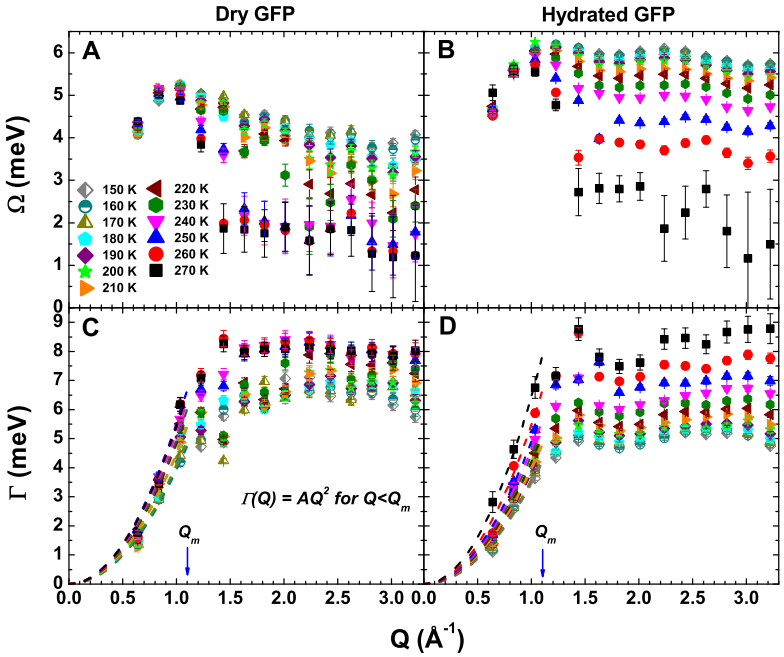

Figure 5.4: Energy dispersion curves and damping constants of low-frequency collective excitations in dry and hydrated GFP samples. Energy dispersion curves (A) in dry and (B) in hydrated GFP samples at temperatures from 150 K to 270 K. The half width at half maximum or damping constants (Γ) of DHO functions as a function of wave-vector transfer Q at temperatures from 150 K to 270 K. The dashed lines are the fitting of (Γ) with relation $\Gamma(Q) = Q^2$ at low Q-values as in ordinary glasses. Q_m refers to the values of Q, nearly above which $\Omega(Q)$ and $\Gamma(Q)$ start to deviate from their usual Q dependence.

Fig. 5.3 A and B for the dry and hydrated GFP samples respectively. These curves show the propagation of acoustic modes of hypersonic waves in the longer wavelength-limit $Q \leqslant Q_m$ at all the measured temperatures from $T = 150$ K to 270 K. Furthermore, for, $Q \geqslant Q_m$ the apparent softening of the localized intraprotein vibrations with increase in temperature

can be observed as indicated by the decrease in excitation energy in both samples, whereas acoustic phonons are nearly temperature independent. The softening of localized phonons is more evident in the hydrated sample. The comparison of energy dispersion curves between the dry and hydrated protein samples are shown in Fig. 5.5 $A-L$ from $T = 150$ K to 260 K. The comparison suggests that the presence of water molecules in protein increase the energy of the collective vibrations due to the increase in the rigidity below the melting point of water. Thus, the above results indicate the low-frequency intraprotein localized phonon modes are highly influenced by hydration and temperature, whereas the low-frequency acoustic phonons are almost temperature independent, but slightly depend on hydration. Moreover, it is quite interesting to note that the way $S(Q)$ show the temperature and hydration dependence in dry and hydrated proteins, reasonably in a similar way the energy of collective excitations vary with temperature and hydration. This behavior strongly confirms the low-frequency intraprotein collective motions are highly structure-dependent similar to the crystals, glasses or liquids [229].

The half width at half maximum of the inelastic side-peaks or the phonon damping constants (Γ) is plotted as a function of Q as shown in Fig. 5.4 C and D. The apparent increase in the value of Γ with temperature suggests the increase in damping of intraprotein collective vibrations due to the instigation of relaxation and diffusion processes. It corresponds to the life-time of the collective excitations [221] and are fitted with a relation $\Gamma(Q) = Q^2$ at low Q-values as in the ordinary glasses [229] and becomes flat or deviate from the usual Q^2-dependence for $Q < Q_m$, which is due to the localized intraprotein vibrations. Further, it is very interesting to note that the protein energy dispersion curve also follows the relation $\Omega(Q_m) \approx \Gamma(Q_m)$ similar to the glasses and glass-forming liquids [229]. In addition, the

ratio Q_m/Q_p measures the fragility of the sample and found to be ∼0.8 and ∼0.7 for the dry and hydrated GFP respectively, much larger than those observed in some glasses and glass-forming liquids like *o*-terphenyl, glycerol, and SiO_2[229].

We further fit the energy dispersion curves in the acoustic branch as shown in Fig. 5.5 $A-L$ by the dashed lines with oversimplified relation given by the Born-von Karman lattice dynamics theory in one dimension [228] expressed as,

$$E(meV) = 4.192 \times 10^{-3} v(m/s) \times Q_m(\mathring{A}^{-1}) sin\Big(\frac{\pi}{2}\frac{Q(\mathring{A}^{-1})}{Q_m(\mathring{A}^{-1})}\Big) \tag{5.3}$$

where v is the velocity of the collective wave propagation. Although the model only considers the nearest neighbor interactions mainly applicable to the single crystals, it successfully fits the data from the amorphous form of protein samples as well [216]. The calculated velocities of the low-frequency acoustic phonons from the dry and hydrated GFPs are compared as shown in Fig. 5.6. It shows the sound velocities are barely temperature dependent with values ranging from 1027 m/s to 1341 m/s for dry and hydrated GFP samples, very close to the sound velocity of ordinary water that is nearly equal to 1500 m/s [210]. Since these sound velocities are due to the low-frequency acoustic modes, these values are much smaller than those velocities observed in other proteins using IXS technique [215–218, 227] due to the high-frequency mode, close to the fast velocity of heavy water of about 3300 m/s [230]. The calculated values of velocities in this study are in good agreement with the average sound velocities of about 1200 m/s in fluid lysozyme using ultrasound velocimetry [231] and 1605 m/s in amorphous myoglobin using Mössbauer effect [232]. Also, the sound velocity of a transverse acoustic mode in a protein active-site mimic [chloro(octaethyporphyrinato)iron(III)] is

found to be nearly 1011 m/s using IXS and vibrational spectroscopy techniques [216]. The slight higher velocity in the hydrated sample than in the dry one is due to the increased rigidness caused by the presence of water molecules inside and around the protein molecules.

Contribution of protein structures to low-frequency collective modes

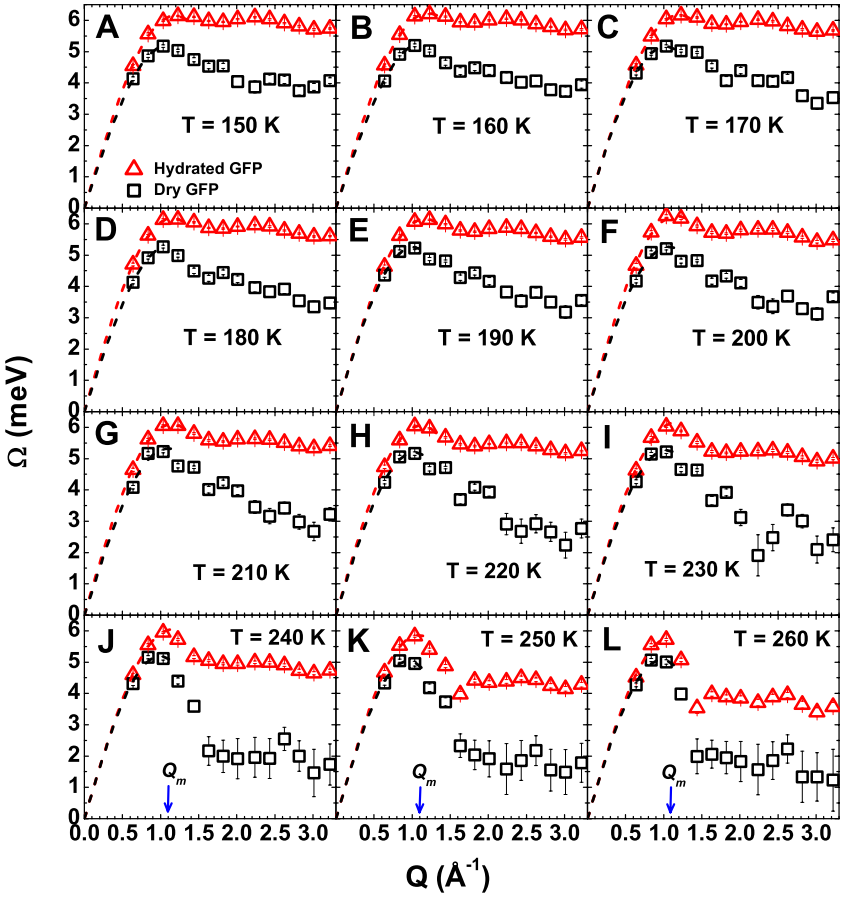

Figure 5.5: Comparison between phonon energy dispersion curves in dry and hydrated GFP samples at different temperature from 150 K to 260 K, where the dashed lines correspond to the fitting the curve with Eq. 5.3.

We observe the low-frequency intraprotein collective excitations in dry and hydrated samples of GFP, whose energy are in the range of 1.0 - 7.0 meV. The energy dispersion curves indicate that the collective motion of protein molecules give rise to the acoustic phonons,

due to the periodic vibrations of predominant secondary structure, β-barrels in GFP. Such phonon propagation takes place in the length scale larger than 5 Å as indicated by the white dashed line in Fig. 5.3 at $Q_m = 1.1$ Å^{-1} as a boundary above which excitations are localized. This size resembles the protein secondary and tertiary structures that carry physical or chemical transformations for enzyme catalysis. Due to the highly disorder and complex structure of amorphous protein samples that lack any periodic orientations, it is not trivial to differentiate longitudinal and transverse modes exclusively [209, 210, 221]. Thus, here we consider the acoustic phonon is the contribution from both modes that are coupled with each other. On the other hand, the localized excitations at $Q > Q_m$ are mainly contributed by intraprotein collective vibrations due to the fluorophore and amino acid residues, which are in the length scale of 2.0 - 5.0 Å[214]. Such phonon has relatively larger excitation energy compared to that of acoustic mode and thus rapidly fluctuates locally without any propagation.

Flexibility induced by temperature and hydration

The flexibility in biomolecules is an essential property for the several biochemical and biophysical processes like molecular reactions, protein-ligand interactions, conformational fluctuations and free-energy minimization for folded state. Thus, the enzymatic activities of proteins are reflected by the response of how flexible and stable they are [18]. The flexibility is mainly driven by the hydration along with the thermodynamic variables like temperature and pressure [28]. From the biophysical point of view, the flexibility is the principal factor for balancing the free-energy during the binding of two or more molecules or protein and ligand for enzyme catalysis [196].

The energy dispersion curves show that the propagation of acoustic phonons in GFP

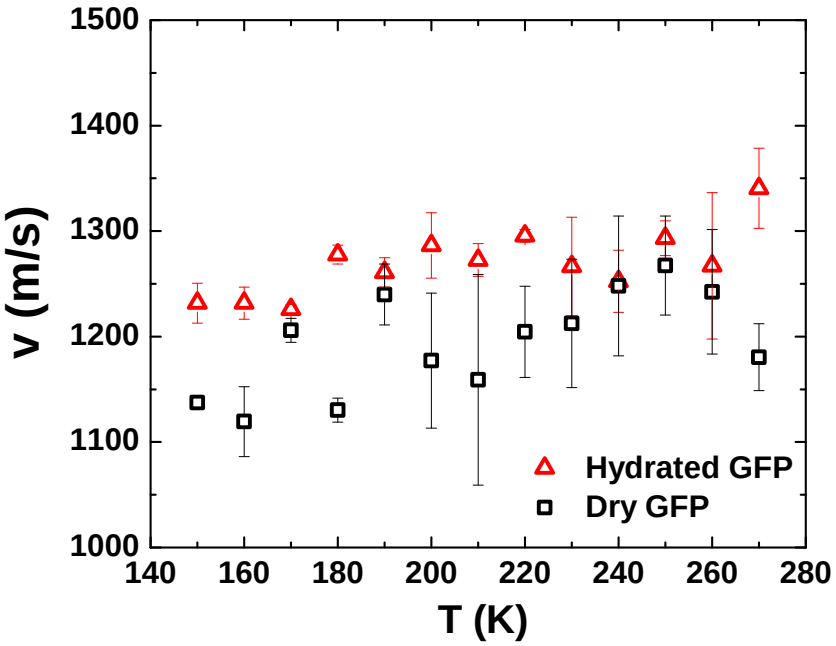

Figure 5.6: Sound velocities of the acoustic phonon propagation in GFP samples. The velocities of acoustic phonon in dry and hydrated GFP samples are compared, which shows the propagation is slightly faster in the hydrated sample, however, remain almost constant with respect to the temperature in both samples.

that are nearly independent of temperature in both dry and hydrated samples. However, the energy of intraprotein localized phonons decreases with rise in temperature. This indicates that the both dry and hydrated proteins become softer and hence more flexible as the temperature is increased. The softening is more evident in the hydrated sample. This behavior supports the fact that water plays a significant role in biological activities. However, the larger values of intraprotein localized excitation energy in GFP upon hydration suggests that the protein becomes more rigid due to the accommodation of water molecules inside the β-barrels and hence the protein lacks the flexibility compared to the dry sample below the melting point of water. This hydration dependence of intraprotein vibrations in

GFP below the melting point of water is in good agreement with the previously reported results of the study of mean-square displacement (MSD) of hydrogen (H) atoms in dry and hydrated GFPs using incoherent neutron scattering experiments [200]. The results from that experiment showed the MSDs of H atoms in the dry sample are larger than those in the hydrated GFP sample, which indicates the dry GFP is more flexible than the hydrated one below the melting point of water [200]. This result is contradictory to the effect of hydration observed in other common globular proteins [31, 37]. Thus, we assumed that the structure of β-barrels that can trap the water molecules within itself play the major role for such contradictory result. On the other hand, one should expect more softening or flexibility in the hydrated sample compared to the dry sample above the melting point of water, similar to the results previously observed in lysozyme and other globular proteins [200, 218, 226].

Role of phonons in enzyme catalysis

The rapid harmonic vibrations or fluctuations in protein occur in the time scale of femtoseconds to picoseconds. Such phenomena include making and breaking of covalent bonds, the formation of hydrogen bonds, and transfer of electron, proton or hydride ions among different chemical groups [11]. These intrinsic dynamics play an essential role in the rates of enzyme catalysis. The enzymatic reactions that mainly occur in the milliseconds time scale are coupled to the bond activation of C-H or C-H $\rightarrow$ C transfer, which often take place in hundreds of femtoseconds [205]. The energies associated with such fluctuations are in the range of few millielectronvolts [204]. Although these energies are much less than the energy barrier of the transition state, enzymatic reaction takes place due to mechanism of quantum mechanical tunneling [204]. Here so observed phonons that are originated due to coherent vibration of various residues and secondary structures in protein (specifically β-

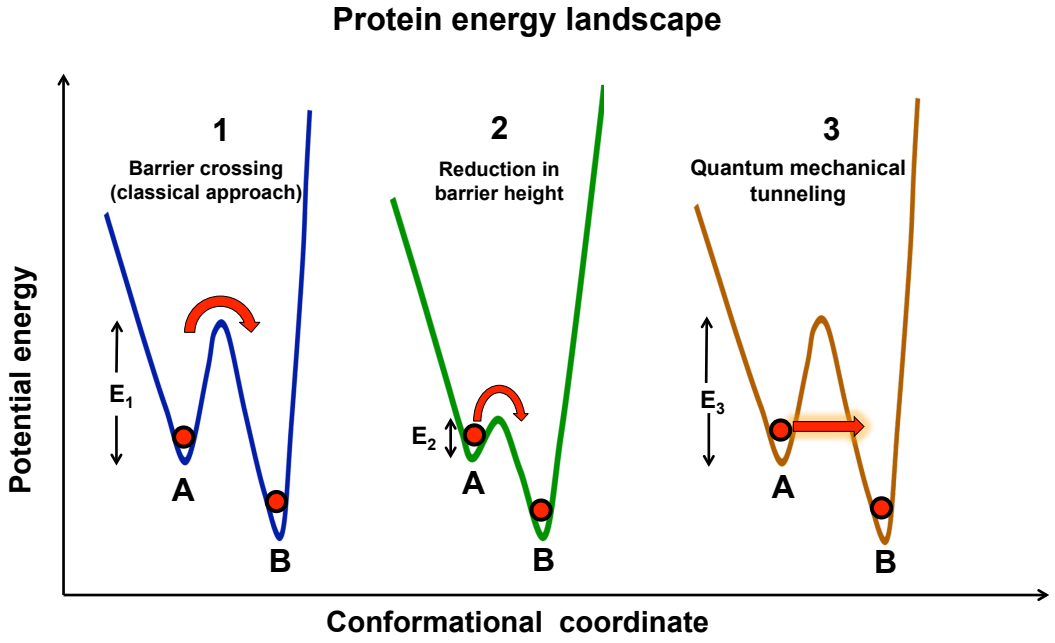

Figure 5.7: Schematic picture of protein complex free energy landscape (EL) for enzyme catalysis mediated by collective excitations or phonons in proteins. 'A' and 'B' denote the two arbitrary conformational substates (CSs), where 'B' is more favorable for enzyme-mediated catalysis. Sampling of one of the possible pathways in multi-dimensional protein EL for the most favorable CS 'B' from partially favorable CS 'A' (1) by crossing the energy barrier, E_1 (classical approach), (2) due to reduction in barrier height to energy barrier (E_2) from higher energy barrier, and (3) through quantum mechanical tunneling across the energy barrier of E_3.

sheets for GFP) with excitation energy of the order of few milli-electronvolts are the possible experimental evidence of dynamic entity playing significant role in enzyme-mediated catalysis. These phonons may be a responsible candidate for sampling the suitable conformation that is capable of carrying out catalytic reactions. Based upon multi-dimensional free EL, there may three possible scenario for the favorable protein conformation required for enzyme catalysis mediated by collective excitations or phonons: (1) crossing the barrier through transporting the necessary thermal energy (classical approach), (2) reducing the height of the barrier by making and breaking the bonds, or (3) quantum mechanical tunneling through

the barrier. The schematic of these processes is illustrated in Fig 5.7.

5.1.4 Conclusion

Our results demonstrate that INS experiment is successful in investigating the low-frequency collective excitations or phonons in proteins. We observe the acoustic phonons in both dry and hydrated GFP samples, which is almost temperature independent. However, the energy of acoustic phonons slightly increases upon hydration, indicating more rigidness than in the dry sample below the melting point of water. On the other hand, the low-frequency localized phonons are highly influenced by hydration and temperature. The hydrated sample possesses the larger energy of localized excitations compared to the dry one, showing more rigidness in protein due to the presence of water molecules inside the β-barrels. This result suggests the loss in conformational flexibility in hydrated GFP in agreement to the previous study [200]. In addition, the decrease in energy of such vibrations with the rise in temperature in both the samples suggests the softening of the protein and hence the increase in flexibility. The velocities of sound propagation in dry and hydrated GFPs are in the range of 1027 m/s to 1341 m/s, which is in good agreement with the calculated values from other techniques like Mössbauer effect [232], ultrasound velocimetry [231], vibrational spectroscopy, and IXS [216]. The hydrated sample shows slightly faster velocity due to increased rigidness.

From a biochemical point of view, our results suggest that the phonons may be the possible factor that links the fast (femtosecond - picosecond) dynamics to enzyme catalysis. Despite the lack of available thermal energy, phonons prefer the favorable conformations or pathways necessary for enzyme catalysis that occurs in millisecond time scale. Thus, the existence of phonons in protein may give a new insight for understanding the biological

functions.

5.2 Collective excitations in protein as a measure of its softness and flexibility

5.2.1 Introduction

It is well-accepted that the protein dynamics together with its native structure play a significant role in enzyme catalysis [14, 18]. However, understanding of the relationship among a protein's structure, dynamics, and function is still a major challenge in the biophysical research. Furthermore, water plays a significant role in the biological activity and function [33, 37, 233]. Several studies have elucidated the minimum hydration level of $h = 0.2$ that forms at least a monolayer of water around the protein is required for the activity of enzymes [25, 37]. The fluctuations of such hydration shell provide the activation energy to overcome the conformational barrier in protein despite the lack of available energy [12].

Inelastic X-ray scattering (IXS) technique is the unique tool to study the collective density fluctuations in amorphous materials, glasses, or liquids [210]. High energy resolution of the order of millielectronvolt (meV) achieved by IXS spectrometers allow for precise investigation of highly damped collective modes and phonon dispersion in topologically disordered systems [208, 209]. Previously, there are evidences from several inelastic neutron scattering (INS) experiments of collective motions in proteins, which are similar to the boson peak in the glass-forming liquids due to the collective excitations or density fluctuations [198–201]. Furthermore, IXS, INS, Brillouin neutron spectroscopy (BNS) and molecular dynamic (MD) simulations have revealed the propagation of acoustic phonons in the proteins and their hydration water in the longer wavelength limit corresponding to the length scale larger than $\sim$1 nm (27-37). However, very few studies reported investigation of local excitations within

the protein secondary structure of less than 1.5 nm [217, 218, 225, 234]. A recent IXS experiment by Wang *et al.* has studied the collective excitations in the protein and concluded that the phonon energy softening and phonon population enhancement in hydrated protein (both native and denatured) is induced by the hydration shell [226]. On the other hand, MD simulation results clearly suggested the strong coupling between the dynamics of protein and its hydration shell exists rather than protein dynamics being slaved to the hydration water [235]. Specifically, the acoustic phonon propagations in the protein and its hydration water are almost identical [215, 216, 235]. This result suggests the collective excitations of the same frequency exist in both subsystems, but are not necessarily slaved to that of the hydration water in the case of protein [235], because the dry protein also shows similar collective excitations as reported in the previous studies [212, 227, 236]. Such phonon modes from the protein and its hydration shell are practically difficult to decouple through the analysis of experimental data, but have been successfully decoupled and studied by MD simulation [235].

For proteins, as a dynamic entity similar to the glasses, it has been a major concern whether the phonon modes exist in native and denatured proteins and how such modes are correlated with the activity of enzymes [226]. In this study, we investigated the collective excitations in hydrated samples of native and denatured human serum albumin (HSA) as a model protein using the IXS technique [237]. HSA is the most prominent protein present in the plasma since ∼60% of the total protein content in the blood serum is HSA [238]. It consists of 585 amino acids having the molecular weight of 66.5 kDa [238]. The molecular structure of HSA consists of three domains (I, II and III) with two subdomains (A and B) each. It has very important properties of binding and transporting insoluble molecules such

as fatty acids, porphyrins and a large variety of drugs [238]. Thus, HSA influences the drug delivery and efficacy that ultimately affect the pharmacokinetic/pharmacodynamic properties of drugs [239, 240]. According to Sudlow's nomenclature, it posesses two major binding sites: hydrophobic subdomains IIA (site I) preferred by heterocyclic anions and IIIA (site II) favored by the aromatic carboxylates [241, 242]. An anticoagulant drug like warfarin and a nonsteroidal anti-inflammatory drug like ibuprofen bind to Sudlow's site I and site II respectively [242]. Such strong binding affinity of these drugs to HSA helps transport and release them on the specific targets. Therefore, the interaction of these drugs with HSA has attracted much attention in the pharmaceutical drug design industries [240]. On the other hand, much less is understood regarding how such drugs affect the local structure and dynamics of HSA. Therefore, we further studied the collective excitations from the samples of warfarin and ibuprofen (pharmaceutical drugs) binding to HSA using IXS technique. Here, we introduce the idea of protein softness (flexibility) revealed by the collective phonon-like excitations within the protein secondary structure to address the concerns outlined above.

Using IXS spectrometer, we measured the dynamic structure factor as a function of energy and momentum transfers, $S(Q, E)$ from the samples within the protein secondary structure of few angstroms (Å) at two temperatures T = 200 K and 300 K (i. e., below and above the dynamic transition temperature, T_D ~220 K [41, 42]; specifically, 300 K is the physiological temperature), where both the propagating collective modes and the non-propagating localized modes are observed. Remarkably, we detected the phonons both in native and denatured HSA consistent with the recently reported results by Wang *et al.* [226]. Such phonons are due to the fluctuations of the protein folded structure in the native sample, or the unfolded domains in the denatured sample, rather than induced by the surrounding

hydration shell. Surprisingly, the collective excitations from the thermally denatured sample of HSA show more softening compared to that of the native sample due to disruption of its secondary and tertiary structures, which further cause loss in protein activity [237]. In addition, the longitudinal sound velocity in denatured HSA significantly decreases due to change in the protein structure. Thus, it gives the notion that the degree of flexibility and stability (a well-accepted measure of protein function) are balanced by the native protein structure for mediating the biological activity. Furthermore, according to the results from the experiments on HSA bound with the drugs, warfarin and ibuprofen, the protein softness or flexibility remains unaltered upon binding with the drugs at the physiological conditions [237]. Therefore, the interaction of such drugs does not really affect the native structure and flexibility of HSA although the binding affinity is very high. Based on these results, we address and generalize the following major concepts: (i) the phonon-like excitations exist in proteins both in native and denatured states; however, the degree of softness (flexibility) determines whether the proteins are functional or not; (ii) the hydration shell with hydration level $0.2 \leq h \leq 0.4$ may not necessarily contribute to the collective excitations, but can be sufficiently coupled to some extent for the activity of the protein; (iii) the collective excitations are highly structure-dependent and thus any structural change may also alter the behavior of such excitations, and (iv) the idea of protein softness (flexibility) and rigidity can be defined in terms of collective excitations that can be further used as a novel approach to understand the enzyme activity.

5.2.2 Methods and materials

Sample preparation

Human serum albumin (Sigma Aldrich A3782) was used as purchased for the experiments.

Thermally denatured HSA was prepared by incubating 25 mg/ml HSA at 85 ^{o}C for 10 hours, and 100 ^{o}C for 20 minutes, before freezing at -80 ^{o}C followed by lyophilization. All the samples were hydrated using the vapor diffusion approach to 44.8% H_2O by mass. Ibuprofen (I4883) and Warfarin (A2250) were purchased from Sigma-Aldrich. For protein-ligand interaction studies, Ibuprofen and Warfarin were dissolved in ethanol and added to a HSA solution (0.242 mM or 16 mg/ml) to a final concentration of 2.42 mM (0.5 mg/ml and 0.75 mg/ml Ibuprofen and Warfarin, respectively). All samples were incubated at room temperature for 1 hour before lyophilization.

The protein samples were prepared for two separate IXS experiments. In experiment 1, native HSA and thermally denatured HSA samples were measured. In experiment 2, we prepared and measured another set of native HSA, HSA bound to warfarin (HSA/warfarin) and HSA bound to ibuprofen (HSA/ibuprofen). For IXS experiments, the protein samples were hydrated with H_2O with hydration level h $\sim$0.4, which forms at least a monolayer of hydration shell, but is not sufficient to form the secondary layer and more [218]. Thus, in the first approximation, the three-dimensional water-water hydrogen bond cannot be formed and therefore, only the scattering signal from the vibrations of protein and water coupled to the protein surfaces are measured.

Inelastic X-ray scattering measurements

The high-resolution IXS spectra were measured at the beamline 3-ID-C, Advanced Photon Source (APS), Argonne National Laboratory using X-ray beam of energy 21.6 keV [243–245]. The data were collected in the Q-range of 2.0 - 32.0 nm^{-1} using four spherically bent silicon analyzers with the energy resolution of 2.1 meV and the energy transfer (E) or the dynamic range was $\pm$25 meV appropriate for the detection of collective excitations in

proteins. The data fitting was done using the peak analysis software PAN in the package data analysis and visualization environment (DAVE) developed at NIST Center for Neutron Research (NCNR) [105].

5.2.3 Results and discussions

Structural features of proteins

At first, the structural property and the quality of the hydrated protein samples were investigated by measuring the static structure factor, $S(Q)$, over the wide momentum transfer range, Q = 2.0 - 32.0 nm^{-1} as shown in Fig. 5.8. The static structure factor is calculated from the integration of $S(Q, E)$ over an energy range measured at each Q-value given by the relation, $S(Q) = \int S(Q, E)\ dE$. Clearly, the two major peaks are observed from all the samples at Q ∼6 nm^{-1} (A) and ∼15 $^{-1}$ (B), which have also been observed in different hydrated proteins such as lysozyme [226], green fluorescent protein [200], beta-lactoglobulin [217], alpha-chymotrypsinogen A [234], myoglobin, haemoglobin and C-phycocyanin [246]. Thus, such structural property can be considered as a universal feature of all the proteins. Peak **A** corresponds to the protein-protein interaction at a relatively larger length scale (in the order of 1 nm); whereas peak **B** represents the spatial order of the secondary structure, beta-sheets of length ∼4.5 $\mathring{A}$ and alpha-helix repeats of ∼5 Å[217, 226]. The absence of a structural peak of bulk water at 19 nm^{-1} [217] assures that the scattering data collected are exclusively from the hydrated protein samples. Furthermore, the distorted peak **B** in $S(Q)$ of the thermally denatured HSA confirms the significant loss in the secondary structure, particularly alpha-helices, and tertiary structure due to break-down of non-covalent bonds, such as hydrogen bonds, and van der Waals interactions [226]. Moreover, we did not see any significant change in the $S(Q)$ of HSA due to binding with the drugs (warfarin and

ibuprofen). This is beacause HSA consists of large hydrophobic cavities in subdomains IIA (site I) and IIIA (site II) that hold drugs without affecting its overall native conformation [240]. These static structure factor measurements assure that any change in dynamic scan data is due to the change in collective dynamic behaviors for different protein samples at different temperatures and conditions.

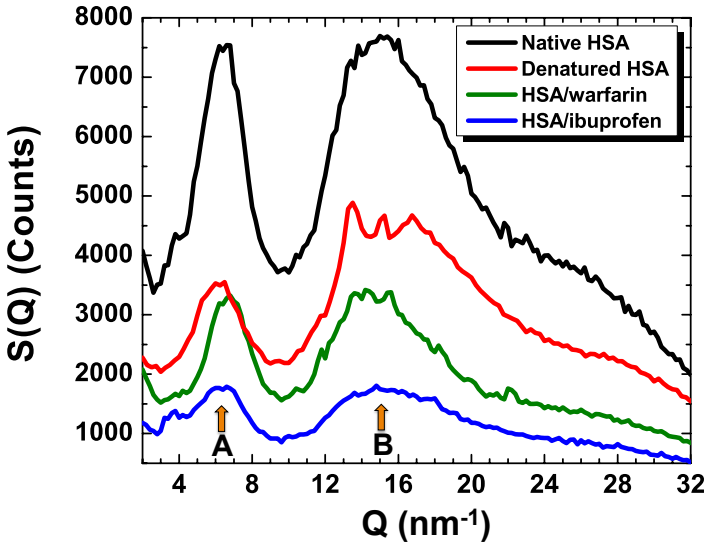

Figure 5.8: Static structure factor $S(Q)$ as functions of Q measured at $T = 300$ K for native HSA, thermally denatured HSA, warfarin bound to HSA (HSA/warfarin) and ibuprofen bound to HSA (HSA/ibuprofen), represented by black, red, green and blue curves, respectively. All the samples are hydrated with hydration level h ∼0.4.

Collective excitations in proteins

The measured IXS spectrum can be expressed as,

$$S(Q,E) = [S_m(Q,E) + A \cdot E + B] \otimes R(Q,E) \tag{5.4}$$

where $S(Q,E)$ is the dynamic coherent structure factor, $S_m(Q,E)$ is the model function,

$(A \cdot E + B)$ is the linear background, $R(E)$ is the resolution function of the instrument, and $\otimes$ is the convolution operator. The model function, $S_m(Q, E)$ can be further expressed as the sum of the delta or Lorentzian function for the central peak (depending upon the dynamic nature of the sample in the specific Q-range) and the damped harmonic oscillator (DHO) function for the Brillouin side peaks due to the collective excitations. The energy resolution function, $R(E)$ is measured from the plexiglass at its structure maxima ($Q \sim$10 nm^{-1}). All the data were fitted with the dynamic range of $\pm$20 meV with Eq. 5.4 using the following model function,

$$S_m(Q,E) = \Big[I_0(Q)\delta(E) + g(E)I_1(Q)\frac{\Gamma(Q)}{\pi}\Big\{ \frac{1}{(E-\Omega(Q))^2 + (\Gamma(Q))^2} - \frac{1}{(E+\Omega(Q))^2 + (\Gamma(Q))^2}\Big\}\Big] \tag{5.5}$$

or

$$S_m(Q,E) = \Big[I_0(Q)\Gamma(E) + g(E)I_1(Q)\frac{\Gamma(Q)}{\pi}\Big\{ \frac{1}{(E-\Omega(Q))^2 + (\Gamma(Q))^2} - \frac{1}{(E+\Omega(Q))^2 + (\Gamma(Q))^2}\Big\}\Big] \tag{5.6}$$

where $I_0(Q)$ and $\delta(E)$ are the elastic intensity and delta function respectively in the elastic component, and $I_0(Q)$, $\Omega = \hbar\omega_p$ (ω_p is the excitation frequency), and $\Gamma(Q)$ are the inelastic intensity, the excitation energy, and the damping factor respectively of DHO function for collective excitations. Also, the Bose thermal factor $g(E)$ for the temperature-dependent

correction in DHO function [222] is given by,

$$g(E) = \frac{1}{(1 - exp(E/k_B T)} \tag{5.7}$$

where k_B is the Boltzmann constant and T is the absolute temperature. The DHO func-

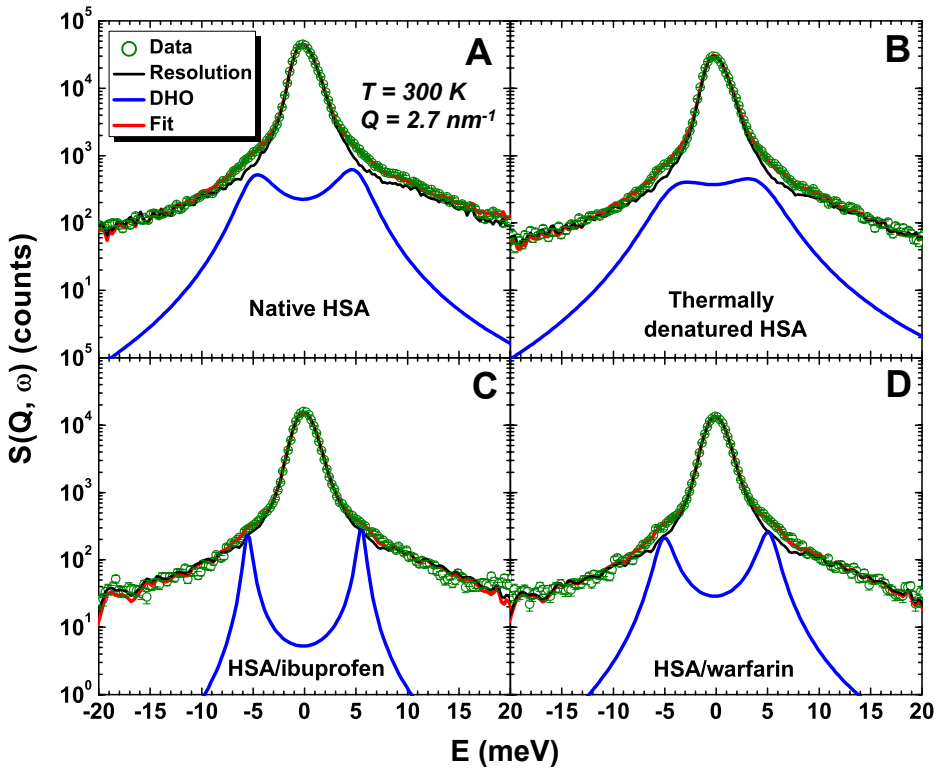

Figure 5.9: Dynamic coherent structure factor measured from (A) native HSA, (B) thermally denatured HSA , (C) HSA/ibuprofen and (D) HSA/warfarin, and corresponding fitting with Eq. 5.4 at $Q = 2.7$ nm^{-1} and $T = 300$ K. The green circles, black, blue and red curves indicate the experimental data, resolution, DHO function with two Brillouin-side peaks and the best fit to the data, respectively. The hydration levels (h) for all the samples were ∼0.4.

tion has been successfully implemented to study the Brillouin-like inelastic side-peaks in liquids [211, 222–224] and amorphous materials [221] including biomolecules [215–217, 225–

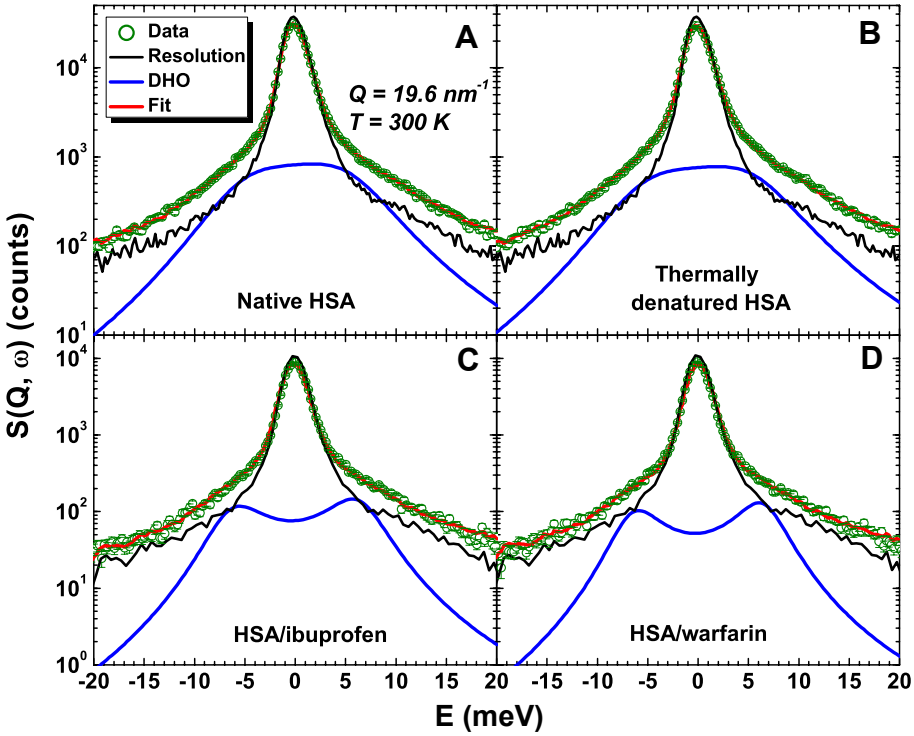

Figure 5.10: Dynamic coherent structure factor measured from (A) native HSA, (B) thermally denatured HSA , (C) HSA/ibuprofen and (D) HSA/warfarin, and corresponding fitting with Eq. 5.4 at $Q = 19.6$ nm^{-1} and $T = 300$ K. The green circles, black, blue and red curves indicate the experimental data, resolution, DHO function with two Brillouin-side peaks and the best fit to the data, respectively. The hydration levels (h) for all the samples were ∼0.4.

227].Also, $L(\Gamma, E)$ is the Lorentzian function given by,

$$\Gamma(E) = \frac{1}{\pi}\frac{\Gamma'(Q)}{\Gamma'^2 + E^2} \tag{5.8}$$

Eq. 5.5 and Eq. 5.6 were implemented to fit the data in the Q-range of 2.1 - 9.3 nm^{-1} and 12.1 - 31.2 nm^{-1} respectively. Here, the use of Eq. 5.6 incorporating the Lorentzian function for the central peak at higher Q-values may be necessitated by the possible rapid diffusion process in the samples.

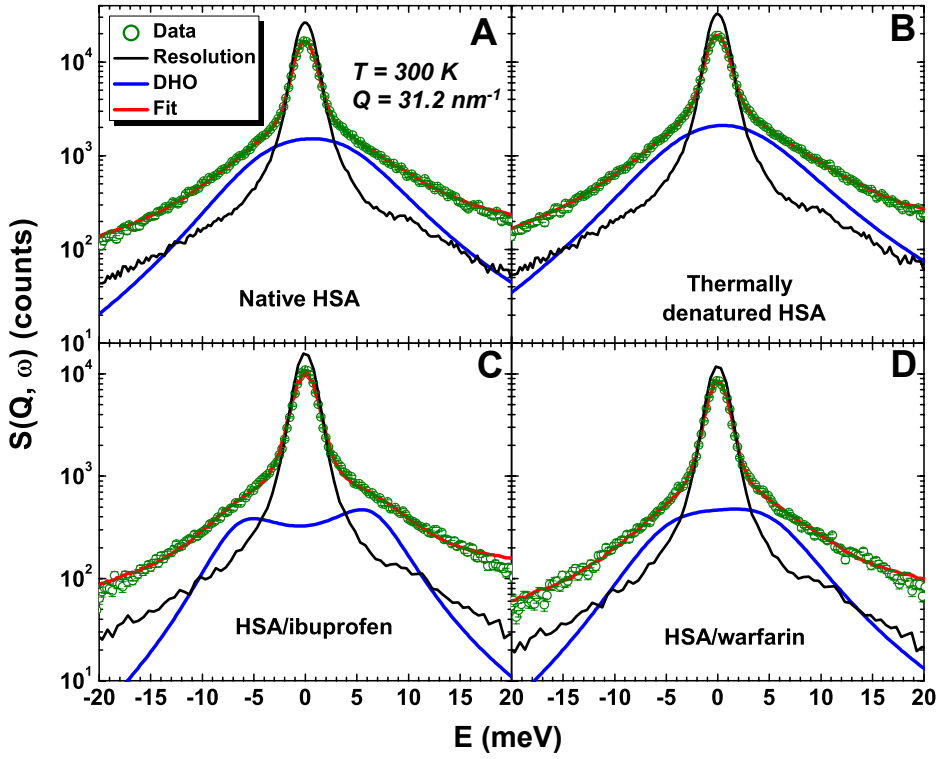

Figure 5.11: Dynamic coherent structure factor measured from (A) native HSA, (B) thermally denatured HSA , (C) HSA/ibuprofen and (D) HSA/warfarin, and corresponding fitting with Eq. 5.4 at $Q = 31.2$ nm^{-1} and $T = 300$ K. The green circles, black, blue and red curves indicate the experimental data, resolution, DHO function with two Brillouin-side peaks and the best fit to the data, respectively. The hydration levels (h) for all the samples were $\sim$0.4.

The dynamic coherent structure factor, $S(Q, E)$ measured using IXS spectrometer from the protein samples and the corresponding fitting with Eq. 5.4 at $T = 300$ K, and $Q = 2.7$ nm^{-1}, $Q = 19.6$ nm^{-1} and $Q = 31.2$ nm^{-1} are shown Fig. 5.9, Fig. 5.10 and Fig. 5.11, respectively. The panels A and B are from experiment 1, whereas panels C and D are from experiment 2 in each of the figures. The model so used for the fitting is either with Eq. 5.5 or Eq. 5.6, depending upon the specific Q-range as discussed above. The green open circles represent the data points, whereas the solid curves with red and blue colors indicate the best fit and the DHO function with Brillouin side peaks, respectively. Clearly, we can see the two

small inelastic peaks on the shoulder of the central peak due to the collective excitations or density fluctuations in the samples. Such weak inelastic peaks are due to the amorphous nature of the samples similar to the glasses or glass forming liquids [221, 225, 227].

Fig. 5.12 shows the dispersion curves Ω vs. Q calculated from the different protein samples. The data shown in panel A, B and C are from experiment 1 and the data in the panels D, E and F are from experiment 2. The dispersion phenomena can be observed roughly up to the Q-value where the peak **B** of the structure factor rises ($\sim$10 nm^{-1}), which corresponds to the spatial order of the secondary structure as discussed in the previous section. Such behavior implies that the protein intermediate and short-range order can define the dispersion curve similar to the Brillouin zone in the crystals [227]. However, at the higher Q-values, the collective excitations seem to be almost Q-independent, and thus can be considered as non-propagating, or localized. Such localized fluctuations are due to the topologically disorder length scale [228] in the sample mainly contributed by intraprotein collective vibrations due to the protein primary structure or amino acid residues such as methyl groups, which are in the length scale of 2.0 - 5.0 Å. On the other hand, the linearity of the curve at the low Q-values indicates the acoustic longitudinal phonons that propagate with certain sound velocity in the samples. The sound velocity of such phonon is calculated from slope of the energy dispersion curve by fitting with a relation given by,

$$\Omega = \hbar v_L Q \tag{5.9}$$

where v_L is the longitudinal sound velocity. The calculated values of longitudinal sound velocity are approximately 2,800 m/s depending upon the nature of the samples as listed in

Table 1, analogous to the values as reported in previous experiments [215–218, 221, 226, 227]. Intriguingly, there is a significant decrease of sound velocity in thermally denatured sample compared to the native one at the room temperature. On the other hand, the significant temperature dependence of characteristic excitation energies can be observed at higher Q-values suggesting the phonon softening for the enzymatic activity as reported before in a similar IXS experiment [218].

The phonon damping constant (Γ) or the half width at half maximum of the inelastic

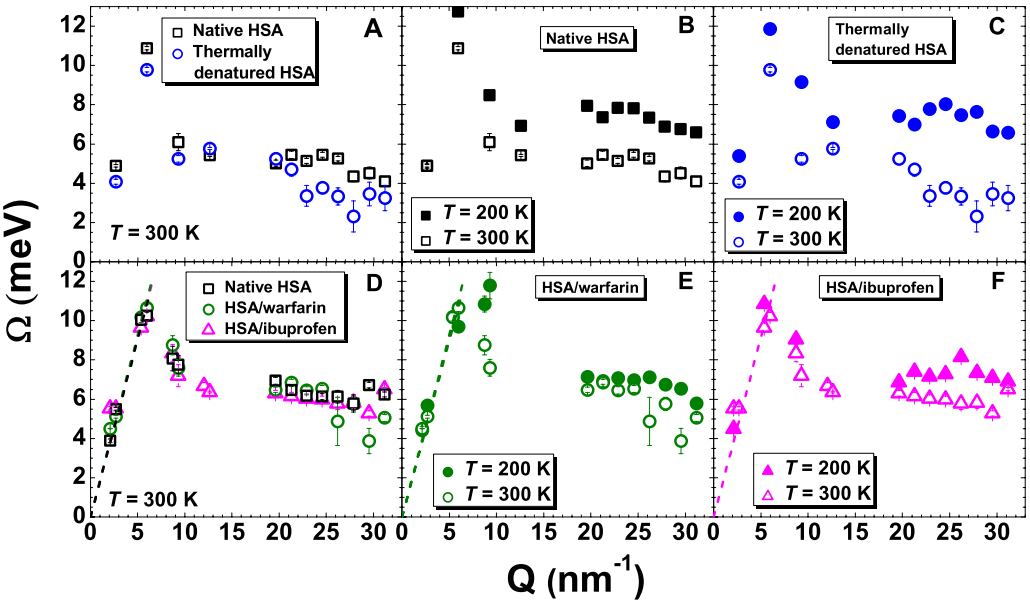

Figure 5.12: Phonon dispersion curves (Ω vs. Q) calculated from native HSA, thermally dentured HSA, HSA/warfarin and HSA/ibuprofen samples with h ~ 0.4 at $T = 200$ K and 300 K. The dashed lines represent the fitting of dispersion curve at low Q-values (acoustic branch) with Eq. 5.3 to calculate the longitudinal velocity (v_L) of the sound wave propagation. The longitudinal sound velocity is calculated for those, which has more than two data points in the acoustic branch of the corresponding dispersion curve.

side-peaks is plotted as functions of Q in Fig. 5.13. It resembles the lifetime of such collective excitations, which follows a power law relation $\Gamma(Q) = AQ^2$ at low Q-values as in the ordinary glasses [221, 225]. The data in Fig. 5.13 A, B and C are calculated from experiment 1,

whereas the data in Fig. 5.13 D, E and F are from experiment 2. Clearly, we can observe the increase in the value of Γ with Q and temperature that indicates the increase in the damping of collective modes due to the activation of the diffusion process in the sample.

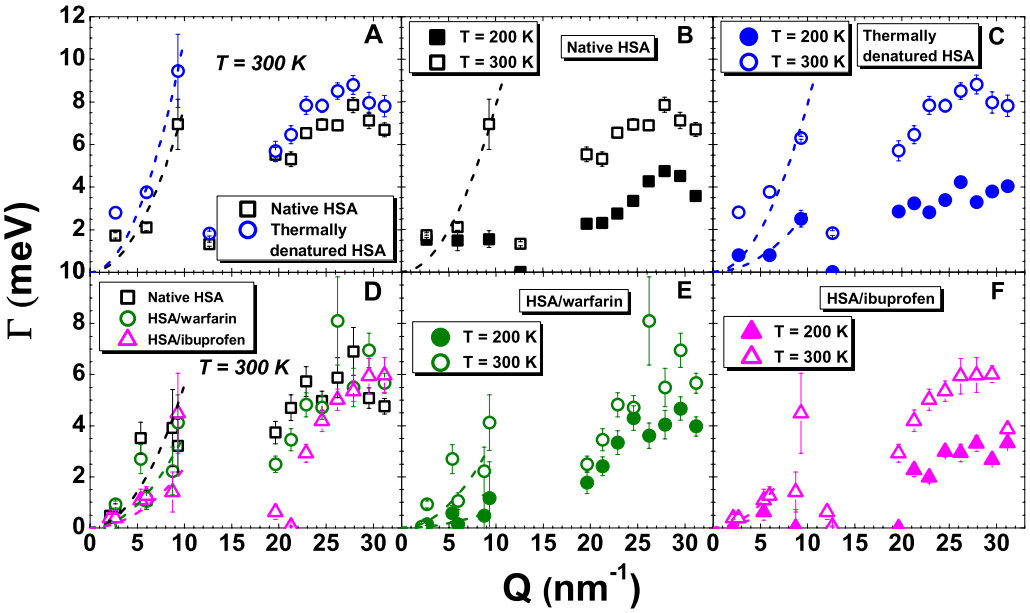

Figure 5.13: Damping constants of phonons calculated from the samples of native HSA, thermally dentured HSA, HSA/warfarin and HSA/ibuprofen samples with h ∼0.4 at T = 200 K and T = 300 K. The dashed lines represent the fitting by a relation, $\Gamma(Q) = AQ^2$ at low Q-values (acoustic branch) similar to the glasses, where an arbitary A is a constant.

Protein denaturation and collective excitations

In order to understand whether the propagation of phonons in protein and its conformational softening behavior persists upon its denaturation, we measured the IXS spectra from both the native and denatured samples of HSA with hydration level h ∼0.4 each. The thermal denaturation significantly affects the protein structure by minimizing the content of alpha-helices and tertiary structures, whereas the beta-sheets are increased [35, 226]. In addition, the thermal denaturation yields the molten globule state and aggregation of HSA [247]. Therefore, the thermally denatured HSA loses its biological activity. The disruption

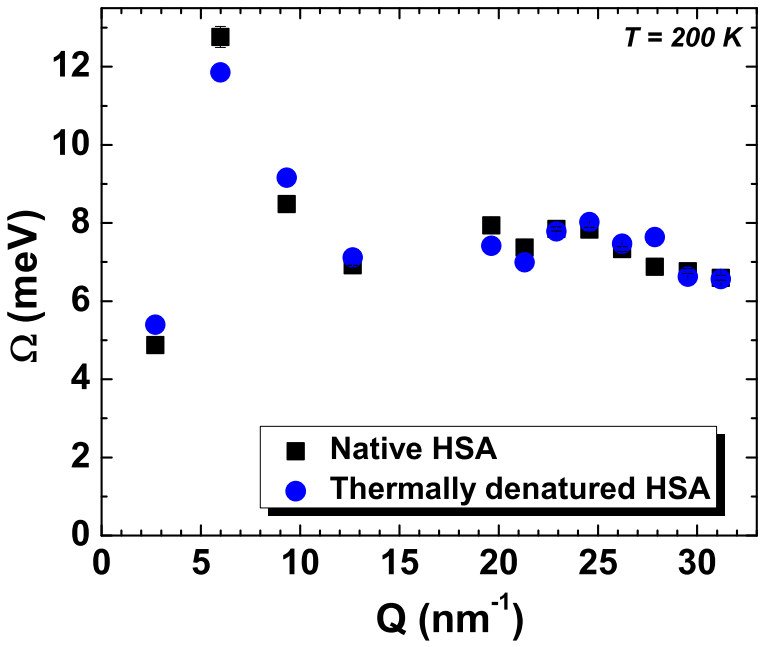

Figure 5.14: Phonon dispersion curves (Ω vs. Q) calculated from native HSA and thermally dentured samples with hydration level $h \sim 0.4$ at $T = 200$ K.

of peak **B** in the measured static structure factor data shown in Fig. 5.8 clearly indicates the characteristic change in the secondary structure of thermally denatured HSA. However, our experimental results show that despite denaturation of HSA, the collective excitations still exist, which is consistent with the results previously observed in denatured lysozyme [226]. Therefore, our results indicate that the phonon-like excitations exist and propagate even through the protein is denatured, which may come from the presence of increased content of beta-sheets and unfolded domains. However, the denaturation affects the softness of the protein at the physiological condition. At room temperature (300 K), we observed a significant decrease in the values of excitation energy at higher Q-values (localized collective mode) in the thermally denatured HSA compared to that of the native HSA, which clearly indicate

the increase in the softness of protein. Such increased softness is due to the breakdown of the weak bonds like hydrogen bonds, van der Waals interaction and salt bridges (that hold protein conformation in the native state) causing the unfolding of protein structure upon denaturation. However, at a much lower measured temperature $T = 200$ K as shown in Fig. 5.14, which is below the dynamic transition temperature and the protein is inactive or unfunctional [69, 189, 248], the dispersion curves in native and thermally denatured samples are identical. Thus, our results suggest that the protein may require certain degree of resillience for the enzymatic activity. If the protein becomes too soft at the room temperature as we observed in the thermally denatured sample, it may lose its biological function. Therefore, the dynamical property of protein such as softness (flexibility) and rigidity (resillience) are balanced by the biomolecules to accomplish their biological activities [249–251], which is schematically shown in Fig. 5.15.

Table 5.1: Longitudinal sound velocities calculated from the fitting of dispersion curves in the acoustic branch with Eq. 5.9.

Samples	v_L(m/s)	
	T = 200 K	**T = 300 K**
Native HSA (Expt. 1)	NA	2758 ± 50
Thermally denatured HSA (Expt. 1)	NA	2450 ± 73
Native HSA (Expt. 2)	3075 ± 69	2744 ± 91
HSA/warfarin (Expt. 2)	2715 ± 158	2809 ± 80
HSA/ibuprofen (Expt. 2)	3085 ± 66	2772 ± 194

Flexibility of HSA upon bound to drugs

HSA has very strong binding sites as the site I (subdomain II A) and site II (subdomain III A). These sites are the hydrophobic cavities capable of holding significant amount of

ligands or drugs [240]. Warfarin and ibuprofen are the drugs that strongly bind to the site I and site II respectively under the physiological conditions. In most of the cases, about 99% of these drugs are bound to the protein under the normal therapeutic environments [252]. Such strong binding affinity sites in HSA is an important property for pharmacokinetic behavior that influences the efficacy and delivery rate of the drugs. A recent study suggests that these drugs also have the ability to stabilize HSA structure and prevent against denaturation by chemical or thermal means [241]. Therefore, as expected, in our measured static structure factor $S(Q)$ (see Fig. 5.8), no significant differences are observed in the peak position between the native unbounded HSA and the drugs-bound HSA samples. Similarly, at the room temperature, there is no substantial difference in dispersion relation from the native HSA, HSA/warfarin and HSA/ibuprofen as shown in Fig. 5.12D. However, in Fig. 5.12 E and F, we can clearly see the softening of protein with the increase in temperature, as suggested by the decrease in the excitation energies at higher Q-values. These results indicate that the local structure and dynamic behavior of native HSA remain unaffected upon binding to drugs due to its strong binding affinity. Therefore, HSA acts as an efficient carrier and transporter of drugs in the plasma that is beneficial for pharmaceutical drug design and delivery.

5.2.4 Conclusion

We report the collective excitations in hydrated protein samples of native HSA, denatured HSA, and HSA bound to the drugs, warfarin and ibuprofen. The collective excitations are primarily due to the protein internal dynamics. However, the contribution of hydration water coupled to the protein surface is crucial for its dynamic activation and its effect on collective excitations cannot be ignored. Here we show both acoustic (propagating) and localized

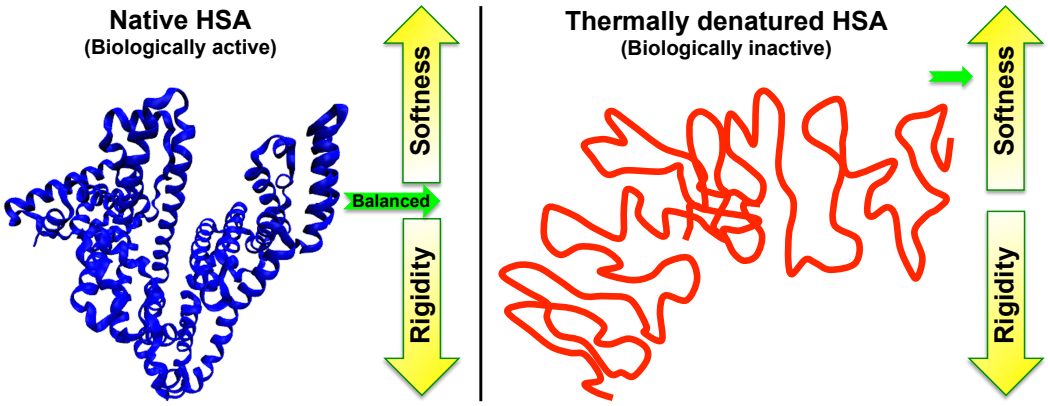

Figure 5.15: Schematic diagram of measure of softness and rigidity in native and denatured protein. (Left) Native structure of human serum albumin (PDB 1O9X), where the structural property, softness and rigidity are balanced by protein for biological function. (Right) Thermally denatured protein, which is softer than the native protein due to the breakdown of weak bonds such as hydrogen bonds, and van der Waals interaction, and loses its activity.

(non-propagating) modes of phonon exist in native and denatured HSA. The acoustic mode is due to the secondary or larger structures, whereas the localized excitations are due to the fluctuations of amino acid residues such as methyl groups. Remarkably, we found softening of localized phonons in denatured HSA compared to native HSA, due to the breakdown of weak forces like hydrogen bonds, van der Waals interaction and salt bridges causing the unfolding of the protein. Therefore, the protein structural property of flexibility and rigidity are balanced by the native protein for its activity. Furthermore, the drugs like warfarin and ibuprofen that have the high binding affinity to site I and site II of HSA respectively do not affect the protein structure in plasma, which is consistent with other crystallography study. Additionally, there is no significant change in protein dispersion curves upon binding to the drugs at room temperature. This result suggests that the dynamic properties of HSA such as collective excitations that are crucial for enzymatic activity in plasma is not affected by the drugs that are bound to HSA. Moreover, these results also confirm that the

collective excitations in protein are highly structure-dependent, similar to glass formers. Any changes in protein local or global conformation can significantly affect its dynamic behavior and therefore its function and activity. Overall, we propose the idea of protein softness (flexibility) and rigidity defined in terms of collective excitations that can be further used as a novel approach to understand the protein activity.

CHAPTER 6 CONFORMATION OF PBP BOUND TO PEPTIDE

6.1 Introduction

Periplasmic ligand-binding proteins (PBP) of gram-negative bacteria and the homologous membrane bound lipoproteins of gram-positive bacteria, along with their cognate membrane embedded permeases, constitute a large class of active transport systems that are responsible for the uptake of sugars, amino acids, anions, peptides and other nutrients [253]. The PBPs have a high specificity for their ligands, with the range of 0.1 M for amino acids and 1 M for sugars, and are the major determinant of transporter specificity [254]. Some of the periplasmic binding proteins also play a role in bacterial chemotaxis by binding to inner membrane receptors.

The three-dimensional X-ray crystal structures of several PBPs have been determined with and without ligands bound. Although they do not share significant amino acid sequence identity, members of the PBP protein family share a bilobed structure with two relatively rigid domains connected by a hinge region that facilitates their movement relative to each other. In the absence of ligand, the protein is in an extended or open conformation. The ligand binds in a deep cleft between the two lobes, bringing the two lobes together in a large conformational change to enclose the ligand in a mechanism similar to a Venus flytrap [255]. Although the open form of the binding proteins exposes a solvent accessible cleft, the closed form encloses the bound ligand in a protected protein interior completely inaccessible to the bulk solvent. This large conformational change upon ligand binding is essential for the recognition of the PBPs by their respective membrane-bound components because it is the ligand bound closed form that is recognized by transporters and chemotaxis receptors.

Residues that interact with the transporter or receptor cluster in patches on the two lobes of the binding protein. The patches are brought near each other due to the conformational change when ligand binds.

Escherichia coli murein peptide permease A (MppA) is the PBP that is required for the uptake of the murein tripeptide, L-alanyl-γ-D-glutamyl-meso-diaminopimelate, (L-Ala-γ-D-Glu-meso-Dap), which is generated by the breakdown of the cell wall and enables the recycling of the cell wall peptides [256]. This unusual peptide contains an L-Ala linked to a D-Glu, and the D-Glu has a γ-linkage to meso-Dap. MppA is a 58 kDa protein that shares overall sequence identity of 46% with the oligopeptide-binding protein OppA and 29% identity with the dipeptide binding protein DppA. It is not found in its own transport operon but uses the oligopeptide permease or the dipeptide permease for transmembrane transport of its ligand [257].

The X-ray crystal structure of MppA with the bound murein tripeptide was recently reported [258]. In order to gain further insight into the conformational changes associated with ligand binding, we have studied the structures of ligand-free and ligand-bound E. coli MppA using small-angle X-ray scattering technique. SAXS data show no significant change in protein conformation upon bound to the peptide. On the other hand, the structure of MppA in aqueous solution calculated using *ab-initio* method closely matches its crystal structure.

6.2 Materials and methods

6.2.1 Sample preparation

The 6-His tagged MppA E. coli strain JM109 harboring the plasmid pQE60, which encodes MppA with a C-terminal 6-histidine tag, was expressed and purified in Prof. Jeffery Constance lab, University of Illinois at Chicago. 2xYT broth with 50 g/mL ampicillin was inoculated with overnight cultures (1:20 dilution) and grown at 37 ^{o}C until the cells reaches an O.D$_{600}$ of 0.4. MppA expression was then induced with 1.0 mM isopropyl--D-thiogalactopyranoside (IPTG). The cultures were grown for four more hours at 25 ^{o}C and then harvested by centrifugation. The cell pellet was washed once in 100 mM Tris-HCl, pH 7.6, and frozen at -80 ^{o}C until further use. The cells were re-suspended in 100 mM Tris-HCl, pH 7.6 (binding buffer), and lysed by sonication. The cell suspension was centrifuged at 10,000 x g for 30 minutes to remove cell debris. The cleared lysate was incubated with Ni-NTA beads (Qiagen), which were pre-equilibrated with binding buffer, for two hours at 4 ^{o}C with gentle agitation. The beads were washed with eighty column volumes of binding buffer followed by ten column volumes of wash buffer (0.3 M NaCl, 0.1 M $KHPO_4$, pH 7.0, 10 mM imidazole, 5% glycerol). The protein was eluted with five column volumes of elution buffer (0.3 M NaCl, 0.1 M $KHPO_4$, pH 7.0, 0.5 M imidazole, 5% glycerol). The buffer was then changed to 100 mM Tris-HCl, pH 7.6, by dialysis. This was followed by an ammonium sulfate precipitation step in which 55% ammonium sulfate saturation was obtained by gradually adding solid ammonium sulfate with constant stirring on ice. The resulting solution was centrifuged at 12,000 rpm (17211 x g) for 30 mins, and the pellet was discarded. Additional ammonium sulfate was added to the supernatant to achieve 80% saturation, and

the solution was centrifuged again. MppA is obtained in the pellet fraction. The pellet was re-suspended in 100 mM Tris-HCl, pH 7.6, and dialyzed overnight against the same buffer to remove ammonium sulfate. This fraction, which usually contained almost pure MppA, was concentrated by ultrafiltration to 10 mg/mL concentration by using spin concentrators. The protein was visualized by SDS-PAGE on a 12% polyacrylamide gel. Finally, for the SAXS measurements, the protein concentration was made ∼1 mg/ml.

6.2.2 Small-angle X-ray scattering measurements

SAXS measurements on the MppA samples were done on the BioCAT undulator beamline 18-ID at the Advanced Photon Source, Argonne National Laboratory. About 120 μL of protein solution were housed in a water-jacket flow cell maintained at 4 ^{o}C and exposed to focused X-ray beam of 12 keV using a syringe pump 3 m from the detector. This minimized the radiation damage and covered the q-range of 0.006 - 0.48 Å^{-1}. The 3-seconds frame of scattering data were collected for 550 times for each sample and the corresponding buffer for background subtraction. Each measured frame was checked carefully for radiation damage and the best data were choseen for the averaging. The average scattering curves, $I(q)$ were normalized to the intensity of the incident X-ray beam.

6.3 Results and discussion

The SAXS intensity profiles of MppA and MppA-peptide in the q-range of 0.01 Å^{-1} - 0.3 Å^{-1} are shown in Fig. 6.1 A and B respectively. The high quality data of sample concentration of ∼1 mg/ml show no sign of aggregation as confirmed by the zero-slope at the low q-values. For the low-resolution three-dimensional structure determination of protein conformation, the overall shape-parameters are calculated from the measured scattering curves such as forward scattering intensity ($I(0)$), radius of gyration, R_g (mean square distances

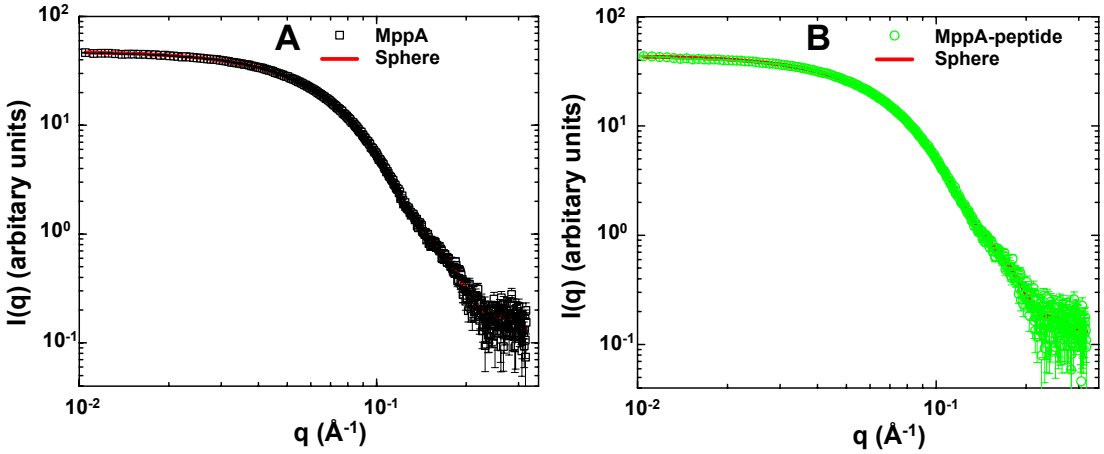

Figure 6.1: SAXS intensity profiles of (A) MppA and (B) MppA-peptide. The solid red curves are the fitting of intensities with spherical form factor, which best fit the data.

from the center of mass weighted by electron densities), shape and the maximum dimension of the protein in solution. The determination of such parameters is described in the following sections below.

6.3.1 Guinier analysis

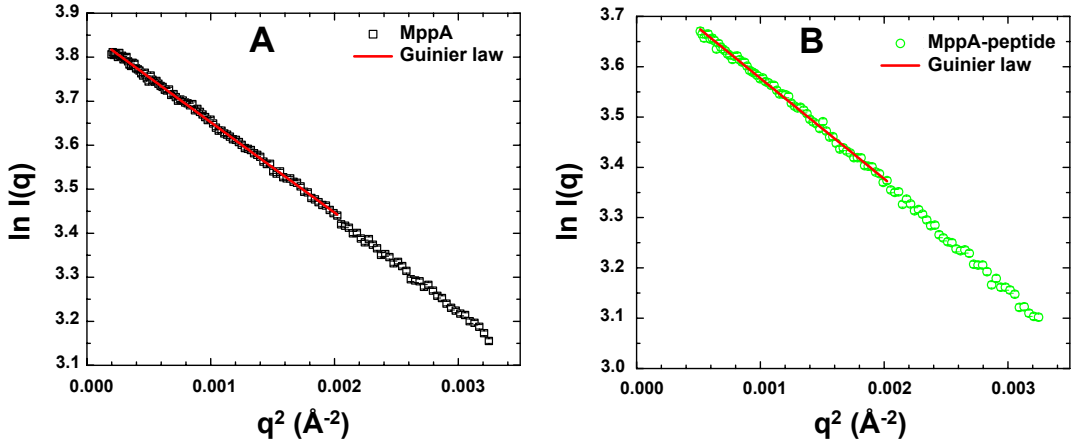

Figure 6.2: Guinier plots for (A) MppA and (B) MppA-peptide. The solid red curves are the Guinier fits, where the slope gives the radius of gyration (R_g) of the monodisperse particle.

For the monodisperse solution of globular particles, the radius of gyration is determined

by Guinier analysis as expressed in Eq. 6.1 below [59],

$$I(q) \approx I(0)e^{-R_g^2 q^2/3} \tag{6.1}$$

The slope of the linear region of a Giunier plot, $\ln I(q)$ vs. q^2 provides the value of R_g such that $q_{max}R_g$ <1.3. The Guinier analysis of MppA and MppA-peptide are shown in Fig. 6.2. We found the values of R_g are 24.8± 0.1 Å and 24.5± 0.1 Å for MppA and MppA-peptide, not a significant change upon binding of MppA with the peptide.

6.3.2 Kratky analysis

The dimensionless Kratky plot ($I(q)(qR_g)^2/I(0)$ vs. qR_g) as shown in Fig. 6.3 is carried out to determine the degree of compactness or folding/unfolding of the protein conformation [259]. This analysis distinguishes the fully or partially unfolded protein structure. In general, a globular folded protein conformation shows a bell-shaped profile between 0< qR_g <3 with a single pronounced maximum at qR_g ∼1.7 regardless of the size of the protein [259]. The dimensionless Kratky plots of MppA and MppA-peptide clearly show the feature that confirms the folded protein structure in solution.

6.3.3 Pair distance distribution function

The radius of gyration calculated from Guinier approximation has a limitation that it does not take into account of the data of whole q-range [59, 259]. Thus, in order to validate, the R_g and $I(0)$ is also calculated from the indirect Fourier transform methods, which yields

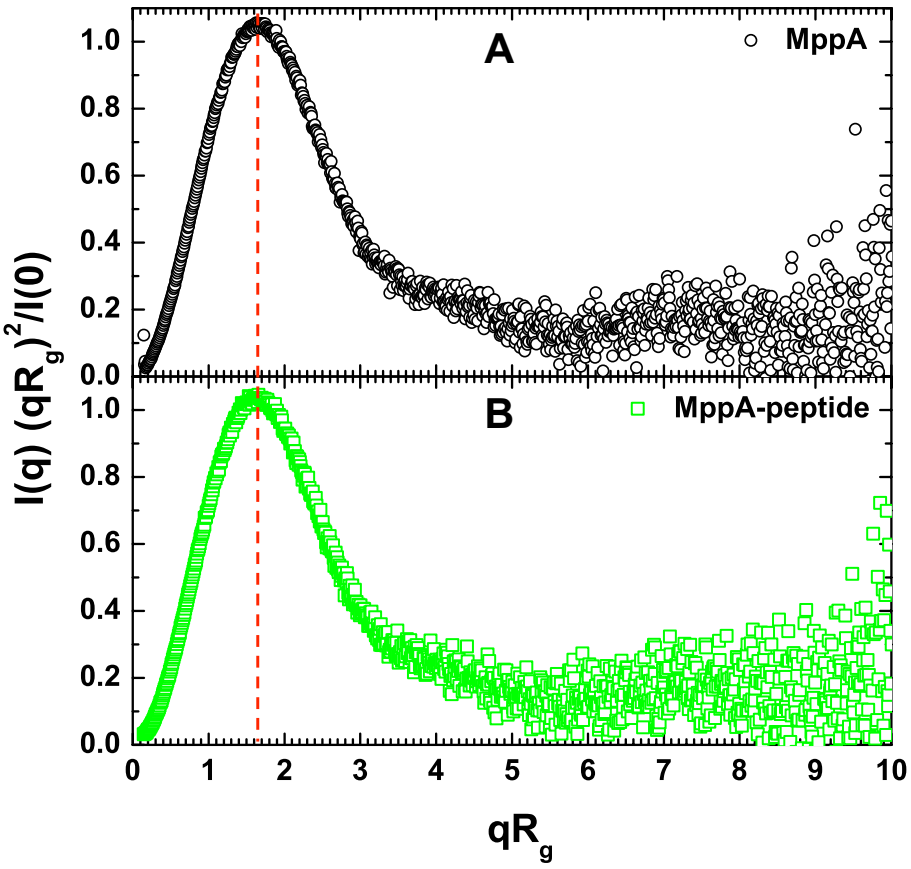

Figure 6.3: Kratky plots for (A) MppA and (B) MppA-peptide, which has the bell-shaped feature in the range $0< qR_g <3$ with maximum at $qR_g \sim 1.7$. These plots strongly confirms that the protein has compact folded structure in solution.

the pair distance distribution function, $P(r)$ given by Eq. 6.2,

$$P(r) = \frac{r^2}{2\pi^2} \int_0^\infty q^2 I(q) \frac{sin(qr)}{qr} dr \tag{6.2}$$

$P(r)$ provides the information about the distribution of interatomic distances in macromolecules, which in turn reflects the overall shape of the particle in solution. The different shapes such as sphere, cylinder, rod-like and elliptic are characterized by unique shape of $P(r)$ function. For instance, globular particles yield a bell-shaped $P(r)$ function with a max-

imum at $r = D_{max}/2$, where r is the approximate radius of the particle having maximum dimension D_{max}. On the other hand multi-domain particles yield $P(r)$ curve with multiple shoulders and oscillations, which correspond to the inter- and intra-subunit domains in macromolecule. Here, the calculated $P(r)$ from the intensity profiles of MppA and MppA-peptide as shown in Fig. 6.4 show a bell-shaped curve with maximum at $r = 29.54$ Å with $D_{max} = 77.75$ Å and $r = 29.77$ Å with $D_{max} = 74.43$ Å, respectively. This clearly indicates both the samples have spherical shape as true for globular proteins. The calculated values of real space R_g and $I(0)$ are almost similar to that calculated from the Guinier analysis as listed in Table 6.1.

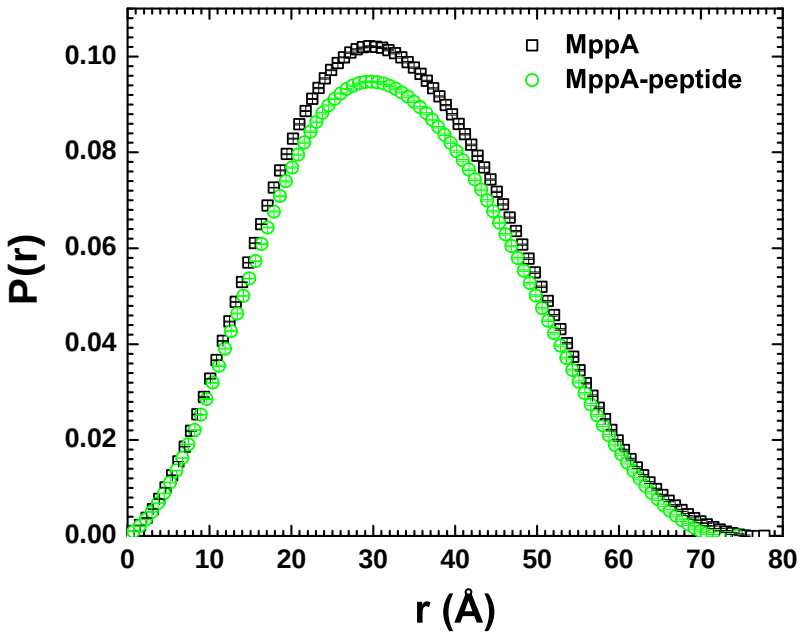

Figure 6.4: Pair distance distribution functions of MppA and MppA-peptide. The bell-shaped curves with maximum at 'r' represent the spherically shaped globular protein having radius 'r'.

Table 6.1: Radius of gyration of MppA and MppA-peptide calculated from Guinier and P(r) analysis.

	R_g (Å)	
	Guinier analysis	P(r) analysis
MppA	24.8±0.1	25.28±0.02
MppA-peptide	24.5±0.1	25.08±0.02

6.3.4 *Ab-initio* modeling

The low-resolution 3D structure of MppA and MppA-peptide from 1D SAXS intensity profiles are determined from the SAXS data using *ab-initio* method of automated bead modeling [259]. It can be done using the program dummy atom model minimization (DAMMIN) or dummy atom model minimization fast (DAMMIF) available in the small-angle scattering data analysis software ATSAS to reconstruct the 3D envelope of the protein structure. This program considers the algorithm of a collection of M (>>1) number of densely packed beads inside a constrained spherical search volume. The constrained search volume is predetermined from the real space R_g and D_{max} as calculated from $P(r)$ analysis of experimental SAXS intensity profile. The particle structure is described by the binary string X of length M, where each of the bead is randomly assigned to the solvent or solute. The simulated annealing is used to start the reconstruction of the shape of the particle by minimizing the value of χ^2, which is achieved from the best fit of experimental scattering intensity by the calculated scattering intensity. The χ^2 to measure the discrepancy is expressed as,

$$\chi^2 = \frac{1}{N-1}\sum_{i=1}^{N}\left(\frac{I_{exp}(q_i) - cI_{cal}(q_i)}{\sigma(q_i)}\right)^2 \tag{6.3}$$

where N is the number of data points, σ is the uncertainty (or standard deviation), and c is the scaling factor.

The reconstruction of 3D structure from *ab-initio* model is limited by the assumption of a

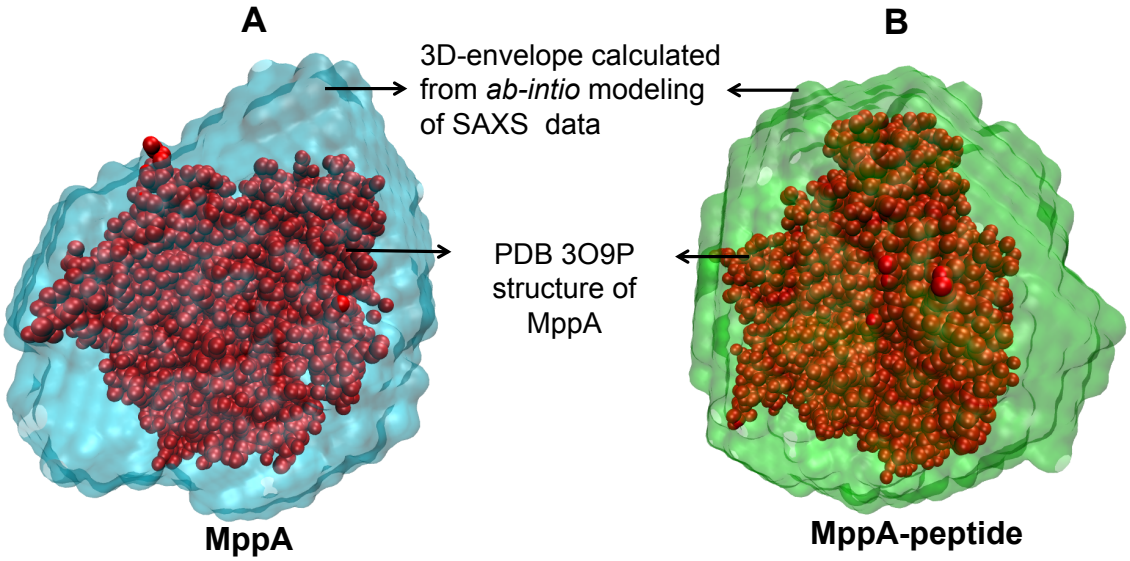

Figure 6.5: 3D reconstruction of (A) MppA and (B) MppA-peptide from measured SAXS data using the programs DAMMIF, SUPCOMB and DAMAVER in software package ATSAS.

uniform electron density within the particle, which is only based on the fitting the scattering profile below q ~0.3 Å^{-1}. Each run gives the low-resolution 3D envelope of the particle, which is repeated for about 10 to 20 times. In addition, each 3D envelope is superimposed to the known high-resolution crystal structure of the particle. The superposition of the ensemble of calculated envelope is carried out by another program SUPCOMB available in ATSAS. Once all the 3D envelopes are superpositioned, then the average of all the envelopes is determined by the program DAMAVER, also available in the same software package. Finally, the low-resolution 3D structure of particle is determined from the *ab-initio* modeling. Here, we implemented DAMMIF, which is followed by SUPCOMB and DAMAVER to determine the

3D conformation of MppA and MppA-peptide as shown in Fig. 6.5. Since the *ab-initio* reconstruction is considered as a low-resolution, we do not see significant change in 3D envelope calculated from MppA-peptide SAXS data from MppA. It can also be possible that there may be very small conformational change in MppA structure, which is beyound the instrumental resolution. Strictly speaking, the change may of the order of few angstroms. However, the 3D envelope determined from the *ab-initio* modeling perfectly matches the 3D crystal structure of MppA [258].

6.4 Conclusion

In this work, we investigated the ligand-free and ligand-bound conformation of MppA. The measured SAXS data is used to reconstruct the 3D envelope of the samples from *ab-initio* modeling using the programs DAMMIF, SUPCOMB and DAMAVER available in the software package ATSAS. The analysis of the SAXS data do not show any significant conformational change in MppA upon bound to the peptide. This may be due to the very small conformational change of the order of few angstroms, which is not accessible within instrumental resolution. On the other hand, the 3D resconstruction of MppA structure from the intensity of SAXS measurement under physiological condition almost matches its crystal structure.

CHAPTER 7 SUMMARY AND OUTLOOK

In this chapter, I will briefly summarize and discuss the different experimental results from the study of protein's conformation and dynamics using neutron and X-ray scattering.

Although there are several other techniques such as X-ray/neutron crystallography, solid-state nuclear magnetic resonance (NMR), and atomic-force microscopy (AFM), Raman spectroscopy, dielectric spectroscopy,and terahertz spectroscopy to study the protein structure and dynamics, we showed that neutron and X-ray scattering are equally powerful techniques to study the structure-dynamic-function correlation, which provided a new insight to understand the enzyme activity. The property of right wavelength and momentum transfer of X-ray and neutron are the key to probe the structure and dynamic phenomena at atomic/molecular length scale, which are not quite accessible to other techniques. Specifically, neutron scattering has a great advantage due to its unique capability to 'see' mainly the hydrogen atoms, which is enormously present in all the biomolecules.

7.1 Struture of biomolecules at physiological conditions

One of the major challenges is to study the biomolecular structure at native environment. So far a large number of crystal structures of protein, RNA, DNA and other biomolecules have been revealed, which has played a vital role in understanding their biological functions. However, the crystal structures do not possess the native conformation. In addition, biomolecules are inactive in the absence of water and the crystal structure ignores the interaction with hydration water. Moreover, it is not easy to crystallize the protein, particularly the membrane proteins. Therefore, taking into consideration of above concerns, we studied the protein structures in aqueous solution, which are very close to their native environment.

For instance, in chapter 4, we demonstrated the study of the membrane protein, rhodopsin in aqueous solution using detergents that mimics the native membrane-like environment. SAXS data from protein-detergent complex (PDC) in solution are quite tough to analyze. It is because 1D intensity profile includes the coupled signals from detergent and protein. Moreover, the contribution from free detergent micelles is very difficult to deal with. We followed the idea of Lipfert et al. and found insignificant effect of free detergent micelles in the SAXS signal [156, 160]. Then, we used some theoretical shape model function to extract the shape and size of PDC in solution. This method provided the information that the detergent micelles of CHAPS and DDM form a belt of corona around the rhodopsin and hence solubilize and stabilize the rhodopsin in its native conformation. According to SAXS results, we characterize the amount of detergent needed to preserve the native conformation of rhodopsin in aqueous solution. However, the mechanism of photoactivation of rhodopsin cannot be studied using SAXS method. Therefore, we used the contrast match SANS technique to eliminate the signal of detergent micelles surrounding the rhodopsin. SANS results revealed the activation mechanism in rhodopsin, which is quite different than what have been observed in its crystal form. The quantitative analysis of SANS data indicate that the rhodopsin active structure has the radius of gyration larger by about 9 Å compared to its inactive conformation. Further, it suggests the oligomerization of rhodopsin in PDC. This result is consistent with other reported results of rhodopsin in its native membrane. Specifically, we propose the two dimers densely packed together to form a tetramer in PDC. Such oligomerization is crucial for the rapid activation of its cognate G protein, transducin. Therefore, it should be noted that SAXS and SANS cannot be just considered as complementary tools to other methods. Regardless of low-resolution information, SAXS and SANS provided

the information about the arrangement of rhodopsin-detergent complex and the mechanism of rhodopsin activation, which was not reported before. Similarly, in chapter 6, we used SAXS technique to investigate the conformational change in periplasmic ligand-binding proteins, MppA upon bound to peptide. Due to low resolution of SAXS, the measurements do not show any significant change in MppA structure, when it is bound to the peptide. However, the 3D reconstruction of MppA conformation calculated using *ab-intio modeling*, perfectly matches it crystal structure.

7.2 Significance of β-relaxation dynamics of proteins

Although the biological processes such as the enzyme catalysis and ligand binding are slow phenomena occurring in the time range of few microseconds to milliseconds, the fast motion in the time scale of few picoseconds to nanoseconds, also known as β-relaxation dynamics are crucial for biological functions. The β-relaxation dynamics provides the necessary conformational flexibility to protein, as a result of which, slow processes take place. Quasi-elastic neutron scattering (QENS) is the unique tool to probe the β-relaxation dynamics in protein since this technique measures the single-particle correlation function of hydrogen atom in protein, where more than 50% of the atoms in protein is hydrogen.

Using QENS, we studied the β-relaxation dynamics of deep-sea hyperthermophilic protein and model mesophilic protein mimicking the similar environment deep under the sea. The β-relaxation dynamics revealed that the hyperthermophilic protein from deep-sea preserves its conformational flexibility and maintain its enzymatic activity under high pressure and temperature, which is supposedly due to its highly symmetric and closed oligomeric structure. On the other hand, the mesophilic protein loses its conformational flexibility and physiological dynamic behavior under such extreme conditions due to pressure-driven vol-

ume reduction of intramolecular spacing. Furthermore, the β-relaxation dynamics revealed the mechanism of activation of G-protein-coupled receptor induced by retinal cofactor. Such dynamics show a broadly distributed relaxation of hydrogen atom dynamics in membrane protein, rhodopsin crucial for biological activity, as only observed for globular proteins previously. Interestingly, the QENS results indicate the significant differences in the intrinsic protein dynamics of the dark-state rhodopsin versus the ligand-free apoprotein, opsin, which is due to the influence of the covalently bound retinal ligand. As a novel approach, we introduced the idea of β-relaxation dynamics to construct a generic free-energy landscape that explains the dynamical properties of thermophilic protein under high pressure and temperature, and the intrinsic dynamics of ligand-bound and ligand-free conformations of GPCR.

7.3 Implications of collective vibrations to enzyme function

Another major challenge in protein science is to understand the correlation between the rapid fluctuations of the order of femtoseconds and enzyme catalysis, which is very less understood. Therefore, the collective excitations due to the protein secondary structure have been of considerable interest in the past few years. With the use of state-of-the-art inelastic neutron and X-ray scattering techniques, we studied and revealed the glass-like low-frequency collective excitations in protein. Such excitations provide the notion of protein softness and flexibility that are ultimately related to the activity of protein. The data suggested the existence of both propagating and non-propagating collective modes exist in protein on the length scale larger and shorter than the protein secondary structure, respectively that help to overcome the conformational barrier, crucial for enzyme catalysis. The apparent softening of protein with rise in temperature revealed the conformational flexibility for biological activity. In addition, the results showed that the collective excitations

are structure-dependent as confirmed by the analogous behavior of static structure factor and phonon dispersion curves with respect to temperature and hydration. Furthermore, the non-propagating localized phonon-like excitations suggest that the protein becomes softer due to breakdown of weak non-covalent bonds (responsible for preserving the native conformation) upon thermal denaturation. Thus, these results provide the notion that the protein requires necessary rigidity along with flexibility for the enzyme activity.

APPENDIX A COMPARISON OF SAXS INTENSITY OF PDC

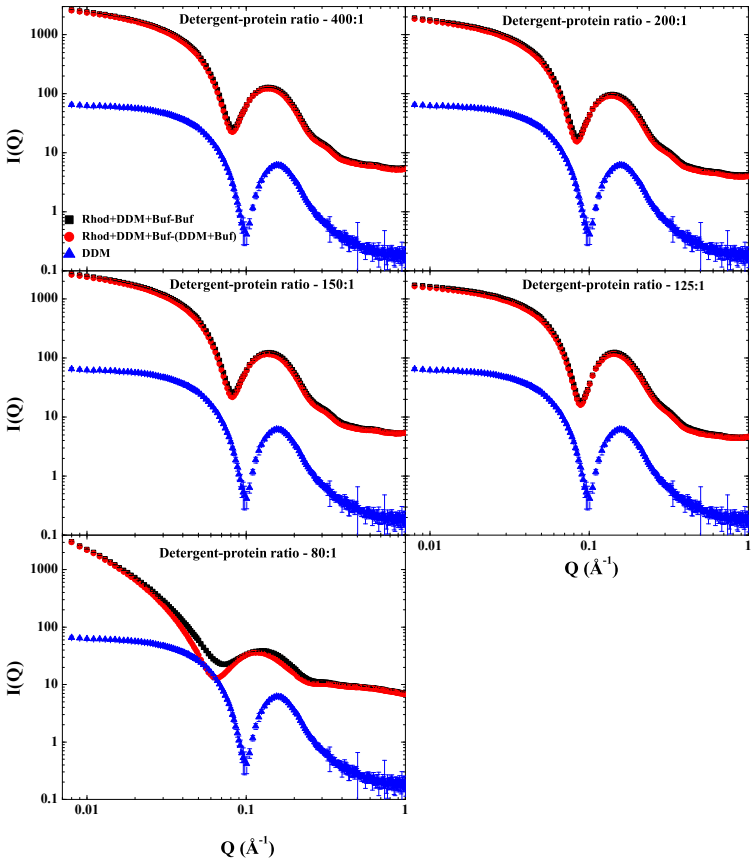

Figure A.A.1: Comparison of SAXS intensities calculated by subtracting the buffer and buffer plus detergent signal from the protein-detergent complex (PDC), which indicates that the intensity of buffer and buffer plus detergent is much low compared to that of PDC.

APPENDIX B INS RAW DATA FROM GFP

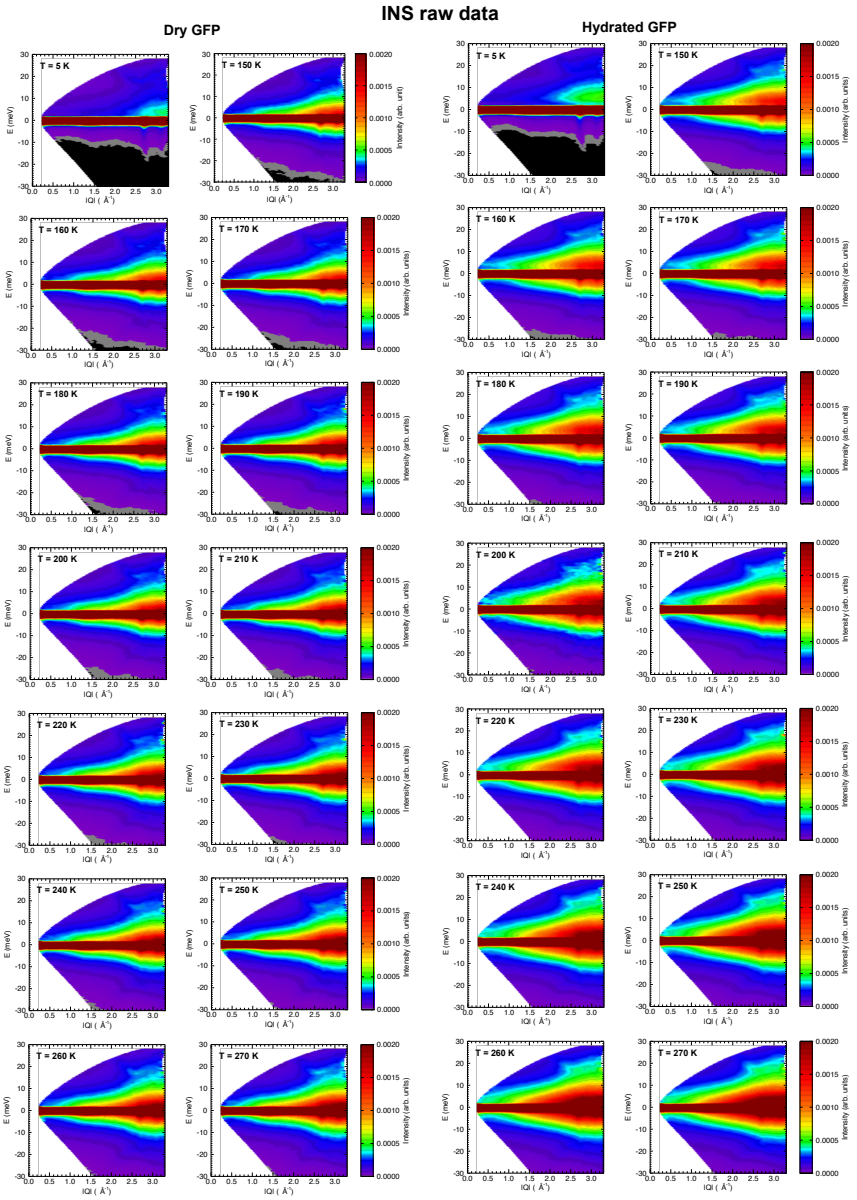

Figure A.B.1: The contour plots of inelastic neutron scattering (INS) raw data collected from dry and hydrated samples of green fluorescent protein (GFP) at all the measured temperatures from 150 K to 270 K with temperature step of 10 K.

APPENDIX C PROJECTS NOT INCLUDED ON THIS DISSERTATION

C.1 Role of Antifreeze Glycoproteins in Preventing Ice-formation

C.1.1 Scientific importance

Antifreeze glycoproteins (AFGPs) are the important biological complex and a novel set of proteins that can prohibit the formation of ice. The AFGPs can be extracted from the blood plasma of Antarctic notothenioid and northern cod. These proteins consist of the repeating tripeptide units of (Ala-Ala-Thr)n with little sequence alteration. The basic purpose of these types of proteins is to help the fish to endure in subzero temperature. The blood serums of these fish become frozen at -2 ^{o}C that is 1 ^{o}C below the melting point and create the non-equilibrium, termed as thermal hysteresis (TH). TH is responsible for the activity of these proteins. It is observed that threonine residues in Antifreeze protein (AFP) play a significant role and their hydroxyl groups might be responsible for the high interaction of AFP to the ice crystals [260–262]. Besides the academic point of view, numerous biomedical and commercials applications are there to justify the study of the AFGPs for a detailed understanding of its unique characteristics. For example, its understanding can be enormously helpful for prohibiting the recrystallization of ice, synthesizing new cryoprotectants for the conservation of tissues, cells and food storage [263]. We recently studied the protein dynamics to see whether and how these AFGPs behave above and below the ice-point temperature compared to other proteins.

C.2 Interaction of Water and Biomolecules with Nanodiamond Surfaces

C.2.1 Scientific importance

Diamond is an outstanding material in many respects. Moreover, nanodiamond (ND) inherits the most of the superior properties of bulk diamond and delivers them at the nanoscale. These properties include superior hardness and Young's modulus, biocompatibility, optical properties and fluorescence due to Nitrogen-Vacancy (NV) centers, high thermal conductivity, electrical resistivity, chemical stability, and the resistance of ND to harsh environments [264]. In past years, scientists have explored the potential of ND for biomedical applica-

tions, such as protein mimics [264] and drug delivery in cancer treatment [265]. The ND has excellent properties needed for drug delivery platform, such as high biocompatibility, the ability to carry a broad range of therapeutics, dispersibility in water and scalability, and the potential for targeted therapy - possibly in combination with imaging [264]. The large and fully available surface of ND particles, terminated with a large number of tunable functional groups, enables high drug loadings through different mechanisms ranging from adsorption to covalent binding. Showcasing bovine serum albumin (BSA), it has been recently shown [266] that the surface functional groups are a key parameter for the protein sorption behavior in template carbon nanotubes with controlled diameter. However, for a practically important drug delivery system such as ND, current literature lacks systematic studies of the interactions among ND surfaces, biomolecules, and water which are imperative to establish a basic understanding of the mechanisms that will determine and limit the biomedical application of ND [267]. Recent advances in purification, deagglomeration, and surface modification of NDs [264] open new exciting possibilities for studying the biomolecules-carbon nanoparticle interactions using ND as a model nanomaterial composed of stable, nearly spherical particles, fully tunable surface chemistry, and with a great potential for biomedical applications. As the first step, we used the quasi-elastic neutron scattering to understand the interaction of hydration shell with the ND surfaces.

C.3 Dynamics of tRNA and its Hydration Water on 3D Graphene Foams

C.3.1 Scientific importance

Three Dimensional (3D) graphene foams (3D-GFs) are graphene-based composites and macroscopic structures, which can be fabricated by template-directed chemical vapor deposition (CVD) method [268]. 3D-GFs have a macroscopic foam-like appearance and are highly compressible and ultralight due to their unique structure assembled from 2D graphene sheets [269]. Different from structures formed with small pieces of chemically derived graphene sheets, CVD grown 3D-GF is a monolith of a graphene network, and all the graphene sheets within 3D-GF are in direct contact with each other without breaks, but at the same time

are well separated [268]. Therefore, the charge carriers can move rapidly with a low barrier through the continuous CVD graphene building blocks [268, 269]. Up to now, 3D-GF has shown extraordinary electrical and mechanical properties and has been utilized in electronics and energy storage/conversion systems [268, 270]. The recent study has reported that 3D-GFs offer a powerful platform for neural stem cells research, neural tissue engineering, and neural prostheses [271]. Although 3D-GF is a relatively new material and its biomedical applications are still under investigation, graphene-based nanomaterials have been successfully demonstrated as biocompatible materials in a broad range of biomedical applications, including biosensing, bioimaging, drug/gene delivery, and cell culture scaffolds [272, 273].

The drug delivery functionality of nanomaterials is highly impacted by the interactions between biomolecules and nanomaterial surfaces. Nanomaterials in contact with biological fluids are covered by a selected group of biomolecules to form a corona that interacts with biological systems [274, 275]. Using bovine serum albumin (BSA), it has been recently shown [266] that the surface functional groups are a key parameter for the protein adsorption behavior in template carbon nanotubes with controlled diameter. However, the study of the structure and dynamics of the corona interface remains challenging and no traditional methods at present can resolve the puzzle [275]. Recently, we studied the dynamic behavior of tRNA on the surface of 3D-GFs in the presence of hydration shell using quasi-elastic neutron scattering technique.

REFERENCES

[1] A. Kessel and N. Ben-Tal. Introduction to proteins: Structure, function, and motion. *CRC Press*, 2011.

[2] J. M. Berg, J. L. Tymoczko, and L. Stryer. Biochemistry, Fifth Edition. *W. H. Freeman*, 2002.

[3] E. Buxbaum. Fundamentals of protein structure and function. *Springer International Publishing*, 2015.

[4] G. A. Petsko and D. Ringe. Protein structure and function. *New Science Press*, 2004.

[5] R. E. Dickerson and I. Geis. The structure and action of proteins. *Harper & Row*, 1969.

[6] https://en.wikipedia.org/wiki/Amino*acid*/*mediaFile*:*Proteinprimarystructure.svg*.

[7] http://oregonstate.edu/instruction/bi314/summer09/Fig-02-19-0.jpg.

[8] http://cen.xraycrystals.org/lysozyme.html.

[9] http://www.wikidoc.org/index.php/File:Catalase*Structure.png*.

[10] J. A. McCommon. Protein dynamics. *Rep. Prog. Phys.*, 47:1–46, 1984.

[11] S. Hay and N. S. Scrutton. Good vibrations in enzyme-catalysed reactions. *Nat. Chem.*, 4:161–168, 2012.

[12] P. K. Agarwal. Enzymes: An integrated view of structure, dynamics and function. *Microb. Cell Fact.*, 5:1–12, 2006.

[13] N. Boekelheide, R. Salomón-Ferrer, and T. F. Miller III. Dynamics and dissipation in enzyme catalysis. *Proc. Natl. Acad. Sci. U. S. A.*, 108:16159–16163, 2011.

[14] K. A. Henzler-Wildman, M. Lei, V. Thai, S. J. Kerns, M. Karplus, and D. Kern. A

hierarchy of timescales in protein dynamics is linked to enzyme catalysis. *Nature*, 450:913–916, 2007.

[15] U. Mayor, N. R. Guydosh, C. M. Johnson, J. G. Grossmann, S. Sato, G. S. Jas, S. M. V. Freund, D. O. V. Alonso, V. Daggett, and A. R. Fersht. The complete folding pathway of a protein from nanoseconds to microseconds. *Nature*, 421:863–867, 2003.

[16] M.-H. Seo, J. Park, E. Kim, S. Hohng, and H.-S. Kim. Protein conformational dynamics dictate the binding affinity for a ligand. *Nat. Commun.*, 5:3724, 1–7, 2014.

[17] E. Kim, S. Lee, A. Jeon, J. M. Choi, H.-S. Lee, S. Hohng, and H.-S. Kim. A single-molecule dissection of ligand binding to a protein with intrinsic dynamics. *Nat. Chem. Biol.*, 9:313–318, 2013.

[18] K. Henzler-Wildman and D. Kern. Dynamic personalities of proteins. *Nature*, 450:964–972, 2007.

[19] H. Frauenfelder, F. Parak, and R. D. Young. Conformational substates in proteins. *Ann. Rev. Biophys. Biophys. Chem.*, 17:451–479, 1988.

[20] A. Ramanathan, A. J. Savol, C. J. Langmead, P. K. Agarwal, and C. S. Chennubhotla. Discovering conformational sub-states relevant to protein function. *PLoS One*, 6:e15827, 2011.

[21] H. Frauenfelder, S. G. Sligar, and P. G. Wolynes. The energy landscapes and motions of proteins. *Science*, 254:1598–1603, 1991.

[22] M. Lagi, P. Baglioni, and S.-H. Chen. Logarithmic decay in single-particle relaxation of hydrated lysozyme powder. *Phys. Rev. Lett.*, 103:108102, 1–4, 2009.

[23] R. H. Austin, H. Frauenfelder, S. S. Chan, C. E. Schulz, W. S. Chan, G. U. Nienhaus,

and R. D. Young. The physics of proteins: An introduction to biological physics and molecular biophysics. *Springer New York*, 2010.

[24] J. A. Rupley, E. Gratton, and G. Careri. Water and globular proteins. *Trends Biochem. Sci.*, 8:18–22, 1983.

[25] J. A. Rupley and G. Careri. Protein hydration and function. *Adv. Protein Chem.*, 41:37, 1991.

[26] M. Tarek and D. J. Tobias. The dynamics of protein hydration water: A quantitative comparison of molecular dynamics simulations and neutron-scattering experiments. *Biophys. J.*, 79:3244–3257, 2000.

[27] X.-Q. Chu, M. Gajapathy, K. L. Weiss, E. Mamontov, J. D. Ng, and L. Coates. Dynamic behavior of oligomeric inorganic pyrophosphatase explored by quasielastic neutron scattering. *J. Phys. Chem. B*, 116:9917–9921, 2012.

[28] U. R. Shrestha, D. Bhowmik, J. R. D. Copley, M. Tyagi, J. B. Leão, and X.-Q. Chu. Effects of pressure on the dynamics of an oligomeric protein from deep-sea hyperthermophile. *Proc. Natl. Acad. Sci. U. S. A.*, 112:13886–13891, 2015.

[29] X.-Q. Chu, E. Mamontov, H. O'Neill, and Q. Zhang. Temperature dependence of logarithmic-like relaxational dynamics of hydrated tRNA. *J. Phys. Chem. Lett.*, 4:936–942, 2013.

[30] F. Gabel. Protein dynamics in solution and powder measured by incoherent elastic neutron scattering: The influence of Q-range and energy resolution. *Eur. Biophys. J.*, 34:1–12, 2005.

[31] S. Magazù, G. Maisano, F. Migliardo, and C. Mondelli. Mean-square displacement re-

lationship in bioprotectant systems by elastic neutron scattering. *Biophys. J.*, 86:3241–3249, 2004.

[32] J. D. Nickels, H. O'Neill, L. Hong, M. Tyagi, G. Ehlers, K. L. Weiss, Q. Zhang, Z. Yi, E. Mamontov, J. C. Smith, and A. P. Sokolov. Dynamics of protein and its hydration water: Neutron scattering studies on fully deuterated GFP. *Biophys. J.*, 103:1566–1575, 2012.

[33] P. W. Fenimore, H. Frauenfelder, B. H. McMahon, and F. G. Parak. Slaving: Solvent fluctuations dominate protein dynamics and functions. *Proc. Natl. Acad. Sci. U. S. A.*, 99:16047–16051, 2002.

[34] H. Frauenfelder, P. W. Fenimore, G. Chen, and B. H. McMahon. Protein folding is slaved to solvent motions. *Proc. Natl. Acad. Sci. U. S. A.*, 103:15469–15472, 2006.

[35] E. Mamontov, H. O'Neill, and Q. Zhang. Mean-squared atomic displacements in hydrated lysozyme, native and denatured. *J. Biol. Phys.*, 36:291–297, 2010.

[36] S. Khodadadi, J. H. Roh, A. Kisliuk, E. Mamontov, M. Tyagi, S. A. Woodson, R. M. Briber, and A. P. Sokolov. Dynamics of biological macromolecules: Not a simple slaving by hydration water. *Biophys. J.*, 98:1321–1326, 2010.

[37] A. P. Sokolov, J. H. Roh, E. Mamontov, and V. García Sakai. Role of hydration water in dynamics of biological macromolecules. *Chem. Phys.*, 345:212–218, 2008.

[38] S. Khodadadi and A. P. Sokolov. Protein dynamics: From rattling in a cage to structural relaxation. *Soft Matter*, 11:4984–4998, 2015.

[39] W. Doster, S. Cusack, and W. Petry. Dynamical transition of myoglobin revealed by inelastic neutron scattering. *Nature*, 337:754–756, 1989.

[40] J. H. Roh, J. E. Curtis, S. Azzam, V. N. Novikov, I. Peral, Z. Chowdhuri, R. B. Gregory, and A. P. Sokolov. Influence of hydration on the dynamics of lysozyme. *Biophys. J.*, 91:2573–2588, 2006.

[41] J. H. Roh, V. N. Novikov, R. B. Gregory, J. E. Curtis, Z. Chowdhuri, and A. P. Sokolov. Onsets of anharmonicity in protein dynamics. *Phys. Rev. Lett.*, 95:038101, 1–4, 2005.

[42] G. Zaccaï. How soft is a protein? A protein dynamics force constant measured by neutron scattering. *Science*, 288:1604–1607, 2000.

[43] G. L. Squires. Introduction to the theory of thermal neutron scattering. *Cambridge University Press*, Cambridge, 3^{rd} edition, 2012.

[44] M. Bée. Quasielastic neutron scattering: Principles and applications in solid state chemistry, biology, and materials science. *Adam Hilger*, 1988.

[45] P. Lindner and Th. Zemb. Neutron, X-ray and light scattering : Introduction to an investigative tool for colloidal and polymeric systems, volume 23. *North-Holland*, Netherlands, 1991.

[46] Th. Zemb and P. Lindner. Neutron, X-rays and light. Scattering methods applied to soft condensed matter. *North-Holland*, Netherlands, 2002.

[47] C. E. Blanchet and D. I. Svergun. Small-angle X-ray scattering on biological macromolecules and nanocomposites in solution. *Annu. Rev. Phys. Chem.*, 64:37–54, 2013.

[48] L. A. Feigin and D. I. Svergun. Structure analysis by small-angle X-ray and neutron scattering. Plenum Press, *New York and London*, 1987.

[49] T. Brückel, G. Heger, D. Richter, G. Roth, and R. Zorn. Neutron scattering. Lectures

of the JCNS laboratory course held at Forschungszentrum Jülich and the research reactor FRM II of TU Munich in cooperation with RWTH Aachen and University of Münster, volume 39. *Forschungszentrum Jülich GmbH*, 2012.

[50] F. Gabel, D. Bicout, U. Lehnert, M. Tehei, M. Weik, and G. Zaccaï. Protein dynamics studied by neutron scattering. *Q. Rev. Biophys.*, 35:327–367, 2002.

[51] M. Tehei, R. Daniel, and G. Zaccaï. Fundamental and biotechnological applications of neutron scattering measurements for macromolecular dynamics. *Eur. Biophys. J.*, 35:551–558, 2006.

[52] T. A. Harroun, G. D. Wignall, and J. Katsaras. Neutron scattering for biology, pages 1–18. *Springer Berlin Heidelberg*, Berlin, Heidelberg, 2006.

[53] A. Berthaud, J. Manzi, J. Pérez, and S. Mangenot. Modeling detergent organization around aquaporin-0 using small-angle X-ray scattering. *J. Am. Chem. Soc.*, 134:10080–10088, 2012.

[54] U. R. Shrestha, D. Bhowmik, S. M. D. C. Perera, U. Chawla, A. V. Struts, V. Graziano, S. Qian, W. T. Heller, M. F. Brown, and X.-Q. Chu. Small-angle neutron and X-ray scattering reveal conformational differences in detergents affecting rhodopsin activation. *Biophys. J.*, 108:39a, 2015.

[55] C. Sardet, A. Tardieu, and V. Luzzati. Shape and size of bovine rhodopsin: A small-angle X-ray scattering study of a rhodopsin-detergent complex. *J. Mol. Biol.*, 105:383–407, 1976.

[56] H. B. Osborne, C. Sardet, M. Michel-Villaz, and M. Chabre. Structural study of rhodopsin in detergent micelles by small-angle neutron scattering. *J. Mol. Biol.*,

123:177–206, 1978.

[57] A. J. Jackson. Introduction to small-angle neutron scattering and neutron reflectometry. *NIST Center for Neutron Research*, 2008.

[58] D. A. Jacques and J. Trewhella. Small-angle scattering for structural biology - expanding the frontier while avoiding the pitfalls. *Protein Sci.*, 19:642–657, 2010.

[59] M. H. J. Koch, P. Vachette, and D. I. Svergun. Small-angle scattering: A view on the properties, structures and structural changes of biological macromolecules in solution. *Q. Rev. Biophys.*, 36:147–227, 2003.

[60] D. I. Svergun and M. H. J. Koch. Small-angle scattering studies of biological macromolecules in solution. *Rep. Prog. Phys.*, 66:1735, 2003.

[61] C. Neylon. Small angle neutron and X-ray scattering in structural biology: Recent examples from the literature. *Eur. Biophys. J.*, 37:531–541, 2008.

[62] J. R. D. Copley and J. C. Cook. The disk chopper spectrometer at NIST: A new instrument for quasielastic neutron scattering studies. *Chem. Phys.*, 292:477–485, 2003.

[63] E. Mamontov and K. W. Herwig. A time-of-flight backscattering spectrometer at the Spallation Neutron Source, BASIS. *Rev. Sci. Instrum.*, 82:085109, 1–10, 2011.

[64] A. Meyer, R. M. Dimeo, P. M. Gehring, and D. A. Neumann. The high-flux backscattering spectrometer at the NIST Center for Neutron Research. *Rev. Sci. Instrum.*, 74:2759–2777, 2003.

[65] C. A. Orengo, A. E. Todd, and J. M. Thornton. From protein structure to function. *Curr. Opin. Struct. Biol.*, 9:374–382, 1999.

[66] H. Frauenfelder, G. Chen, J. Berendzen, P. W. Fenimore, H. Jansson, B. H. McMahon,

I. R. Stroe, J. Swenson, and R. D. Young. A unified model of protein dynamics. *Proc. Natl. Acad. Sci. U. S. A.*, 106:5129–5134, 2009.

[67] F. G. Parak and E. W. Knapp. A consistent picture of protein dynamics. *Proc.Natl. Acad. Sci. U. S. A.*, 81:7088–7092, 1984.

[68] H. Frauenfelder and D. T. Leeson. The energy landscape in non-biological and biological molecules. *Nat. Struct. Biol.*, 5:757–759, 1998.

[69] R. H. Austin, K. W. Beeson, L. Eisenstein, H. Frauenfelder, and I. C. Gunsalus. Dynamics of ligand-binding to myoglobin. *Biochemistry*, 14:5355–5373, 1975.

[70] J. N. Onuchic, Z. Luthey-Schulten, and P. G. Wolynes. Theory of protein folding: The energy landscape perspective. *Annu. Rev. Phys. Chem.*, 48:545–600, 1997.

[71] C. Hofmann, T. J. Aartsma, H. Michel, and J. Köhler. Direct observation of tiers in the energy landscape of a chromoprotein: A single-molecule study. *Proc. Natl. Acad. Sci. U. S. A.*, 100:15534–15538, 2003.

[72] A. Kitao, S. Hayward, and N. Go. Energy landscape of a native protein: Jumping-among-minima model. *Proteins: Struct., Funct., Genet.*, 33:496–517, 1998.

[73] L. Milanesi, J. P. Waltho, C. A. Hunter, D. J. Shaw, G. S. Beddard, G. D. Reid, S. Dev, and M. Volk. Measurement of energy landscape roughness of folded and unfolded proteins. *Proc. Natl. Acad. Sci. U. S. A.*, 109:19563–19568, 2012.

[74] X. Q. Chu, M. Lagi, E. Mamontov, E. Fratini, P. Baglioni, and S.-H. Chen. Experimental evidence of logarithmic relaxation in single-particle dynamics of hydrated protein molecules. *Soft Matter*, 6:2623–2627, 2010.

[75] F. A. A. Mulder, B. Hon, A. Mittermaier, F. W. Dahlquist, and L. E. Kay. Slow

internal dynamics in proteins: Application of NMR relaxation dispersion spectroscopy to methyl groups in a cavity mutant of T4 lysozyme. *J. Am. Chem. Soc.*, 124:1443–1451, 2001.

[76] V. Calandrini and G. R. Kneller. Influence of pressure on the slow and fast fractional relaxation dynamics in lysozyme: A simulation study. *J. Chem. Phys.*, 128:065102, 1–8, 2008.

[77] X.-Q. Chu, A. Faraone, C. Kim, E. Fratini, P. Baglioni, J. B. Leão, and S.-H. Chen. Proteins remain soft at lower temperatures under pressure. *J. Phys. Chem. B Lett.*, 113:5001–5006, 2009.

[78] A. Filabozzi, A. Deriu, M. T. Di Bari, D. Russo, S. Croci, and A. Di Venere. Elastic incoherent neutron scattering as a probe of high pressure induced changes in protein flexibility. *Biochim. Biophys. Acta*, 1804:63–67, 2010.

[79] K. Heremans and L. Smeller. Protien structure and dynamics at high pressure. *Biochim. Biophys. Acta*, 1386:353–370, 1998.

[80] E. Mamontov, H. O'Neill, Q. Zhang, and S. M. Chathoth. Temperature dependence of the internal dynamics of a protein in an aqueous solvent: Decoupling from the solvent viscosity. *Chem. Phys.*, 424:12–19, 2013.

[81] R. F. Tilton Jr. Effects of temperature on protein structure and dynamics: X-ray crystallographic studies of the protein ribonuclease-A at nine different temperatures from 98 to 320 K. *Biochemistry*, 31:2469–2481, 1992.

[82] G. K. Dhindsa, M. Tyagi, and X.-Q. Chu. Temperature-dependent dynamics of dry and hydrated beta-casein studied by quasielastic neutron scattering. *J. Phys. Chem.*

B, 118:10821–10829, 2014.

[83] R. Day, B. J. Bennion, S. Ham, and V. Daggett. Increasing temperature accelerates protein unfolding without changing the pathway of unfolding. *J. Mol. Biol.*, 322:189–203, 2002.

[84] N. N. Khechinashvili, J. Janin, and F. Rodier. Thermodynamics of the temperature-induced unfolding of globular proteins. *Prot. Sci.*, 4:1315–1324, 1995.

[85] F. Meersman, C. Atilgan, A. J. Miles, R. Bader, W. Shang, A. Matagne, B. A. Wallace, and M. H. Koch. Consistent picture of the reversible thermal unfolding of hen egg-white lysozyme from experiment and molecular dynamics. *Biophys. J.*, 99:2255–2263, 2010.

[86] H. Frauenfelder, N. A. Alberding, A. Ansari, D. Braunstein, B. R. Cowen, M. K. Hong, I. E. T. Iben, J. B. Johnson, S. Luck, M. C. Marden, J. R. Mourant, P. Ormos, L. Reinisch, R. Scholl, A. Schulte, E. Shyamsunder, L. B. Soremen, P. J. Steinbach, A. H. Xie, R. D. Young, and K. T. Yue. Proteins and pressure. *J. Phys. Chem.*, 94:1024–1037, 1990.

[87] V. V. Mozhaev, K. Heremans, J. Frank, P. Masson, and C. Balny. High pressure effects on protein structure and function. *Proteins: Struct., Funct., Genet.*, 24:81–91, 1996.

[88] M. Gross and R. Jaenicke. Proteins under pressure: The influence of high hydrostatic pressure on structure, function and assembly of proteins and protein complexes. *Eur. Biophys. J.*, 221:617–630, 1994.

[89] H. Li, H. Yamada, and K. Akasaka. Effect of pressure on the tertiary structure and dynamics of folded basic pancreatic trypsin inhibitor. *Biophys. J.*, 77:2801–2812, 1999.

[90] B. B. Boonyaratanakornkit, C. B. Park, and D. S. Clark. Pressure effects on intra- and intermolecular interactions within proteins. *Biochim. Biophys. Acta*, 1595:235–249, 2002.

[91] J. Roche, J. A. Caro, D. R. Norberto, P. Barthe, C. Roumestand, J. L. Schlessman, A. E. García, B. E. Garcia-Moreno, and C. A. Royer. Cavities determine the pressure unfolding of proteins. *Proc. Natl. Acad. Sci. U. S. A.*, 109:6945–6950, 2012.

[92] K. E. Prehoda, E. S. Mooberry, and J. L. Markley. Pressure denaturation of proteins: Evaluation of compressibility effects. *Biochemistry*, 37:5785–5790, 1998.

[93] N. Hillson, J. N. Onuchic, and A. E. García. Pressure-induced protein-foldingyunfolding kinetics. *Proc. Natl. Acad. Sci. U. S. A.*, 96:14848–14853, 1999.

[94] I. Daniel, P. Oger, and R. Winter. Origins of life and biochemistry under high-pressure conditions. *Chem. Soc. Rev.*, 35:858–875, 2006.

[95] K. O. Stetter. Hyperthermophiles in the history of life. *Philos. Trans. R. Soc. Lond., B, Biol. Sci.*, 361:1837–1843, 2006.

[96] E. Ohmae, C. Murakami, K. Gekko, and C. Kato. Pressure effects on enzyme functions. *J. Biol. Macromol.*, 7:23–29, 2007.

[97] R. C. Hughes, L. Coates, M. P. Blakeley, S. J. Tomanicek, P. Langan, A. Y. Kovalevsky, J. M. García-Ruiz, and J. D. Ng. Inorganic pyrophosphatase crystals from Thermococcus thioreducens for X-ray and neutron diffraction. *Acta Crystallogr. Sect. F Struct. Biol. Cryst. Commun.*, 68:1482–1487, 2012.

[98] M. L. Byrne-Steele and J. D. Ng. Expression, purification and preliminary X-ray analysis of proliferating cell nuclear antigen from the archaeon Thermococcus thioreducens.

Acta Crystallogr. Sect. F Struct. Biol. Cryst. Commun., 65:906–909, 2009.

[99] W. Carrillo, A. García-Ruiz, I. Recio, and M. V. Moreno-Arribas. Antibacterial activity of hen egg white lysozyme modified by heat and enzymatic treatments against oenological lactic acid bacteria and acetic acid bacteria. *J. Food Prot.*, 77:1732–1739, 2014.

[100] G. E. Matthyssens, G. Simons, and L. Kanarek. Study of the thermal-denaturation mechanism of hen egg-white lysozyme through proteolytic degradation. *Eur. J. Biochem.*, 26:449–454, 1972.

[101] S. Hikima, J.-I. Hikima, J. Rojtinnakorn, I. Hirono, and T. Aoki. Characterization and function of kuruma shrimp lysozyme possessing lytic activity against Vibrio species. *Gene*, 316:187–195, 2003.

[102] E. V. Pikuta, D. Marsic, T. Itoh, A. K. Bej, J. Tang, W. B. Whitman, J. D. Ng, O. K. Garriott, and R. B. Hoover. Thermococcus thioreducens sp. nov., a novel hyperthermophilic, obligately sulfur-reducing archaeon from a deep-sea hydrothermal vent. *Int. J. Syst. Evol. Microbiol.*, 57:1612–1618, 2007.

[103] S. Fujiwara, M. Plazanet, F. Matsumoto, and T. Oda. Internal motions of actin characterized by quasielastic neutron scattering. *Eur. Biophys. J.*, 40:661–671, 2011.

[104] F. Volino and A. J. Dianoux. Neutron incoherent scattering law for diffusion in a potential of spherical symmetry: General formalism and application to diffusion inside a sphere. *Mol. Phys.*, 41:271–279, 1980.

[105] R. T. Azuah, L. R. Kneller, and Y. Qiu. DAVE: A comprehensive software suite for the reduction, visualization, and analysis of low energy neutron spectroscopic data. *J.*

Res. Natl. Inst. Stand. Technol., 114:341–358, 2009.

[106] G. Caliskan, R. M. Briber, D. Thirumalai, V. García-Sakai, S. A. Woodson, and A. P. Sokolov. Dynamic transition in tRNA is solvent induced. *J. Am. Chem. Soc.*, 128:32–33, 2006.

[107] S. Dellerue, A.-J. Petrescu, J. C. Smith, and M.-C. Bellissent-Funel. Radially softening diffusive motions in a globular protein. *Biophys. J.*, 81:1666–1676, 2001.

[108] G. R. Kneller. Quasielastic neutron scattering and relaxation processes in proteins: Analytical and simulation-based models. *Phys. Chem. Chem. Phys.*, 7:2641–2655, 2005.

[109] C. A. Angell. Formation of glasses from liquids and biopolymers. *Science*, 267:1924–1935, 1995.

[110] P. Etchegoin. Glassylike low-frequency dynamics of globular proteins. *Phys. Rev. E*, 58:845–848, 1998.

[111] I. E. T. Iben, D. Braunstein, W. Doster, H. Frauenfelder, M. K. Hong, J. B. Johnson, S. Luck, P. Ormos, A. Schulte, P. J. Steinbach, A. H. Xie, and R. D. Young. Glassy behavior of a protein. *Phys. Rev. Lett.*, 62:1916–1919, 1989.

[112] J. L. Green, J. Fan, and C. A. Angell. The protein-glass analogy: Some insights from homopeptide comparisons. *J. Phys. Chem.*, 98:13780–13790, 1994.

[113] W. Götze and L. Sjögren. Relaxation processes in supercooled liquids. *Rep. Prog. Phys.*, 55:241–376, 1992.

[114] K.-C. Chou. Low-frequency motions in protein molecules: β-sheet and β-barrel. *Biophys. J.*, 48:289–297, 1985.

[115] B. F. Rasmussen, A. M. Stock, D. Ringe, and G. A. Petsko. Crystalline ribonuclease A loses function below the dynamical transition at 220 K. *Nature*, 357:423–424, 1992.

[116] D. Ringe and G. A. Petsko. The 'glass transition' in protein dynamics: What it is, why it occurs, and how to exploit it. *Biophys. Chem.*, 105:667–680, 2003.

[117] L. Meinhold, J. C. Smith, A. Kitao, and A. H. Zewail. Picosecond fluctuating protein energy landscape mapped by pressure-temperature molecular dynamics simulation. *Proc. Natl. Acad. Sci. U. S. A.*, 104:17261–17265, 2007.

[118] P. A. Calligari, V. Calandrini, J. Ollivier, J. B. Artero, M. Hartlein, M. Johnson, and G. R. Kneller. Adaptation of extremophilic proteins with temperature and pressure: Evidence from Initiation Factor 6. *J. Phys. Chem. B*, 119:7860–7873, 2015.

[119] Y. O. Kamatari, H. Yamada, K. Akasaka, J. A. Jones, C. M. Dobson, and L. J. Smith. Response of native and denatured hen lysozyme to high pressure studied by 15N/1H NMR spectroscopy. *Eur. J. Biochem.*, 268:1782–1793, 2001.

[120] B. W. Matthews. Proteins under pressure. *Proc. Natl. Acad. Sci. U. S. A.*, 109(18):6792–6793, 2012.

[121] M. Refaee, T. Tezuka, K. Akasaka, and M. P. Williamson. Pressure-dependent changes in the solution structure of hen egg-white lysozyme. *J. Mol. Biol.*, 327:857–865, 2003.

[122] E. Dahlhoff and G. N. Somero. Pressure and temperature adaptation of Cytosolic Malate-Dehydrogenases of shallow-living and deep-living marine-invertebrates - Evidence for high body temperatures in hydrothermal vent animals. *J. Exp. Biol.*, 159:473–487, 1991.

[123] K. Palczewski. G protein-coupled receptor rhodopsin. *Annu. Rev. Biochem.*, 75:743–

767, 2006.

[124] D. M. Rosenbaum, S. G. F. Rasmussen, and B. K. Kobilka. The structure and function of G-protein-coupled receptors. *Nature*, 459:356–363, 2009.

[125] K. D. Ridge and K. Palczewski. Visual rhodopsin sees the light: Structure and mechanism of G protein signaling. *J. Biol. Chem.*, 282:9297–9301, 2007.

[126] I. S. Moreira. Structural features of the G-protein/GPCR interactions. *Biochim. Biophys. Acta - General Subjects*, 1840:16–33, 2014.

[127] X. E. Zhou, K. Melcher, and H. E. Xu. Structure and activation of rhodopsin. *Acta Pharmacol. Sin.*, 33:291–299, 2012.

[128] T. W. Schwartz and W. L. Hubbell. Structural biology: A moving story of receptors. *Nature*, 455:473–474, 2008.

[129] M. C. Lagerström and H. B. Schioth. Structural diversity of G protein-coupled receptors and significance for drug discovery. *Nat. Rev. Drug Discov.*, 7:339–357, 2008.

[130] E. Malmerberg, P. H. M. Bovee-Geurts, G. Katona, X. Deupi, D. Arnlund, C. Wickstrand, L. C. Johansson, S. Westenhoff, E. Nazarenko, G. F. X. Schertler, A. Menzel, W. J. de Grip, and R. Neutze. Conformational activation of visual rhodopsin in native disc membranes. *Sci. Signal.*, 8:ra26, 2015.

[131] T.-Y. Kim, T. Schlieter, S. Haase, and U. Alexiev. Activation and molecular recognition of the GPCR rhodopsin - Insights from time-resolved fluorescence depolarisation and single molecule experiments. *Eur. J. Cell. Biol.*, 91:300–310, 2012.

[132] C. Altenbach, A. K. Kusnetzow, O. P. Ernst, K. P. Hofmann, and W. L. Hubbell. High-resolution distance mapping in rhodopsin reveals the pattern of helix movement

due to activation. *Proc. Natl. Acad. Sci. U. S. A.*, 105:7439–7444, 2008.

[133] J. Li, P. C. Edwards, M. Burghammer, C. Villa, and G. F. X. Schertler. Structure of bovine rhodopsin in a trigonal crystal form. *J. Mol. Biol.*, 343:1409–1438, 2004.

[134] A. M. Preininger, J. Meiler, and H. E. Hamm. Conformational flexibility and structural dynamics in GPCR-mediated G protein activation: A perspective. *J. Mol. Biol.*, 425:2288–2298, 2013.

[135] H.-W. Choe, Y. J. Kim, J. H. Park, T. Morizumi, E. F. Pai, N. Krausz, K. P. Hofmann, P. Scheerer, and O. P. Ernst. Crystal structure of metarhodopsin II. *Nature*, 471:651–655, 2011. 10.1038/nature09789.

[136] T. Okada, O. P. Ernst, K. Palczewski, and K. P. Hofmann. Activation of rhodopsin: New insights from structural and biochemical studies. *Trends Biochem. Sci.*, 26:318–324, 2001.

[137] J. Standfuss, P. C. Edwards, A. D'Antona, M. Fransen, G. Xie, D. D. Oprian, and G. F. X. Schertler. The structural basis of agonist-induced activation in constitutively active rhodopsin. *Nature*, 471:656–660, 2011.

[138] J. Standfuss, G. Xie, P. C. Edwards, M. Burghammer, D. D. Oprian, and G. F. X. Schertler. Crystal structure of a thermally stable rhodopsin mutant. *J. Mol. Biol.*, 372:1179–1188, 2007.

[139] D. Fotiadis, Y. Liang, S. Filipek, D. A. Saperstein, A. Engel, and K. Palczewski. Atomic-force microscopy: Rhodopsin dimers in native disc membranes. *Nature*, 421:127–128, 2003.

[140] D. Fotiadis, Y. Liang, S. Filipek, D. A. Saperstein, A. Engel, and K. Palczewski. The G

protein-coupled receptor rhodopsin in the native membrane. *FEBS Lett.*, 564:281–288, 2004.

[141] R. Medina, D. Perdomo, and J. Bubis. The hydrodynamic properties of dark- and light-activated states of n-Dodecyl-D-Maltoside-solubilized bovine rhodopsin support the dimeric structure of both conformations. *J. Biol. Chem.*, 279:39565–39573, 2004.

[142] B. Jastrzebska, D. Fotiadis, G. F. Jang, R. E. Stenkamp, A. Engel, and K. Palczewski. Functional and structural characterization of rhodopsin oligomers. *J. Biol. Chem.*, 281:11917–11922, 2006.

[143] A. V. Botelho, T. Huber, T. P. Sakmar, and M. F. Brown. Curvature and hydrophobic forces drive oligomerization and modulate activity of rhodopsin in membranes. *Biophys. J.*, 91:4464–4477, 2006.

[144] M. V. Petoukhov and D. I. Svergun. Applications of small-angle X-ray scattering to biomacromolecular solutions. *Int. J. Biochem. Cell Biol.*, 45:429–437, 2013.

[145] L. He, A. Piper, F. Meilleur, R. Hernandez, W. T. Heller, and D. T. Brown. Conformational changes in Sindbis virus induced by decreased pH are revealed by small-angle neutron scattering. *J. Virol.*, 86(4):1982–1987, 2012.

[146] H. Stuhrmann. Small-angle scattering and its interplay with crystallography, contrast variation in SAXS and SANS. *Acta Crystallogr. Sect. A*, 64:181–191, 2008.

[147] D. I. Svergun and M. H. J. Koch. Small-angle scattering studies of biological macromolecules in solution. *Rep. Prog. Phys.*, 66:1735, 2003.

[148] R. P. Rambo and J. A. Tainer. Bridging the solution divide: Comprehensive structural analyses of dynamic RNA, DNA, and protein assemblies by small-angle X-ray

scattering. *Curr. Opin. Struct. Biol.*, 20:128–137, 2010.

[149] H. Takeno, A. Maehara, D. Yamaguchi, and S. Koizumi. A structural study of an organogel investigated by small-angle neutron scattering and synchrotron small-angle X-ray scattering. *J. Phys. Chem. B*, 116:7739–7745, 2012.

[150] P. Yin, B. Wu, E. Mamontov, L. L. Daemen, Y. Cheng, T. Li, S. Seifert, K. Hong, P. V. Bonnesen, J. K. Keum, and A. J. Ramirez-Cuesta. X-ray and neutron scattering study of the formation of core-shell-type polyoxometalates. *J. Am. Chem. Soc.*, 138:2638–2643, 2016.

[151] R. K. Le, B. J. Harris, I. J. Iwuchukwu, B. D. Bruce, X. Cheng, S. Qian, W. T. Heller, H. O'Neill, and P. D. Frymier. Analysis of the solution structure of Thermosynechococcus elongatus photosystem I in n-dodecyl-β-d-maltoside using small-angle neutron scattering and molecular dynamics simulation. *Arch. Biochem. Biophys.*, 550-551:50–57, 2014.

[152] P.-C. Chen and J. S. Hub. Structural properties of protein-detergent complexes from SAXS and MD simulations. *J. Phys. Chem. Lett.*, 6:5116–5121, 2015.

[153] E. Di Cola, I. Grillo, and S. Ristori. Small angle x-ray and neutron scattering: Powerful tools for studying the structure of drug-loaded liposomes. *Pharmaceutics*, 8, 2016.

[154] D. Anunciado, D. K. Rai, S. Qian, V. Urban, and H. O'Neill. Small-angle neutron scattering reveals the assembly of alpha-synuclein in lipid membranes. *Biochim. Biophys. Acta*, 1854:1881–1889, 2015.

[155] Y. N. Dahdal, V. Pipich, H. Rapaport, Y. Oren, R. Kasher, and D. Schwahn. Small-angle neutron scattering studies of mineralization on BSA coated citrate capped gold

nanoparticles used as a model surface for membrane scaling in RO wastewater desalination. *Langmuir*, 30:15072–15082, 2014.

[156] J. Lipfert and S. Doniach. Small-angle X-ray scattering from RNA, proteins, and protein complexes. *Annu. Rev. Biophys. Biomol. Struct.*, 36:307–327, 2007.

[157] U. S. Jeng, T.-L. Lin, J. M. Lin, and D. L. Ho. Contrast variation SANS for the solution structure of the β-amyloid peptide 1-40 influenced by SDS surfactants. *Physica B: Condens. Matter*, 385-386:865–867, 2006.

[158] S. L. Martin, L. He, F. Meilleur, R. H. Guenther, T. L. Sit, S. A. Lommel, and W. T. Heller. New insight into the structure of RNA in red clover necrotic mosaic virus and the role of divalent cations revealed by small-angle neutron scattering. *Arch. Virol.*, 158:1661–1669, 2013.

[159] S. Mehan, V. K. Aswal, and J. Kohlbrecher. Cationic versus anionic surfactant in tuning the structure and interaction of nanoparticle, protein, and surfactant complexes. *Langmuir*, 30:9941–9950, 2014.

[160] J. Lipfert, L. Columbus, V. B. Chu, S. A. Lesley, and S. Doniach. Size and shape of detergent micelles determined by small-angle X-ray scattering. *J. Phys. Chem. B*, 111:12427–12438, 2007.

[161] A. M. Seddon, P. Curnow, and P. J. Booth. Membrane proteins, lipids and detergents: Not just a soap opera. *Biochim. Biophys. Acta - Biomembranes*, 1666:105–117, 2004.

[162] A. V. Struts, U. Chawla, S. M. Perera, and M. F. Brown. Investigation of rhodopsin dynamics in its signaling state by solid-state deuterium NMR spectroscopy. *Methods Mol. Biol.*, 1271:133–158, 2015.

[163] E. Ritter, P. Piwowarski, P. Hegemann, and F. J. Bartl. Light-dark adaptation of channelrhodopsin C128T mutant. *J. Biol. Chem.*, 288:10451–10458, 2013.

[164] E. Ritter, K. Zimmermann, M. Heck, K. P. Hofmann, and F. J. Bartl. Transition of rhodopsin into the active metarhodopsin II state opens a new light-induced pathway linked to Schiff base isomerization. *J. Biol. Chem.*, 279:48102–48111, 2004.

[165] M. Allaire and L. Yang. Biomolecular solution X-ray scattering at the National Synchrotron Light Source. *J. Synchrotron Radiat.*, 18:41–44, 2011.

[166] W. T. Heller, G. W. Lynn, V. S. Urban, K. Weiss, and D. A. A. Myles. The bio-SANS small-angle neutron scattering instrument at Oak Ridge National Laboratory. *Neutron News*, 19:22–23, 2008.

[167] D. I. Svergun, S. Richard, M. H. J. Koch, Z. Sayers, S. Kuprin, and G. Zaccaï. Protein hydration in solution: Experimental observation by X-ray and neutron scattering. *Proc. Nat. Acad. Sci. U. S. A.*, 95:2267–2272, 1998.

[168] R. C. Oliver, J. Lipfert, D. A. Fox, R. H. Lo, S. Doniach, and L. Columbus. Dependence of micelle size and shape on detergent alkyl chain length and head group. *PLoS One*, 8:e62488, 2013.

[169] A. Caretta, P. J. Stein, and R. Tirindelli. Rhodopsin-detergent micelles aggregate upon activation of cyclic guanosine monophosphate phosphodiesterase. *Biochemistry*, 29:2652–2657, 1990.

[170] L. Columbus, J. Lipfert, H. Klock, I. Millett, S. Doniach, and S. A. Lesley. Expression, purification, and characterization of Thermotoga maritima membrane proteins for structure determination. *Protein Sci.*, 15:961–975, 2006.

[171] V. R. Ramakrishnan, A. Darszon, and M. Montal. A small angle X-ray scattering study of a rhodopsin-lipid complex in hexane. *J. Biol. Chem.*, 258:4857–4860, 1983.

[172] S. Abel, F.-Y. Dupradeau, E. P. Raman, A. D. MacKerell, and M. Marchi. Molecular simulations of dodecyl-β-maltoside micelles in water: Influence of the headgroup conformation and force field parameters. *J. of Phys. Chem. B*, 115:487–499, 2011.

[173] K. Y. Chung, S. G. Rasmussen, T. Liu, S. Li, B. T. DeVree, P. S. Chae, D. Calinski, B. K. Kobilka, Jr. Woods, V. L., and R. K. Sunahara. Conformational changes in the G protein Gs induced by the beta2 adrenergic receptor. *Nature*, 477:611–615, 2011.

[174] A. J. Venkatakrishnan, X. Deupi, G. Lebon, C. G. Tate, G. F. Schertler, and M. M. Babu. Molecular signatures of G-protein-coupled receptors. *Nature*, 494:185–194, 2013.

[175] A. V. Struts, G. F. Salgado, and M. F. Brown. Solid-state 2H NMR relaxation illuminates functional dynamics of retinal cofactor in membrane activation of rhodopsin. *Proc. Natl. Acad. Sci. U. S. A.*, 108:8263–8268, 2011.

[176] A. V. Struts, G. F. J. Salgado, K. Martnez-Mayorga, and M. F. Brown. Retinal dynamics underlie its switch from inverse agonist to agonist during rhodopsin activation. *Nat. Struct. Mol. Biol.*, 18:392–394, 2011.

[177] S. Kawamura, M. Gerstung, A. T. Colozo, J. Helenius, A. Maeda, N. Beerenwinkel, P. S. Park, and D. J. Muller. Kinetic, energetic, and mechanical differences between dark-state rhodopsin and opsin. *Structure*, 21:426–437, 2013.

[178] M. Mahalingam, K. Martinez-Mayorga, M. F. Brown, and R. Vogel. Two protonation switches control rhodopsin activation in membranes. *Proc. Natl. Acad. Sci. U. S. A.*, 105:17795–17800, 2008.

[179] S. O. Smith. Structure and activation of the visual pigment rhodopsin. *Annu. Rev. Biophys*, 39:309–328, 2010.

[180] T. Okada, K. Takeda, and T. Kouyama. Highly selective separation of rhodopsin from bovine rod outer segment membranes using combination of divalent cation and alkyl(thio)glucoside. *Photochem. Photobiol.*, 67:495–499, 1998.

[181] E. Mamontov and X.-Q. Chu. Water-protein dynamic coupling and new opportunities for probing it at low to physiological temperatures in aqueous solutions. *Phys. Chem. Chem. Phys.*, 14:11573–11588, 2012.

[182] L. Hong, N. Smolin, B. Lindner, A. P. Sokolov, and J. C. Smith. Three classes of motion in the dynamic neutron-scattering susceptibility of a globular protein. *Phys. Rev. Lett.*, 107:148102, 1–4, 2011.

[183] U. R. Shrestha, S. M. D. C. Perera, D. Bhowmik, U. Chawla, E. Mamontov, M. F. Brown, and X.-Q. Chu. Quasi-elastic neutron scattering reveals ligand-induced protein dynamics of a G-protein-coupled receptor. *J. Phys.Chem. Lett.*, 7:4130–4136, 2016.

[184] M. I. Aveldaño. Phospholipid solubilization during detergent extraction of rhodopsin from photoreceptor disk membranes. *Arch. Biochem. Biophys.*, 324:331–343, 1995.

[185] X.-Q. Chu, E. Mamontov, H. O'Neill, and Q. Zhang. Apparent decoupling of the dynamics of a protein from the dynamics of its aqueous solvent. *J. Phys. Chem. Lett.*, 3:380–385, 2012.

[186] S. M. Chathoth, E. Mamontov, Y. B. Melnichenko, and M. Zamponi. Diffusion and adsorption of methane confined in nano-porous carbon aerogel: A combined quasi-elastic and small-angle neutron scattering study. *Microporous Mesoporous Mater.*,

132:148–153, 2010.

[187] M. A. Lill. Efficient incorporation of protein flexibility and dynamics into molecular docking simulations. *Biochemistry*, 50:6157–6169, 2011.

[188] R. Vogel and F. Siebert. Conformations of the active and inactive states of opsin. *J. Biol. Chem.*, 276:38487–38493, 2001.

[189] D. Vitkup, D. Ringe, G. A. Petsko, and M. Karplus. Solvent mobility and the protein 'glass' transition. *Nat. Struct. Mol. Biol.*, 7:34–38, 2000. 10.1038/71231.

[190] S.-H. Chen, L. Liu, E. Fratini, P. Baglioni, A. Faraone, and E. Mamontov. Observation of fragile-to-strong dynamic crossover in protein hydration water. *Proc. Natl. Acad. Sci. U. S. A.*, 103:9012–9016, 2006.

[191] N. Leioatts, B. Mertz, K. Martinez-Mayorga, T. D. Romo, M. C. Pitman, S. E. Feller, A. Grossfield, and M. F. Brown. Retinal ligand mobility explains internal hydration and reconciles active rhodopsin structures. *Biochemistry*, 53:376–385, 2014.

[192] J. A. McCommon and M. Karplus. The dynamic picture of protein structure. *Acc. Chem. Res.*, 16:187–193, 1983.

[193] M. Karplus, J. A. McCammon, and W. L. Peticolas. The internal dynamics of globular protein. *Crit. Rev. Biochem. Mol. Biol.*, 9:293–349, 1981.

[194] W. Nadler, A. T. Brunger, K. Schulten, and Martin Karplus. Molecular and stochastic dynamics of proteins. *Proc. Natl. Acad. Sci. U.S.A.*, 84:7933–7937, 1987.

[195] S. J. Benkovic, G. G. Hammes, and S. Hammes-Schiffer. Free-energy landscape of enzyme catalysis. *Biochemistry*, 47:3317–3321, 2008.

[196] K.-C. Chou. Low-frequency collective motion in biomacromolecules and its biological

functions. *Biophys. Chem. Rev.*, 30:3–48, 1988.

[197] K. G. Brown, S. C. Erfurth, E. W. Small, and Warner L. Peticolas. Conformationally dependent low-frequency motions of proteins by laser Raman spectroscopy. *Proc. Natl. Acad. Sci. U. S. A.*, 69:1467–1469, 1972.

[198] W. Schirmacher, G. Diezemann, and C. Ganter. Harmonic vibrational excitations in disordered solids and the "Boson Peak". *Phys. Rev. Lett.*, 81:136–139, 1998.

[199] H. Shintani and H. Tanaka. Universal link between the boson peak and transverse phonons in glass. *Nat. Mater.*, 7:870–877, 2008.

[200] J. D. Nickels, S. Perticaroli, H. O'Neill, Q. Zhang, G. Ehlers, and A. P. Sokolov. Coherent neutron scattering and collective dynamics in the protein, GFP. *Biophys. J.*, 105:2182–2187, 2013.

[201] S. Perticaroli, J. D. Nickels, G. Ehlers, E. Mamontov, and A. P. Sokolov. Dynamics and rigidity in an intrinsically disordered protein, β-casein. *J. Phys. Chem. B*, 118:7317–7326, 2014.

[202] J. A. Fornés. H-Bond vibrations of the α-helix. *Phys. Chem. Chem. Phys.*, 3:1086–1088, 2001.

[203] K.-C. Chou. Low-frequency vibrations of helical structures in protein molecules. *Biochem. J.*, 209:573–583, 1983.

[204] J. P. Klinman and A. Kohen. Hydrogen tunneling links protein dynamics to enzyme catalysis. *Annu. Rev. Biochem.*, 82:471–496, 2013.

[205] C. M. Cheatum and A. Kohen. Relationship of femtosecond-picosecond dynamics to enzyme-catalyzed H-transfer. *Top. Curr. Chem.*, 337:1–39, 2013.

[206] S. D. Schwartz and V. L. Schramm. Enzymatic transition states and dynamic motion in barrier crossing. *Nat. Chem. Biol.*, 5:551–558, 2009.

[207] G. Careri, P. Fasella, E. Gratton, and W. P. Jencks. Statistical time events in enzymes: A physical assessment. *Crit. Rev. Biochem. Mol. Biol.*, 3:141–164, 1975.

[208] V. V. Brazhkin and K. Trachenko. Collective excitations and thermodynamics of disordered state: New insights into an old problem. *J. Phys. Chem. B*, 118:11417–11427, 2014.

[209] J.-B. Suck. Inelastic neutron scattering applied to the investigation of collective excitations in topologically disordered matter. *Condens. Matter Phys.*, 11:7–18, 2008.

[210] E. Burkel. Phonon spectroscopy by inelastic X-ray scattering. *Rep. Prog. Phys.*, 63:171–232, 2000.

[211] A. Cunsolo, C. N. Kodituwakku, F. Bencivenga, M. Frontzek, B. M. Leu, and A. H. Said. Transverse dynamics of water across the melting point: A parallel neutron and X-ray inelastic scattering study. *Phys. Rev. B*, 85:174305, 1–12, 2012.

[212] M. C. Bellissent-Funel, J. Teixeira, S.-H. Chen, B. Dorner, H. D. Middendorf, and H. L. Crespi. Low-frequency collective modes in dry and hydrated proteins. *Biophys. J.*, 56:713–716, 1989.

[213] G. N. Phillips Jr. Structure and dynamics of green fluorescent protein. *Curr. Opin. Struct. Biol.*, 7:821–827, 1997.

[214] F. Yang, L. G. Moss, and G. N. Phillips Jr. The molecular structure of green fluorescent protein. *Nat. Biotechnol.*, 14:1246–1251, 1996.

[215] B. M. Leu, A. Alatas, H. Sinn, E. E. Alp, A. H. Said, H. Yavas, J. Zhao, J. T. Sage,

and W. Sturhahn. Protein elasticity probed with two synchrotron-based techniques. *J. Chem. Phys.*, 132:085103, 1–7, 2010.

[216] B. M. Leu, J. T. Sage, N. J. Silvernail, W. R. Scheidt, A. Alatas, E. E. Alp, and W. Sturhahn. Bulk modulus of a protein active-site mimic. *J. Phys. Chem. B*, 115:4469–4473, 2011.

[217] K. Yoshida, S. Hosokawa, A. Q. Baron, and T. Yamaguchi. Collective dynamics of hydrated beta-lactoglobulin by inelastic X-ray scattering. *J. Chem. Phys.*, 133:134501, 1–7, 2010.

[218] Z. Wang, C. E. Bertrand, W. S. Chiang, E. Fratini, P. Baglioni, A. Alatas, E. E. Alp, and S. H. Chen. Inelastic X-ray scattering studies of the short-time collective vibrational motions in hydrated lysozyme powders and their possible relation to enzymatic function. *J. Phys. Chem. B*, 117:1186–1195, 2013.

[219] W. T. Heller, H. M. O'Neill, Q. Zhang, and G. A. Baker. Characterization of the influence of the ionic liquid 1-butyl-3-methylimidazolium chloride on the structure and thermal stability of green fluorescent protein. *J. Phys. Chem. B*, 114:13866–13871, 2010.

[220] G. E. Granroth, A. I. Kolesnikov, T. E. Sherline, J. P. Clancy, K. A. Ross, J. P. C. Ruff, B. D. Gaulin, and S. E. Nagler. SEQUOIA: A newly operating chopper spectrometer at the SNS. *J. Phys.: Conf. Ser.*, 251:012058, 2010.

[221] E. A. Pogna, C. Rodriguez-Tinoco, M. Krisch, J. Rodriguez-Viejo, and T. Scopigno. Acoustic-like dynamics of amorphous drugs in the THz regime. *Sci. Rep.*, 3:1–5, 2013.

[222] E. Mamontov, A. De Francesco, F. Formisano, A. Laloni, L. Sani, B. M. Leu, A. H.

Said, and A. I. Kolesnikov. Water dynamics in a lithium chloride aqueous solution probed by brillouin neutron and X-ray scattering. *J. Phys. Condens. Matter*, 24:064102, 1–9, 2012.

[223] A. Orecchini, A. Paciaroni, A. De Francesco, C. Petrillo, and F. Sacchetti. Collective dynamics of protein hydration water by Brillouin neutron spectroscopy. *J. Am. Chem. Soc.*, 131:4664–4669, 2009.

[224] E. Cornicchi, F. Sebastiani, A. De Francesco, A. Orecchini, A. Paciaroni, C. Petrillo, and F. Sacchetti. Collective density fluctuations of DNA hydration water in the time-window below 1 ps. *J. Chem. Phys.*, 135:025101, 1–7, 2011.

[225] D. Liu, X.-Q. Chu, M. Lagi, Y. Zhang, E. Fratini, P. Baglioni, A. Alatas, A. Said, E. Alp, and S.-H. Chen. Studies of phononlike low-energy excitations of protein molecules by inelastic X-ray scattering. *Phys. Rev. Lett.*, 101:135501, 1–4, 2008.

[226] Z. Wang, W. S. Chiang, P. Le, E. Fratini, M. Li, A. Alatas, P. Baglioni, and S. H. Chen. One role of hydration water in proteins: Key to the "softening" of short time intraprotein collective vibrations of a specific length scale. *Soft Matter*, 10:4298–4303, 2014.

[227] A. Paciaroni, A. Orecchini, M. Haertlein, M. Moulin, V. Conti Nibali, A. De Francesco, C. Petrillo, and F. Sacchetti. Vibrational collective dynamics of dry proteins in the terahertz region. *J. Phys. Chem. B*, 116:3861–3865, 2012.

[228] E. Mamontov, S. B. Vakhrushev, Yu A. Kumzerov, A. Alatas, and H. Sinn. Acoustic phonons in chrysotile asbestos probed by high-resolution inelastic X-ray scattering. *Solid State Commun.*, 149:589–592, 2009.

[229] F. Sette, M. H. Krisch, C. Masciovecchio, G. Ruocco, and G. Monaco. Dynamics of glasses and glass-forming liquids studied by inelastic X-ray scattering. *Science*, 280:1550–1555, 1998.

[230] J. Teixeira, M. C. Bellissent-Funel, S. H. Chen, and B. Dorner. Observation of new short-wavelength collective excitations in heavy water by coherent inelastic neutron scattering. *Phys. Rev. Lett.*, 54:2681–2683, 1985.

[231] H. Pfeiffer and K. Heremans. Apparent sound velocity of lysozyme in aqueous solutions. *Chem. Phys. Lett.*, 361:226–230, 2002.

[232] K. Achterhold and F. G. Parak. Proteins dynamics: Determination of anisotropic vibrations at the haem iron of myoglobin. *J. Phys.: Condens. Matter*, 15:S1683–S1692, 2002.

[233] Y. Levy and J. N. Onuchic. Water mediation in protein folding and molecular recognition. *Annu. Rev. Biophys. Biomol. Struct.*, 35:389–415, 2006.

[234] M. Li, X.-Q. Chu, E. Fratini, P. Baglioni, A. Alatas, E. E. Alp, and S.-H. Chen. Phonon-like excitation in secondary and tertiary structure of hydrated protein powders. *Soft Matter*, 7:9848, 2011.

[235] V. Conti Nibali, G. D'Angelo, A. Paciaroni, D. J. Tobias, and M. Tarek. On the coupling between the collective dynamics of proteins and their hydration water. *J. Phys. Chem. Lett.*, 5:1181–1186, 2014.

[236] X.-Q. Chu, U. R. Shrestha, H. M. O'Neill, Q. Zhang, A. I. Kolesnikov, and E. Mamontov. Investigation of phonon-like excitations in hydrated protein powders by neutron scattering. *Biophys. J.*, 106:236a, 2014.

[237] U. R. Shrestha, D. Bhowmik, K. W. Van Delinder, E. Mamontov, H. O'Neill, Q. Zhang, A. Alatas, and X.-Q. Chu. Collective excitations in protein as a measure of balance between its softness and rigidity. *J. Phys. Chem. B*, 2017 (DOI: 10.1021/acs.jpcb.6b10245).

[238] T. R. Guizado. Analysis of the structure and dynamics of human serum albumin. *J. Mol. Model.*, 20:2450, 2014.

[239] M. Fasano, S. Curry, E. Terreno, M. Galliano, G. Fanali, P. Narciso, S. Notari, and P. Ascenzi. The extraordinary ligand binding properties of human serum albumin. *IUBMB Life*, 57:787–796, 2005.

[240] F. Yang, Y. Zhang, and H. Liang. Interactive association of drugs binding to human serum albumin. *Int. J. Mol. Sci.*, 15:3580–3595, 2014.

[241] L. Galantini, C. Leggio, P. V. Konarev, and N. V. Pavel. Human serum albumin binding ibuprofen: A 3D description of the unfolding pathway in urea. *Biophys. Chem.*, 147:111–122, 2010.

[242] S. Baroni, M. Mattu, A. Vannini, R. Cipollone, S. Aime, P. Ascenzi, and M. Fasano. Effect of ibuprofen and warfarin on the allosteric properties of haem-human serum albumin. *Eur. J. Biochem.*, 268:6214–6220, 2001.

[243] A. Alatas, B. M. Leu, J. Zhao, H. Yavaş, T. S. Toellner, and E. E. Alp. Improved focusing capability for inelastic X-ray spectrometer at 3-ID of the APS: A combination of toroidal and Kirkpatrick-Baez (KB) mirrors. *Nucl. Instr. Meth. Phys. Res. Sec A: Accelerators, Spectrometers, Detectors and Associated Equipment*, 649:166–168, 2011.

[244] H. Sinn, E. E. Alp, A. Alatas, J. Barraza, G. Bortel, E. Burkel, D. Shu, W. Sturhahn,

J. P. Sutter, T. S. Toellner, and J. Zhao. An inelastic X-ray spectrometer with 2.2 meV energy resolution. *Nucl. Instr. Meth. Phys. Res. Sec A: Accelerators, Spectrometers, Detectors and Associated Equipment*, 467-468(Part 2):1545–1548, 2001.

[245] T. S. Toellner, A. Alatas, and A. H. Said. Six-reflection meV-monochromator for synchrotron radiation. *J. Synchrotron Radiat.*, 18:605–611, 2011.

[246] A. M. Gaspar, S. Busch, M. S. Appavou, W. Haeussler, R. Georgii, Y. Su, and W. Doster. Using polarization analysis to separate the coherent and incoherent scattering from protein samples. *Biochim. Biophys. Acta*, 1804:76–82, 2010.

[247] B. Farruggia and G. A. Picó. Thermodynamic features of the chemical and thermal denaturations of human serum albumin. *Int. J. Biol. Macromolec.*, 26:317–323, 1999.

[248] M. Ferrand, A. J. Dianoux, W. Petry, and G. Zaccaï. Thermal motions and function of bacteriorhodopsin in purple membranes: Effects of temperature and hydration studied by neutron scattering. *Proc. Natl. Acad. Sci. U. S. A.*, 90:9668–9672, 1993.

[249] A. Schlessinger and B. Rost. Protein flexibility and rigidity predicted from sequence. *Proteins*, 61:115–126, 2005.

[250] M. Z. Kamal, T. A. Mohammad, G. Krishnamoorthy, and N. M. Rao. Role of active site rigidity in activity: MD simulation and fluorescence study on a lipase mutant. *PLoS One*, 7:e35188, 2012.

[251] K. Opron, K. Xia, and G. W. Wei. Fast and anisotropic flexibility-rigidity index for protein flexibility and fluctuation analysis. *J. Chem. Phys.*, 140:234105, 1–19, 2014.

[252] I. Petitpas, A. A. Bhattacharya, S. Twine, M. East, and S. Curry. Crystal structure analysis of warfarin binding to human serum albumin: Anatomy of drug site I. *J. Biol.*

Chem., 276:22804–22809, 2001.

[253] G. F.-L. Ames. Structure and mechanism of bacterial periplasmic transport systems. *J. Bioenerg. Biomembr.*, 20:1–18, 1988.

[254] R. Tam and M. H. Saier. Structural, functional, and evolutionary relationships among extracellular solute-binding receptors of bacteria. *Microbiol. Rev.*, 57:320–346, 1993.

[255] A. J. Sharff, L. E. Rodseth, J. C. Spurlino, and F. A. Quiocho. Crystallographic evidence of a large ligand-induced hinge-twist motion between the two domains of the maltodextrin binding protein involved in active transport and chemotaxis. *Biochemistry*, 31:10657–10663, 1992.

[256] J. T. Park, D. Raychaudhuri, H. Li, S. Normark, and D. Mengin-Lecreulx. MppA, a periplasmic binding protein essential for import of the bacterial cell wall peptidel-alanyl-γ-d-glutamyl-meso-diaminopimelate. *J. Bacteriol.*, 180:1215–1223, 1998.

[257] S. Létoffé, P. Delepelaire, and C. Wandersman. The housekeeping dipeptide permease is the Escherichia coli heme transporter and functions with two optional peptide binding proteins. *Proc. Nat. Acad. Sci. U. S. A.*, 103:12891–12896, 2006.

[258] A. Maqbool, V. M. Levdikov, E. V. Blagova, M. Herve, R.S. P. Horler, A. J. Wilkinson, and G. H. Thomas. Compensating stereochemical changes allow murein tripeptide to be accommodated in a conventional peptide-binding protein. *J. Biol. Chem.*, 286:31512–31521, 2011.

[259] H. D. T. Mertens and D. I. Svergun. Structural characterization of proteins and complexes using small-angle X-ray solution scattering. *J. Struct. Biol.*, 172:128–141, 2010.

[260] J. G. Duman. Antifreeze and ice nucleator proteins in terrestrial arthropods. *Annu. Rev. Physiol.*, 63:327–357, 2001.

[261] K. Meister, S. Ebbinghaus, Y. Xu, J. G. Duman, A. DeVries, M. Gruebele, D. M. Leitner, and M. Havenith. Long-range protein-water dynamics in hyperactive insect antifreeze proteins. *Proc. Natl. Acad. Sci. U. S. A.*, 110:1617–1622, 2013.

[262] A. D. J. Haymet, L. G. Ward, M. M. Harding, and C. A. Knight. Valine substituted winter flounder 'antifreeze': Preservation of ice growth hysteresis. *FEBS Lett.*, 430:301–306, 1998.

[263] S. Venketesh and C. Dayananda. Properties, potentials, and prospects of antifreeze proteins. *Crit. Rev. Biotechnol.*, 28:57–82, 2008.

[264] V. N. Mochalin, O. Shenderova, D. L. Ho, and Y. Gogotsi. The properties and applications of nanodiamonds. *Nat. Nano.*, 7:11–23, 2012.

[265] X. Li, J. Shao, Y. Qin, C. Shao, T. Zheng, and L. Ye. TAT-conjugated nanodiamond for the enhanced delivery of doxorubicin. *J. Mater. Chem.*, 21:7966–7973, 2011.

[266] M. V. Kharlamova, V. N. Mochalin, M. R. Lukatskaya, J. Niu, V. Presser, S. Mikhalovsky, and Y. Gogotsi. Adsorption of proteins in channels of carbon nanotubes: Effect of surface chemistry. *Mater. Express*, 3:1–10, 2013.

[267] V. C. Sanchez, A. Jachak, R. H. Hurt, and A. B. Kane. Biological interactions of graphene-family nanomaterials: An interdisciplinary review. *Chem. Res. Toxicol.*, 25:15–34, 2012.

[268] Z. Chen, W. Ren, L. Gao, B. Liu, S. Pei, and H.-M. Cheng. Three-dimensional flexible and conductive interconnected graphene networks grown by chemical vapour deposi-

tion. *Nat. Mater.*, 10:424–428, 2011.

[269] H. Hu, Z. Zhao, W. Wan, Y. Gogotsi, and J. Qiu. Ultralight and highly compressible graphene aerogels. *Adv. Mater.*, 25:2219–2223, 2013.

[270] F. Yavari, Z. Chen, A. V. Thomas, W. Ren, H.-M. Cheng, and N. Koratkar. High sensitivity gas detection using a macroscopic three-dimensional graphene foam network. *Sci. Rep.*, 1:166, 2011.

[271] N. Li, Q. Zhang, S. Gao, Q. Song, R. Huang, L. Wang, L. Liu, J. Dai, M. Tang, and G. Cheng. Three-dimensional graphene foam as a biocompatible and conductive scaffold for neural stem cells. *Sci. Rep.*, 3:1604, 2013.

[272] M. Zhang, Y. Cao, Y. Chong, Y. Ma, H. Zhang, Z. Deng, C. Hu, and Z. Zhang. Graphene oxide based theranostic platform for T1-weighted magnetic resonance imaging and drug delivery. *ACS Appl. Mater. Interfaces*, 5:13325–13332, 2013.

[273] X. Sun, Z. Liu, K. Welsher, J. T. Robinson, A. Goodwin, S. Zaric, and H. Dai. Nano-graphene oxide for cellular imaging and drug delivery. *Nano Res.*, 1:203–212, 2008.

[274] G. K. Dhindsa, D. Bhowmik, M. Goswami, H. O'Neill, E. Mamontov, B. G. Sumpter, L. Hong, P. Ganesh, and X.-Q. Chu. Enhanced dynamics of hydrated tRNA on nanodiamond surfaces: A combined neutron scattering and MD simulation study. *J. Phys. Chem. B*, 120:10059–10068, 2016.

[275] S. Devineau, J.-M. Zanotti, C. Loupiac, L. Zargarian, F. Neiers, S. Pin, and J. P. Renault. Myoglobin on silica: A case study of the impact of adsorption on protein structure and dynamics. *Langmuir*, 29:13465–13472, 2013.

2.0

SCIENTIFIC CONTRIBUTIONS

• **Shrestha UR**, Bhowmik D, Van Delinder KW, Mamontov E, O'Neill H, Zhang Q, Alatas A, Chu X-Q. Collective excitations in protein as a measure of balance between its softness and rigidity. *J. Phys. Chem. B* 2017, **121**(5): 923-930

• **Shrestha UR**, Perera SMDC, Bhowmik D, Chawla U, Mamontov E, Brown MF, Chu X-Q. Quasi-elastic neutron scattering reveals ligand-induced protein dynamics of a G-protein-coupled receptor. *J. Phys. Chem. Lett.* 2016, **7**: 4130-4136.

• **Shrestha UR**, Bhowmik D, Copley JRD, Tyagi M, Leão JB, Chu X-Q. Effects of pressure on the dynamics of an oligomeric protein from deep-sea hyperthermophile. *Proc. Natl. Acad. Sci. U. S. A.* 2015, **112**(45): 13886-13891.

• Bhowmik D, Dhindsa GK, **Shrestha UR**, Mamontov E, Chu X-Q. Effect of nanodiamond surfaces on drug delivery systems. *arXiv:1609.02656 [physics.bio-ph]* 2016.

• **Shrestha UR**, Bhowmik D, O'Neill HM, Zhang Q, Kolesnikov AI, Mamontov E, Chu X-Q. Investigation of glass-like low-frequency collective motions in green fluorescent protein. (*To be submitted*)

• **Shrestha UR**, Bhowmik D, Qian S, Chu X-Q. Contrast match small-angle neutron scattering reveals the conformational change in photoactivation mechanism of rhodopsin. (*in prep.*)

• **Shrestha UR**, Bhowmik D, Tyagi M, Zhou W, Mamontov E, Chu X-Q. Diffusive motion of hydration shell on the surface of nanodiamonds shows an encouraging pathways for therapeutic drug delivery. (*in prep.*)

• Bhowmik D, **Shrestha UR**, Dhindsa GK, Sharp M, Stingaciu LR, Chu X-Q. Investigation of slow-domain motion of a large oligomeric protein using neutron spin-echo and small-anlgle neutron scattering. (*in prep.*)

• **Shrestha UR**, Bhowmik D, Heller WT, Chu X-Q. Conformational stability of hyperthermophilic protein at high temperature studied by small-angle neutron scattering. (*in prep.*)

CONFERENCE PRESENTATIONS

• 'Ligand-Induced Dynamical Change of G-Protein-Coupled Receptor Revealed by Neutron Scattering', contributed talk at APS March meeting, 2017.

• 'Balance between Protein Softness and Rigidity Assessed by Inelastic X-ray Scattering', poster presentation at Annual Meeting of Biophysical Society, 2017.

• 'Quasi-elastic neutron scattering reveals the effects of pressure on dynamics of a hyperthermophilic protein from deep-sea', contributed talk at American Conference on Neutron Scattering, 2016.

• 'Effects of pressure on the dynamics of a hyperthermophilic protein revealed by quasi-elastic neutron scattering', contributed talk at APS March meeting, 2016.

• 'Effects of pressure on the dynamics of a hyperthermophilic protein from deep-sea', poster presented at 7^{th} Graduate Research Day, Department of Physics and Astronomy, Wayne State University, 2016.

• 'Mechanism of activation of G-protein-coupled receptor revealed by neutron scattering experiments', poster presented at 6^{th} Graduate Research Day, Department of Physics and Astronomy, Wayne State University, 2015.

• 'Neutron scattering experiments revealed the conformational change and flexibility in rhodopsin upon light activation', contributed talk at 6^{th} Annual Midwest Graduate Research Symposium, University of Toledo, 2015.

• 'Small-angle neutron and X-ray scattering reveal conformational changes in rhodopsin activation', contributed talk at APS March Meeting, 2015.

• 'Probing the domain motions of an oligomeric protein from deep-sea hyperthermophile by neutron spin-echo', poster presented at 59^{th} Annual Meeting of Biophysical Society, 2015.

• 'Rhodopsin photoactivation dynamics revealed by quasi-elastic neutron scattering', poster presented at 59^{th} Annual Meeting of Biophysical Society, 2015.

• 'Small-angle neutron and X-ray scattering reveal conformational differences in detergents affecting rhodopsin activation', contributed talk at 59^{th} Annual Meeting of Biophysical So-

ciety, 2015.

• 'Dynamics of a large oligomeric protein under high pressure studied by neutron scattering', poster presented at American Conference on Neutron Scattering, 2014.

• 'Photoactivation of a GPCR rhodopsin studied by small-angle neutron scattering', poster presented at American Conference on Neutron Scattering, 2014.

• 'Dynamics of a large oligomeric protein under high pressure studied by neutron scattering', presented at 5^{th} Graduate Research Day, Department of Physics and Astronomy, Wayne State University, 2014.

• 'Dynamic behavior of a large oligomeric protein IPPase under extreme conditions', poster presented at 9^{th} Annual Midwest Conference on Protein Folding, Assembly and Molecular Motions, University of Notre Dame, 2014.

• 'Investigation of phonon-like excitations in hydrated protein powders by neutron scattering', presented at 58^{th} Annual Meeting of Biophysical Society, 2014.

• 'Dynamic behavior of oligomeric inorganic pyrophosphatase (IPPase) studied by quasi-elastic neutron scattering', poster presented at 58^{th} Annual Meeting of Biophysical Society, 2014.

ABSTRACT

EXPLORING THE PHYSICS OF PROTEINS AT MOLECULAR LEVEL BY NEUTRON AND X-RAY SCATTERING

by

UTSAB R. SHRESTHA

May 2017

Advisor: Dr. Xiang-Qiang Chu

Major: Physics

Degree: Doctor of Philosophy

Protein conformational dynamics are believed to ultimately govern the biological activities and functions of proteins. Hence, a deeper understanding of the protein dynamics is crucial for elucidating the structural pathways or the transition mechanisms necessary for regulating the physical and chemical processes. The direct correlation of a wide range of protein dynamics to function still remains unclear, posing a major challenge to biophysical community. In this dissertation, the relationships among the protein's conformation, dynamics and function are investigated using the state-of-the-art neutron and X-ray scattering techniques. Taking the advantage of comparable wavelength or momentum of neutron and X-ray to that of the atoms within biomolecules, we studied the protein dynamics at the molecular level over the timescale of a few femtoseconds to nanoseconds regime. Our results demonstrate that the protein dynamic behavior is similar to that of glass forming liquids, where the relaxation process is non-exponential and the collective excitations are highly damped. Specifically, picosecond to nanosecond dynamics, also known as beta-relaxation process decays logarithmically over the time. Remarkably, such dynamic phenomena revealed the direct experimental evidences of structure-dynamics-function relationship of a

large variety of protein family, such as a large hyperthermophilic protein, a membrane protein, and the native and denatured globular proteins.

First, we used quasi-elastic neutron scattering (QENS) to study the dynamics of a hyperthermophilic protein from the deep-sea on the timescale of pisosecond to nanosecond, and revealed that the dynamic property of a mesophilic protein is largely affected by the high pressure and temperature. Specifically, high pressure distorts the protein energy landscape and therefore the activity, while the hyperthermophilic protein restrains such effects.

Next, the mechanisms of light activation of a G-protein-coupled receptor (GPCR) prototype, rhodopsin, were studied using small-angle neutron scattering (SANS) and QENS. The SANS data indicated the large conformational change in rhodopsin upon photoactivation; the QENS results revealed the significant difference in the intrinsic protein dynamics between the dark-state rhodopsin and the ligand-free apoprotein, opsin. These observed conformational and dynamical differences in rhodopsin upon photoactivation are due to the influence of the covalently bound retinal chromophore. Eventually, we successfully applied the concept of generic energy landscape based upon the dynamic behavior possessed by the proteins to explain their activities.

In the third project, the phonon-like collective excitations in proteins were investigated using inelastic neutron and X-ray scattering techniques. Such excitations correspond to the intrinsic protein dynamics necessary to overcome the conformational barriers, crucial for enzyme catalysis and ligand-binding. Our data show the apparent softening of protein with rise in temperature, corresponding to the protein conformational flexibility. Specifically, our results suggest that the native globular protein balances the protein conformational flexibility and rigidity for the biological activity.

Lastly, we used small-angle X-ray scattering (SAXS) to study the conformational change in periplasmic ligand-binding protein (PBP) upon bound to peptide. The three-dimensional shape reconstruction of a periplasmic protein MppA computed from SAXS intensity profile using ab-initio modeling perfectly matches its crystal structure.

AUTOBIOGRAPHICAL STATEMENT

Utsab R. Shrestha

Education

2012 -	Ph.D. in Physics, Wayne State University
2012 - 2015	M.S in Physics, Wayne State University
2007 - 2009	M.Sc. in Physics, Tribhuvan University, Nepal
2004 - 2007	B.Sc. in Physics, Tribhuvan University, Nepal

Teaching/Research Experience

2012 -	Graduate research/teaching assistant, Wayne State University
2009 - 2012	Instructor, Gyankunj Higher Secondary School, Nepal

Awards

2016	Knoller fellowship, Wayne State University
2015 - 2016	Rumble fellowship, Wayne State University
2014 - 2016	Outstanding poster, 5^{th}, 6^{th} and 7^{th} Annual Graduate Research Conference, Physics department, Wayne State University
2015	The Shirley Chan Student Travel Award, Division of Biological Physics (DBIO), American Physical Society
2014 & 2016	Student Travel Award, American Conference on Neutron Scattering
2014	Education Travel Award, 58^{th} Annual Meeting of Biophysical Society